CARBON CYCLING IN CANADIAN COASTAL WATERS: PROCESS STUDIES OF THE SCOTIAN SHELF AND THE SOUTHEASTERN BEAUFORT SEA

by

Elizabeth H. Shadwick

Submitted in partial fulfillment of the requirements
for the degree of Doctor of Philosophy

at

Dalhousie University
Halifax, Nova Scotia
August 2010

DALHOUSIE UNIVERSITY

DEPARTMENT OF OCEANOGRAPHY

The undersigned hereby certify that they have read and recommend to the Faculty of Graduate Studies for acceptance a thesis entitled "CARBON CYCLING IN CANADIAN COASTAL WATERS: PROCESS STUDIES OF THE SCOTIAN SHELF AND THE SOUTHEASTERN BEAUFORT SEA" by Elizabeth H. Shadwick in partial fulfillment of the requirements for the degree of Doctor of Philosophy.

Dated: August 18, 2010

External Examiner: Nicholas R. Bates

Research Supervisor: Helmuth Thomas

Examining Committee: Kumiko Azetsu-Scott

Katja Fennel

Jonathan Grant

Jinyu Sheng

DALHOUSIE UNIVERSITY

DATE: August 18, 2010

AUTHOR: Elizabeth H. Shadwick

TITLE: CARBON CYCLING IN CANADIAN COASTAL WATERS: PROCESS STUDIES OF THE SCOTIAN SHELF AND THE SOUTHEASTERN BEAUFORT SEA

DEPARTMENT OR SCHOOL: Department of Oceanography

DEGREE: PhD CONVOCATION: October YEAR: 2010

Permission is herewith granted to Dalhousie University to circulate and to have copied for non-commercial purposes, at its discretion, the above title upon the request of individuals or institutions.

_____

Signature of Author

for my family

for whatever we lose (like a you or a me),
it's always our self we find in the sea.
- E. E. Cummings

TABLE OF CONTENTS

List of Tables . . . . . **x**

List of Figures . . . . . **xi**

Abstract . . . . . **xiv**

List of Symbols . . . . . **xv**

Acknowledgements . . . . . **xvi**

Chapter 1 Introduction **1**

1.1 Motivation 1

1.2 The Global Carbon Cycle 3

1.3 The Coastal Ocean 5

1.4 Continental Shelf Systems 7

1.5 The Scotian Shelf 7

1.6 The Arctic Ocean 9

1.7 The Beaufort Sea 12

1.8 Thesis Objectives 13

1.9 Thesis Outline 14

Chapter 2 Methods **15**

2.1 Carbonate Chemistry 15

2.2 Laboratory Analysis 20

2.2.1 Determination of DIC by Coulometric Titration 20

2.2.2 Determination of TA by Potentiometric Titration 21

2.2.3 Calibration with Reference Material 22

2.3 Underway pCO_2 Measurement 22

2.4 The CARIOCA Buoy 24

Chapter 3 CO_2 in the Coastal Ocean: A Case Study on the Scotian Shelf . 26
3.1 Introduction . . . 26
3.2 The Carbon Cycle and the Coastal Ocean . . . 29
3.3 Data and Methods . . . 31
3.4 Physical and Biological Conditions on the Scotian Shelf . . . 32
3.4.1 Coastal and Shelf-edge Upwelling . . . 33
3.4.2 Temperature and Salinity . . . 33
3.4.3 Winter Convection . . . 35
3.4.4 Water Mass Composition . . . 35
3.4.5 Biological Production . . . 38
3.4.6 The North Atlantic Oscillation . . . 40
3.5 The CO_2 System on the Scotian Shelf . . . 41
3.5.1 Seasonal Variations in DIC and pCO_2 . . . 44
3.5.2 Air-Sea CO_2 Fluxes . . . 48
3.6 Discussion . . . 49
3.6.1 Trophic Status and Atmospheric CO_2 . . . 49
3.6.2 Interannual Variability . . . 51
3.6.3 Ocean Acidification . . . 53
3.7 Conclusion . . . 56

Chapter 4 Seasonal Variability of DIC and pCO_2 on the Scotian Shelf . . 58
4.1 Abstract . . . 58
4.2 Introduction . . . 59
4.3 Oceanographic Setting . . . 60
4.4 Data and Methods . . . 65
4.4.1 Sampling and Analytical Procedures . . . 65
4.4.2 Application of a 1-D Model . . . 68
4.4.3 Model Inputs . . . 73
4.4.4 Error Estimation . . . 75
4.5 Results . . . 77
4.5.1 The Annual Cycle of pCO_2 . . . 77
4.5.2 The Annual Cycle of DIC . . . 80
4.5.3 Model Results . . . 82

4.5.4 Net Community Production . . . 87
4.6 Discussion . . . 89
4.6.1 Post-Bloom Summer Production . . . 89
4.6.2 Trophic Status . . . 91
4.7 Conclusion . . . 92
4.8 Acknowledgements . . . 92

Chapter 5 Air-Sea CO_2 Fluxes on the Scotian Shelf . . . 93
5.1 Abstract . . . 93
5.2 Introduction . . . 94
5.3 Oceanographic Setting . . . 94
5.4 Methods . . . 96
5.5 Results and Discussion . . . 98
5.5.1 Multiple Linear Regression . . . 98
5.5.2 Interpretation of Regression Coefficients . . . 99
5.5.3 Spatial Extapolation and Validation . . . 102
5.5.4 Seasonal and Interannual Variability of pCO_2 . . . 107
5.5.5 Multi-Annual Variability of pCO_2 . . . 109
5.5.6 Shelf-Wide CO_2 Fluxes . . . 111
5.5.7 The Scotian Shelf in the Larger Global Context . . . 118
5.6 Conclusion . . . 121
5.7 Acknowledgements . . . 121
5.8 Appendix A: Interpretation of the SST Regression Coefficient . . . 122
5.9 Appendix B: Sable Island Winds Versus Model Winds . . . 125

Chapter 6 Inorganic Carbon in the Arctic Archipelago . . . 127
6.1 Abstract . . . 127
6.2 Introduction . . . 128
6.3 Oceanographic Setting . . . 130
6.4 Data and Methods . . . 132
6.4.1 Sample Collection and Analysis . . . 132
6.4.2 Water Mass Definitions . . . 133
6.5 Results . . . 135

6.5.1 Water mass Composition . . . 135
6.5.2 The Carbonate System . . . 136
6.5.3 Deep Water Carbon Storage . . . 141
6.5.4 Carbon Export to the North Atlantic . . . 145
6.5.5 Impact of Increased Sea-ice Melt . . . 146
6.6 Conclusions . . . 147
6.7 Acknowledgments . . . 148

Chapter 7 Seasonal Variability of the CO_2 System in Amundsen Gulf . . . 149
7.1 Abstract . . . 149
7.2 Introduction . . . 150
7.3 Oceanographic Setting . . . 151
7.4 Methods . . . 153
7.4.1 Sampling and Analytical Measurements . . . 153
7.4.2 Model Description . . . 156
7.4.3 Advection . . . 157
7.4.4 Freshwater . . . 159
7.4.5 Air-Sea CO_2 Flux . . . 160
7.4.6 Diffusion . . . 161
7.4.7 Biological Processes . . . 162
7.4.8 Error Estimation . . . 163
7.4.9 Dissolved Organic Carbon . . . 164
7.5 Results . . . 165
7.5.1 Annual Cycles . . . 168
7.5.2 Processes Controlling Variability of DIC and TA . . . 173
7.5.3 Atmospheric CO_2 Uptake . . . 175
7.6 Discussion . . . 176
7.6.1 Nutrient Uptake and Net Community Production . . . 176
7.6.2 Surface CO_2 Undersaturation . . . 180
7.7 Conclusion . . . 182
7.8 Acknowledgments . . . 183

Chapter 8 Conclusion 188
8.1 The Scotian Shelf 188
8.2 Amundsen Gulf 190
8.3 Similarities and Differences 191
8.4 Perspectives 195
8.4.1 Natural versus Anthropogenic Variability 195
8.4.2 Arctic Sea-Ice Retreat 196
8.4.3 Carbon-based Approaches to Constrain Remote-Sensing 197

Bibliography 199

List of Tables

Table 2.1 Concentrations of conservative ions in seawater 18

Table 4.1 Comparison of independent observations of pCO_2. 68

Table 4.2 Monthly estimates of each of the terms in Eq. 4.6. 83

Table 5.1 Notation for different time-series of chlorophyll-a 97

Table 5.2 Non-standardized and normalized regression coefficients 99

Table 5.3 Comparison of pCO_2(MLR) with 3 independent observations . . . 108

Table 5.4 Shelf wide annual air-sea CO_2 fluxes on the Scotian Shelf 118

Table 6.1 End-member properties for water masses in the Arctic Archepelago 134

Table 7.1 Monthly estimates of percentage ice-cover in Amundsen Gulf . . . 161

Table 7.2 Estimates of uncertainty associated with the terms in Eqs. 7.3 to 7.8 164

Table 7.3 Concentrations of DIC in sea-ice 171

Table 7.4 Monthly and annual estimates of NCP and air-sea CO_2 flux 177

Table 8.1 Comparison between controls of DIC on the Scotian Shelf and in Amundsen Gulf 193

LIST OF FIGURES

Figure 1.1 Reconstructed temperature, CO_2, and dust from the Vostok ice core 2

Figure 1.2 Atmospheric CO_2 measured at Mauna Loa, Hawaii 3

Figure 1.3 The present-day global carbon cycle 4

Figure 1.4 Sampling stations as part of the AZMP program 8

Figure 1.5 Bathymetric map of the Arctic Ocean 10

Figure 1.6 Schematic representation of the Arctic halocline 11

Figure 1.7 Sampling stations as part of the CFL program 13

Figure 2.1 The speciation of carbonic acid in seawater as a function of pH . . 17

Figure 2.2 The coulometric titration cell assembly 22

Figure 2.3 Instrumentation of the CARIOCA buoy 25

Figure 3.1 Oceanographic setting on the Scotian Shelf 30

Figure 3.2 Surface temperature and salinity on the Scotian Shelf 34

Figure 3.3 Sections of temperature and salinity along the Halifax Line 36

Figure 3.4 A climatology of the central Scotian Shelf 37

Figure 3.5 Relationship between TA, $\delta^{18}O$, and salinity on the Scotian Shelf . 39

Figure 3.6 The effect of various processes on DIC and TA 42

Figure 3.7 Surface pCO_2 corrected for the effect of water temperature 45

Figure 3.8 Sections of DIC and TA along the Halifax Line 47

Figure 3.9 Hourly surface water pCO_2 from an autonomous mooring 48

Figure 3.10 Seasonal profiles of DIC 49

Figure 3.11 Annual cycles of wind speed and air-sea CO_2 flux 50

Figure 3.12 Sea surface temperature anomaly 52

Figure 3.13 Profiles of pCO_2, pH, and Ω_{ar} along the Halifax Line 54

Figure 4.1 Locations of sampling stations on the Scotian Shelf 61

Figure 4.2 Seasonal maps of SST on the Scotian Shelf 62

Figure 4.3 A climatology of the central Scotian Shelf 64
Figure 4.4 Hourly pCO_2 measured by the CARIOCA buoy 66
Figure 4.5 Annual cycles of SST and surface salinity at station HL2 67
Figure 4.6 The relationship between TA and salinity on the Scotian Shelf . . . 69
Figure 4.7 Annual cycles of surface DIC and TA at station HL2 70
Figure 4.8 Schematic representation of the box-model used at station HL2 . . 72
Figure 4.9 Annual cycle of mixed-layer depth at station HL2 73
Figure 4.10 The relationship between DIC and salinity on the Scotian Shelf . . 74
Figure 4.11 Profiles of DIC and AOU at station HL2 75
Figure 4.12 Temperature-normalized surface pCO_2 at station HL2 79
Figure 4.13 Annual cycle of air-sea CO_2 fluxes at station HL2 81
Figure 4.14 Annual cycles of each of the terms in Eq. 4.6 85
Figure 4.15 Controls on DIC and pCO_2 at station HL2 86
Figure 4.16 Annual cycle of chl-a concentration and biomass at station HL2 . . 88

Figure 5.1 The hydrographic setting on the Scotian Shelf 95
Figure 5.2 The relationship between k and mixed-layer depth 101
Figure 5.3 Model controls on pCO_2 101
Figure 5.4 Locations of grid boxes for spatial extrapolation 102
Figure 5.5 Satellite-derived SST and Chl-a 104
Figure 5.6 Validation of pCO_2(MLR) for grid boxes 1 through 4 106
Figure 5.7 Validation of pCO_2(MLR) for grid boxes 5 through 7 107
Figure 5.8 Monthly values of SST, k, pCO_2 and air-sea CO_2 flux 110
Figure 5.9 SST and ΔpCO_2 and atmospheric CO_2 anomalies 112
Figure 5.10 Annual mean surface Chl-a from 1999 to 2008 114
Figure 5.11 Annual mean SST from 1999 to 2008 115
Figure 5.12 Annual mean surface pCO_2 from 1999 to 2008 116
Figure 5.13 Shelf-wide air-sea CO_2 fluxes from 1999 to 2008 117
Figure 5.14 A comparison of the Scotian Shelf and Amundsen Gulf CO_2 systems 120
Figure 5.15 Frequency analysis of the SST regression coefficient 124

Figure 5.16 Comparison between observed and modelled wind speed 126
Figure 5.17 Comparison between fluxes computed with different winds 126

Figure 6.1 Locations of sampling stations in the Arctic Archipelago 131
Figure 6.2 Fractions of meteoric and sea-ice melt water 135
Figure 6.3 Profiles of DIC and TA in the Arctic Archipelago 137
Figure 6.4 Profiles of pH and Ω_{Ar} in the Arctic Archipelago 138
Figure 6.5 The inorganic carbon system in the Arctic Archipelago 139
Figure 6.6 Salinity-normalized DIC in the Arctic Archipelago 142
Figure 6.7 Subsurface concentrations of DIC and AOU 144

Figure 7.1 Oceanographic setting in Amundsen Gulf 152
Figure 7.2 Locations of sampling stations in Amundsen Gulf 154
Figure 7.3 Schematic representation of the two-box model 157
Figure 7.4 Changes in surface TA versus changes in surface salinity 160
Figure 7.5 Property plots of the inorganic carbon system in Amundsen Gulf . 167
Figure 7.6 Temporal evolution water properties 170
Figure 7.7 Seasonal profiles of salinity, DIC, TA, pCO_2, pH, and Ω_{ar} 172
Figure 7.8 Controls on DIC, TA, and DOC in Amundsen Gulf 184
Figure 7.9 The annual cycle of air-sea CO_2 flux in Amundsen Gulf 185
Figure 7.10 Annual cycle of NCP in Amundsen Gulf 185
Figure 7.11 A DIC budget for Amundsen Gulf 186
Figure 7.12 Biologically-mediated changes in DIC in Amundsen Gulf 187

Figure 8.1 Comparison of the Scotian Shelf and Amundsen Gulf systems . . . 194

ABSTRACT

Much research has been devoted to understanding the ocean carbon cycle because of its prominent role in controlling global climate. Coastal oceans remain a source of uncertainty in global ocean carbon budgets due to their individual characteristics and their high spatial and temporal variability. Recent attempts to establish general patterns suggest that temperate and high-latitude coastal oceans act as sinks for atmospheric carbon dioxide (CO_2). In this thesis, carbon cycling in two Canadian coastal ocean regions is investigated, and the uptake of atmospheric CO_2 is quantified.

A combination of ship-board measurements and highly temporally resolved data from an autonomous mooring was used to quantify the seasonal to multi-annual variability in the inorganic carbon system in the Scotian Shelf region of the northwestern Atlantic for the first time. The Scotian Shelf, unlike other shelf seas at similar latitude, acts as a source of CO_2 to the atmosphere, with fluxes varying over two orders of magnitude in space and time between 1999 and 2008.

The first observations of the inorganic carbon system in the Amundsen Gulf region of the southern Beaufort Sea, covering the full annual cycle, are also presented. Air-sea CO_2 fluxes are computed and a carbon budget is balanced. The Amundsen Gulf system acts as a moderate sink for atmospheric CO_2; seasonal ice-cover limits winter CO_2 uptake despite the continued undersaturation of the surface waters. Biological production precedes the ice break-up, and the growth of under-ice algae constitutes nearly 40% of the annual net community production.

The Scotian Shelf may be described as an estuarine system with an outflow of surface water, and intrusion of carbon-rich subsurface water by a combination of wind-driven mixing, upwelling and convection, which fuels the CO_2 release to the atmosphere. In contrast, Amundsen Gulf may be described an anti-estuarine, or downwelling, system, with an inflow of surface waters and an outflow of subsurface waters. Wind-driven and convective mixing are inhibited by ice-cover and restrict the intrusion of carbon- and nutrient-rich waters from below, maintaining the CO_2 uptake by the surface waters.

LIST OF SYMBOLS

Roman symbol	Description	Units
AOU	Apparent Oxygen Utilization	μmol kg^{-1}
Chl-a	Chlorophyll-a concentration	μg m^{-3}
CO_2	Carbon Dioxide	no units
DIC	Dissolved Inorganic Carbon	μmol kg^{-1}
DOC	Dissolved Organic Carbon	μmol kg^{-1}
k	gas transfer velocity	cm hr^{-1}
NCP	net community production	mol m^{-2} yr^{-1}
pCO_2	partial pressure of CO_2	μatm
POC	Particulate Organic Carbon	μmol kg^{-1}
SST	sea-surface temperature	°C
TA	Total Alkalinity	μmol kg^{-1}

Greek symbol	Description	Units
α	coefficient of solubility	mol m^{-3} atm^{-1}
Ω	calcium carbonate saturation state	no units

ACKNOWLEDGEMENTS

First and foremost, I thank my supervisor Helmuth Thomas for his encouragement, support and guidance over the past four years. I have been fortunate to have a supervisor whose door was always open, and who made me feel from the first day that I was working with him and not only for him. Helmuth has spent many hours and days, if not weeks answering my endless questions about oceanography and carbon chemistry, and preparing me for cruises and conferences. All of the work presented in this thesis has been immeasurably improved by the long discussions we've had and the thoughtful comments Helmuth has made.

I am grateful to John Cullen and Keith Thompson for their valuable input on several of my thesis chapters. I thank Kumiko Azetsu-Scott for her advice and support, and also for the use of her lab at B.I.O and her help getting me organized for my many cruises on the Hudson. I am grateful to Katja Fennel, Jon Grant and Jinyu Sheng for their role as committee members and for their feedback on my research. I'd like to thank Erica Head, Ed Horne, and Jeff Spry for making my cruises on the Hudson such a pleasure and for the all the help they have given over the last four years. I'm grateful to Blair Greenan for his work with the CARIOCA buoy and to Richard Davis for his help with the initial data processing. I thank Tim Papakyriakou for the opportunity to return to the Arctic, and both Tim and Brent for their help with the collection and analysis of data. Thank you to Friederike, Doris, and Stephanie for their help collecting field data.

I am grateful to my mom for all her support over the many, many, years I've been a student, and to my dad for inspiring me to pursue the highest level of education. I am so very thankful for my brother William without whom I would be utterly lost. Thank you to friends, both old and new, for the laughter and the memories. Thank you especially to Debbie, Josee, Laura, Ramon, Eve, Dan, Alexis, Myriam and Sebastian; without you my time in the Arctic would have been a much smaller adventure. Thank you to Katy, Amy and Leah whose support is felt over great distances. Finally, I am grateful for, and to, Stéphane who simply makes everything better.

CHAPTER 1

INTRODUCTION

1.1 Motivation

Carbon dioxide is a greenhouse gas second in importance only to water vapor. The vast majority of the carbon in the atmosphere-ocean system is found in the oceans as dissolved carbon dioxide (CO_2), also called dissolved inorganic carbon (DIC). An understanding of the global carbon cycle in the past, present, and future necessitates an accurate quantification of the role played by the ocean. Ice cores from Greenland and Antarctica provide well-preserved records of atmospheric CO_2 in air-bubbles trapped within the ice (*Petit et al.*, 1999). Analyzes of these ice cores indicates that atmospheric CO_2 concentrations have varied according to the regular oscillation over the well-known glacial to interglacial cycle with a period of 100,000 years (Fig. 1.1). The concentration of atmospheric CO_2 over the last 400,000 years ranged from 200 to 290 ppm (Fig. 1.1). Low atmospheric CO_2 concentrations are associated with glacial periods, or ice-ages, and higher concentrations are associated with interglacial periods; it has been suggested these climate oscillations may be driven by oceanic processes (e.g. *Broecker*, 1987; *Toggweiler*, 1999; *Sigman and Boyle*, 2000; *Toggweiler et al.*, 2006). Today the atmospheric CO_2 concentration is roughly 390 ppm (Fig. 1.2); the burning of fossil fuels, agricultural activity, changing land use, and deforestation have contributed to rising concentrations of atmospheric CO_2 over the last several hundred years. The invasion of this anthropogenic CO_2 to the ocean has caused a decline in surface ocean pH.

Despite their modest surface areas, compared to the open ocean, the coastal ocean and continental shelves play a significant role in the biogeochemical cycling of carbon. These regions receive a large supply of carbon and nutrients from upwelling, atmospheric and riverine inputs, and they sustain disproportionately high biological activity, given

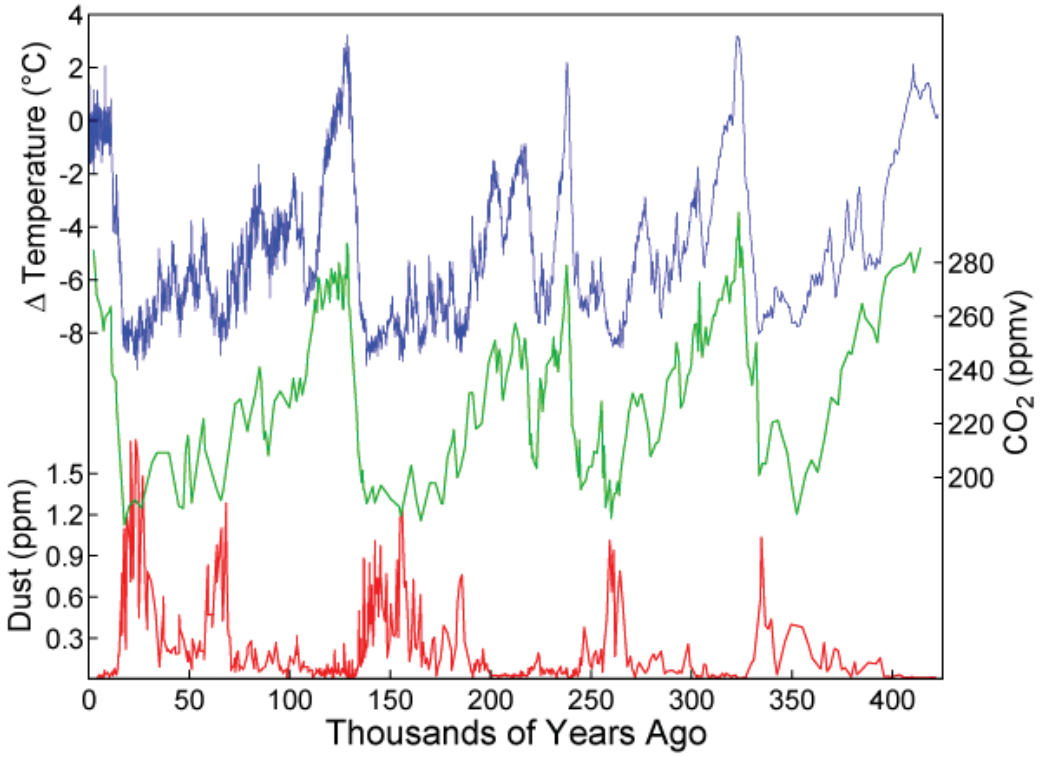

Figure 1.1: Reconstructed temperature (blue), atmospheric CO_2 (green) and dust from the Vostok ice core in Antarctica over the last 420,000 years. Figure follows *Petit et al.* (1999).

their small surface area, relative to the open ocean. The role of the coastal ocean in the global ocean uptake of atmospheric CO_2 has been under debate for some time (*Smith and Mackenzie*, 1987; *Smith and Hollibaugh*, 1993; *Cai et al.*, 2003; *Borges et al.*, 2005; *Borges*, 2005; *Bates*, 2006; *Cai et al.*, 2006). A recent synthesis of observational data suggests that globally, continental shelves act as sinks for atmospheric CO_2 (*Chen and Borges*, 2009). However, compared to the open ocean, the CO_2 system in the coastal ocean and continental shelves remains largely understudied. The research presented here is motivated by the need to characterize coastal regions with respect to their role in the ocean carbon cycle. The primary controls on seasonal variability of the inorganic carbon system in two Canadian coastal settings are investigated. This research contributes to the on-going global efforts to quantify the role of the coastal ocean in the global ocean uptake of atmospheric CO_2.

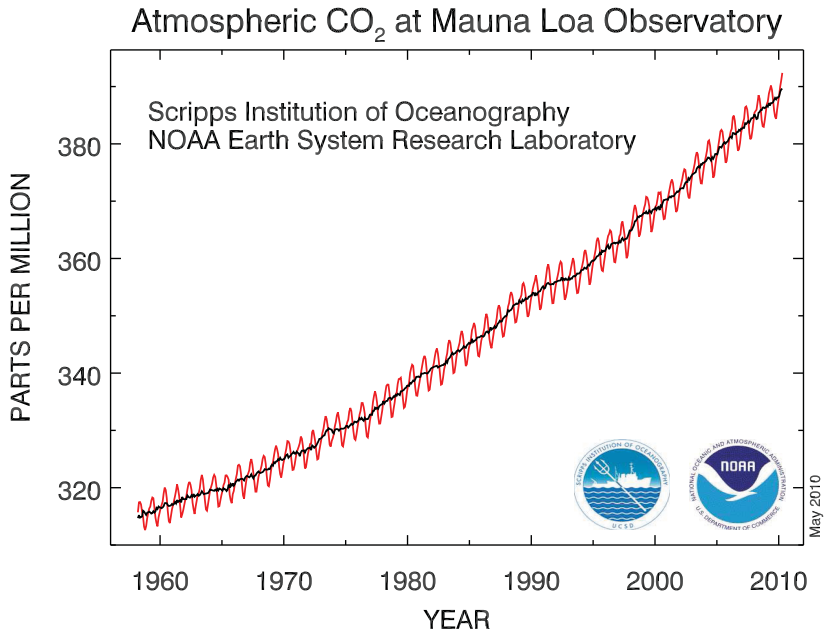

Figure 1.2: The variation in the concentration of atmospheric CO_2 since 1958 measured at Mauna Loa, Hawaii. (Figure from *Dr. Pieter Tans, NOAA/ESRL (www.esrl.noaa.gov/gmd/ccgg/trends/)*).

1.2 The Global Carbon Cycle

The carbon cycle comprises many different biological, chemical and physical processes acting to transfer carbon between the major storage pools called reservoirs. The global carbon cycle is dominated by four major carbon reservoirs: the atmosphere, the terrestrial biosphere (including plants, trees, soils and frozen soils or permafrost), the oceans, and the underlying sediments (including fossil fuel deposits and carbonate rocks). Carbon dioxide is exchanged between the atmosphere and the ocean by gas transfer, and between biota and the other reservoirs by photosynthesis and respiration, while rivers play an important role in the delivery of dissolved and particulate carbon from land to the ocean. Hundreds of millions of years ago, and over millions of years, this cycle drove the formation of the fossil fuels that provide energy to our modern societies.

The global carbon budget is a balance of the exchanges of carbon that take place between these reservoirs (Fig. 1.3). In pre-industrial times, the carbon system was in roughly steady state with fluxes into and out of the carbon reservoirs in balance. The release of CO_2 into the atmosphere by the combustion of these fossil fuels has increased

pre-industrial concentrations from roughly 280 ppm to present day levels of nearly 390 ppm (Fig. 1.2) (*Kling et al.*, 2007). Over only decades the combustion of fossil fuels releases quantities of carbon to the atmosphere that accumulated in the fossil fuel reservoirs over millions of years. The conversion of tropical forest to agricultural land releases additional CO_2 to the atmosphere. The anthropogenic release of CO_2 is currently larger than can be balanced by (natural) biological and geological removal processes which act over much longer timescales.

Roughly half of the anthropogenic CO_2 emitted to the atmosphere is taken up by the ocean (*Sabine et al.*, 2004). Phytoplankton convert CO_2 to particulate organic carbon (POC), a portion of which is transported out of the surface layer by sinking, and therefore removed from the atmosphere by a combination of biological and physical processes (*Gruber and Sarmiento*, 2002). The oceans act as a significant reservoir for inorganic carbon, containing 50 times more CO_2 than the atmosphere (*Kling et al.*, 2007). Small changes in the ocean carbon cycle can thus influence atmospheric CO_2 concentrations (*Zeebe and Wolf-Gladrow*, 2001). The need to accurately balance the ocean carbon cycle is therefore an important issue in current global climate research.

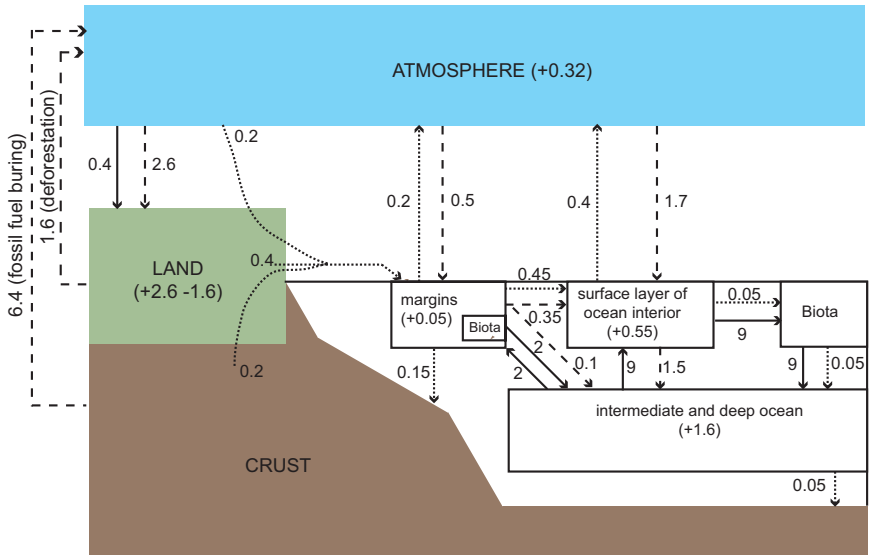

Figure 1.3: The present-day global carbon cycle. The fluxes are in units of Pg C yr^{-1}. The dotted arrows indicate the fate of terrigenous carbon discharged to the ocean. The dashed arrows represent anthropogenic carbon fluxes. The values in parentheses indicate the rate of increase (Pg C yr^{-1}) for a given reservoir. The figure modified from *Thomas et al.* (2009a).

1.3 The Coastal Ocean

Despite tremendous efforts during the last decade (*Sabine et al.*, 2004; *Takahashi et al.*, 2009), the assessment of the ocean sink for CO_2 still remains subject to uncertainty. One of the reasons for this uncertainty is the fact that coastal and shelf seas have, to a large extent, been ignored in estimates of global carbon budgets. Carbon dioxide constitutes the main carbon carrier between the atmosphere and the coastal ocean, thereby linking atmospheric, terrestrial and open ocean regimes. The CO_2 cycle in the coastal ocean is influenced by terrestrial runoff, upwelling and mixing of carbon-rich waters from below the surface, photosynthesis, respiration, the production and consumption of dissolved organic matter, and air-sea exchange of CO_2. Although coastal oceans represents only 8% of the total ocean surface area (*Wollast*, 1991), they makes a disproportionately high contribution to the global ocean biological production and to carbon and nutrient fluxes in the marine environment (*Gattuso et al.*, 1998; *Borges*, 2005; *Borges et al.*, 2005). Roughly one-fifth to one-third, of the global marine primary production takes place in these seas (*Wollast*, 1991; *Gattuso et al.*, 1998). Furthermore, in coastal environments the ocean's biological pump operates more efficiently than in the open ocean (*Chavez et al.*, 2007). The coastal ocean plays a prominent role in the absorption of atmospheric CO_2, potentially transferring it to the deep ocean via the continental shelf pump - a mechanism that feeds cold, dense, carbon-rich waters from the shelf region to the sub-surface waters of the adjacent deep ocean (*Tsunogai et al.*, 1999; *Thomas et al.*, 2004; *Bozec et al.*, 2005).

Sustained time-series measurements of physical and biogeochemical variables have done much to resolve uncertainties in carbon cycling for a few important study sites (e.g., Bermuda, Hawaii) (*Bates et al.*, 1996; *Karl and Lukas*, 1996), and the applications of sustained measurements to coastal regions has increased in recent years (*Hood and Merlivat*, 2001; *Lefèvre et al.*, 2002; *Schiettecatte et al.*, 2006, 2007; *Omar et al.*, 2010). Carbon fluxes have been investigated in several coastal ocean and continental shelf regions in the last few years (e.g., *Peng et al.*, 1999; *Thomas and Schneider*, 1999; *Frankignoulle and Borges*, 2001; *DeGrandpre et al.*, 2002; *Cai et al.*, 2003; *Thomas et al.*, 2005b; *Bozec et al.*, 2006; *Jiang et al.*, 2008). However, these environments exhibit strong spatial and temporal heterogeneity, and integrative global assessments have not yet achieved high fidelity (*Borges*, 2005).

Bulk carbon budgets have recently been established for several coastal ocean regions.

The North Sea, for example, acts as a net sink for CO_2 in the summer season, with this absorbed carbon then exported to the North Atlantic (*Bozec et al.*, 2005; *Thomas et al.*, 2005b). Both the East China Sea and the West Florida Shelf have been shown to act as sinks for atmospheric CO_2 in spring, though these estimates were based on limited data (*Peng et al.*, 1999). A carbon budget for the Arctic Ocean shows that this region acts as a moderate net sink for atmospheric CO_2 (*Anderson et al.*, 1998a). In all cases the establishment of an accurate water budget is essential, since gross and net carbon fluxes associated with water mass transport are usually the dominant terms in the overall carbon budget (*Peng et al.*, 1999; *Thomas et al.*, 2005b). While some biological and physical mechanisms can be inferred, the individual characteristics of specific coastal regions will determine whether the system acts as a net source or sink for atmospheric CO_2, emphasizing the requirement of individual regional assessments (*Borges et al.*, 2005).

There have been attempts to extrapolate the results of regional assessments to a broader scale by using classification schemes such as 'degree of openness' and 'freshwater influence' (*Chen and Borges*, 2009; *Urban et al.*, 2009). However, these attempts have been largely unsuccessful due to the importance of the individual biogeochemical characteristics, such as ecosystem diversity and the carbon system characteristics of the freshwater source (*Cai et al.*, 2003; *Borges*, 2005). In a recent synthesis of available observational data for the coastal oceans, *Chen and Borges* (2009) suggest that the majority of continental shelf seas in temperate and high-latitude regions tend to act as sinks for atmospheric CO_2 annually, while shelves in lower-latitude regions tend to be oversaturated with respect to the atmosphere, and act as sources of CO_2. The research presented here includes a case study of the CO_2 system in a temperate (Scotian Shelf), and a high-latitude (Amundsen Gulf) continental shelf region. In the case of the Scotian Shelf, the direction of the annual air-sea flux opposes the general trend found in the global synthesis of *Chen and Borges* (2009). It is unlikely that the results reported here would be appropriately extrapolated to other regions. Instead these findings highlight the need for case-by-case assessments of coatal ocean carbon systems to better constrain the global contribution from these regions. This work contributes to the on-going effort to understand the carbon system in the global coastal ocean by characterizing two Canadian continental shelf systems.

1.4 Continental Shelf Systems

The continental shelf is the extended perimeter of the continent. These shelves were part of the continents during glacial periods, but are under water during interglacial periods such as the present day. The continental shelves are covered with relatively shallow seas, which are also referred to as continental margins, regional seas or the coastal ocean. Because of the important role that these regions play in global biogeochemical cycling of carbon and nutrients, they have been the recent focus of several global scale programs[1] (*Chen et al.*, 2003; *Chen and Borges*, 2009). *Meybeck et al.* (2007) define a regional sea or coastal ocean as a partially enclosed portion of the ocean that has limited exchange of water, and dissolved and particulate matter, with the open ocean. The same definition has been employed in the research presented here. These regional seas, or coastal oceans, are further classified according to the degree of connection with the open ocean and the width of the continental shelf (*Meybeck et al.*, 2007). According to this classification scheme, the Scotian Shelf is considered an 'open' regional sea system, which is not separated from the open ocean by narrows, and it's boundary with the ocean is dominated by coastline. The Arctic Archipelago is, by contrast, considered the archetype of a 'coastal archipelago', dominated by islands on a wide continental shelf (*Meybeck et al.*, 2007).

1.5 The Scotian Shelf

The Scotian Shelf is a highly productive area of the Canadian northwestern Atlantic ocean. This shelf region hosts active fisheries and aquaculture, and is also impacted by oil and gas exploration. The Scotian Shelf plays an important role in the carbon cycling of the North Atlantic Ocean as a whole. The circulation on the Scotian Shelf is dominated by Labrador Current and the Gulf Stream. The Scotian Shelf is uniquely positioned at the junction between the subpolar and subtropical gyres (*Greatbatch*, 2000). One of the dominant climate modes influencing circulation and hydrographic conditions in the region is the North Atlantic Oscillation (NAO) (*Petrie*, 2007). The NAO driven variability has the potential to mask longer-term trends in the carbon cycle on the Scotian Shelf[2].

[1] e.g. Joint Global Ocean Flux Study (JGOFS), Land-Ocean Interaction in the Coastal Zone (LOICZ), Integrated Marine Biogeochemistry and Ecosystem Research (IMBER), and a partnership between these two called the Continental Margins Task Team (CMTT)

[2] A more complete description of the Scotian Shelf region is given in Chapter 3.

Inorganic carbon data was collected in the region from 2006 to 2008. Using a combination of ship-board sampling (see section 2.2 and Chapter 3), an autonomous mooring (see section 2.3), and remotely-sensed data (Chapter 5) a quantitative assessment of the processes controlling variability in the CO_2 system on the Scotian Shelf over seasonal, interannual, and multi-annual timescales was made.

The Canadian Department of Fisheries and Oceans (DFO) implemented the Atlantic Zone Monitoring Program (AZMP) in 1998. The primary goal of the AZMP is the maintenance of a long-term, relatively high temporal resolution, observational program in the Canadian Northwestern Atlantic Ocean. To this end, the collection and analysis of physical, chemical, and biological data was carried out on twice annual cruises along four primary transect lines (Fig 1.4), with more frequent sampling occurring at a number of fixed stations. The AZMP cruises took place aboard the CCGS Hudson in spring and autumn each year. The duration of each cruise was approximately 3 weeks. Samples were collected at roughly 40 stations along four transect lines.

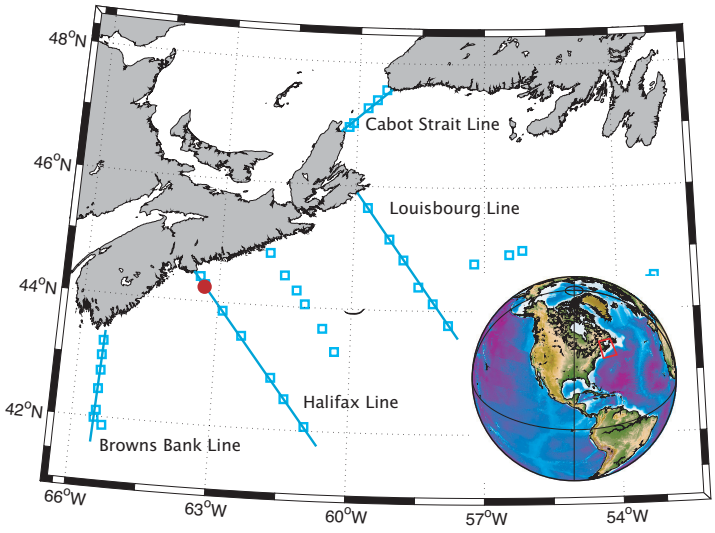

Figure 1.4: Locations of stations sampled along four primary transect lines on the Scotian Shelf as part of the AZMP. Open squares indicate stations sampled on twice annual cruises in April and September. Additional stations, also shown by the open blue squares, outside of the primary transects are occupied if time permits. The location of station 'Halifax Line 2' (HL2) is indicated by the red circle.

1.6 The Arctic Ocean

The Arctic Ocean is the most land-dominated of all the ocean basins. The Arctic Ocean is largely enclosed by the numerous islands of the Canadian Arctic Archipelago and the extended platform of the Siberian shelf (Fig. 1.5). Pacific water enters the Arctic Ocean through the narrow, relatively shallow, Bering Strait. This water is diverted westward along the shelf to the Chukchi Sea, and eastward toward the Canadian Archipelago via the Alaska Coastal Current (*Mathis et al.*, 2007). Sea-ice is formed when cold polar winds blow over the relatively shallow Chukchi Sea. Warm, salty, Atlantic water enters the Arctic Ocean at the surface through the Greenland and Norwegian Seas; these waters cool and sink (*Rudels et al.*, 1996). The formation of sea-ice removes fresh water from the surface; the rejected brine is dense and sinks (Fig. 1.6). These dense waters make up the Arctic halocline, a layer of cold water that acts as a barrier between the sea-ice and surface water and the deeper, warmer, Atlantic-origin, water (*Rudels et al.*, 1996). The presence of this halocline barrier prevents the heat from the Atlantic water from warming the upper water column and melting the sea ice.

River inflow to the Arctic is dominated, on a volume basis, by Eurasian rivers, with their North American counterparts playing a lesser role. Attempts to quantitatively describe the freshwater budget for this region have been made (*Anderson et al.*, 2004; *Peterson et al.*, 2006; *Serreze et al.*, 2006), though observational data remain sparse. Despite the paucity of long term observational data, a trend has emerged from the studies carried out in the Arctic: a significant, sustained, and wide spread freshening of the waters has taken place over the last decades (*McPhee et al.*, 1998; *Dickson*, 1999; *Johnson and Polyakov*, 2001; *Lammers et al.*, 2001; *Peterson et al.*, 2002, 2006). The Arctic Ocean plays an important role in the global ocean circulation; the formation of North Atlantic Deep water occurs in the Norwegian Sea (Fig. 1.5). North Atlantic Deep Water (NADW) is comprised of water from the Labrador Sea, the Denmark Strait Overflow, and the Greenland Sea. The formation of NADW is an important feature of the global thermohaline circulation enabling the Gulf Stream to transport heat from the tropics northward towards Europe. It has been suggested that a freshening of the Arctic Ocean may have consequences for NADW formation (*Peterson et al.*, 2002); the formation of a low salinity surface layer may increase stratification enough to hinder the formation of deep water in the North Atlantic (*Rahmstorf*, 2002).

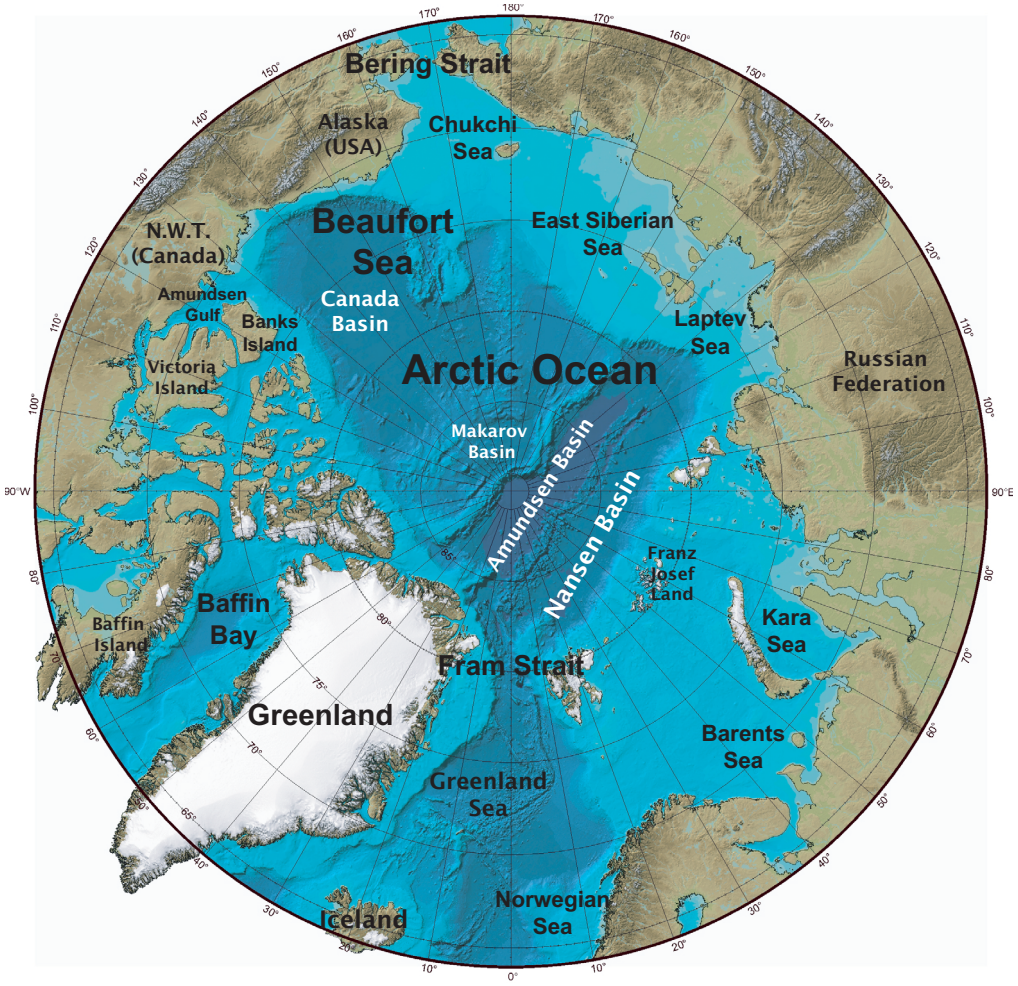

Figure 1.5: A bathymetric map of the Arctic Ocean and surrounding continental shelf and regional seas (*Jakobsson et al.*, 2008).

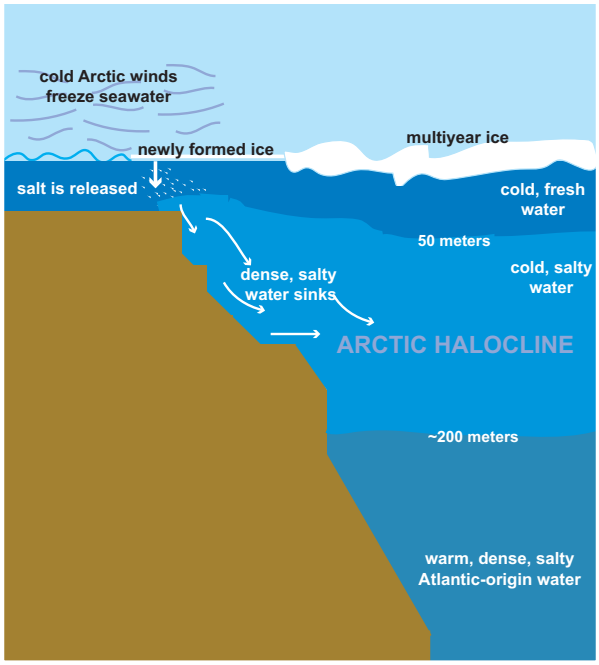

Figure 1.6: A schematic representation of the Arctic halocline. Sea-ice formation releases salt increasing the density of the water and forcing it to sink below the surface. This forms a barrier between the cold, fresh surface water and the warm, salty Atlantic bottom water.

The Arctic Ocean constitutes the link between the North Pacific and North Atlantic Oceans. Thus, anthropogenic changes occurring in the Arctic may be propagated downstream to the sub-polar North Atlantic. These changes are not limited to physical processes (e.g. freshening); high latitude and polar ocean's are expected to be the first to experience aragonite undersaturation as a consequence of anthropogenic CO_2 uptake (*Orr et al.*, 2005). However, due to the paucity of data in this remote region, the Arctic Ocean's role in the global ocean carbon cycle is often underestimated or neglected. As a result, only a few baseline assessments of the carbon system in the Arctic have been made, focused largely on data collected in the ice-free summer and autumn periods (e.g. *Anderson et al.*, 1998a,b; *Fransson et al.*, 2001; *Bates et al.*, 2005; *Kaltin and Anderson*, 2005), and these assessments remain largely unconnected (*Bates and Mathis*, 2009). Before a reliable assessment of the vulnerability of this system to climate change can be made, present-day carbon stocks must be quantified, and natural variability understood. To address this need, the inorganic carbon system in the Amundsen Gulf region of the southern Beaufort is investigated over a complete annual cycle and the dominant processes quantified (Chapter 7).

1.7 The Beaufort Sea

The Beaufort Sea is located north and west of a bottom topography-following path joining Point Barrow, Alaska, and Prince Patrick Island in the Canadian Archipelago, with a surface area of roughly 4.5×10^5 km^2. The Beaufort Sea plays an integral role in the circulation of the Arctic Ocean as a whole. The surface circulation in the Beaufort Sea is dominated by the anticyclonic Beaufort Gyre which can, depending on the year, extend northward through the Canada Basin to reach the Markarov Basin (*Aagaard*, 1984) (Fig. 1.5). The Beaufort Gyre, a wind-driven circulation caused by a mean anticyclonic high pressure dome in the atmosphere, maintains the high concentrations of sea-ice in the central Arctic Ocean (*Macdonald et al.*, 1999). The flow of subsurface waters is reversed, dominated by the cyclonic Beaufort Undercurrent (*Aagaard*, 1984; *Carmack and MacDonald*, 2002).

The southern Beaufort Sea is influenced by the Mackenzie River. The Mackenzie discharges roughly 2.9×10^{11} m^3 yr^{-1} of freshwater (*Stewart et al.*, 1998), making it the fourth largest Arctic river after the Yenisei, the Lena and the Ob, and the largest river in the North American sector of the Arctic. The Mackenzie discharges to the Arctic Ocean via a vast delta which is an important site for large colonies of sea birds, fish and marine mammals (*Carmack and MacDonald*, 2002). There are two canyons on the Mackenzie shelf (Mackenzie and Kugmallit), oriented perpendicularly to the coast, where upwelling events have been observed, particularly under north-east winds (*Carmack and MacDonald*, 2002; *Lanos*, 2009). Amundsen Gulf is situated in the southeastern Beaufort Sea (Fig. 1.5). It is bounded to the north by Banks Island, to the East by Victoria Island, and to the south by the coast of the North West Territories. Amundsen Gulf is open on the western side where it communicates with the Beaufort Sea through a 150 km gateway between Cape Bathurst and Banks Island. A recurrent physical feature in the region is the Cape Bathurst polynya. The polynya exhibits strong interannual variability with respect to the extent and timing of the polynya opening (*Arrigo et al.*, 2008; *Lanos*, 2009). In general the polynya opens in mid- to late-June and the open water season in Amundsen Gulf extends well into October.

Data from the Arctic Archipelago and the Amundsen Gulf regions were collected as part of the Circumpolar Flaw Lead (CFL) System Study. The CFL project was one of the largest International Polar Year (IPY) field programs in the Arctic. The project was

carried out on board the CCGS Amundsen in the Southern Beaufort Sea, south of Banks Island, NWT, and primarily in Amundsen Gulf, from October 2007 to August 2008 (Fig. 1.7). Throughout the winter months the ship was deliberately frozen into the ice, making weekly visits to the open flaw lead system and affording us the opportunity to over-winter the icebreaker the study region. Our group at Dalhousie collectively manned 8, 6-week legs over the course of the 13-month field season. Research groups from McGill University, the University of Manitoba, and the Institute of Ocean Sciences, complemented the annual sampling with support from colleagues from Gothenburg University in Sweden.

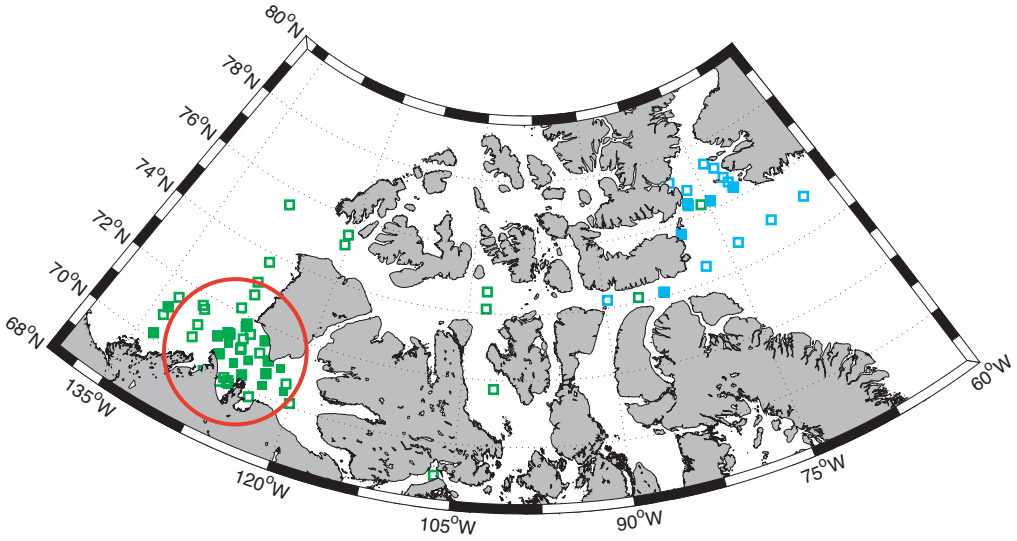

Figure 1.7: Locations of stations occupied as part of the CFL project from October 2007 to August 2008 (green) and stations occupied on ArcticNet cruises (blue) in September 2007, and September 2008. Open symbols indicate stations that were occupied only once, and closed symbols indicate stations that were occupied more than once. The Amundsen Gulf region is enclosed by the red circle.

1.8 Thesis Objectives

The overarching goal of this research was to quantify the coastal ocean uptake of atmospheric CO_2 on the Scotian Shelf, and in Amundsen Gulf. More specifically, on the Scotian Shelf, the objectives were to identify and quantify the controls on the seasonal variability of mixed-layer dissolved inorganic carbon (DIC) and partial pressure of CO_2 (pCO_2). This analysis was extrapolated spatially and temporally to inter- and multi-annual timescales with the application of remotely sensed data. Similarly, in Amundsen Gulf, the

objective was to investigate the full annual cycle of the carbonate system and to quantify the processes controlling the variability in this region. An additional objective pertaining to the Arctic Archipelago was to determine the distribution of water masses and carbon characteristics in the region, and to estimate the eastward transport of carbon to the North Atlantic.

1.9 Thesis Outline

This thesis is organized as follows: Chapter 2 gives an overview of the carbonate system in seawater, a description of the laboratory methods used in the analysis of water samples collected, along with a detailed description of the acquisition of pCO_2 data from an autonomous mooring. Chapter 3 is a synthesis of the general characteristics of the carbonate system on the Scotian Shelf and may be considered as a case study of the CO_2 system in a coastal environment. Chapters 4 through 7 are manuscripts that have been submitted to peer-reviewed journals, with the content of the chapter consistent with the submitted manuscript. Therefore, each of these chapters begins with a general introduction describing the objectives presented in each article. Similarly, the methods used are described in each chapter and the results are presented and discussed. Chapter 4 focuses on the seasonal variability of mixed-layer pCO_2 and DIC on the Scotian Shelf. Chapter 5 builds on the results obtained in Chapter 4 and extends the analysis both spatially and in time; a 10-year hind-cast of pCO_2 and air-sea CO_2 fluxes on the Scotian Shelf is presented. Chapter 6 focuses on the export of inorganic carbon in the Arctic Archipelago, both from the surface to subsurface layer, and from the Pacific to the Atlantic. Chapter 7 presents the full annual cycle of the CO_2 system in the Amundsen Gulf region, and the major controls on seasonal variability are investigated. Chapter 8 is comprised of a synthesis of the preceding chapters and the implications of this research are discussed in a wider context.

CHAPTER 2

METHODS

This chapter gives an overview of the methods used, and only briefly presented, in Chapters 4 through 7. A description of the carbonate system in the ocean is given, along with the system of equations used to compute unknown parameters from measured variables. The laboratory methods used in the analysis of sea water samples to determine the concentrations of dissolved inorganic carbon (DIC) and total alkalinity (TA) are described in detail. Details of the ship-board underway system used to measure surface water CO_2 partial pressure (pCO_2) are also presented. Finally, a description of the acquisition of continuous pCO_2 data from the autonomous, moored, CARIOCA buoy is given.

2.1 Carbonate Chemistry

Carbon dioxide exists in the ocean in four different species: aqueous carbon dioxide (CO_2), carbonic acid (H_2CO_3), bicarbonate (HCO_3^-), and carbonate ion (CO_3^{2-}). The carbonate species are related by the following equilibrium reactions:

$$CO_2 + H_2O \leftrightarrow H_2CO_3 \tag{2.1}$$

$$H_2CO_3 \leftrightarrow H^+ + HCO_3^- \tag{2.2}$$

$$HCO_3^- \leftrightarrow H^+ + CO_3^{2-}. \tag{2.3}$$

Carbonic acid is unstable, and the dissociation to form H^+ and HCO_3^- is favored (Eq. 2.2). The carbonate system is particularly important in regulating the pH of seawater and the exchange of carbon dioxide between the terrestrial biosphere, the atmosphere and the oceans. The vast majority of the carbon in the ocean occurs as HCO_3^-, with CO_3^{2-},

and CO_2 making up the remainder. The unstable H_2CO_3 is generally accounted for in a quantity CO_2^*:

$$[H_2CO_3] + [CO_2] = [CO_2^*] \tag{2.4}$$

The various dissolved species of CO_2 are plotted as a function of pH in the Bjerrum diagram in Figure 2.1. The concentration of CO_2 in seawater is given by Henry's law:

$$[CO_2] = \alpha(T, S) fCO_2, \tag{2.5}$$

where α is the solubility coefficient of CO_2 in seawater, which depends on both temperature (T) and salinity (S) (*Weiss*, 1974), and fCO_2 is the fugacity of CO_2 in units of μatm. The partial pressure of CO_2 (pCO_2) may be computed from the fugacity using a correction for the non-ideal behaviour of the gas mixture in air:

$$fCO_2 = \gamma pCO_2, \tag{2.6}$$

where γ is the fugacity coefficient. The fugacity coefficient varies between 0.996 and 0.997 over temperatures ranging from 0 to 30°C (*Zeebe and Wolf-Gladrow*, 2001).

To describe the carbonate system in seawater, stoichiometric equilibrium constants, which are related to the concentrations of the carbonate species, are used:

$$K_1^* = \frac{[HCO_3^-][H^+]}{[CO_2^*]} \tag{2.7}$$

$$K_2^* = \frac{[CO_3^{2-}][H^+]}{[HCO_3^-]}, \tag{2.8}$$

where the equilibrium constants depend on temperature, pressure and salinity. The sum of the dissolved species CO_2^*, HCO_3^- and CO_3^{2-}, is called total dissolved inorganic carbon (DIC):

$$DIC \equiv \Sigma CO_2 = [CO_2^*] + [HCO_3^-] + [CO_3^{2-}]. \tag{2.9}$$

Total alkalinity (TA) is a conservative quantity such as mass or salt, in the sense that its concentration is unaffected by changes in temperature or pressure, and can be thought of a quantity that keeps track of the charge balance of seawater. Total alkalinity can be

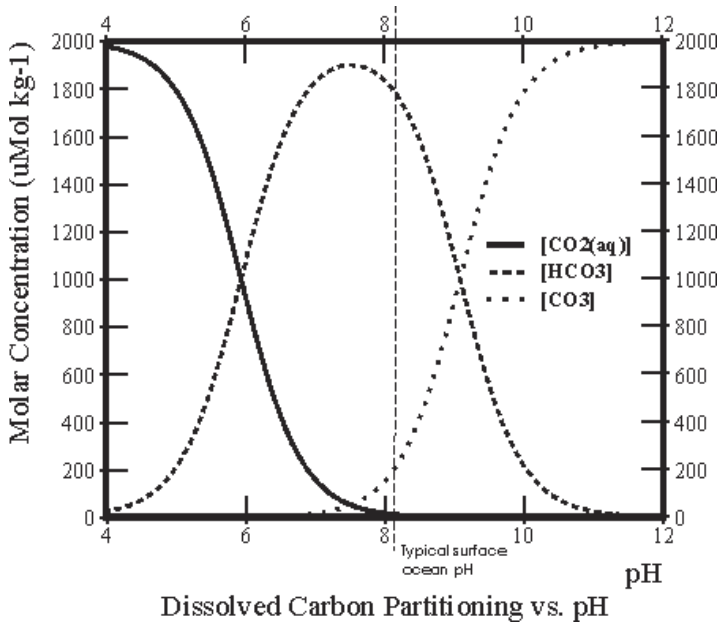

Figure 2.1: The fractions of carbonic acid in seawater as a function of pH. The pH of the ocean today is indicated.

expressed in terms of the charge imbalance of the major ions in seawater, i.e.:

$$\mathrm{TA} = \sum(\text{cations of strong bases}) - \sum(\text{anions of strong acids}), \tag{2.10}$$

with a strong bases defined by dissociation constant $\mathrm{pK_a} > 4.5$, and strong acids defined by $\mathrm{pK_a} < 4.5$ at 25°C:

$$\mathrm{TA} = [\mathrm{Na^+}] + 2[\mathrm{Mg^{2+}}] + 2[\mathrm{Ca^{2+}}] + [\mathrm{K^+}] - [\mathrm{Cl^-}] - 2[\mathrm{SO_4^{2-}}] - [\mathrm{NO_3^-}]. \tag{2.11}$$

Table 2.1 lists the concentrations and charge concentrations of the major ions in seawater. It can be seen from the total charge concentrations, 605.0 mmol $\mathrm{kg^{-1}}$ and 602.8 mmol $\mathrm{kg^{-1}}$, for the cations and anions respectively, that there is a small charge imbalance (2.2 mmol $\mathrm{kg^{-1}}$), which is equal to the total alkalinity in seawater. Total alkalinity has further been defined, with respect to the buffer capacity of seawater, by *Dickson* (1981) as the number of moles of hydrogen ion equivalent to the excess of proton acceptors (bases formed from weak acids with dissociation constant $\mathrm{pK_a} > 4.5$ at 25°C) over proton donors (strong acids with $\mathrm{pK_a} < 4.5$ at 25°C) in one kg of sample seawater. For the major species found in seawater, the expression for total alkalinity following Dickson's

Table 2.1: Concentrations, [c_i] (mmmol kg^{-1}), and charge concentrations, [q_i] = z_i[c_i] (mmol kg^{-1}), with z_i the charge, of the major ions in seawater at S=35. Table follows *Zeebe and Wolf-Gladrow* (2001).

Cations	[c_i]	[q_i]	Anions	[c_i]	[q_i]
Na^+	467.8	467.8	Cl^-	545.5	545.5
Mg^{2+}	53.3	106.5	SO_4^{2-}	28.2	56.4
Ca^{2+}	10.3	20.6	Br^-	0.8	0.8
K^+	9.9	9.9	F^-	0.1	0.1
Sr^{2+}	0.1	0.2			
Total		605.0	Total		602.8

definition is:

$$\mathrm{TA} = [\mathrm{HCO_3^-}] + 2[\mathrm{CO_3^{2-}}] + [\mathrm{B(OH)_4^-}] + [\mathrm{OH^-}] + [\mathrm{HPO_4^{2-}}] + 2[\mathrm{PO_4^{3-}}] + [\mathrm{SiO(OH)_3^-}] + [\mathrm{NH_3}] + [\mathrm{HS^-}] - [\mathrm{H^+}] - [\mathrm{HSO_4^-}] - [\mathrm{HF}] - [\mathrm{H_3PO_4}]. \tag{2.12}$$

Equation 2.12 is often approximated as,

$$\mathrm{TA} \simeq [\mathrm{HCO_3^-}] + 2[\mathrm{CO_3^{2-}}] + [\mathrm{B(OH)_4^-}] + [\mathrm{OH^-}] - [\mathrm{H^+}], \tag{2.13}$$

where the more minor components have been neglected. There are several processes which cause changes in TA in the ocean. For example, the precipitation of calcium carbonate ($CaCO_3$) by organisms such as coccolithophorids, foraminifera, pteropods, and corals, and the dissolution of calcareous shells and skeletons alter TA. The precipitation of 1 mol of $CaCO_3$ reduces TA by 2 moles. This can be seen as a decrease in Ca^{2+} (Eq. 2.11), or in CO_3^{2-} (Eq. 2.12). The assimilation of nitrogen by marine organisms, and the release of inorganic nitrogen by remineralization will also cause changes in TA. The uptake of 1 mole of NO_3^- by algae increases TA by one mole (Eq. 2.11), assuming that the electro-neutrality of the organism is maintained by a parallel uptake of H^+ or release of OH^- (Eq. 2.12) (*Brewer and Goldman*, 1976). The absorption of CO_2^* by seawater will, in contrast, not cause a change in alkalinity, since the resulting H_2CO_3 (Eq. 2.2), a weak acid, dissociates to form H^+ and HCO_3^- and the total charge remains unchanged.

The pH however will be decreased as a result of the absorption of CO_2 due to the H^+ produced (Eqs. 2.2 to 2.3). The addition of a strong acid, such as hydrochloric acid (HCl), to seawater will decrease TA by the addition of Cl^- (Eq. 2.11) and H^+ (Eq. 2.12) and also decrease the pH.

As discussed above, the formation and dissolution of calcium carbonate ($CaCO_3$) play an important role in the inorganic carbon system in seawater. A determining factor with respect to the formation and dissolution of $CaCO_3$ is the calcuim carbonate saturation state of seawater, which is a function the carbonate ion concentration. The $CaCO_3$ saturation state, Ω, is expressed as:

$$\Omega = \frac{[Ca^{2+}] \times [CO_3^{2-}]}{K_{sp}^*}, \tag{2.14}$$

where $[Ca^{2+}]$ and $[CO_3^{2-}]$ are the concentrations of Ca^{2+} and CO_3^{2-} in seawater, repsectively, and K_{sp}^* is the stoichiometric solubility product at in-situ temperature, salinity, and pressure (*Zeebe and Wolf-Gladrow*, 2001). Values of $\Omega > 1$ correspond to supersaturation, or potential formation of $CaCO_3$. Values of $\Omega < 1$ correspond to undersaturation, or potential dissolution of $CaCO_3$. Variations in $[Ca^{2+}]$ in the ocean are relatively small and closely related to changes in salinity (*Zeebe and Wolf-Gladrow*, 2001); the $CaCO_3$ saturation state is therefore more strongly influenced by the carbonate ion concentration.

The equilibrium equations, (Eqs. 2.8 and 2.8), the equation for total dissolved inorganic carbon (Eq. 2.9), and the carbonate alkalinity equation (Eq. 2.13), make up a system of four equations and six unknown variables ($[CO_2^*]$, $[HCO_3^-]$, $[CO_3^{2-}]$, $[H^+]$, DIC, and TA). When two of the variables are known, the system of equations may be used to compute the other four. In practice only $[CO_2^*]$, $[H^+]$ or pH, DIC and TA can be measured directly. For the analysis relating to the Scotian Shelf, presented in Chapters 4 and 5, CO_2 and TA were measured, and DIC computed. In the case of the Arctic Archipelago and the southeastern Beaufort Sea, presented in Chapters 6 and 7, DIC and TA were measured, and CO_2 and pH computed. The unknown parameters were computed using the equations given above and the CO_2Sys program of *Lewis and Wallace* (1998).

Although each of the carbonate system parameters are linearly independent, they are not orthogonal; certain combinations of pairs of measured quantities are therefore more desirable than others to compute the remaining parameters. The combination of DIC and TA is perhaps the most accurate, since the measurement of these two parameters has an associated accuracy of ± 2 and 3 μmol kg^{-1} respectively, and the estimated error

in the computation of pCO_2 is less than 4μatm. The combination of pH, or $[H^+]$, and TA is also quite accurate with a smaller error in the computed pCO_2 (less than 2μatm), but a somewhat larger error in the computed DIC on the order of 4 μmol kg^{-1}. The least desirable combination is pCO_2 and pH which result in errors in the computed DIC and TA significantly larger (on the order of 15 μmol kg^{-1}) than the uncertainty in the measurement (*Zeebe and Wolf-Gladrow*, 2001).

2.2 Laboratory Analysis

Water samples were collected directly from the rosette and injected with a solution of supersaturated mercuric-chloride ($HgCl_2$) to halt biological activity. Samples were stored in the dark at 4°C to await analysis. Samples were analyzed for concentrations of DIC and TA using a VINDTA 3C (Versatile Instrument for the Determination of Total Alkalinity, by Marianda). The methods for the determination of DIC and TA are given in more detail in the following sections.

2.2.1 Determination of DIC by Coulometric Titration

Using a peristaltic pump, a volume of sea water sample is delivered to the sample pipette. The contents of the pipette are then injected into a stripping chamber containing approximately $1.2\ \mathrm{cm}^3$ of phosphoric acid ($8.5\%\ H_3PO_4$). The carbonate species react with the H_3PO_4, and the solution is stripped of CO_2 by bubbling a carrier gas through a glass frit submerged in the acidified sample. The carrier gas is pure N_2 from a compressed gas cylinder, and is passed through a column of soda lime to ensure that the gas is free of CO_2. The amount of extracted CO_2 from the seawater sample is determined by trapping the CO_2 in an absorbent solution containing ethanolomine and a pH senstive dye, and the subsequent electrochemical titration of the hydroxyethylcarbonic acid that is produced.[1]

A coulometer cell with a two chambers is used (Fig. 2.2). The primary chamber is filled with approximately $100\ \mathrm{cm}^3$ of cathode solution (UIC Inc.) which contains the ethanolamine as reactive agent, dymethylsulfoxide (DMSO), and the pH sensitive dye. The smaller, side chamber, is filled with anode solution (UIC Inc.) to approximately 1 cm below the liquid level of the cathode solution. The anode solution contains potassium iodide in water, and to ensure that the solution remains saturated, potassium iodide crystals

[1] the description of the coulometric titration follows *Dickson et al.* (2007).

are added to the small coulometer chamber. The cathode is platinum (Pt), while the anode is silver (Ag). The relevant chemical reactions occurring in the coulometer cell are:

$$CO_2 + HO(CH_2)_2NH_2 \rightarrow HO(CH_2)_2NHCOO^- + H^+ \tag{2.15}$$

and

$$H^+ + OH^- \rightarrow H_2O, \tag{2.16}$$

leading to an acidification of the cathode solution and a corresponding colour change of the dye (Eq. 2.15). The hydroxide ions (OH^-) are generated at the cathode by the electrolysis of water:

$$H_2O + e^- \rightarrow \frac{1}{2}H_2(g) + OH^-, \tag{2.17}$$

and silver is oxidized,

$$Ag(s) \rightarrow Ag^+ + e^-. \tag{2.18}$$

The OH^- (Eq. 2.17) is used to titrate the hydroxyethylcarbonic acid. The coulometer measures the amount of charge, or the number of electrons (e^-) needed to produce the amount of OH^- required to bring the dye back to its original color. Using Faraday's second law of electrolysis[2] the quantity of charge measured is converted to a molar quantity, or concentration (μmol kg^{-1}) of DIC.

2.2.2 Determination of TA by Potentiometric Titration

Using a peristaltic pump, a volume of sea water sample is delivered to the sample pipette. The contents of the pipette are then injected into a open titration cell with an outer water jacket connected to a re-circulating water bath maintained at 25°C to control the temperature of the sample during the titration. A solution of hydrochloric acid, (HCl), is made up in a solution of sodium chloride to approximate the ionic strength of seawater. This acid is delivered in doses of $0.150\ \mathrm{cm}^3$ to the titration cell by a computer controlled piston burette (Metrohm). A magnetic stirrer is used to mix the solution during the titration. The progress of the titration is monitored by measuring the evolution of the potential between the pair of electrodes. Total alkalinity is then computed automatically by the VINDTA LabView software using a modified Gran approach (*Dickson et al.*, 2007).

[2]Faraday's 2nd law of electrolysis states that for a given quantity of electricity the quantity of substance produced is proportional to its weight. Mathematically, $\mathrm{n} = \mathrm{Q}/\mathrm{F}$, where n is the number of moles produced, Q is the quantity of charge [C], and F is Faraday's constant equal to 96,484 C mol^{-1}.

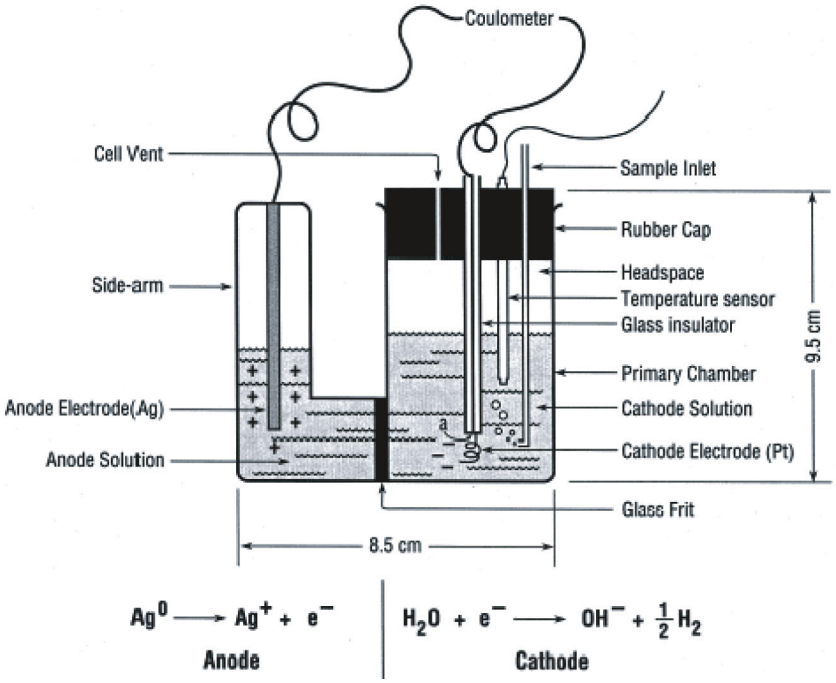

Figure 2.2: The coulometric titration cell assembly and the cathodic and anodic half reactions for the coulometric titration of the H^+ from the acid formed by the reaction of CO_2 and ethanolamine. Figure modified from *Johnson et al.* (1998).

2.2.3 Calibration with Reference Material

Certified Reference Materials (CRMs) are $500\ \mathrm{cm}^3$ volumes of seawater with precisely determined concentrations of DIC and TA, provided by A. G. Dickson, (Scripps Institution of Oceanography). These CRMs are analyzed using the methods described above at the beginning and the end of a measurement period, and the resulting values of DIC and TA used to calibrate our sample measurements. This routine CRM analysis ensures that the uncertainty of the DIC and TA measurements is less than 2 μmol kg^{-1} and 3 μmol kg^{-1} respectively.

2.3 Underway $\mathrm{pCO_2}$ Measurement

The partial pressure of carbon dioxide in air that is in equilibrium with a sample of seawater is defined as the product of the total pressure of equilibration (P) and the mole fraction of CO_2 ($x(CO_2)$):

$$\mathrm{pCO_2} = P\,x\,(\mathrm{CO_2}). \tag{2.19}$$

The principle of the pCO_2 measurement is based on the equilibration of a fixed volume of air with a stream of seawater. The volume of air that flows through the equilibrator is negligible compared to the volume of seawater. As such, the CO_2 content of the air adjusts to equilibrium with the seawater while the CO_2 content of the seawater remains relatively unchanged.

In our system, a continuous flow of seawater, from an intake located mid-ship, roughly 3 meters below the water surface, passes through an open system equilibration cell which is also vented to the atmosphere via a length of tubing from the system to the ship's deck. A fixed volume of air is pumped constantly through the system, to keep it in equilibrium with the continuously renewed seawater phase. The water chamber of the equilibrator is filled with approximately $500\ \mathrm{cm}^3$ of constantly renewed seawater. The air enters via a glass tube and coarse frit, and is then bubbled through the water. After passing through the equilibrator this air flow is then circulated through a non-dispersive infra-red gas analyzer (LiCor, LI-7000) where the mole fraction of CO_2 is measured relative to a CO_2 free reference gas. The Li-Cor system is a dual channel gas analyzer that simultaneously measures the mole fraction of CO_2 and of H_2O. The measured mole fraction of CO_2 is then corrected to dry air using the measured mole fraction of water vapor:

$$x\,\mathrm{CO}_2^{\mathrm{dry}} = x\,\mathrm{CO}_2^{\mathrm{wet}}(f(x\,\mathrm{H_2O})), \tag{2.20}$$

where $f(x\mathrm{H_2O})$ is a function of the mole fraction of water vapor, and the superscript 'wet' refers to the measured value of the mole fraction of CO_2 (*Körtzinger et al.* (1996)). The pCO_2 at 100% humidity is then computed based on the ambient, equilibrator, pressure (P) and the saturation water vapor pressure (w):

$$\mathrm{pCO_2} = x\,\mathrm{CO}_2^{\mathrm{dry}}(P - w). \tag{2.21}$$

The saturation water vapor pressure is computed as a function of the absolute temperature of the seawater, (T_{abs}), which is measured and recorded using a temperature sensor located inside the equilibrator. The system is calibrated daily using both a CO_2-free N_2 gas, and a CO_2 calibration gas prepared by the U.S. National Oceanic and Atmospheric Administration (NOAA).

2.4 The CARIOCA Buoy

A Carbon Interface Ocean-Atmosphere (CARIOCA) buoy was deployed at station HL2, located roughly 30 km offshore from Halifax (44.3°N and 63.3°W), in April 2007. The autonomous, moored, buoy makes hourly measurements of $\mathrm{pCO_2}$ (μatm), salinity, near surface sea and air temperatures (°C), chlorophyll-a fluorescence (μg $\mathrm{l^{-1}}$), and atmospheric pressure (kPa) at roughly 1 m above the sea-surface. The instrumentation is shown schematically in Fig. (2.3). The $\mathrm{pCO_2}$ measurements are made by an automated spectrophotometric technique.[3] The two main components of the $\mathrm{pCO_2}$ system are the exchanger cell and an optical detector. A $\mathrm{CO_2}$-permeable silicon membrane in the exchanger cell separates seawater from a pH sensitive color indicator (thymol blue). The diffusion of $\mathrm{CO_2}$ across the membrane equilibrates the concentration of $\mathrm{CO_2}$ in seawater and in the color indicator. After gas exchange, with a time constant of roughly 30 minutes, the dye is transfered to an optical cell where its absorbance is measured at both wavelengths of 596 nm and 810 nm. Since the color indicator does not absorb at 810 nm, this provides a background reading. The absorbance measured at 596 nm gives the pH of the dye, which is a function of its $\mathrm{CO_2}$ content. A Sea-Bird (SBE 41) conductivity sensor and a Betatherm thermistor are used to acquire salinity and temperature data. Chlorophyll-a fluorescence was determined by a Wetlab miniature fluorometer (WETstar), and is expressed in relative units. Measured chlorophyll-a from the mooring site is used to calibrate the fluorescence data. Hourly data from the CARIOCA are uploaded and transmitted daily via the ARGOS satellite system.

[3] Description of the spectrophotometric method follows *Bakker et al.* (2001), and *Bates et al.* (2001).

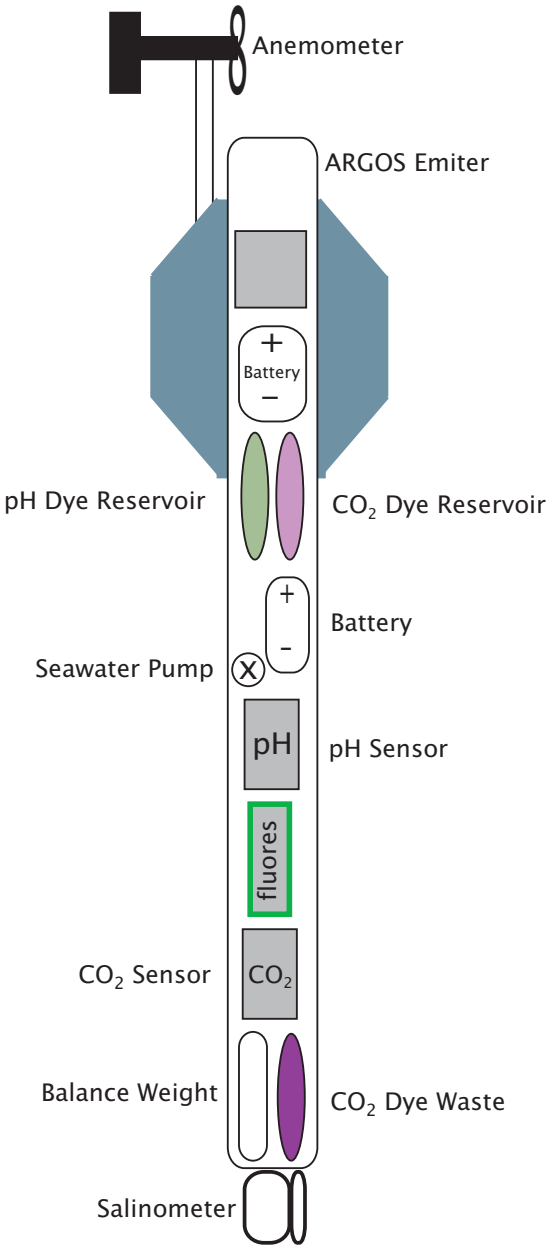

Figure 2.3: A schematic representation of the instrumentation of the CARIOCA buoy.

CHAPTER 3

CO_2 IN THE COASTAL OCEAN: A CASE STUDY ON THE SCOTIAN SHELF

This chapter presents an overview of the ocean carbon system with emphasis on the coastal ocean, and a particular focus on the Scotian Shelf region. The carbon cycle is discussed in the context of the larger ecosystem and oceanographic picture. The major drivers of the seasonal changes in surface ocean carbon in this region and the implications for the uptake of atmospheric CO_2 are discussed. Longer-term variability is also discussed with respect to both natural cycles, and anthropogenic forcing. While the focus of the paper is certainly scientific, the theme is realtively broad, as it is intended to appeal to the wider readership of the *Ocean Yearbook*, a publication of the International Ocean Institute, in co-operation with the Marine and Environmental Law Institute at the Schulich School of Law at Dalhousie University[1]. An an in-depth scientific evaluation of the material presented in the following sections is given in Chapters 4 and 5.

3.1 Introduction

The Atlantic Coast of Canada hosts rugged beaches, picturesque fishing villages, and rich Maritime history. This region is also home to an area called the Scotian Shelf, a 700 km long section of the continental shelf off Nova Scotia. Bounded by the Laurentian Channel to the northeast, and by the Northeast Channel and the Gulf of Maine to the southwest, it varies in width from 120 to 240 km covering roughly 120,000 km^2 with an average

[1] This chapter comprises a manuscript by E. H. Shadwick and H. Thomas entitled *CO_2 in the Coastal Ocean: A Case Study on the Scotian Shelf* submitted to The Ocean Yearbook.

depth is 90 m (Fig. 3.1). The Scotian Shelf, along with the Grand Banks, is one of the most heavily utilized fishing areas in the Canadian Atlantic region. The region also hosts a Marine Protected Area, and is home several species of marine mammals and deep-sea corals that are threatened by the commercial fishing industry (*Gass and WIllison*, 2005; *Vanderlaan and Taggart*, 2007). The major commercial fish species are ground-fish that live on, or near, the bottom, including cod, haddock, pollock, halibut, and various species of flatfish; the principal pelagic fish species (by biomass) on the continental shelf are herring, mackerel, bluefin tuna, and capelin (*Zwanenburg et al.*, 2002). The Scotian Shelf is a critical habitat for the endangered North Atlantic right whale, with some 30% of the remaining population occupying a feeding area in Roseway Basin and the Bay of Fundy (*Vanderlaan and Taggart*, 2007). The northern bottlenose whale is found offshore in the deep waters along the shelf edge, particularly in the Gully region east of Sable Island, where a unique, non-migratory population of individuals feeds on abundant squid (*Hooker et al.*, 2002). In the northwest Atlantic, the major breeding colonies of gray seals are located on the sea-ice in the Gulf of St. Lawrence and on Sable Island, with smaller colonies along the Eastern Shore of Nova Scotia and Cape Breton (*Bowen et al.*, 2003). The Nova Scotian coast is an important migratory staging area for waterfowl and shorebirds, while offshore waters host wintering dovekies, murres, shearwaters, and common eiders (*Brown*, 1988). Furthermore, a wide range of economically important shellfish species are found here, many with important spawning and nursery grounds in the region. The source of food to these marine mammals, fish and sea birds comes from the lower trophic levels, comprised of phytoplankton and zooplankton. Photosynthesis by phytoplankton fixes inorganic carbon, or carbon dioxide (CO_2), using energy from sunlight. These plants are grazed by zooplankton, which are in turn eaten by fish, and whales, and thus the carbon fixed by phytoplankton makes its way into the food web. Despite their moderate surface areas, coastal seas and continental margins such as the Scotian Shelf play a crucial role in global ocean carbon cycle due to their high ecosystem (*Borges et al.*, 2005; *Cai et al.*, 2006) activity as detailed in the following sections.

Acidification of the oceans through uptake of anthropogenic CO_2 has become an active area of research over the last few years (*Orr et al.*, 2005; *Doney*, 2006; *Kleypas and Langdon*, 2006). International activities are being initiated in response to the unprecedented threat of ocean acidification to marine ecosystems at the global scale. Continuing

acidification of the oceans has irreversibly been triggered by the rising concentration of atmospheric CO_2 and mitigation measures are presently lacking. It has been shown that the vulnerability of North Atlantic Ocean waters to acidification increases in shallow and high latitude regions, primarily as a function of decreasing temperature and chemical composition (*Thomas et al.*, 2007). The Canadian Atlantic coast is thus particularly vulnerable to the effects of acidification as a high latitude, shallow shelf sea, influenced by arctic and subarctic waters. Eutrophication is defined as an increase of primary production in an ecosystem, as a result of an increased availability of nutrients. Eutrophication is often the result of pollution from sewage or agricultural fertilizers, which increase the concentrations of nitrate and phosphate, and may negatively impact the marine ecosystem by depleting oxygen and lowering water quality (*Ryther and Dunstan*, 1971). Increased nutrient input from land via rivers, groundwater or the atmosphere, plays a further role in affecting coastal waters both by potentially altering ecosystem structure, and by influencing the pH (*Galloway et al.*, 2004; *Doney et al.*, 2007; *Thomas et al.*, 2009b; *Borges and Gypens*, 2010). Ocean acidification most directly impacts organisms that form calcium carbonate ($CaCO_3$) shells and skeletons, because acidity increases the solubility of $CaCO_3$ (e.g. *Riebesell et al.*, 2000; *Delille et al.*, 2005; *Gazeau et al.*, 2007). These organisms include phytoplankton such as coccolithophores, zooplankton such as pteropods and foramnifera, sea urchins, mollusks and corals. Since $CaCO_3$ shells and skeletons are naturally more soluble at lower temperature and higher pressure, high latitude and deep-water ecosystems are more vulnerable to the added stress of ocean acidification. Furthermore, early life stages often carry thinner, more fragile shells, potentially making them more vulnerable to changing environmental conditions. Many calcifying organisms play a crucial role in the marine food web and are thus directly relevant to the human food supply. These organisms may themselves be commercially exploitable, as in the case of oysters, mussels and scallops, or support other commercially exploitable species by serving as prey or habitat. Shellfish aquaculture continues to grow in Nova Scotia (*d'Entremont*, 2009).

Here we report findings from the very first detailed study of the inorganic carbon cycle on the Scotian Shelf. Our study deepens the understanding of the carbon system in Canadian coastal waters. An understanding of the coastal ocean response to both natural and human-induced forcing is essential to the assessment of prospects and risks to

fisheries and aquaculture in our maritime regions. There is a general global consensus that the 'business as usual' treatment of anthropogenic CO_2 emission through the burning of fossil fuels should be exchanged for strategies that reduce societal dependence on CO_2 to mitigate and manage future environmental impacts. However, in order to assess the effectiveness of any current, or future, mitigation strategy, accurate quantification of CO_2 emissions and their environmental impacts must be made to ensure that the reductions of CO_2 emissions are actually met. Assessing the impact of anthropogenic change is complicated by the lack of baseline studies in many regions. Coastal ocean regions are particularly poorly studied compared to their open ocean counterparts, despite their importance to society through fisheries and aquaculture. Pristine ocean conditions no longer exist; coastal environments have long been subjected to human activities through sewage treatment and the use of fertilizer and other and pollutants. It is therefore difficult to assess relatively short-term impacts on systems that have been under the influence of anthropogenic forcing for centuries. However, over the last decade, it has become clear that sustained time-series observations are essential to understanding natural and anthropogenic changes in the global carbon cycle on land, in the ocean, and in the atmosphere. Model simulations validated with high quality observational data can improve our understanding of complex systems and their response to environmental change. Canada's oceans are a valuable living and non-living resource providing food, power, transport, and security as well as recreation to our society. Measures to monitor the ocean's response to change will help to inform policy aimed at mitigating the effects of climate change and developing strategies to sustainably manage Canada's marine resources.

3.2 The Carbon Cycle and the Coastal Ocean

The carbon cycle is governed by many different biological, chemical and physical processes, which transfer carbon between the major storage pools called reservoirs. The global carbon cycle is comprised of four major carbon reservoirs: (1) the atmosphere, (2) the terrestrial biosphere, including plants, trees, and soils, (3) the oceans, (4) the sediments, including fossil fuel deposits and carbonate rocks. The global carbon budget is a balance of the exchanges of carbon that take place between these reservoirs over various time scales. Before the industrial revolution, the global carbon cycle was in balance with fluxes into the carbon reservoirs equal to flux out of the reservoirs. The release of

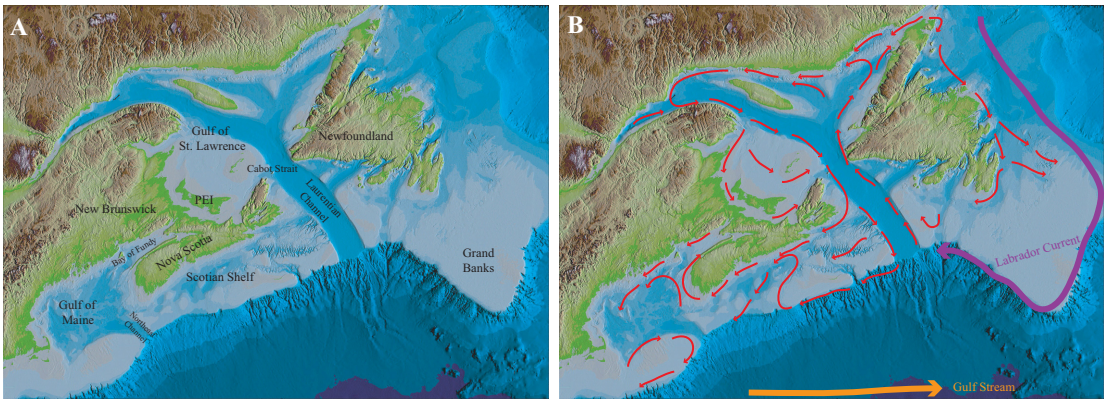

Figure 3.1: The Scotian Shelf and the larger geographic setting (a) and a schematic representation of the dominant, mean circulation in the region (b). The Labrador Current and the Gulf Stream are also shown schematically.

CO_2 into the atmosphere by the combustion of fossil fuels over the past several centuries has increased the atmospheric concentrations from roughly 280 ppm to present day levels of nearly 390 ppm (*Kling et al.*, 2007). Over a relatively short period of only decades, the burning of fossil fuels has released quantities of carbon to the atmosphere that accumulated in the sedimentary reservoirs over millions of years. The conversion of tropical forest to agricultural land and cement production release additional CO_2 to the atmosphere. The anthropogenic release of CO_2 is currently larger than can be balanced by natural removal processes which act over much longer timescales.

The oceans act as a significant reservoir for inorganic carbon, containing 50 times more CO_2 than the atmosphere (*Gruber et al.*, 2004). Furthermore, roughly half of the anthropogenic CO_2 emitted to the atmosphere is taken up by the ocean (*Gruber et al.*, 2004; *Sabine et al.*, 2004). Phytoplankton convert CO_2 to particulate organic carbon (POC), and a portion of this POC sinks out of the surface layer, therefore removing CO_2 from the atmosphere (*Gruber and Sarmiento*, 2002). Coastal seas and continental margins play an important role in the global carbon cycle by providing a link between the terrestrial, oceanic, and atmospheric reservoirs (*Walsh*, 1991; *Andersson and Mackenzie*, 2004). Compared to the open ocean, the proximity of the surface sediments to the air-sea interface, in both space and time, is enhanced in the coastal ocean (*Thomas et al.*, 2009a). Although the coastal ocean represents only 8% of the total ocean surface area, roughly one-fifth to one-third, of the global marine primary production takes place in these seas (*Walsh*, 1991; *Gattuso et al.*, 1998). Furthermore, the coastal ocean plays a prominent role

in the absorption of atmospheric CO_2, potentially transferring it to the deep ocean via the continental shelf pump - a mechanism that delivers cold, dense, carbon-rich waters from the shallow shelf regions to the subsurface layer of the adjacent deep ocean where they are sequestered from the atmosphere (*Tsunogai et al.*, 1999; *Thomas et al.*, 2004; *Bozec et al.*, 2005). However, a recent modeling study (*Fennel and Wilkin*, 2009) suggests that the continental shelf pump mechanism, which has the potential to transport dissolved carbon off the continental shelf, does not operate on the Scotian Shelf. Vertical sinking of organic material is insufficient for carbon export since this material is re-exposed to the surface under conditions of deep winter mixing, which will be discussed in more detail (see Sections 3.5.1). Roughly 50% of the global population lives within 100 km of the shore; the North American Atlantic coast is heavily populated and thus directly impacted by anthropogenic activity (*Najjar et al.*, 2010). Before reliable assessment of the vulnerability of coastal systems to climate change can be made, present-day carbon stocks and fluxes must be quantified, and natural variability understood. Carbon fluxes have been investigated in several coastal ocean and continental shelf regions in the last few years (e.g. *Peng et al.*, 1999; *Thomas and Schneider*, 1999; *Frankignoulle and Borges*, 2001; *Cai et al.*, 2003; *Thomas et al.*, 2005b; *Bozec et al.*, 2006). However, these environments exhibit strong spatial and temporal heterogeneity, and integrative global assessments have not yet achieved high fidelity (*Borges et al.*, 2005; *Cai et al.*, 2006; *Chen and Borges*, 2009). The research presented here reflects the state of knowledge of the CO_2 system in the Scotian Shelf region.

3.3 Data and Methods

The discrete chemical and hydrographic data from the year 2008 presented in the following sections was collected on the Canadian Coast Guard Ship Hudson as part of the Atlantic Zone Monitoring Program (AZMP)[2]. The Canadian Department of Fisheries and Oceans (DFO) implemented the AZMP in 1998. The primary goal of the AZMP is the maintenance of a long-term, relatively high temporal resolution, observational program in the Canadian Northwestern Atlantic Ocean. Cruises took place in April and September 2008. Approximately 350 seawater samples were collected on each cruise from the

[2]For details of the AZMP see: http://www.bio.gc.ca/monitoring-monitorage/azmp-pmze

entire water column with higher vertical resolution within the euphotic zone, along four primary transect lines covering the Scotian Shelf regions. Seawater samples were tapped from 20-L Niskin bottles mounted on a General Oceanic 24-bottle rosette fitted with a conductivity, temperature and depth sensor (CTD, SeaBird) such that all chemical data are associated with high precision in-situ temperature, salinity and oxygen data.

With respect to the CO_2 system in seawater, there are four measureable parameters: the partial pressure of CO_2 (pCO_2) dissolved inorganic carbon (DIC), total alkalinity (TA), and pH (see also Chapter 2). With measurements of any two of these parameters, the other two measureable parameters can be computed. Following seawater collection, measurements of DIC and TA were made by coulometric and potentiometric titration, respectively, using a Versatile Instrument for the Determination of Total Alkalinity (VINDTA 3C, Marianda) (*Johnson et al.*, 1993). Routine analysis of Certified Reference Materials (provided by A. G. Dickson, Scripps Institution of Oceanography) ensured that the uncertainty of the DIC and TA measurements was less than 2 and 3 μmol kg^{-1}, respectively. Following the determination of DIC and TA, a computation of pH and aragonite saturation state Ω_{Ar} was made using the standard set of carbonate system equations using the dissociation constants of *Mehrbach et al.* (1973) refit by *Dickson and Millero* (1987) and the CO2Sys program of *Lewis and Wallace* (1998) (see also Chapters 2 and 4).

In addition to discrete samples of DIC and TA, continuous measurements of pCO_2 from an autonomous moored CARIOCA buoy are presented. The CARIOCA buoy was moored at station Halifax Line 2, (HL2, 44.3°N and 63.3°W) from April to December, 2007; January to July, 2008; and October, 2009 to February 2010. The CARIOCA buoy makes hourly measurements of sea-surface temperature (SST), sea-surface salinity, chlorophyll-a (chl-a) concentration, and pCO_2. The pCO_2 measurements were made by an automated spectrophotometer technique (*Bates et al.*, 2001). Atmospheric CO_2 and wind speed data presented were measured at the Sable Island Meteorological station (43.9°N and 60.3°W) and were provided by Environment Canada.

3.4 Physical and Biological Conditions on the Scotian Shelf

The Scotian Shelf is uniquely located at the junction of the North Atlantic sub-polar and sub-tropical gyres, downstream of the St. Lawrence River system (*Loder et al.*, 1997).

The Scotian Shelf is considered an open continental shelf, or regional sea system, as opposed to a closed system as in the case of the Arctic Archipelago (*Meybeck et al.*, 2007). The shelf-scale circulation is dominated by the Nova Scotia Current, which flows to the southwest roughly parallel to the coast, and an extension of the Labrador Current, flowing in the same direction, along the shelf edge (Fig. 3.1). Water transport by the Nova Scotian Current varies seasonally in strength and reaches peak values of roughly 2 Sv in winter and spring, with a summer minimum of 0.4 Sv (*Loder et al.*, 2003). Smaller scale circulation features are generated by topographic steering around submarine banks, (i.e. Browns Bank, Sable Island Bank, and Georges Bank) and cross-shelf channels (*Loder et al.*, 1988; *Hannah et al.*, 2001). Tidal forcing, episodic wind-driven upwelling, and winter convection also influence the region (*Petrie et al.*, 1987; *Loder et al.*, 1997; *Greenan et al.*, 2004). Wind-driven upwelling and winter convection will be discussed in more detail in sections 3.4.1 and 3.4.3 respectively.

3.4.1 Coastal and Shelf-edge Upwelling

A persistent alongshore wind with the coast on the left (looking downwind) in the northern hemisphere will result in an offshore flow in the surface waters, which is compensated by a shoreward flow of deeper waters, which are upwelled to the surface. Coastal upwelling and the associated favorable wind conditions on the Scotian Shelf have long been recognized (*Hachey*, 1935). Strong winds, of speeds greater than 10 m s^{-1}, blowing to the northeast, and persisting for several days, force relatively cold, saline, water toward the surface, displacing the warmer, fresher water offshore (*Petrie*, 1983). Upwelling events have frequently been observed in the coastal regions of the Scotian Shelf, and modeling studies have reproduced these observed events (*Petrie*, 1983; *Donohue*, 2000). Furthermore, these events may play a role in initiating and sustaining the spring phytoplankton bloom by displacing nutrient-depleted surface water and bring nutrient-rich waters up to the surface (*Greenan et al.*, 2004).

3.4.2 Temperature and Salinity

The seasonal cycle of sea-surface temperature on the Scotian Shelf has an annual range of nearly 20°C (from an annual minimum of 0°C to an annual maximum of 18°C or 20°C), which is among the largest in the world (*Umoh and Thompson*, 1994). The seasonal variation in sea-surface temperature is primarily due to surface heat fluxes over the

Scotian Shelf (*Umoh and Thompson*, 1994). The mean temperature and salinity in the upper 10 m of the water column in early April, reflecting winter and spring conditions, and in September, reflecting summer and autumn conditions, are shown in Fig. 3.2. In the spring, the advection of sub-zero waters from Cabot Strait influences surface water temperature, which is nearly homogeneous on the inner shelf. The southwestern outflow from Cabot Strait can also be identified as the major source of freshwater to the region. The salinity increases further offshore due to the northward transport of warm, saline, Gulf Stream waters (Fig. 3.1). In autumn, the surface temperature is warmest in the central Scotian Shelf and increases with the distance from shore. The waters in Cabot Strait remain relatively cool. The peak in river discharge from the St. Lawrence is delivered to the Scotian Shelf between June and October; surface salinity is typically decreased by 1 unit, from roughly 30.5 to 29.5, as a result of this input (Fig. 3.3) (*Loder et al.*, 1997).

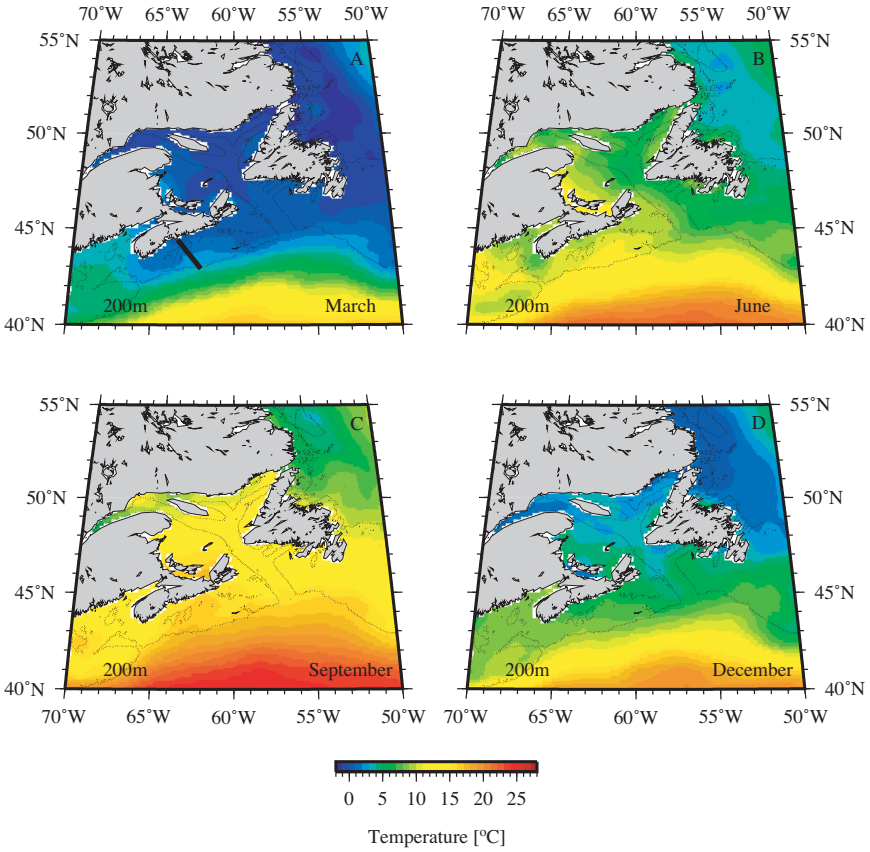

Figure 3.2: Mean temperature and salinity in the upper 10 meters of the water column on the Scotian Shelf in September and April. The solid line in (A) indicates the transect referred to as the 'Halifax Line'. The section plots shown subsequent figures were generated from samples collected along this transect.

3.4.3 Winter Convection

The minimum sea-surface temperature on the Scotian Shelf ranges between 1 and 2°C (Fig. 3.2). The minimum winter air temperature over the Scotian Shelf is much colder[3], with temperatures ranging from -20 to -5°. The surface of the ocean therefore loses heat to the atmosphere when the air temperature is less than the sea-surface temperature. The loss of heat causes the surface waters to become colder, and more dense. These dense waters will sink and be replaced by warmer waters from below. The process, called convective mixing, can also occur due to surface evaporation which leaves behind salty, dense waters which will sink and below the underlying fresher water. Convection occurs in winter season on the Scotian Shelf. In this region wind speed exerts some control over the depth of convective mixing; an increase in wind strength removes more heat from the surface waters and deepens the extent of the convection. The impact of winter convection can be seen in the increase in the depth of penetration of relatively warm waters (down to 50 meters) in the autumn and winter (Fig. 3.4a). The impact of winter convection on the seasonal cycle of CO_2 on the Scotian Shelf will be discussed in more detail in Sections 3.4.2 and 3.4.3.

3.4.4 Water Mass Composition

The origin and composition of water masses along the northeastern North American coast are well known (*Bigelow*, 1927; *Hachey*, 1942; *Chapman and Beardsley*, 1989; *Loder et al.*, 1998). As many as eight distinct water masses have been identified on the Scotian Shelf on the basis of oxygen isotope and salinity data (*Khatiwala et al.*, 1999; *Houghton and Fairbanks*, 2001). For simplicity, the water column in the region can be characterized by a two-layer system in winter when relatively fresh shelf water overlies more saline slope-derived water. In summer it is characterized by a three-layer system with the development of a warm, shallow, surface layer overlying the two-layer system (*Loder et al.*, 1997). Sections of temperature and salinity in late summer (September) and early spring (April) are shown in Figure 3.3. In early spring (and winter), the upper 60 meters of the water column are well mixed and dominated by cold, relatively fresh water originating in the Gulf of St. Lawrence; underlying this is warmer, more saline, slope water (Figs. 3.3a, 3.3b, and 3.4). In summer and early autumn the water column is strongly stratified.

[3]Air temperature data from the Sable Island Meteorological Station from 1971 to 2000 (http://www.climate.weatheroffice.gc.ca)

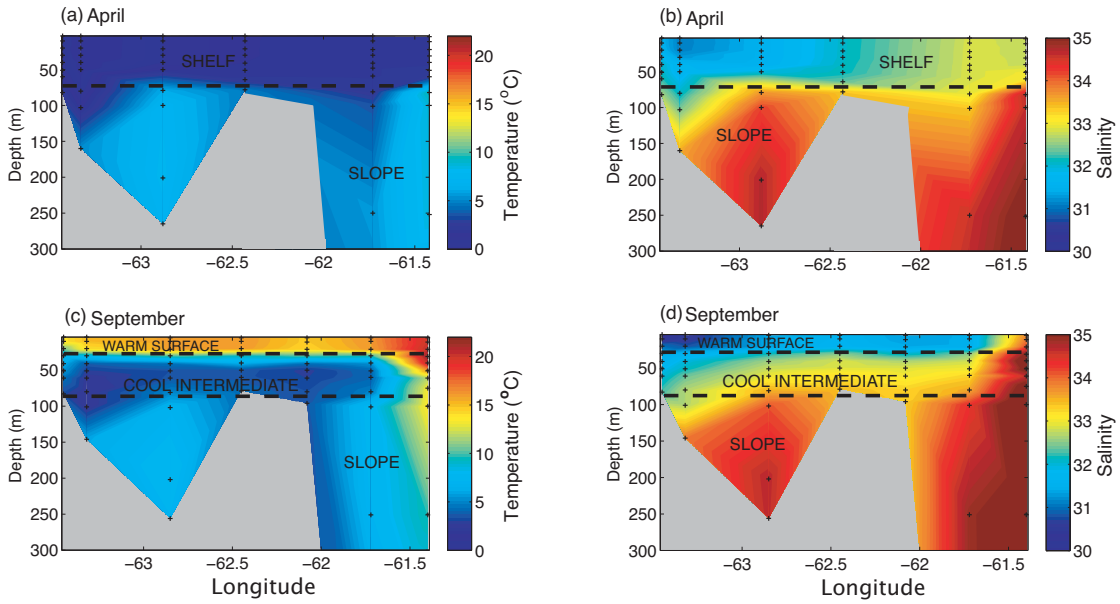

Figure 3.3: Sections of temperature and salinity based on discrete data collected in April and September 2008 along the Halifax Line transect (shown in Fig. 3.2a). In winter the water column can be described by a simple two-layer system (a and b), while in summer surface warming causes a three-layer system to develop (c and d). The boundaries between water masses are schematically shown by the black dashed lines, however in the real ocean setting these boundaries needn't lie along a constant depth.

The near-surface waters warm to greater than 16°C forming a shallow surface layer and forcing the shelf water down to form a cold intermediate layer. The warmer, more saline slope water is present beneath the intermediate layer (Figs. 3.3c, 3.3d, and 3.4). In all seasons the freshest waters are found near the surface and near the coast, and the more saline slope waters found at depth and further offshore.

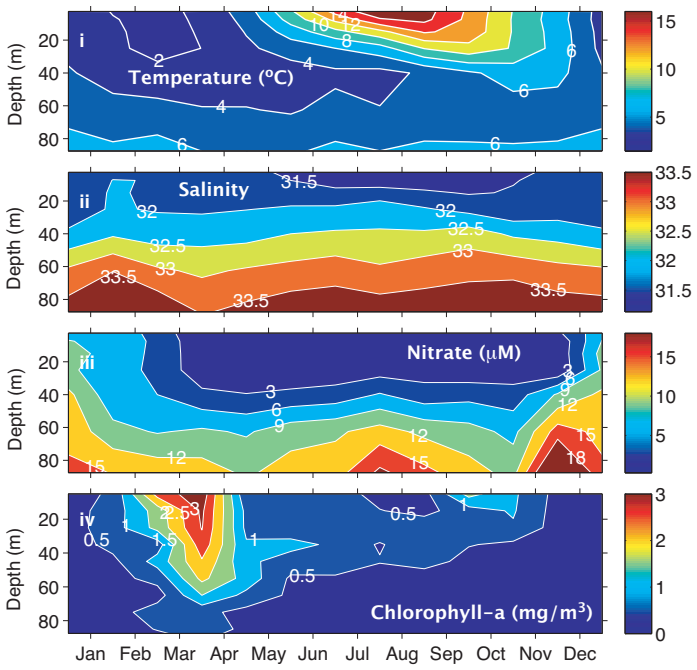

Figure 3.4: A climatology of (a) temperature, (b) salinity, (c) nitrate, and (d) chlorophyll-a concentration for the central Scotian Shelf (43-45° and 62-64°W), based on historical archives from the Bedford Institute of Oceanography. This climatology demonstrates the coincidence of spring bloom and the nutrient depletion of the upper part of the water column in this area of the continental shelf.

Most of the total alkalinity (TA) in seawater originates from the river input due to the weathering of (predominately carbonate) rocks on land (*Morel and Hering*, 1993). The absolute value of TA in a given volume of seawater in the ocean therefore largely corresponds to the salinity of that water. There is a strong linear relationship between TA and salinity (Fig. 3.5a) on the Scotian Shelf. This would suggest a two end-member system in the region, with a less saline water mass from the Gulf of St. Lawrence mixing with a more saline, Gulf Stream influenced, water mass from the open ocean further offshore. There is a seasonal signal in this two-end member mixing relationship evident

in the change in the slope and intercept of the linear fit to the TA and salinity data. This seasonality is investigated further by the application of seawater oxygen isotope ($\delta^{18}O$) data.

There are few conservative water mass tracers that can be used in the ocean, and $\delta^{18}O$ is among them. Furthermore, this parameter allows freshwater from different sources (rivers, sea-ice, precipitation) to be distinguished. The relationship between $\delta^{18}O$ and salinity in the Scotian Shelf region is given in Figure 3.5b. We identify three source waters on the Scotian Shelf: (1) Warm Slope Water (WSW) is Labrador Slope water modified by mixing with warm saline waters of Gulf Stream origin; (2) Labrador Shelf water (LShW) enters the Gulf of St. Lawrence, via the inner branch of the Labrador current, at intermediate depth through the Strait of Belle Isle; and (3) St. Lawrence Estuary Water (SLEW) which is strongly influenced by freshwater flowing out of the St. Lawrence River. The composition of the water in the Scotian Shelf region is a mixture of these three source waters (SLEW, LShW and WSW) with the magnitude of the contribution from SLEW varying seasonally (Fig. 3.5b inset), changing the slope of the relationship between TA and salinity in the region (Fig. 3.5a). In September, the Scotian Shelf receives the maximum discharge from the Gulf of St. Lawrence and the contribution from SLEW is also at a maximum. In contrast, in April the Scotian Shelf receives a much smaller contribution from SLEW due to the formation of sea ice in the Gulf of St. Lawrence in winter, and is more strongly influenced by LShW at this time (Fig. 3.5b). A typical value of glacial melt-water and Arctic river water in the Labrador Sea is $\delta^{18}O = -21^{o}/_{oo}$ (*Khatiwala et al.*, 1999). The black dashed line in Figure 3.5b represents the mixing between WSW and Arctic river waters, the LShW falls to the right of this mixing line due to the influence of brine rejection during sea-ice formation, which increases salinity without changing the $\delta^{18}O$. Thus, while there is information to be gained from the relationship between TA and salinity on the Scotian Shelf a more sensitive parameter is needed for a complete description of the water masses in this region.

3.4.5 Biological Production

The North Atlantic spring phytoplankton bloom is an annually occurring, widespread, biological event. As the days lengthen in the northern hemisphere spring, the increased availability of light and nutrients, which have accumulated over the winter, fuel the growth of phytoplankton in the surface ocean. This bloom begins north of the Sargasso Sea and

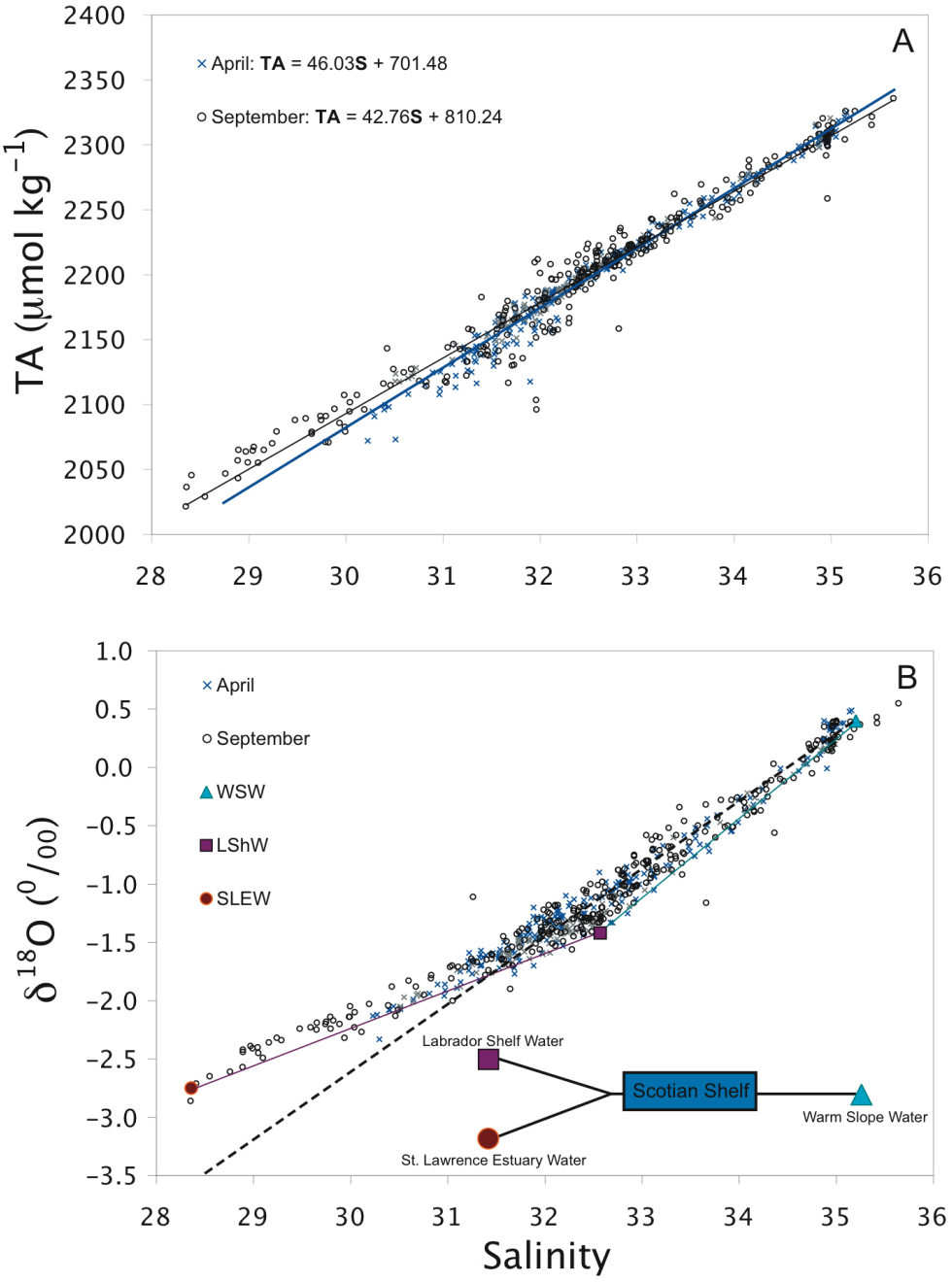

Figure 3.5: (a) The relationship between total alkalinity (TA) and salinity on the Scotian Shelf based on discrete data collected in April (blue x) and September (open circles) of 2008. The linear best-fit lines for spring (n=419, r^2=0.97, p<0.001) and autumn (n=384, r^2=0.91, p<0.001) are also given. (b) The relationship between $\delta^{18}O$ and salinity in spring (blue x) and autumn (open circles). A schematic representation of water mass composition on the Scotian Shelf is shown in the bottom right corner. At surface and intermediate depths SLEW and LShW mix, largely in the Gulf of St. Lawrence; WSW occupies the lower water column in the region. Seasonality in the contribution of SLEW reflects formation of sea-ice in the St. Lawrence estuary.

moves northward through the Atlantic into the North Sea constituting a significant sink for atmospheric CO_2 (*Siegel et al.*, 2002). Magnitude, timing, and extent of this bloom vary from year to year (e.g. *Greenan et al.*, 2008). Chlorophyll-a fluorescence is often used as a proxy for phytoplankton biomass (Fig. 3.4 iv) (*Kiefer*, 1973; *Falkowski and Kiefer*, 1985). During the spring bloom on the Scotian Shelf, which occurs with remarkable consistency near the first week in April each year, chlorophyll-a concentration increases nearly tenfold in a matter of days. This rapid increase in phytoplankton biomass utilizes the nutrients, which have accumulated in the subsurface as result of organic matter remineralization, or respiration, and which are brought up to the surface. The spring bloom is dominated by large phytoplankton size-classes and is terminated by the exhaustion of nitrate and silicate (*Mousseau et al.*, 1996). The phytoplankton community on the Scotian Shelf is mainly comprised of diatom species, providing the main food source to planktonic animals and bottom-dwelling filter feeders. On the Scotian Shelf the spring bloom is the dominant control on phytoplankton biomass, though the more moderate summer production also plays a role (see Chapters 4 and 5). The spring bloom accounts for roughly one third of the total annual primary production on the Scotian Shelf which ranges from 60 to 130 g C m^{-2} yr^{-1} (*Fournier et al.*, 1977; *Mills and Fournier*, 1979). It represents the dominant source of primary productivity, setting the upper limit on organic matter export, production of higher trophic levels, and supply to benthic communities (*Eppley*, 1981). During the remainder of the year surface nitrate concentrations remain fairly low (Fig. 3.4iii) and smaller sized phytoplankton dominate. Local vertical mixing, or upwelling, may re-supply nutrients to the surface layer in summer, and production continues through October (see Chapter 4). The organic matter produced by the phytoplankton fuels higher trophic levels.

3.4.6 The North Atlantic Oscillation

One of the important climate modes affecting circulation and hydrographic properties in eastern Canadian waters is the North Atlantic Oscillation. The North Atlantic Oscillation (NAO) Index is defined by the difference in sea-level pressure (SLP) between the Icelandic Low and the Azores High (*Thompson and Wallace*, 2001). The relative strengths and positions of these two systems vary from year to year, controlling the strength and position of the prevailing westerly winds. A large SLP difference between the two locations corresponds to a positive NAO index, a small SLP difference to a negative NAO index.

The NAO is the dominant atmospheric forcing over the North Atlantic Ocean influencing air temperature, wind, and precipitation. During positive phases of the NAO, the prevailing westerly winds become more intense and the North Atlantic storm track shifts to the north. This northward shift results in warmer, milder conditions over the western North Atlantic ocean and along the east coast of North America and in northern Europe, and colder, more stormier conditions over Greenland (*Hurrell*, 1996). During negative phases of the NAO the situation is reversed; the westerly winds diminish in intensity and the storm track is shifted to the south. This results in colder, stormier conditions in the western North Atlantic and over the eastern North American coast, warmer milder conditions over Greenland, and colder, drier conditions in northern Europe (*Hurrell*, 1996).

The NAO also impacts the circulation patterns of the North Atlantic Ocean. In negative phases of the NAO convection in the Labrador Sea becomes more shallow, and volume transport by the Labrador Current increases. In contrast, during positive phases of the NAO convection in the Labrador Sea is deeper and more intense, and transport by the shallow Labrador Current is decreased (*Dickson*, 1997). It has been shown that the NAO can influence hydrographic properties on the northeastern Atlantic continental shelf (*Petrie*, 2007). During periods of negative NAO index, relatively cold, fresh, conditions are seen on the eastern Scotian Shelf and Gulf of St. Lawrence due to the increased transport of Labrador slope water to the region (*Petrie*, 2007). Over the last decade the NAO index has generally been negative or near-neutral; the impact on the carbon system in the Scotian Shelf as a potential consequence of the NAO will be discussed in more detail (see Section 3.5.2 and also Chapter 5).

3.5 The CO_2 System on the Scotian Shelf

It is useful to describe processes affecting the carbonate system in seawater with respect to the associated changes in dissolved inorganic carbon (DIC) and TA, which are shown schematically in Figure 3.6. With respect to the inorganic carbon system, photosynthesis and aerobic respiration are the dominant biological processes. Photosynthesis by algae can be described by the following equation:

$$106\mathrm{CO_2} + 122\mathrm{H_2O} + 16\mathrm{HNO_3} + \mathrm{H_3PO_4} \rightarrow [(\mathrm{CH_2O})_{106}(\mathrm{NH_3})_{16}\mathrm{H_3PO_4}]_{\mathrm{organic}} + 138\mathrm{O_2}. \tag{3.1}$$

Photosynthesis produces, on average, organic matter with carbon and nutrients in Redfield ratio, i.e. C:N:P = 106:16:1 (*Redfield et al.*, 1963). Photosynthesis therefore reduces DIC, as 106 moles of CO_2 per mole of H_3PO_4 are consumed in the production of organic matter. There is a modest increase in TA (16 moles) by photosynthesis due to the consumption of nitrate (NO_3^-) (e.g. *Goldman and Brewer*, 1980). Respiration converts organic matter to inorganic carbon (and nutrients) and DIC is increased, with a corresponding, modest, decrease in TA. The formation of calcium carbonate ($CaCO_3$) reduces both DIC and TA in the ratio of 1:2, while dissolution has the opposite effect. The uptake of atmospheric CO_2 increases DIC, but TA remains unchanged since the charge balance in the system has not been affected. Similarly, the out-gassing of CO_2 from the ocean decreases DIC without changing TA.

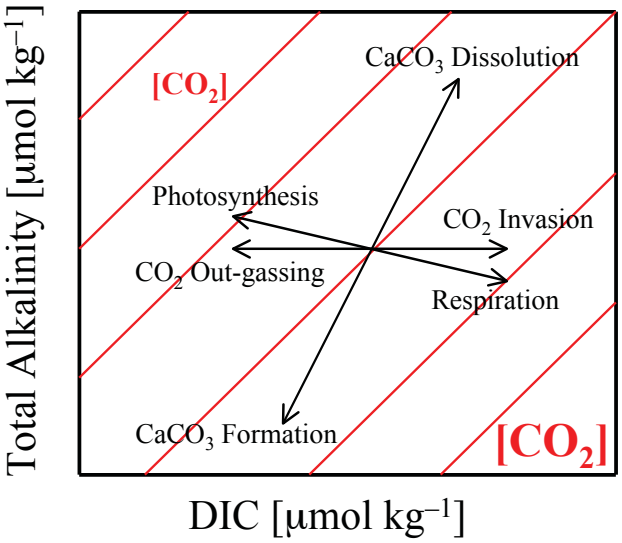

Figure 3.6: The effect of various processes on DIC and TA (arrows). The solid diagonal lines indicate levels of constant dissolved CO_2, increasing from the top left to the bottom right.

As discussed above, the formation and dissolution of calcium carbonate ($CaCO_3$) play an important role in the inorganic carbon system in seawater. A determining factor with respect to the formation and dissolution of $CaCO_3$ is the calcium carbonate saturation state of seawater. The $CaCO_3$ saturation state, Ω, is expressed as:

$$\Omega = \frac{[Ca^{2+}][CO_3^{2-}]}{k_{sp}^*} \tag{3.2}$$

where $[Ca^{2+}]$ and $[CO_3^{2-}]$ are the concentrations of Ca^{2+} and CO_3^{2-} in seawater, respectively, and K_{sp}^* is the stoichiometric solubility product at in-situ temperature, salinity, and pressure (*Zeebe and Wolf-Gladrow*, 2001). Due to the quasi-conservative behavior of calcium in the ocean, variations in $[Ca^{2+}]$ are relatively small and closely related to changes in salinity (*Zeebe and Wolf-Gladrow*, 2001); the $CaCO_3$ saturation state is therefore more strongly influenced by the carbonate ion concentration, which will be discussed in more detail (Section 3.5.3). Values of $\Omega > 1$ correspond to supersaturation, permitting formation of $CaCO_3$ and values of $\Omega < 1$ correspond to undersaturation, permitting dissolution of $CaCO_3$.

The concentration of CO_2 is related to the partial pressure (pCO_2) by Henry's Law:

$$[CO_2] = \alpha pCO_2, \tag{3.3}$$

where α is the Henry's constant, or coefficient of solubility, which depends mainly on temperature and to a lesser degree on salinity (*Weiss*, 1974). Water temperature exerts a strong control on pCO_2 (Fig. 3.7) and the relationship between the two variables is well understood. For a 1°C change in temperature we expect a 4% change in pCO_2 (*Takahashi et al.*, 2002). In other words, for 1°C of warming, at a mean pCO_2 of 400 μatm, we expect an increase in of 16 μatm. An exchange of CO_2 between the atmosphere and the ocean occurs when there is a gradient in CO_2 across the air-sea interface. The mass transfer of CO_2 is largely driven by the concentration difference between the atmosphere and the sea surface, and the turbulence at the air-sea interface. The air-sea exchange of CO_2 is computed using the following equation:

$$F_{CO_2} = k\alpha\Delta pCO_2, \tag{3.4}$$

where F_{CO_2} (mol C m^{-2} s^{-1}) is the air-sea CO_2 flux, k (m s^{-1}) is the gas transfer velocity parameterized as a function of wind speed, α (mol atm^{-1} m^{-3}) is the coefficient of solubility, and ΔpCO_2 is the gradient of pCO_2 between the sea-surface and the atmosphere (i.e. $\Delta pCO_2 = pCO_2{}^{sea} - pCO_2{}^{air}$). The gas transfer velocity was computed with the formulation of *Wanninkhof* (1992) for short-term winds, and hourly wind speeds measured at the Sable Island Meteorological Station.

3.5.1 Seasonal Variations in DIC and pCO_2

During the winter the surface waters of the Scotian Shelf are quite cold (near 0°C), and the pCO_2 is relatively constant and supersaturated with respect to atmospheric CO_2 with values of roughly 420 μatm (Fig. 3.7). The surface DIC concentrationr is at its maximum in winter due in part to respiration of organic matter, but mainly to the delivery of carbon-rich water from below (Fig. 3.8). In winter, the mixed-layer deepens due to wind forcing and convection, and waters with higher concentrations of inorganic carbon and nutrients are delivered to the surface layer. With the onset of the spring bloom the surface waters of the Scotian Shelf rapidly become undersaturated with respect to atmospheric CO_2. In 2008, the surface pCO_2 decreased from 430 μatm to 250 μatm over a period of nine days (Fig. 3.9). There is a corresponding decrease in DIC in the surface layer between winter and spring due to the uptake of inorganic carbon to fuel the phytoplankton bloom. Heterotrophic organisms graze much of the algae produced by the bloom. However, some of the organic matter produced at the surface will accumulate, become heavy, and sink out of the surface layer. The remineralization (or respiration) of the organic matter exported to the subsurface layer increases the concentration of DIC in this layer.

The strength of the bloom, is largely determined by the winter pre-conditioning of the system. Strong winter winds and a deep mixed-layer supply more inorganic nutrients to fuel the spring bloom than a shallower, more poorly mixed water column. The spring bloom occurs when the water is still near the minimum winter temperature (Fig. 3.7) allowing the competing effects of thermodynamics (warming increases pCO_2) and biology (photosynthesis decreases pCO_2) to be distinguished. The effect of temperature on pCO_2 is well understood, and an empirical correction to remove the effect of temperature has been defined (*Takahashi et al.*, 2002):

$$\mathrm{pCO_2(T_{mean}) = pCO_2(obs)[exp(0.0423(T_{mean} - T_{obs}))]}, \tag{3.5}$$

where $\mathrm{T_{mean}}$ is the annual mean sea-surface temperature, and 'obs' refers to the observed, or in-situ temperature and pCO_2(obs) refers to the in-situ pCO_2. The correction of pCO_2 to the annual mean temperature allows the effects of non-temperature dependent processes to be clearly seen. In other words, by removing the effect of temperature from pCO_2, the dominant mechanisms, such as photosynthesis or entrainment, acting for example over a particular season, may emerge. The temperature corrected pCO_2 is plotted against in-situ

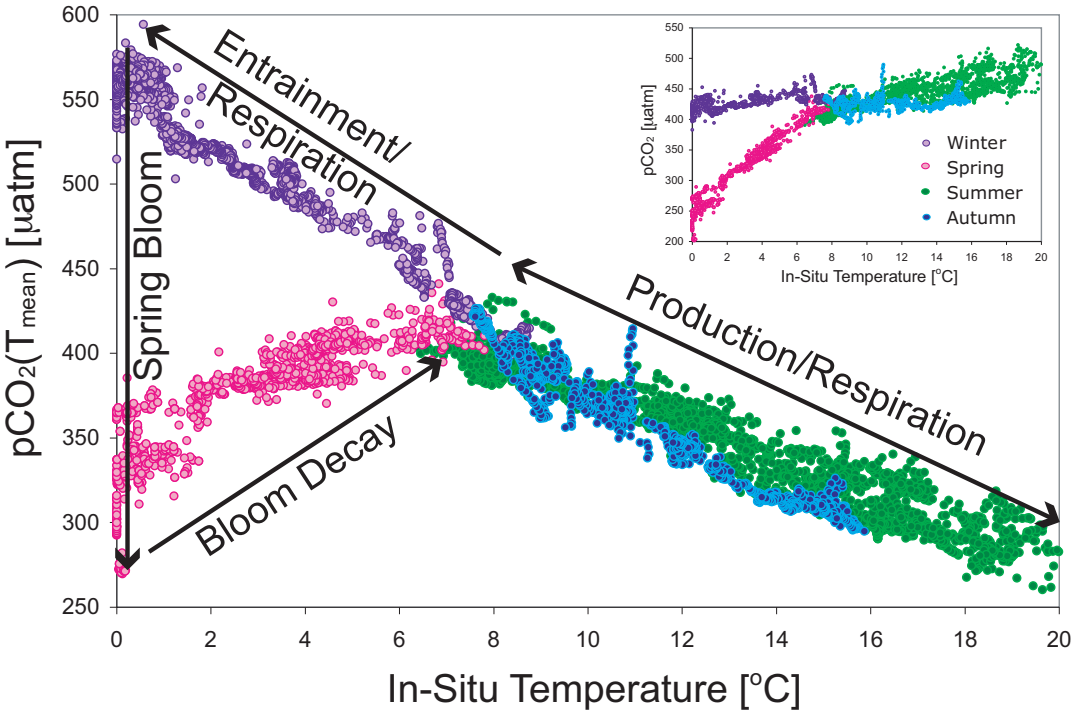

Figure 3.7: Values of surface water pCO_2 are normalized to a constant, annual mean surface temperature (T_{mean} = 7.0°C), and plotted versus their observed temperature. Seasons are distinguished by color. See section 3.4.2. for more discussion on $pCO_2(T_{mean})$. The dominant mechanisms acting in each of the seasons are shown schematically by the black arrows. Inset: surface pCO_2 is plotted against in-situ temperature, with seasons distinguished by color.

temperature with the seasons distinguished by color in Fig. 3.7. It can clearly be seen that the spring bloom occurs at the annual temperature minimum and results in a large reduction of pCO_2. The decay of this bloom is coincident with the warming of the surface waters in late spring, and the $pCO_2(T_{mean})$ increases as photosynthesis ceases and respiration dominates in the surface waters. Over the summer, while the waters warm, $pCO_2(T_{mean})$ continues to decrease indicating the uptake of CO_2 by biological processes outside of the dominant spring bloom. Vertical export of this material fuels the respiration in the subsurface and increases the subsurface DIC concentration between spring and summer (Fig. 3.10). This late summer production reduces the temperature-corrected pCO_2 by almost 100μatm, making a significant contribution to the annual biological production in the region (see Chapter 4). In autumn, the surface waters cool and there is an increase in $pCO_2(T_{mean})$ when the surface waters are dominated by respiration of the organic matter supplied by the late summer production. In autumn, surface DIC concentrations are at the annual minimum due partly to the uptake of CO_2 by biological processes through the spring and summer, but also as a result of dilution of DIC due to the delivery of fresher water from the Gulf St. Lawrence. The autumn subsurface DIC concentration corresponds to the annual maximum due to the remineralization of the accumulated organic matter delivered from the surface layer over the spring and summer. Most of this respired material remains in the subsurface through the summer and early autumn because of the relatively strong stratification over this period, which inhibits vertical mixing (Fig. 3.4). Later in autumn, the frequency and magnitude of storms in the region is increased, breaking down the surface stratification and allowing the carbon-rich subsurface waters to be entrained into the surface layer. In winter, convection also forces DIC-rich water from the subsurface into the surface layer. The autumn and winter values of $\mathrm{pCO_2(T_{mean})}$ are enhanced by roughly 100μatm, due to the combined effects of respiration and mixing, while over the same period the water temperature decreases to the annual minimum.

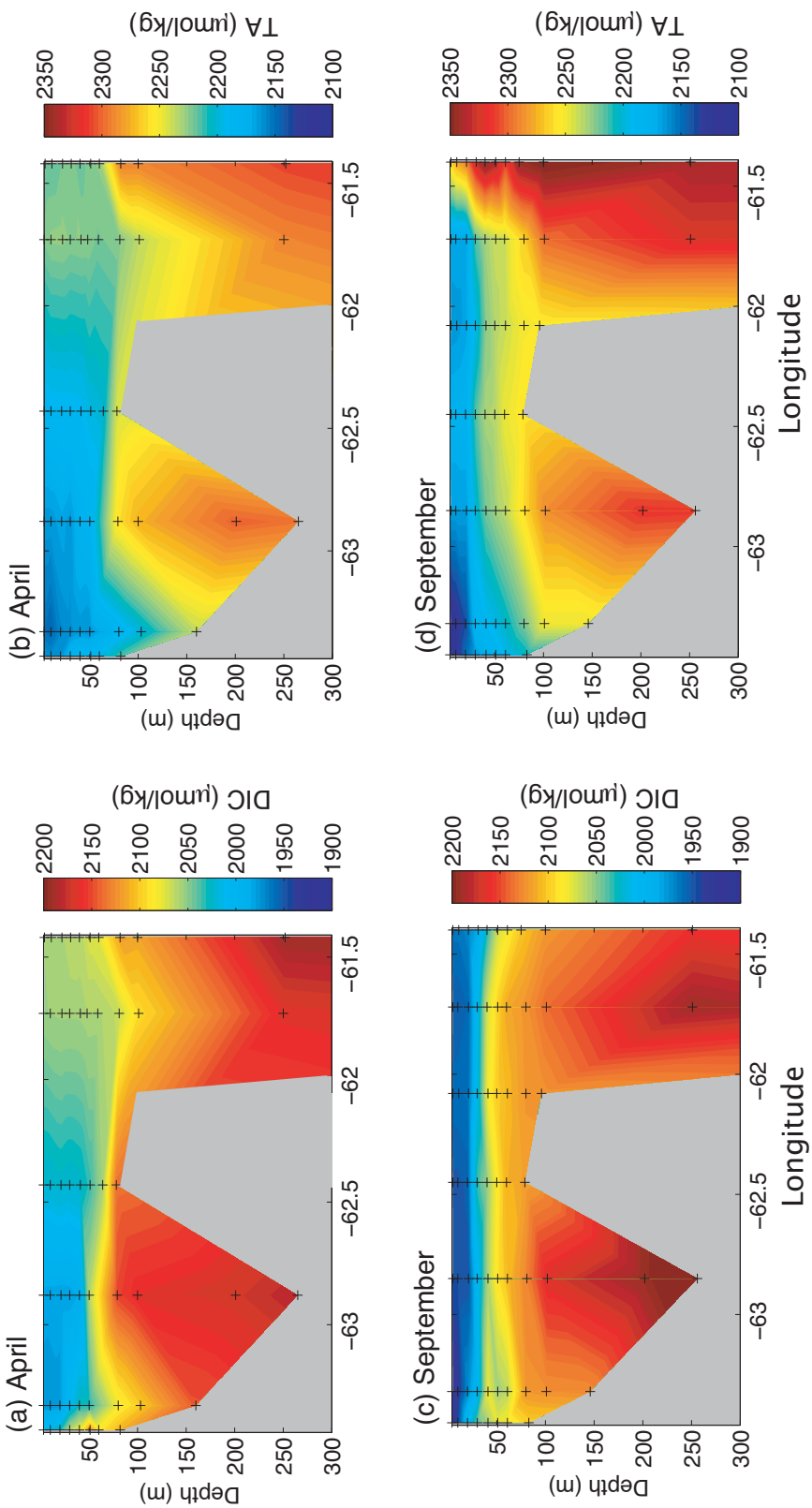

Figure 3.8: Sections of dissolved inorganic carbon (DIC) and total alkalinity (TA) concentration along the Halifax Line transect (shown in Fig. 3.2a) based on discrete data collected in (a and c) April and (b and d) September.

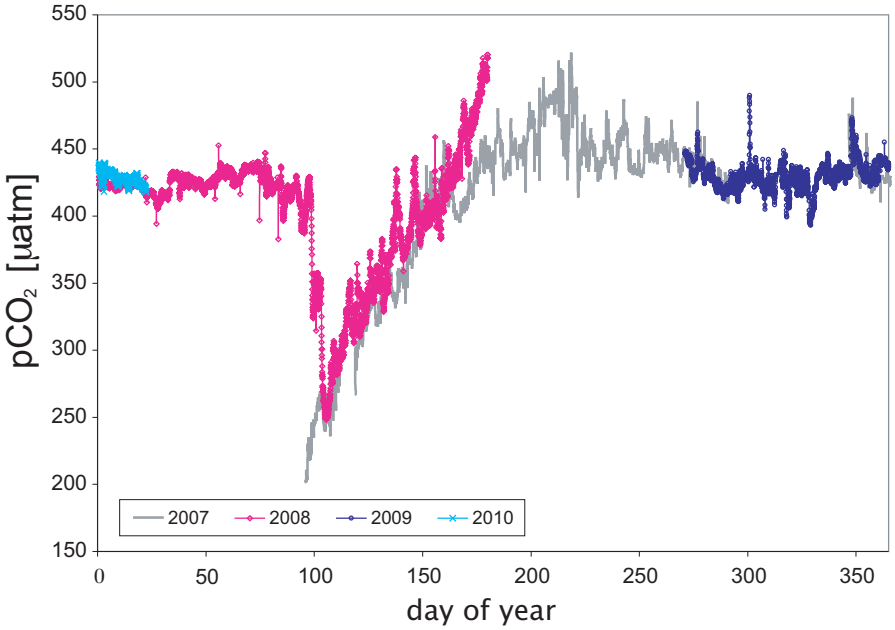

Figure 3.9: Hourly surface water pCO_2 collected at station HL2 (43.3°N, 63.3°W), from 2007 to 2010. The annual cycle is driven by the spring phytoplankton bloom, the summer warming of the surface waters, and the late summer biological production, and shows very little interannual variability over the measurement period.

3.5.2 Air-Sea CO_2 Fluxes

As discussed in the preceding section, the transfer of CO_2 from the atmosphere to the ocean is largely controlled by the gradient in CO_2 concentration between the two reservoirs (ΔpCO_2) and the turbulence at the air-sea interface (Eq. 3.4). The turbulence reflects the sea-state, and wind speed, both in-situ, and in the preceding days and hours, and swell, and breaking waves may also contribute. In general, however, wind speed exerts the primary control on sea-state and turbulence. The annual cycle of integrated monthly wind speed measured at the Sable Island Meteorological Station and the annual cycle of monthly air-sea CO_2 fluxes measured at station HL2 (43.3°N, 63.3°W), are given in Figure 3.11. There is a correlation between wind speed and (the magnitude of the) air-sea CO_2 flux (Eq. 3.4). In winter the waters are supersaturated with respect to atmospheric CO_2, thus the ΔpCO_2 is positive and there is an outgassing of CO_2 to the atmosphere. Over the same period the region experiences high winds which enhance the outgassing of CO_2, and convective mixing which brings DIC-rich water to the surface and increases the ΔpCO_2. In contrast, in April the spring bloom draws down DIC and the surface waters

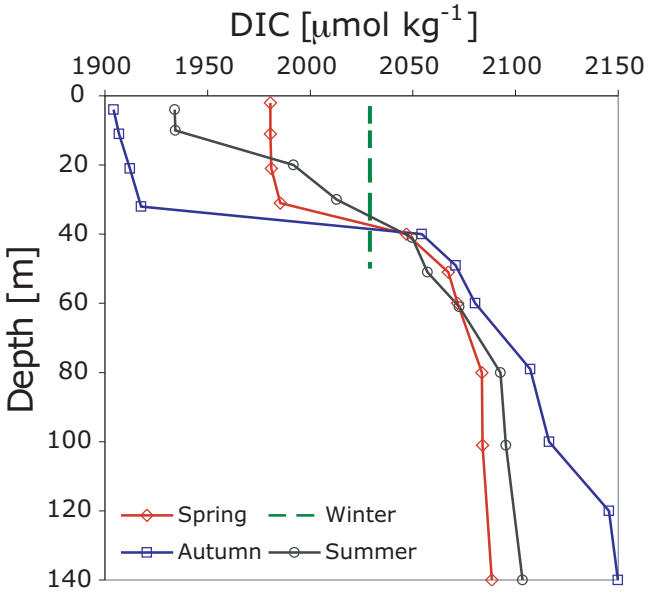

Figure 3.10: Seasonal profiles of DIC at station HL2 in 2008.

are undersaturated with respect to the atmosphere (i.e. $\Delta pCO_2 < 0$). The wind speed is still relatively high in early spring, and there is a strong uptake of CO_2 by the ocean. The much smaller uptake observed in May is primarily due to the decrease in ΔpCO_2 by the decay of the spring bloom and to a reduction in wind speed (Fig. 3.11). Over the summer the winds are much weaker, and although the surface waters are supersaturated with respect to atmospheric CO_2 from June onward, the outgassing is modest compared to the winter season. The magnitude of the flux increases from October due both to the increase in wind speed and the positive evolution of ΔpCO_2 due to the intrusion of CO_2 rich waters from the subsurface and the cessation of biological production in the surface layer.

3.6 Discussion

3.6.1 Trophic Status and Atmospheric CO_2

Oceanic metabolism is an important concept in defining particular regions of the ocean as potential sinks for atmospheric CO_2 (*Smith and Hollibaugh*, 1993). The metabolism, or trophic status, of a marine system, or region, is often described with respect to the production or consumption of organic matter (*Smith and Hollibaugh*, 1993; *Gattuso et al.*, 1998;

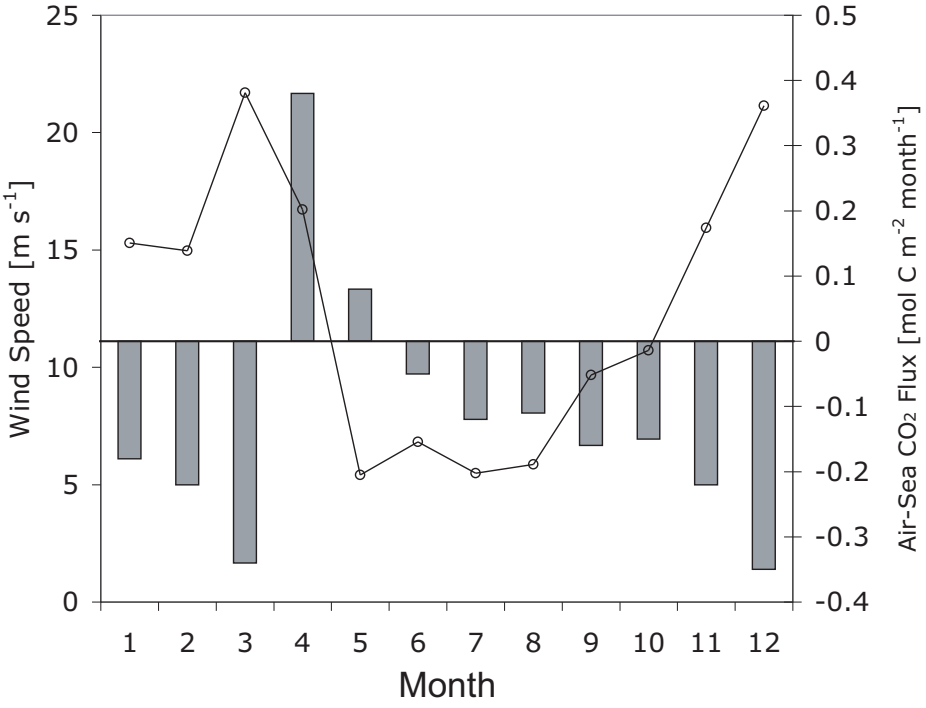

Figure 3.11: The annual cycle of monthly wind speed (m s^{-1}) (line) measured at the Sable Island Meteorological Station, and the air-sea CO_2 flux (mol C m^{-2} $month^{-1}$) (bars) for the year 2008 at station HL2.

Thomas et al., 2005b). Systems are defined as autotrophic if there is a net production of organic matter and a net depletion of inorganic carbon and nutrients, or, in other words, if primary production exceeds respiration. These systems may potentially export this excess organic carbon. The reverse situation defines heterotrophic systems; in this case there is a net consumption of organic matter and a net production, or release, of inorganic carbon and nutrients with respiration dominating gross primary production. Ideally, the atmosphere fuels the CO_2 demand of autotrophic systems with rivers also potentially acting as sources of inorganic carbon (*Thomas et al.*, 2005b). Depending on the initial ΔpCO_2 state of these systems, they may exhibit enhanced CO_2 uptake ($pCO_2^{ocean} < pCO_2^{atm}$), or diminished outgassing of CO_2 to the atmosphere ($pCO_2^{ocean} > pCO_2^{atm}$). Heterotrophic systems require a source of organic carbon to fuel respiration, and in supersaturated conditions, will exhibit enhanced outgassing of CO_2 to the atmosphere, while in undersaturated waters CO_2 uptake will be reduced (*Thomas et al.*, 2005b). Therefore autotrophic systems, though production exceeds respiration, do not necessarily act as sinks for atmospheric CO_2, and respiration-dominated heterotrophic systems do not necessarily release

CO_2 to the atmosphere. The initial conditions of the system, with respect to surface pCO_2, condition this uptake/release. The North Sea, for example, is an overall heterotrophic system that acts as a sink for atmospheric CO_2 over the annual scale (*Lenhart et al.*, 2004; *Thomas et al.*, 2005b). A more general classification would be seasonally stratified systems such as the Gulf of Biscay (*Frankignoulle and Borges*, 2001), or permanently stratified systems such as the Baltic Sea (*Thomas and Schneider*, 1999). The opposite situation, autotrophic systems acting as sources for atmospheric CO_2, is often found in upwelling systems where the intrusion of DIC-rich subsurface water into the surface layer maintains CO_2 supersaturation despite the large production (and export) or organic matter in these systems. The Scotian Shelf acts as an upwelling system in this respect. There is a significant production of organic matter during the spring bloom and also throughout the summer and the surface waters are found to be autotrophic (see Chapter 4). However, the combined effect of summer warming, and the injection of high-carbon subsurface water through wind- or convection-driven vertical mixing or upwelling in autumn and winter, maintains high surface pCO_2, and the region therefore acts as a net source of CO_2 to the atmosphere.

3.6.2 Interannual Variability

Spatial and temporal variability in the coastal ocean is generally much higher than in the open ocean. Interannual variability in the timing, duration, and spatial extent of the spring bloom on the Scotian Shelf has been recorded (*Greenan et al.*, 2004). The effects of this variability extend beyond the bloom period and will certainly influence the CO_2 system in this region. Highly temporally resolved measurements from a single location, (Fig. 3.9), indicate that the annual cycle of pCO_2 follows the same general trend over the observation period with the spring bloom, the summer warming, and the autumn and winter mixing dominating. However, observations from 2010 indicate that the spring bloom occurred nearly 3 weeks earlier than in 2007 and 2008. Furthermore, the sea-surface temperature was nearly 3°C warmer at the beginning of April in 2010 compared to both 2007 and 2008. The full water column sampling of DIC and TA collected on consecutive April and September cruises show the same general patterns. The impact of photosynthesis, the delivery of the freshwater from the Gulf of St. Lawrence, and seasonal warming/cooling, can be seen in the surface waters, while the build up of DIC reflects the corresponding biological activity in the subsurface (Fig. 3.8). However, both the pCO_2 and the DIC and

TA measurements are based on the years 2006 through 2008, and the time-series is likely not long enough for a significant trend to emerge. Interannual variability on the Scotian Shelf is therefore investigated using ten years of sea-surface temperature data obtained by remote sensing (see also Chapter 5).

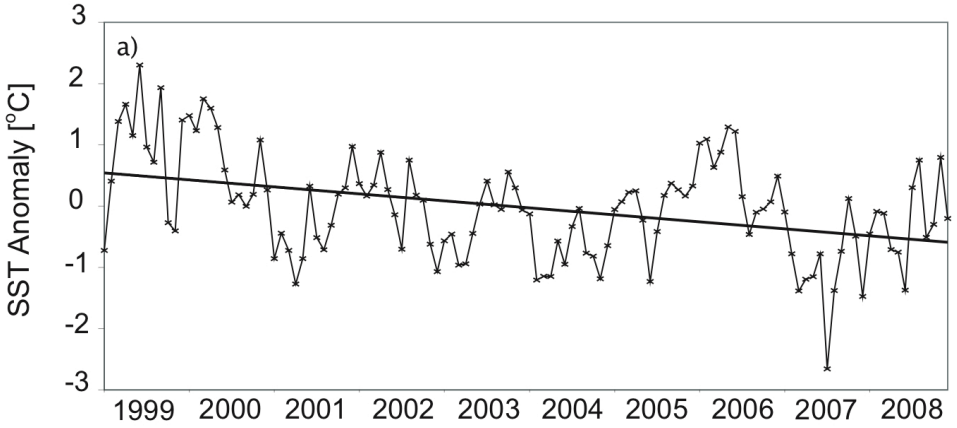

Figure 3.12: Monthly sea-surface temperature anomaly for the central Scotian Shelf from January 1999 through December 2008.

Monthly sea-surface temperature (SST) anomaly for the central Scotian Shelf from 1999 to 2008 is plotted in Fig. 3.12. The mean seasonal cycle of SST was computed using the mean value for each month over the ten-year period[4] (i.e. mean of all January values, mean of all February values, etc.). The SST anomaly is defined as the deviation from the mean seasonal cycle. The SST anomaly indicates a cooling of 0.13°C per year, or 1.3°C over the decade. As discussed in section 3.3.6, this cooling is likely associated with the enhanced delivery of cold water from the Labrador Sea to the Scotian Shelf and may reflect the local expression of the NAO (*Petrie*, 2007). Since temperature exerts a strong control on surface water pCO_2, and consequently ΔpCO_2, this decadal trend towards colder water will have consequences for the inorganic carbon system and air-sea CO_2 fluxes on the Scotian Shelf. A cooling of 1.3°C over ten years would result in a decrease in ΔpCO_2 of roughly 23 μatm over the same period, using the 4% change in pCO_2 for a 1°C change in temperature, and a mean value of pCO_2 = 420 μatm. This decrease in ΔpCO_2, on the order of 20 μatm over the decade, has a non-negligible (weakening) effect on the outgassing of CO_2 to the atmosphere, driving the system towards uptake (see

[4]The 10-yr record of SST was obtained from the Bedford Institude of Oceanography archive for the central Scotian Shelf (43-45°N, and 62-64°W) for the period from 1999 to 2008.

Chapter 5).

3.6.3 Ocean Acidification

As described briefly above, the rise in atmospheric CO_2 due to fossil fuel emissions is partially offset by the ocean's uptake of CO_2 (*Sabine et al.*, 2004). As CO_2 dissolves in seawater the pH is reduced, making the water more acidic; this process has recently been coined 'ocean acidification' (*Caldeira and Wickett*, 2003; *Orr et al.*, 2005). During the 20th century, increasing concentrations of atmospheric CO_2 have decreased the surface ocean pH by 0.1 units (*Hoegh-Guldberg et al.*, 2007). Should CO_2 concentration continue to rise, by the end of this century, changes in surface ocean pH that are greater in magnitude and also faster than those experienced during the transitions from glacial to interglacial periods may occur (*Pearson and Palmer*, 2000). Such large changes in ocean pH have likely not been experienced on the planet for the past 21 million years (*Pearson and Palmer*, 2000). The reaction between CO_2 and DIC in seawater reduces the availability of carbonate ions; coincident with the 0.1 unit decrease in pH is a depletion of seawater carbonate (CO_3^{2-}) concentrations by roughly 30 μmol kg^{-1} (*Hoegh-Guldberg et al.*, 2007). Acidification will directly impact a wide range of marine organisms that build shells from calcium carbonate, from planktonic coccolithophores, to mollusks, to shallow-water and deep-sea corals. Aragonite is the dominant crystalline form of calcium carbonate deposited in the skeletons of deep-sea corals. Experimental studies have shown that increasing seawater CO_2 decreases coral calcification and growth by the inhibition of aragonite formation as carbonate ion concentrations decrease (*Kleypas and Langdon*, 2006). A change in carbonate ion concentration results in a proportional change in the aragonite saturation state (Ω_{ar}) such that as ocean acidification continues, surface ocean Ω_{ar} values will decline. In regions where $\Omega_{ar} > 1.0$, the formation of skeletons and shells is possible. Conversely, if $\Omega_{ar} < 1.0$, the water is corrosive and the dissolution of aragonite shells can occur.

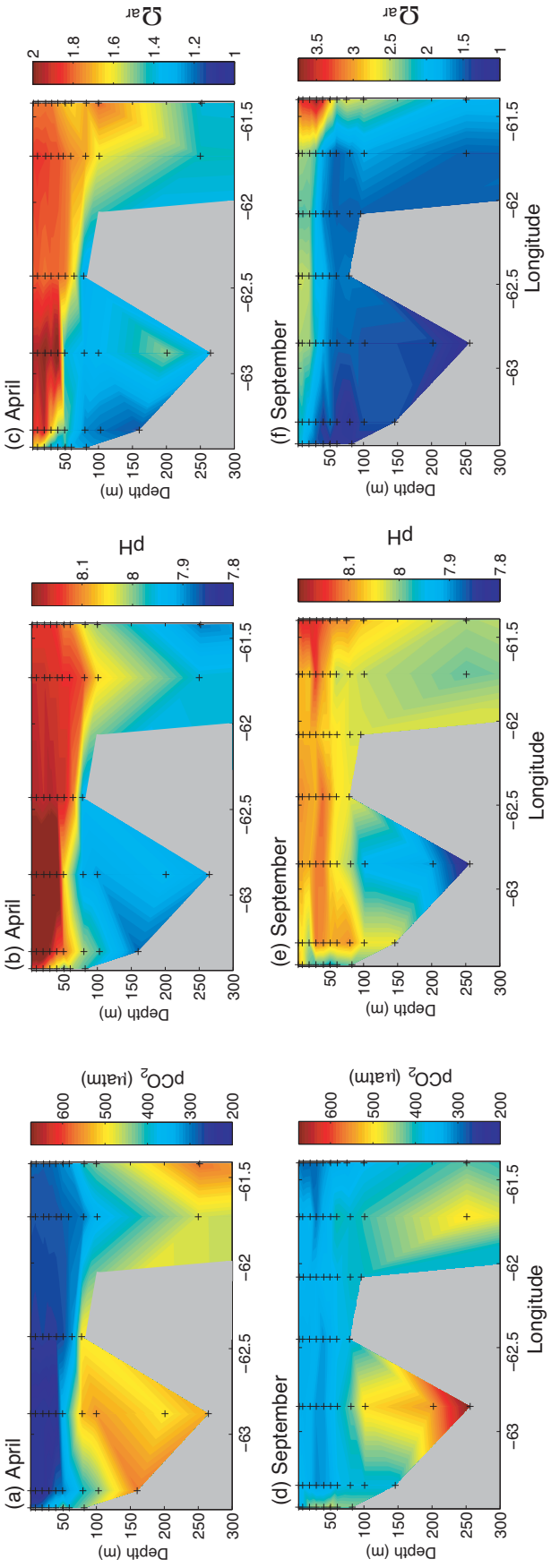

Figure 3.13: Sections of pCO_2, pH, and Ω_{ar} along the Halifax Line transect based on discrete data collected in April (top panels) and September (bottom panels). Please note the change in scale for Ω_{ar} between April and September.

The average surface ocean pH is roughly 8.1; on the Scotian Shelf the surface values are slightly above this global mean. The seasonal profiles of Ω_{ar} do not indicate widespread conditions of undersaturation, however, the saturation state is relatively low in this region (Fig. 3.13). As in the case of pCO_2 and DIC, the limited time-series of data presented here does not allow a longer-term trend to be distinguished. The decadal decrease in SST and corresponding decrease in ΔpCO_2 drives the system on the Scotian Shelf towards greater uptake of CO_2 and consequently lower pH, adding complexity to any observed trend in acidification in this region. In April the surface water pH (and Ω_{ar}) are relatively high due to the uptake of CO_2 by photosynthesis. However at a depth of 150 to 200 m in April, Ω_{ar} approaches undersaturation in the relatively high pCO_2 near-shore waters (Fig. 3.13). Although much of the acidic character of these subsurface waters is the natural result of seasonal respiration at intermediate depth, the ocean, and the North Atlantic in particular, continues to accumulate anthropogenic CO_2 (*Sabine et al.*, 2004). Upwelling is a common physical feature on the Scotian Shelf (*Petrie et al.*, 1987). This process brings high-carbon, low Ω_{ar} waters to the surface and exposes coastal organisms living on or near the sea floor to less saturated waters. Using the annual average sea-surface temperature (SSTavg = 7°C), sea-surface salinity (SSSavg = 30.9), surface TA (TAavg = 2150 μmol kg^{-1}), surface DIC (DICavg = 1950 μmol kg^{-1}), and surface pCO_2 (pCO2(avg) = 420 μatm), the average annual surface aragonite saturation state is Ω_{Ar} = 1.48. If we assume that the surface waters of the Scotian Shelf equilibrate with the atmosphere with respect to the concentration of CO_2, the aragonite saturation state in the surface waters will reach aragonite undersaturation when the atmospheric concentration of CO_2 rises above 675 μatm, or 1.7 times the current level of 390 μatm. According to the model estimates of the Intergovernmental Panel on Climate Change (IPCC), under a variety of emission strategies, atmospheric emissions will reach 675 μatm between 2080 and 2100 (*Watson*, 2001).

It has been suggested that these upwelling could potentially magnify the effects of acidification (*Feely et al.*, 2008). However, we might consider this point from the opposite side: waters from the deep ocean are presently (naturally) acidified due to the remineralization of organic matter, which produces CO_2 and lowers pH. These waters could be considered the least vulnerable to the effects of acidification since their natural range of pH is low. On the other hand, coastal ecosystems in areas which do not experience episodic

upwelling, and areas influenced by rivers could be considered most vulnerable due to the direct influence of atmospheric CO_2, potentially shifting these systems toward undersaturation with respect to carbonate minerals. This is in contrast to upwelling waters, which already reveal undersaturation (i.e. $\Omega_{\mathrm{ar}} < 1$). Further complicating the understanding of the role of ocean acidification is the role natural variability occurring over multi-annual time scales. For example, the North Atlantic Ocean sink for CO_2 has weakened over the last decade; this change in CO_2 uptake, and consequently in surface ocean pH, has been linked to the large scale atmospheric and ocean forcing related to the NAO (*Thomas et al.*, 2008). Similarly, the wind-driven upwelling in the Southern Ocean, which brings CO_2 rich waters to the surface and results in a flux of CO_2 to the atmosphere, is influenced by multi-annual variability related to the Southern Annular Mode, and some regions are found to act as CO_2 sinks, decreasing the surface pH, during weak wind regimes (*Borges et al.*, 2008). Thus the vulnerability of a particular ocean system to increased absorption of CO_2, and consequently lower pH, will strongly depend not only on the present day CO_2 uptake (or release) and the anthropogenic increases in atmospheric CO_2, but also on the processes controlling natural variability, which can be significant. These processes may be particularly important in the coastal zone since it is influenced not only by the atmosphere, but also by rivers, sediments, and the adjacent open ocean depending on the timescales of interest (*Meybeck et al.*, 2007; *Thomas et al.*, 2009a). In some coastal systems the effects of eutrophication may be more significant than those related to ocean acidification (*Borges and Gypens*, 2010). The need to identify small changes in a spatially and temporally variable system highlights the importance of understanding the baseline conditions in coastal systems so trends due to anthropogenic forcing may be understood over all relevant timescales.

3.7 Conclusion

The coastal ocean is vulnerable to anthropogenic activities occurring on land since it receives freshwater, nutrient and sedimentary inputs from the coast. These coastal regions play an important role in the absorption of atmospheric CO_2, but also in supplying essential food to human society. The work presented here provides a baseline assessment of the CO_2 system in the Scotian Shelf region and a quantification of the drivers of seasonal and interannual variability (see also Chapters 4 and 5). This region is strongly influenced

by atmospheric forcing through the North Atlantic Oscillation and exhibits significant interannual variability as a result. This natural variability has the potential to mask anthropogenic effects such as the longer-term trend of declining pH as a result of increased uptake of atmospheric CO_2. This research highlights the necessity of long-term monitoring programs to assess the current state of our oceans and predict their response to change.

The global realization that societal dependence on fossil fuels has a profound influence on the health of our planet is leading to advancements in our understanding of natural systems and their vulnerability to change. The ocean is warming and becoming more acidic as a direct consequence of increasing concentrations of atmospheric CO_2. The ramifications of ocean acidification are of clear relevance to the fisheries industry in Atlantic Canada, which has experienced major declines in the recent decades. Shellfish aquaculture and fisheries are important commercial industries in Nova Scotia; commercial aquaculture supplies nearly half of all the fish and shellfish consumed by humans, and increases in this proportion are projected (*d'Entremont*, 2009). Mitigation measures to lessen the impact of the irreversible acidification of the global ocean are presently lacking. Canada has one of the largest coastlines in the world. There is an opportunity for Canada to lead global efforts to adapt to climate change by implementing policies that promote the sustainable use of our ocean resources. The collapse of the Atlantic cod fishery through mismanagement of this living resource need not be a precedent for Canadian fisheries and oceans policy. The challenge presented by climate change and ocean acidification can be met with innovation, adaptation, and policies aimed at a future in which human impact on the environment is reduced.

CHAPTER 4

SEASONAL VARIABILITY OF DIC AND pCO_2 ON THE SCOTIAN SHELF

4.1 Abstract

The seasonal variability of inorganic carbon in the surface waters of the Scotian Shelf region of the Canadian northwestern Atlantic Ocean was investigated. Seasonal variability was assessed using hourly measurements, covering a full annual cycle, of the partial pressure of CO_2, (pCO_2), and hydrographic variables obtained by an autonomous moored instrument (44.3°N and 63.3°W). These measurements were complemented by seasonal shipboard sampling of dissolved inorganic carbon (DIC), total alkalinity (TA), and pCO_2, at the mooring site, and over the larger spatial scale. Biological processes were found to be the dominant control on mixed-layer DIC, with the delivery of carbon-rich subsurface waters also playing an important role. Annual mixed-layer net community production was $3.7\ \mathrm{mol\ C\ m^{-2}\ yr^{-1}}$. The air-sea fluxes of CO_2 were computed using observed hourly wind speeds from the Sable Island Meteorological Station (43.9°N and 60.3°W). The region acts as a net source of CO_2 to the atmosphere on the annual scale, ($F = -1.4$ mol C m^{-2} yr^{-1}), with a reversal of this trend occurring only during the spring phytoplankton bloom, when a pronounced undersaturation of the surface waters is reached for a short period. Outside of the spring bloom period, the competing effects of temperature and biology influence surface pCO_2 in roughly equal magnitude[1].

[1]This chapter comprises a manuscript by E. H. Shadwick, H. Thomas, K. Azetsu-Scott, B. J. W. Greenan, E. Head and E. Horne entitled *Seasonal variability of dissolved inorganic carbon and surface water pCO_2 in the Scotian Shelf region of the Northwestern Atlantic* under revision in Marine Chemistry.

4.2 Introduction

The need to accurately balance the ocean carbon cycle is an important issue in current global climate research. Relative to their surface areas, the coastal oceans are the site of a disproportionately large fraction of ocean productivity (*Cai et al.*, 2003; *Borges et al.*, 2005). Although the coastal ocean represents only 8% of the total ocean surface area, roughly one-fifth to one-third of the global marine primary production takes place in these seas (*Walsh*, 1991). This productivity may be fueled by either terrestrial, atmospheric, or oceanic nutrient inputs, from natural or anthropogenic sources. High biological activity in coastal areas causes enhanced fluxes of CO_2 between the coastal ocean and the atmosphere, and also between coastal and open ocean environments (*Thomas et al.*, 2004; *Chen and Borges*, 2009). Temporal variability in the coastal ocean is faster than that of the open ocean environment. As such, the processes controlling the cycling of carbon in near-shore systems are difficult to resolve without continuous measurement of physical and biogeochemical variables. Sustained time-series measurements have done much to resolve uncertainties in carbon cycling for a number of coastal ocean regions (e.g., the North Sea, Belgian and Tasmanian coastal waters) (*Bozec et al.*, 2006; *Schiettecatte et al.*, 2006, 2007; *Borges et al.*, 2008).

The North American Atlantic coast is fairly densely populated, and is therefore directly impacted by anthropogenic activities. However, baseline assessments of the carbon system, and the development of carbon budgets for these coastal regions have not yet been made (*Najjar et al.*, 2010). A recent global synthesis of observational data from continental shelf regions suggests that temperate and high-latitude shelves largely act as sinks for atmospheric CO_2 (*Chen and Borges*, 2009). The Scotian Shelf is an open, temperate, continental shelf region. The Scotian Shelf is adjacent to the Gulf of Maine, and upstream from the South and Middle Atlantic Bights, three additional open continental shelf systems in both temperate and subtropical regions. Both the South (*Jiang et al.*, 2008) and the Middle Atlantic Bight (*Boehme et al.*, 1998; *DeGrandpre et al.*, 2002) have been found to act as net sinks of atmospheric CO_2 in line with the synthesis of *Chen and Borges* (2009) and the most recent surface ocean CO_2 partial pressure (pCO_2) climatology of *Takahashi et al.* (2009). While outgassing is observed in summer, due to the warming of the surface waters and the corresponding increase in pCO_2, the South and Middle Atlantic Bights

act as sinks for CO_2 in the autumn and winter seasons, in agreement with the classification of *Chen and Borges* (2009). Furthermore, in both the South and Middle Atlantic Bights, temperature is found to be the dominant control on the variability of pCO_2 over the annual cycle (*DeGrandpre et al.*, 2002; *Jiang et al.*, 2008). Modeling studies on the eastern North American continental shelf, including the Scotian Shelf and Gulf of Maine regions, have suggested that the region acts as an annual sink for atmospheric CO_2, and the interannual variability in the air-sea CO_2 flux is in this region is due in part to the North Atlantic Oscillation (*Fennel et al.*, 2008; *Previdi et al.*, 2009). We present the first observationally-based investigation of the inorganic carbon system in the Scotian Shelf region; this study emphasizes the utility of (long-term) time series measurements in the assessment of the carbonate system in coastal regions.

This study combined traditional ship-board sampling with autonomous time-series measurements to unravel the processes controlling the seasonal variability of carbon cycling in this coastal ocean environment. Hourly measurements covering a full annual cycle of pCO_2, and hydrographic variables obtained by an autonomous moored instrument are presented. These measurements were complemented by spring and autumn ship-board sampling of dissolved inorganic carbon (DIC), total alkalinity (TA), and monthly sampling of hydrographic variables, at the mooring site. The controls on surface $\mathrm{pCO_2}$ and DIC were investigated by isolating changes due to variations of temperature, as well as changes due to air-sea CO_2 flux, lateral transport, and biological production. A simple 1-D box model, using a conservation equation for DIC in the surface mixed-layer, was applied to quantify changes in DIC due to biological production throughout the year. Annual air-sea fluxes and mixed-layer net community production (NCP) were estimated.

4.3 Oceanographic Setting

The Scotian Shelf is a highly productive area of the Canadian northwestern Atlantic ocean (Fig. 4.1). This shelf region hosts active fisheries, is heavily influenced by river water input from the Gulf of St. Lawrence, and receives a downstream flow of water from the Labrador Sea. The Scotian Shelf has large temporal and spatial variations in its hydrographic properties as a result of its location downstream of the Gulf of St. Lawrence, and its unique position at the boundary of the North Atlantic sub-polar and subtropical

gyres. The seasonal shelf-scale circulation on the Scotian Shelf is dominated by an equatorward flow, via the Nova Scotian Current, on the inner shelf, and via an extension of the Labrador Current along the shelf edge (*Hannah et al.*, 2001). The Nova Scotian current flows to the southwest, along the coast; transport varies seasonally in strength with peak values of 2 and 2.2 Sv in winter and spring, and a minimum of 0.4 Sv in summer (*Loder et al.*, 2003). Smaller scale circulation features include partial gyres generated by topographic steering around submarine banks, (i.e. Browns Bank, Sable Island Bank, and Georges Bank), and cross-shelf channels (*Loder et al.*, 1988; *Hannah et al.*, 2001).

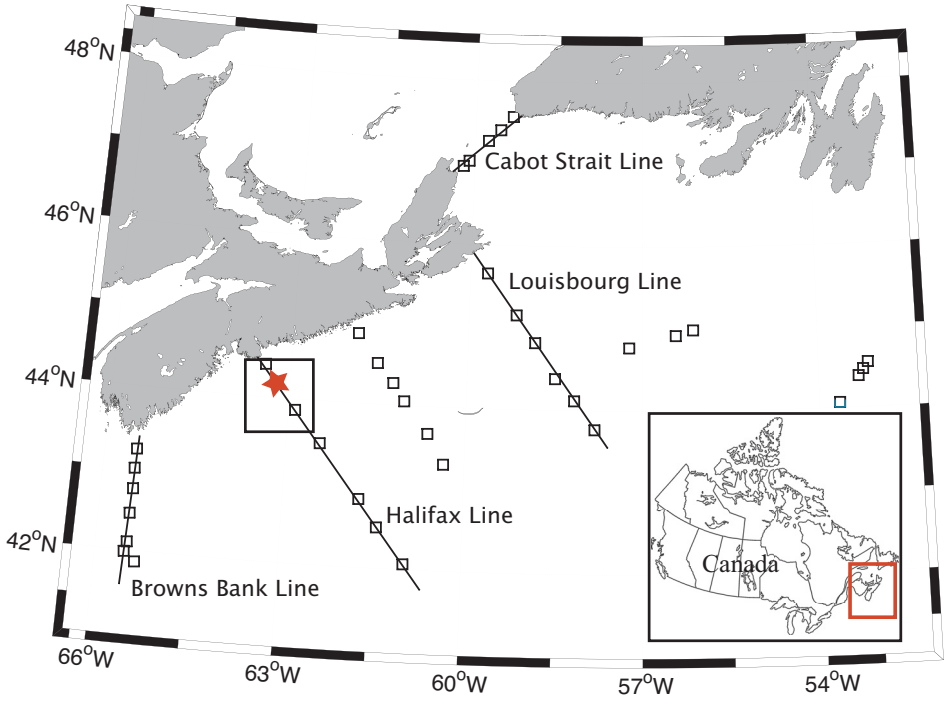

Figure 4.1: Locations of stations sampled along four primary transect lines on the Scotian Shelf as part of the AZMP. Open squares indicate stations sampled on cruises in April 2007, April 2008, and September 2007. The location of station 'Halifax Line 2' (HL2) is indicated by the star.

The dominant source of freshwater to the Scotian Shelf comes from the Gulf of St. Lawrence, via Cabot Strait. This freshwater input is on the order of 3×10^{11} m^3 yr^{-1}. For comparison, the Mississippi River discharges between 2 and 6×10^{11} m^3 yr^{-1} (*Penn*, 2001), while the Sackville River at the mouth of Halifax Harbor discharges roughly 1.5×10^{8} m^3 yr^{-1} (*Kepkay et al.*, 1997). The lowest salinities on the Scotian Shelf (S$<$ 31) are found in the near-shore surface waters, while the deeper slope water has salinity of S$>$ 34 (*Petrie et al.*, 1987; *Umoh and Thompson*, 1994). There are significant seasonal

variations in surface salinity, typically ranging near 1 unit of salinity (*Loder et al.*, 1997), associated with the peak riverine discharge, delivered to the shelf between late June and early October. The region has a large range in seasonal sea-surface temperature (Fig. 4.2). In winter, surface temperatures are influenced by the equatorward, along-shelf, advection of subzero waters originating in Cabot Strait and the southern Newfoundland Shelf waters (*Loder et al.*, 1997), and in summer the water warms to roughly 20°C. However, the short-term variation in temperature on the Scotian Shelf is primarily due to the contribution from the surface heat flux, with horizontal advection, mixing, and diffusion playing a minor role (*Umoh and Thompson*, 1994).

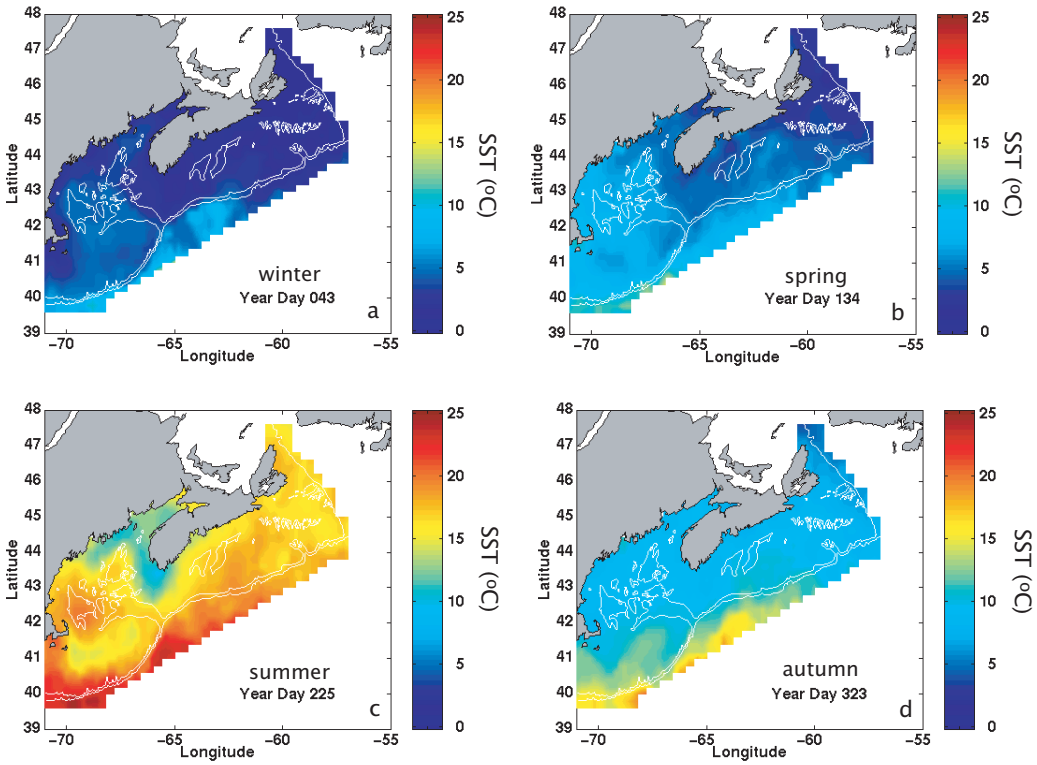

Figure 4.2: Seasonal maps of sea-surface temperature (°C) on the Scotian Shelf. The maps were generated from the data supplied by the Canadian Department of Fisheries and Oceans (*Petrie et al.*, 1996).

The origin and composition of water masses along the northeastern North American coast are well known (*Bigelow*, 1927; *Hachey*, 1942; *Chapman and Beardsley*, 1989; *Loder et al.*, 1998). As many as eight distinct water masses have been identified on the Scotian Shelf on the basis of oxygen isotope and salinity data (*Khatiwala et al.*, 1999; *Houghton and Fairbanks*, 2001). For simplicity, the water column in the region

can be characterized by a two-layer system in winter when relatively fresh shelf water overlies more saline slope-derived water. In summer it is characterized by a three-layer system with the development of a warm, shallow, surface layer overlying the two-layer system (*Loder et al.*, 1997). The Scotian Shelf region is influenced by tidal forcing, while episodic events, such as warm core rings entraining water off the shelf and flushing the deep basins, wind-driven coastal upwelling, and a meandering of the Nova Scotian current, are known to occur in the region (*Petrie et al.*, 1987; *Loder et al.*, 2003; *Greenan et al.*, 2004). The analysis presented here employs a time-step of one month, with a seasonal focus, and therefore does not resolve these features. Furthermore, any net effect of short-term processes are reflected in the monthly sampling applied here.

A climatology of hydrography, nutrients, and chlorophyll concentration in the region, based on historical archives from the Bedford Institute of Oceanography (B.I.O.) is given in Fig. 4.3. The data presented are for the Central Scotian Shelf (CSS) region (43-45°N, and 62-64°W) and cover the period from 1930 to 2000. Monthly averages were computed for the parameters at the depths defined in *Petrie et al.* (1999). The size of this CSS box was chosen to provide robust monthly estimates of nutrients for which sampling is often sparse in the winter period. This climatology demonstrates the coincidence of spring bloom (in the chlorophyll-a record, Fig. 4.3 panel iv) and the nutrient depletion of the upper part of the water column (Fig. 4.3 panel iii) in this area of the continental shelf. The spring phytoplankton bloom makes a major contribution to total annual primary production in this region. This bloom propagates to the north along the Scotian Shelf at roughly $20\ \mathrm{km\ day^{-1}}$, and can clearly be seen in satellite observations of ocean chlorophyll concentration (*Siegel et al.*, 2002). The spring bloom on the Scotian Shelf is dominated by large phytoplankton size-classes and is terminated by the exhaustion of nitrate and silicate (*Mousseau et al.*, 1996). The phytoplankton community is mainly comprised of diatom species, providing the main food source to planktonic animals and bottom-dwelling filter feeders. On the Scotian Shelf the spring bloom is the dominant control on phytoplankton biomass, though the more moderate summer production also plays a role (see section 4.5). The spring bloom accounts for roughly one third of the total annual primary production on the Scotian Shelf which ranges from 60 to 130 g C m^{-2} yr^{-1} (*Fournier et al.*, 1977; *Mills and Fournier*, 1979). It represents the dominant source of primary productivity, setting the upper limit on organic matter export, production of higher trophic levels, and supply

to benthic communities. During the remainder of the year, surface nitrate concentrations remain fairly low (Fig. 4.3) and smaller sized phytoplankton dominate. The spring bloom occurs at the annual surface temperature minimum and is initiated by an increase in the amount of available light on the shelf (*Greenan et al.*, 2004). Coastal upwelling in the Scotian Shelf region, caused by along-shore winds, drives the vertical and cross-shelf exchange of nutrient rich slope water and nutrient depleted surface waters (*Petrie et al.*, 1987). This process may contribute to the supply of nutrients required to support biological production in the region (*Petrie et al.*, 1987; *Greenan et al.*, 2004; *Fennel et al.*, 2006).

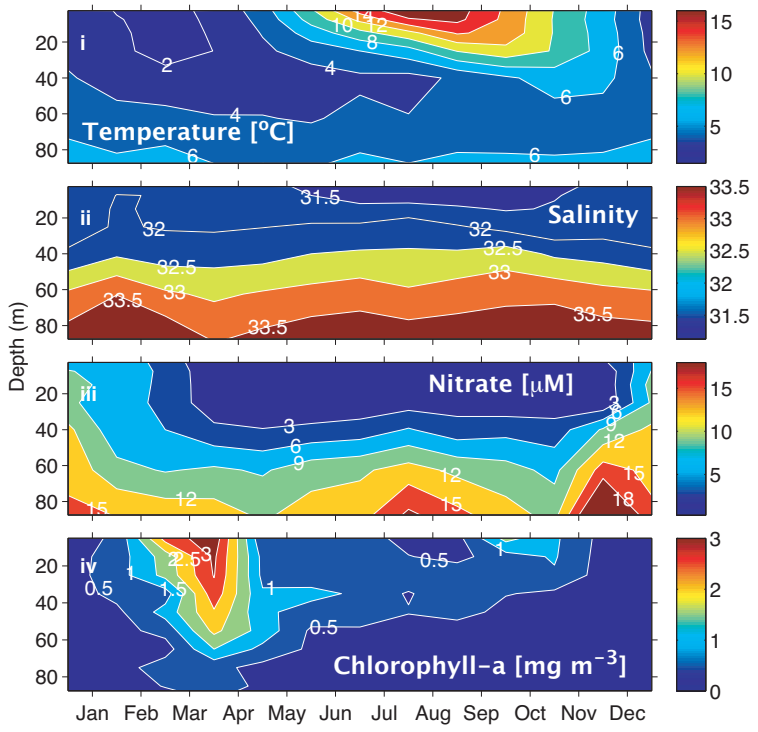

Figure 4.3: A climatology of the central Scotian Shelf based on observations from B.I.O archives. From top: (i) temperature [°C], (ii) salinity, (iii) nitrate [μM] and (iv) chlorophyll-a concentration [mg m^{-3}].

4.4 Data and Methods

4.4.1 Sampling and Analytical Procedures

Hourly measurements of pCO_2, salinity, sea surface temperature, and chlorophyll-a fluorescence, were made using a CARIOCA-2 buoy (*Martec,* moored at station "Halifax Line 2", (hereafter HL2) located at 44.3°N and 63.3°W, roughly 30 km offshore from Halifax, Nova Scotia (Figs. 4.1a, 4.4 and 4.5). The pCO_2 measurements were made by an automated spectrophotometric technique which has been fully described elsewhere (*Bates et al.*, 2000; *Bakker et al.*, 2001; *Bates et al.*, 2001; *Hood and Merlivat*, 2001). Data were uploaded and transmitted daily via the ARGOS satellite system. The CARIOCA was deployed from April to October 2007, and from mid-December 2007 to July 2008. From this time-series, the annual cycle of surface water pCO_2 was re-constructed using observations from January through June, 2008, from July through October, 2007, and December, 2007 (Fig. 4.4). A Sea-Bird (SBE 41) conductivity sensor and a Betatherm thermistor were used to acquire salinity and temperature data, while chlorophyll-a (chl-a) fluorescence was determined by a Wetlab miniature fluorometer (WETstar).

Chl-a fluorescence may be decreased by up to 80% during the day due to the effect of non-photochemical quenching, coincident with the strength of the incoming solar radiation (*Kiefer*, 1973). This effect is reduced by the application of strictly nighttime data during instrument calibration. Nighttime data were taken as a mean chl-a concentration between 0300 and 0600 UTC; data points were interpolated to match discrete chl-a measurements from ship-board occupations at HL2. A linear regression was used to determine the relationship between the CARIOCA fluorometer and discrete, measured chl-a values (r^2=0.76, N=29, $p<0.001$). This relationship was then applied to calibrate the CARIOCA chl-a time-series.

Discrete bottle samples were collected on two spring and one autumn cruise as part of the Atlantic Zone Monitoring Program (AZMP) at stations distributed along four transects throughout the Scotian Shelf (Fig. 4.1). Cruises took place in April and September 2007, and April 2008. Approximately 350 samples were collected on each cruise from the entire water column with higher vertical resolution within the euphotic zone at all stations shown in Fig. 1. DIC and TA samples were tapped from 20-L Niskin bottles mounted on a General Oceanic 24-bottle rosette fitted with a SeaBird CTD such that all chemical data are associated with high precision in-situ temperature, salinity and oxygen

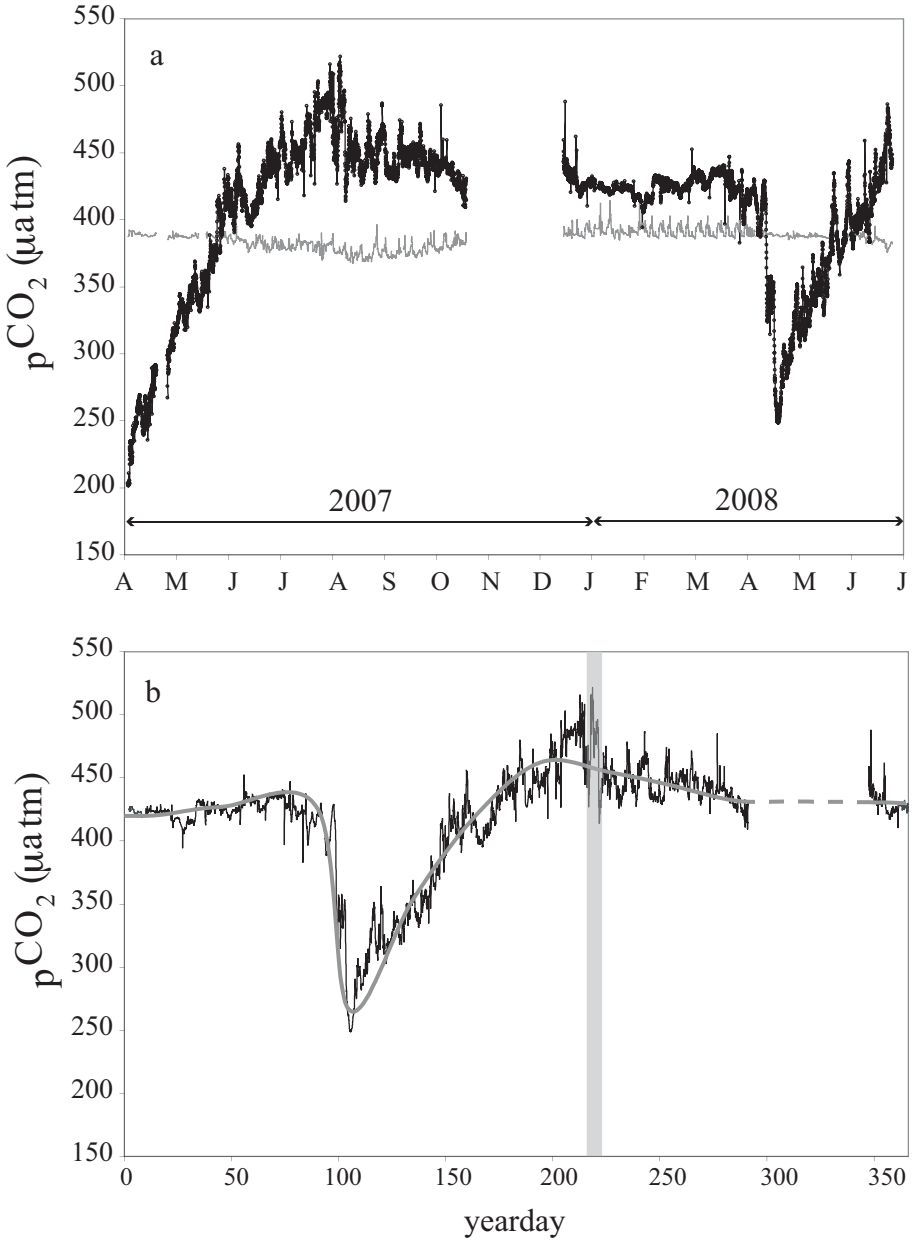

Figure 4.4: (a) Hourly pCO_2 data measured by the CARIOCA buoy. The in-situ time series is given in black. The atmospheric CO_2 concentration measured at the nearby Sable Island station is given in gray. (b) An annual composite of surface water pCO_2 constructed from the time series shown in (a). The hourly data is given by the black line. The bold line is the (running) average over 14 days.

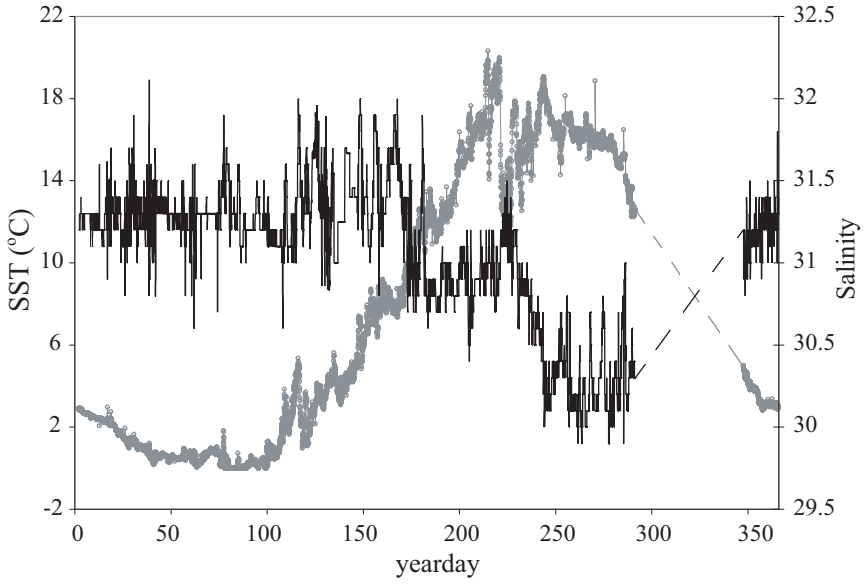

Figure 4.5: An annual composite of surface salinity (black), and SST (gray) measured hourly by the CARIOCA buoy at station HL2. Salinity and SST data from occupations of HL2 in November and December confirm that the linear interpolation over the period when hourly observations are missing (dashed lines) is acceptable

data. Following water collection, DIC and TA samples were poisoned with a solution of $HgCl_2$ to halt biological activity and stored in the dark at $4°C$ to await analysis. DIC and TA were analyzed by coulometric and potentiometric titration, respectively, using a VINDTA 3C (Versatile Instrument for the Determination of Titration Alkalinity by Marianda) (see for example *Johnson et al.*, 1993, *Fransson et al.*, 2001, or *Bates et al.*, 2005 for a full description of the analytical methods for the determination of DIC and TA). Routine analysis of Certified Reference Materials (provided by A. G. Dickson, Scripps Institution of Oceanography) ensured that the uncertainty of the DIC and TA measurements was less than 2 to 3 μmol kg^{-1}, respectively. Following the determination of DIC and TA, discrete pCO_2 ($pCO_2^d = f(DIC, TA)$), was computed using the standard set of carbonate system equations, excluding nutrients, with the CO_2Sys program of *Lewis and Wallace* (1998). We used the equilibrium constants of *Mehrbach et al.* (1973) refit by *Dickson and Millero* (1987). The calcium (Ca^{2+}) concentration was assumed to be conservative and calculated from salinity. A comparison of the CARIOCA pCO_2 and the (computed) discrete pCO_2 is given in Table 4.1. Additional hydrographic data, including profiles of temperature, salinity, and chl-a, were collected on monthly, or bimonthly, occupations of HL2.

A linear relationship between TA and salinity (n=784, r^2= 0.92, $p<0.001$, Fig. 4.6) was

Table 4.1: The pCO_2 from the CARIOCA buoy is compared to $\mathrm{pCO_2^d}$ computed from discrete samples of DIC and TA at station HL2. The values are given in units of μatm.

(dd/mm/yy)	pCO_2(CARIOCA)	$\mathrm{pCO_2^d}$(DIC, TA)
12/04/07	203±2	210 ± 5
02/05/07	327±2	322 ± 5
10/08/07	443±2	434 ± 5
18/10/07	418±2	408 ± 5
06/04/08	424±2	435 ± 5
14/04/08	249±2	242 ± 5

derived using samples collected on AZMP cruises throughout the whole water column at all stations in spring and autumn (Fig. 4.1). This relationship was used to compute an annual cycle of surface TA concentration (Fig. 4.7a) at station HL2, using the hourly salinity data measured by the CARIOCA buoy at the same location (Fig. 4.5a). TA and $\mathrm{pCO_2}$ were then used to compute the annual cycle of DIC (Fig. 4.7a) using the CO_2Sys program (*Lewis and Wallace*, 1998) as described above.

The air-sea $\mathrm{CO_2}$ flux (F) was computed using the conventional flux equation:

$$F = k\alpha\Delta\mathrm{pCO_2}, \tag{4.1}$$

where k and α are the gas transfer velocity and solubility coefficient (*Weiss*, 1974) respectively, and $\Delta\mathrm{pCO_2}$ is the gradient in $\mathrm{pCO_2}$ between the ocean and the atmosphere. The gas transfer velocity, k, was computed using the formulation of Wanninkhof (1992) for short-term winds and observed hourly wind speed. Hourly wind speed was measured by Environment Canada the Sable Island Meteorological Station (43.9°N and 60.3°W), at a height of 10 m. Petrie and Smith (1977) have shown that winds measured at Sable Island are representative of winds on the Scotian Shelf. Hourly atmospheric pCO_2 was also measured by Environment Canada at the Sable Island station. A negative flux indicates a transfer from the ocean into the atmosphere.

4.4.2 Application of a 1-D Model

A diagnostic model was used to calculate the net change in DIC based on contributions from the processes controlling the variability of DIC in the surface mixed-layer allowing the for the addition/removal of DIC from below. The following conservation equation,

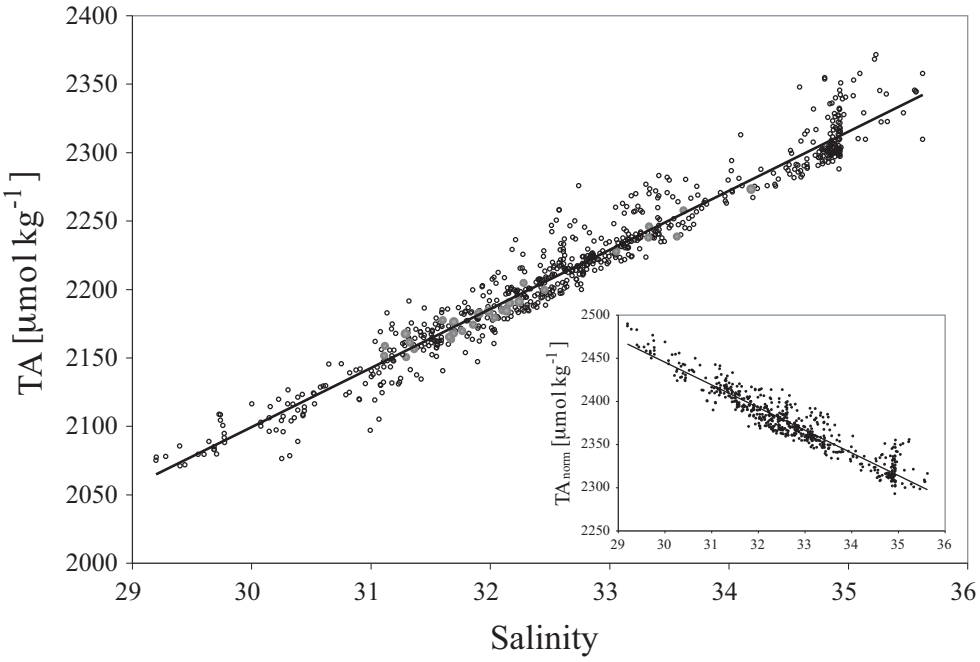

Figure 4.6: TA and salinity data obtained from discrete samples collected throughout the Scotian Shelf at all stations shown in Fig. 1. All TA samples from the entire water column, collected on both the spring and autumn cruises are plotted. A linear regression yielded the following equation, $\mathrm{TA} = 43.14\mathrm{S} + 805$ ($n = 784$, r^2=0.92, $p < 0.001$). Data from station HL2 are plotted in gray, and justify the use of the given linear relationship between TA and salinity at this location to compute the annual cycle of TA shown in Fig. 4.7a. Inset: TA normalized to a constant salinity ($\mathrm{TA_{norm}} = 35\mathrm{TA}/\mathrm{S}$).

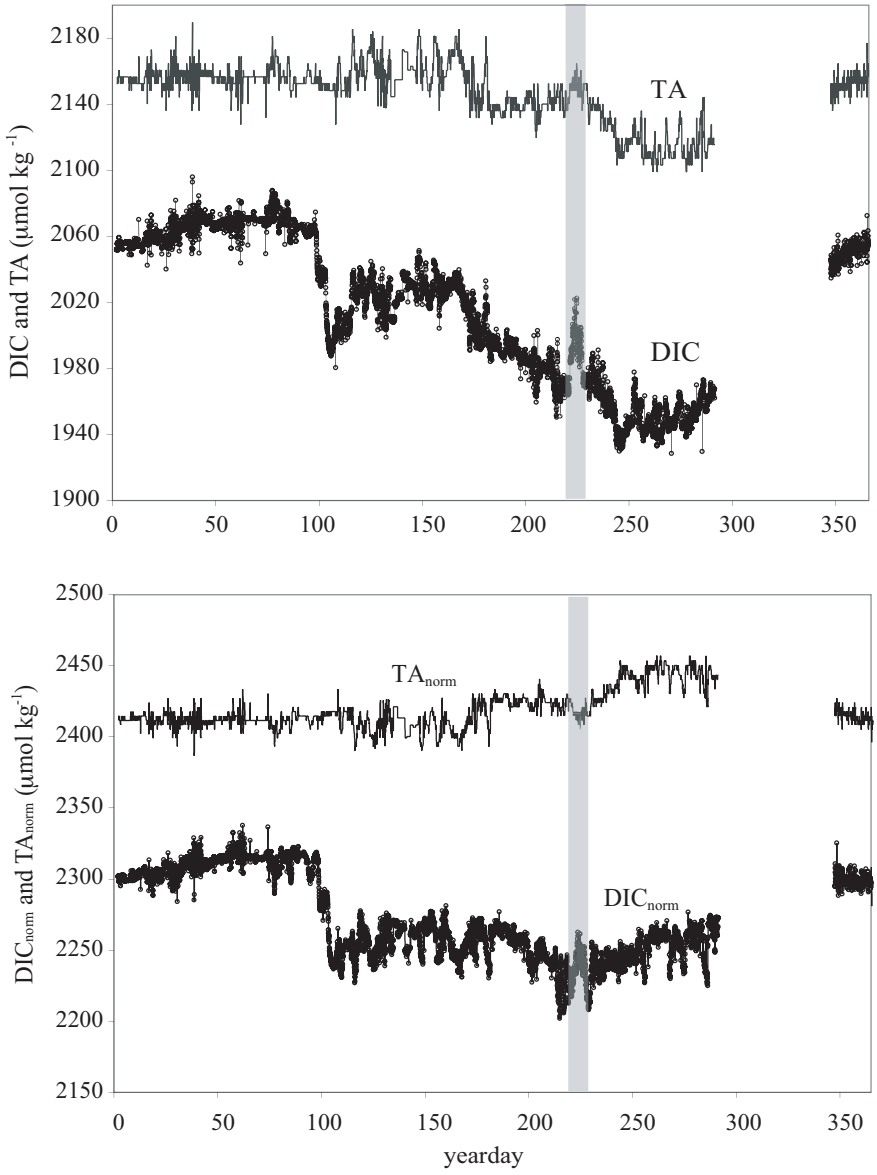

Figure 4.7: (a) Annual cycles of hourly surface TA and DIC concentrations. TA was computed from the hourly CARIOCA salinity data, and the linear relationship between salinity and TA for the region (shown in Fig. 4.6). DIC was computed using the $\mathrm{pCO_2}$ time-series from the CARIOCA and the annual cycle of TA. (b) Annual cycles of hourly salinity-normalized surface TA ($\mathrm{TA_{norm}}$) and DIC ($\mathrm{DIC_{norm}} = 35\mathrm{DIC/S}$) concentrations.

modified from Gruber et al. (1998), describes the changes in DIC in the mixed-layer:

$$\frac{\mathrm{dDIC}}{\mathrm{dt}} = \frac{\mathrm{F}}{\mathrm{h}} + \frac{1}{\mathrm{h}}\,\mathrm{K_z}\frac{\mathrm{dDIC}}{\mathrm{dz}}\Big|_{\mathrm{tc}} + \frac{1}{\mathrm{h}}\left(\frac{\mathrm{dK_x}\frac{\mathrm{dDIC}}{\mathrm{dx}}}{\mathrm{dx}}\right) + \frac{1}{\mathrm{h}}\,\Theta\left(\frac{\mathrm{dh}}{\mathrm{dt}}\right)(\mathrm{DIC_{tc}} - \mathrm{DIC}) + \mathrm{Jtrsp} - \mathrm{Jncp}, \tag{4.2}$$

where the terms on the right hand side of the equation represent, respectively, the contribution from (1) air-sea CO_2 flux, (2) vertical diffusion, (3) horizontal diffusion, (4) vertical entrainment, (5) a source term for horizontal advection, and (6) a source term for biological processes with the subscript 'ncp' referring to net community production. The variable mixed-layer depth is denoted h (m), $\mathrm{K_z}$ ($\mathrm{m^2\ s^{-1}}$) is the vertical diffusivity at the base of the mixed-layer, $\mathrm{dDIC/dz|_{tc}}$ (μmol $\mathrm{kg^{-1}\ m^{-1}}$) is the vertical gradient of DIC at the base of the mixed-layer, $\mathrm{K_x}$ ($\mathrm{m^2\ s^{-1}}$) is the horizontal diffusivity, $\mathrm{dDIC/dx}$ (μmol $\mathrm{kg^{-1}\ m^{-1}}$) is the horizontal gradient in DIC, $\mathrm{DIC_{tc}}$ (μmol $\mathrm{kg^{-1}}$) is the DIC concentration in the thermocline (tc), below the mixed-layer. The Heaviside function, $\Theta = \Theta(\mathrm{dh/dt})$ insures that shoaling of the mixed-layer, (when $(\mathrm{dh/dt}) < 0$), does not introduce new water into the mixed-layer, and only a deepening of the mixed-layer introduces water from the underlying layer. The horizontal diffusion term been neglected from Eq. 4.2 as this term is assumed small, and any contribution should be accounted for in the Jtrsp term. Measurements of surface DIC in April and September indicate that the gradient between two stations on the same transect line (Fig. 4.1) is roughly 30 μmol $\mathrm{kg^{-1}}$ over roughly 2.2×10^4 m, or 1.4×10^{-3} μmol $\mathrm{kg^{-1}\ m^{-1}}$. The gradient between surface DIC along the Halifax and along the Louisbourg Line (Fig. 4.1) is roughly 50 μmol $\mathrm{kg^{-1}}$ over 2.6×10^5 m, or 1.9×10^{-4} μmol $\mathrm{kg^{-1}\ m^{-1}}$. In the subsequent analysis, the contributions from both horizontal and vertical diffusion are included in the estimate of Jtrsp (i.e. $\mathrm{Jtrsp} = \mathrm{V.Diff} + \mathrm{H.Diff} + \mathrm{H.Adv}$). Eq. 4.2 was simplified to the following conservation equation for mixed-layer DIC:

$$\frac{\mathrm{dDIC}}{\mathrm{dt}} = \frac{\mathrm{F}}{\mathrm{h}} + \frac{1}{\mathrm{h}}\,\Theta\left(\frac{\mathrm{dh}}{\mathrm{dt}}\right)(\mathrm{DIC_{tc}} - \mathrm{DIC}) + \mathrm{Jtrsp} - \mathrm{Jncp} + \psi, \tag{4.3}$$

where the last term on the right-hand side, ψ, is the model error.

Eq. 4.3 was applied by means of a vertically one-dimensional box representation of the mixed-layer. This is shown schematically in Fig. 4.8. The upper box represents the mixed-layer, and the lower box the thermocline. The mixed-layer box exchanges CO_2 with the atmosphere across the air-sea interface. The boundary between the mixed-layer

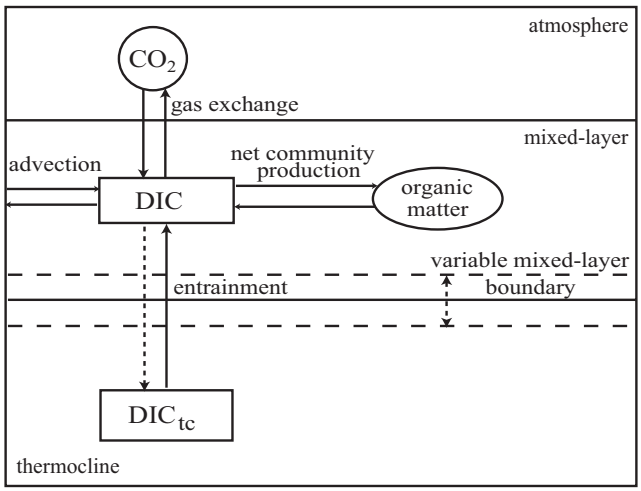

Figure 4.8: (a) Schematic representation of the one-dimensional, two box, ocean model used in the study of the seasonal carbon cycle on the Scotian Shelf. Dissolved inorganic carbon is modeled only in the mixed-layer. The other carbon reservoirs are only included to establish boundary conditions. The depth of the mixed-layer is variable, thereby entraining carbon-rich water from the thermocline (tc). (Figure modified from *Gruber et al.* (1998).

and the thermocline is permitted to move up and down depending on the (monthly mean) mixed-layer depth (Fig. 4.9). The concentration of DIC was assumed homogeneous in the mixed-layer. Horizontal transport (Jtrsp) moves water through the mixed-layer. The potential contribution from the formation/dissolution of calcium carbonate ($CaCO_3$) was assumed negligible. The relationship between salinity normalized TA ($\mathrm{TA_{norm}} = 35\mathrm{TA/S}$) and salinity revealed nearly conservative behaviour (Fig. 4.6 inset), supporting the assumption that calcification can be neglected, despite evidence of summer coccolithophore blooms in the region (*Brown and Yoder*, 1993; *Towsend et al.*, 1994). There appears to be an accumulation of TA near S=35, present in both the observed and normalized TA, which may indicate the dissolution of $CaCO_3$. However, waters of S=35 are representative of samples collected in the lower water column, significantly further offshore than station HL2 (Fig. 4.1). The possible contribution from sedimentary processes was neglected. It was also assumed that the surface mixed-layer is isolated from the sea-floor; the water depth is at HL2 roughly 200 meters, and the depth of the mixed-layer ranged from 10-60 meters at the annual scale (Fig. 4.9).

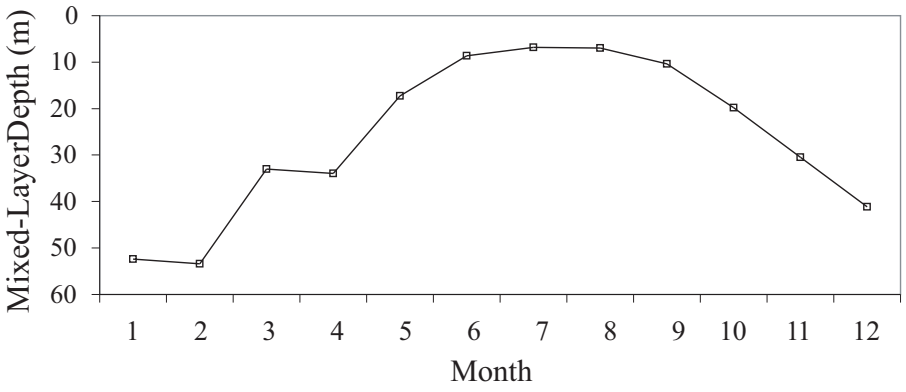

Figure 4.9: Monthly values of mixed-layer depth estimated from profiles of temperature ($\Delta T \geq 0.5$°C at station HL2

4.4.3 Model Inputs

The diagnostic model analysis of the seasonal carbon cycle in the mixed-layer was restricted to the year 2008, when measurements are available at the monthly timescale. The depth of the mixed-layer was estimated from profiles of temperature from monthly occupations at the mooring site (Fig. 4.9). The thickness of the surface mixed-layer shows a large seasonal variability, mainly caused by changes in surface wind-stress and heat exchange. Monthly values of ($\mathrm{dDIC/dt}$) were computed (by central difference) from the annual time series of mixed-layer DIC (Fig. 4.7a).

Monthly values of air-sea CO_2 flux were computed according to the method described in Section 4.4.1. The transport term, which also includes the contributions from horizontal and vertical diffusion, and horizontal and vertical advection, was estimated empirically using the relationship between DIC and salinity. Discrete DIC samples are plotted against the corresponding measured salinity (n=784, r^2=0.74, p<0.001) in Fig. 4.10. Please note that these discrete data are independent of the annual cycle of DIC and salinity obtained from the CARIOCA buoy. The salinity-dependent changes in DIC, which were assumed due to horizontal transport, and vertical and horizontal diffusion, are described by this relationship,

$$\mathrm{DIC_S} = 46.5\mathrm{S} + 546.4, \tag{4.4}$$

and

$$\mathrm{Jtrsp} = \frac{\mathrm{dDIC_S}}{\mathrm{dt}}. \tag{4.5}$$

We assumed that local salinity-dependent processes such as precipitation and evaporation

could be neglected. Previous studies have used the seasonal differences in the relationship between DIC and salinity to evaluate the salinity-dependent changes in DIC (*Thomas and Schneider*, 1999; *Osterroht and Thomas*, 2000; *Bozec et al.*, 2006). This method of empirically isolating changes due to horizontal transport does not allow for a complete description of the horizontal processes in the region. However, its inclusion in the 1-D approach presented here, allowed changes due to transport and biology, often grouped together (*Olsen et al.*, 2008; *Omar et al.*, 2010), to be unraveled.

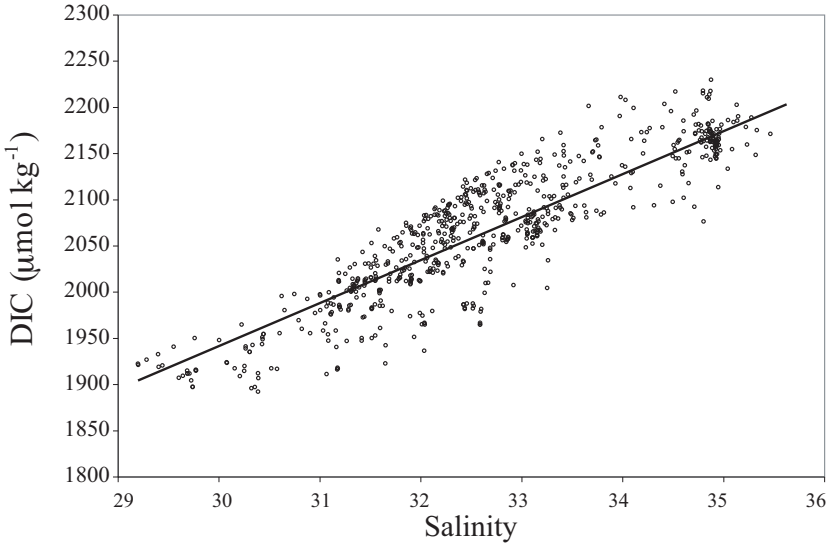

Figure 4.10: DIC and salinity data obtained from discrete samples collected throughout the Scotian Shelf at all stations shown in Fig. 1. All DIC samples from the entire water column, collected on both the spring and autumn cruises were plotted. A linear regression yields the following equation: $\mathrm{DIC_S} = 46.5\mathrm{S} + 546$ ($n = 784$, r^2=0.74, $p < 0.001$). This relationship was used to compute the salinity-dependent changes in DIC to approximate the Jtrsp term.

The vertical entrainment term was quantified based on DIC concentration below the mixed layer. $\mathrm{DIC_{tc}}$ was taken from measured profiles of DIC from the mooring site (Fig. 4.11a). For the months when a measured profile of DIC was not available (Feb, Jul, Nov, Dec) Eq. 4 was used to compute a profile of DIC from the observed profile of salinity at HL2 for that month, and from this an estimate of $\mathrm{DIC_{tc}}$ was made.

The change in DIC due to biology (Jncp), was then computed from the DIC conservation equation:

$$-\mathrm{Jncp} = \frac{\mathrm{dDIC}}{\mathrm{dt}} - \frac{\mathrm{F}}{\mathrm{h}} - \frac{1}{\mathrm{h}}\,\Theta\left(\frac{\mathrm{dh}}{\mathrm{dt}}\right)(\mathrm{DIC_{tc}} - \mathrm{DIC}) - \left(\frac{\mathrm{dDIC_S}}{\mathrm{dt}}\right) - \psi, \qquad (4.6)$$

where the last two terms on the right-hand side are Jtrsp estimated using Equation 4.5, and ψ, which represents the error.

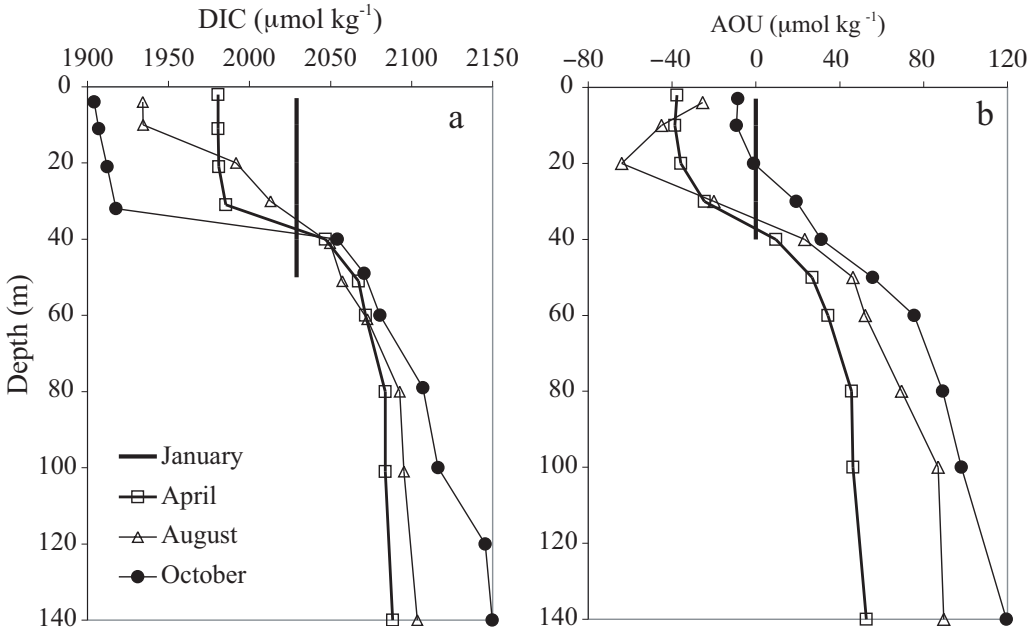

Figure 4.11: Profiles of (a) DIC and (b) AOU in January, April, August, and October. The April, August, and October profiles result from discrete measurements of samples collected at the mooring site. The January DIC profile was estimated from the January surface DIC concentration, and the corresponding mixed-layer depth. The January AOU profile was estimated from the saturation oxygen concentration using the January values of surface salinity and temperature, and mixed-layer depth.

4.4.4 Error Estimation

The uncertainty in the computed Jncp term includes the uncertainty associated with each of the terms in Eq. 4.6. The $\mathrm{pCO_2}$ measurements were accurate (2 μatm), and the error associated with the DIC computation (from known values of $\mathrm{pCO_2}$ and TA) is fairly small (less than 10 μmol $\mathrm{kg^{-1}}$) (*Dickson*, 1990). However, we computed DIC from the hourly time series of $\mathrm{pCO_2}$ and the hourly estimate of TA, based on the relationship between TA and S (Fig. 4.6) and the hourly salinity data from the CARIOCA buoy (Fig. 4.5). The standard error associated with the computation of TA from salinity was 12 μmol $\mathrm{kg^{-1}}$, which we considered as a reasonable estimate of the uncertainty associated with computed time series of DIC. The monthly change in DIC (dDIC/dt) had an associated uncertainty ranging from 0.1 to 0.7 mol C $\mathrm{m^{-2}}$ $\mathrm{month^{-1}}$. There is a relatively large

error associated with the air-sea CO_2 flux term, resulting from the parameterization of the gas transfer velocity (*Watson et al.*, 2009). We computed the air-sea CO_2 flux using the parameterization of *Wanninkhof* (1992). The uncertainty associated with the monthly air-sea flux was determined from the standard deviation of the flux computed with the parameterization of *Wanninkhof* (1992) and the flux computed with the parameterization of *Nightingale et al.* (2000). The uncertainty associated with the air-sea CO_2 flux ranged from 0.01 to 0.2 mol C m^{-2} $month^{-1}$. The vertical gradients used to compute the vertical entrainment term were small compared to the measured values and had the same uncertainty as the discrete DIC measurements (on the order of 5 μmol kg^{-1}). The uncertainty associated with the monthly estimates of the vertical entrainment term ranged from 0.04 to 0.3 mol C m^{-2} $month^{-1}$. The relationship between DIC and salinity (Fig. 4.10) indicated that 74% of the variability in DIC is due to changes in salinity. The uncertainty in the Jtrsp term was therefore assumed to be equal to 26% of the observed monthly mixed-layer DIC, and ranged from 0.2 to 1.2 mol C m^{-2} $month^{-1}$. The uncertainty in each of the terms on the right-hand side of Eq. 6 were propagated to estimate the uncertainty associated with Jncp which ranged from 0.4 to 1.3 mol C m^{-2} $month^{-1}$.

The model uncertainty (ψ) was estimated by means of a Monte Carlo simulation of Jncp (with the simulated series referred to as Jncp*), and it was assumed that a reasonable estimate of ψ was the standard deviation of Jncp*. The inputs for the simulation were randomly generated from distributions which most closely match the data; 10,000 points were chosen randomly for each of the model variables using random number generators in MATLAB (Mathworks, Inc.). Following a test for normality and uniformity, a normal distribution was used for the 'dDIC/dt' and 'Jtrsp', (or $\mathrm{dDIC_S/dt}$) terms, and a uniform distribution was used for the 'vertical entrainment' and 'flux' terms. The uniform distribution requires the maximum value, while the normal distribution requires the mean and standard deviation. These values were taken from the monthly values of each of the terms on the right hand side of Eq. 4.6:

$$\mathrm{Jncp^*} = \mathrm{M_{dDIC/dt}} - \mathrm{M_{Flux}} - \mathrm{M_{V.Ent}} - \mathrm{M_{Jtrsp}}, \tag{4.7}$$

where 'M' indicates the randomly generated series. The equation was solved for Jncp* (10,000 times), and the standard deviation of Jncp* used as the magnitude of ψ. The

resulting uncertainty is 15 μmol kg^{-1}, or 0.5 mol C m^{-2} using an annual average mixed-layer depth of 27 m. The uncertainty estimated with the Monte Carlo approach was roughly equal to the lower bound of the uncertainty estimated with the conventional error propagation.

4.5 Results

4.5.1 The Annual Cycle of $\mathrm{pCO_2}$

The partial pressure of $\mathrm{CO_2}$ in seawater is controlled by several physical and biogeochemical factors. Changes in temperature, salinity, alkalinity, and DIC will influence $\mathrm{pCO_2}$, with changes in temperature and DIC having the strongest influence. Hourly measurements of surface water $\mathrm{pCO_2}$ from January to December are given in Fig. 4.4b. Wintertime $\mathrm{pCO_2}$ indicated supersaturation with respect to the atmosphere and had a relatively constant value of roughly $420\ \mu\mathrm{atm}$. The onset of the spring phytoplankton bloom can clearly be seen in early April with a sharp drop in $\mathrm{pCO_2}$ to a minimum value of roughly $240\ \mu\mathrm{atm}$ over a period of less than two weeks. The post-bloom recovery was seen over the next 120 days, coincident with the summer warming of the surface waters from yearday 100 to yearday 225 (Fig. 4.5). The $\mathrm{pCO_2}$ quickly reached supersaturation, with a maximum $\mathrm{pCO_2}$ of roughly 460 $\mu\mathrm{atm}$ by yearday 225. This was followed by a period of fairly constant $\mathrm{pCO_2}$, extending from early September to the end of the year. The autumn bloom, though evident in satellite images of the region, was not visible in the $\mathrm{pCO_2}$ time series. While this second bloom is smaller than the spring bloom (*Greenan et al.*, 2004), it occurs as surface waters are cooling, which should act to enhance the decrease in $\mathrm{pCO_2}$. Despite the combined effect of photosynthesis and decreasing water temperature, the autumn bloom, as a single, short-term event, remained undetected within the higher frequency variability of the $\mathrm{pCO_2}$ observations. Calcification during the autumn bloom would increase the $\mathrm{pCO_2}$, potentially masking the drawdown by photosynthesis. However, we can not presently confirm, or exclude the contribution from calcification.

Hourly $\mathrm{pCO_2}$ data during the 2008 spring phytoplankton bloom are shown in Fig. 4.4a. The bloom was initiated on April 6th, and lasted roughly 8 days, until the 14th of April, when $\mathrm{pCO_2}$ concentrations began to increase. The $\mathrm{pCO_2}$ and DIC concentrations at the onset of the bloom were 424 μatm and 2070 μmol kg^{-1} respectively. The $\mathrm{pCO_2}$ and

DIC concentration at the termination of there bloom were 294 μatm and 1987 μmol kg^{-1} respectively. The depth of the mixed layer at the mooring station was 30 meters, measured on an April 10th occupation of station HL2. The resulting carbon draw-down over the bloom period was $\Delta \mathrm{DIC}_{\mathrm{bio}} = 1.7 \ \mathrm{mol\ C\ m^{-2}}$. Assuming no other source or sink was acting during this period, this drawdown was ascribed to biological uptake.

In-situ pCO_2 is plotted against in-situ SST, with the seasons distinguished by color in Fig. 4.12a. The large range in surface temperature, particularly in the transition from spring to summer, and summer to autumn, from near zero to roughly 20° can be seen. There is a correspondingly large range in pCO_2 from roughly 200 μatm at the height of the spring bloom (Fig. 4.12a, in pink), to greater than 500 μatm at the maximum SST (Fig. 4.12a, in green). By contrast, the autumn (Fig. 4.12a, in blue) and winter (Fig. 4.12a, in purple) pCO_2 are roughly constant between 400 μatm and 450 μatm, indicating supersaturation with respect to atmospheric CO_2 over this period. The effect of temperature on $\mathrm{pCO_2}$ is well understood from thermodynamic relationships, allowing the correction of the observed time series, ($\mathrm{pCO_2(obs)}$), to a mean temperature, ($\mathrm{T_{mean}}$), via the equation of Takahashi et al. (2002):

$$\mathrm{pCO_2(T_{mean}) = pCO_2(obs)[exp(0.0423(T_{mean} - T_{obs}))]}. \tag{4.8}$$

Values of $\mathrm{pCO_2}$ corrected to a constant, annual mean, temperature ($\mathrm{T_{mean}} = 7.0^{\mathrm{o}}\mathrm{C}$) are plotted against in-situ temperature ($\mathrm{T_{obs}}$) in Fig. 4.12. The spring values (in pink) show the April $\mathrm{pCO_2}$ minimum due to phytoplankton bloom, and the post-bloom recovery when DIC was resupplied due to respiration and remineralization. The decay of the bloom was coincident with the onset of surface warming. The summertime values (in green) ranged from $6^{\mathrm{o}}\mathrm{C}$ to $20^{\mathrm{o}}\mathrm{C}$; $\mathrm{pCO_2}$ was reduced due to on-going photosynthesis and to out-gassing driven by the warming of the waters. The post-bloom, summer, production is discussed in more detail in Section 4.6.1. In autumn $\mathrm{pCO_2}$ was reduced and increased steadily as the water cooled, reflecting the transition between production and respiration in the system. In contrast to the other seasons, the winter values (in purple) covered a much smaller range in water temperature, which was fairly constant during this period. The winter data showed increased values of $\mathrm{pCO_2}$ due respiration and entrainment of carbon-rich subsurface waters. Factors other than temperature were investigated in detail by looking at the variability of surface DIC concentration over the annual cycle.

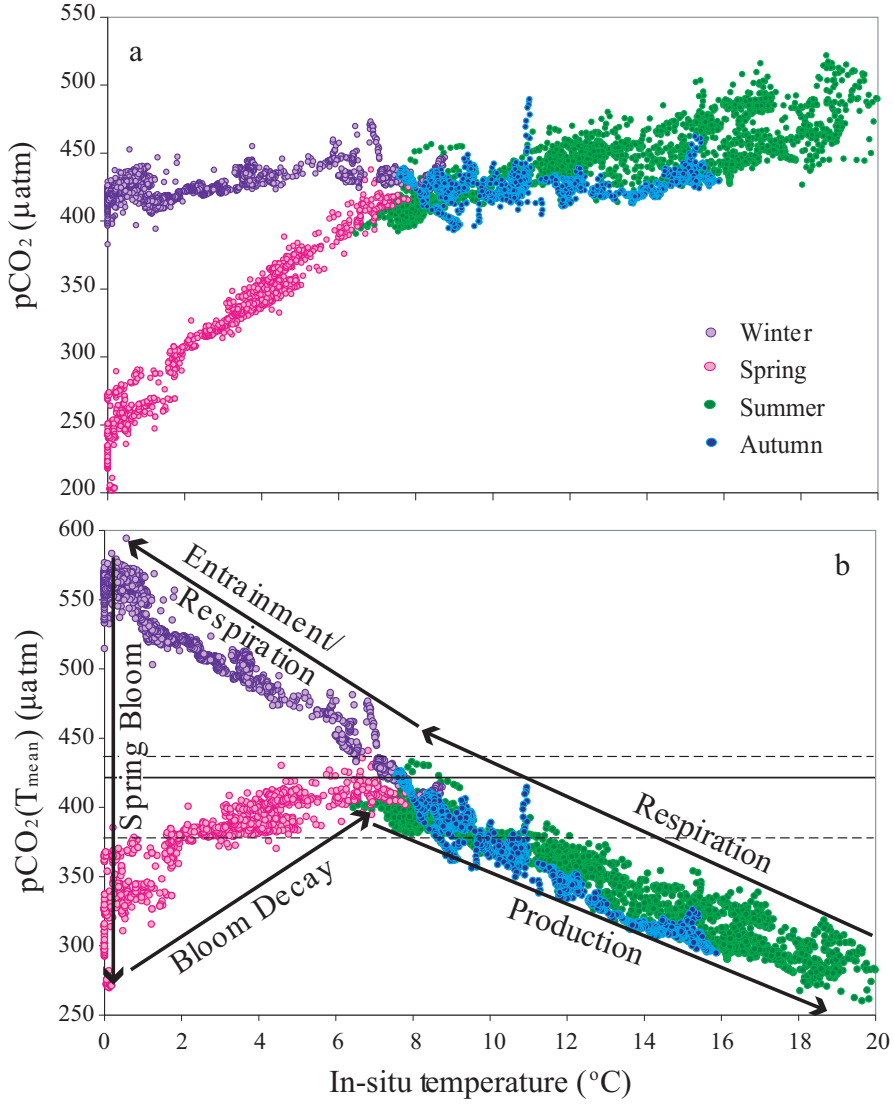

Figure 4.12: (a) In-situ pCO_2 versus in-situ temperature with seasons distinguished by color. (b) Temperature-normalized pCO_2 versus in-situ temperature. The average value of $\mathrm{pCO_2(T_{mean})}$ at $\mathrm{T_{mean}}$ is given by the solid line (415 μatm), while the maximum (435) and minimum (375) values at this temperature are given by the dashed lines. The dominant mechanisms acting in each of the seasons are shown schematically by the black arrows. The spring values (pink) include the months April and May; the summer values (green) include June, July, and August; the autumn values (blue) include September and October; and the winter values (purple) include last week of December, January, February and March.

4.5.2 The Annual Cycle of DIC

As described by Eq. 4.2, DIC is affected by the air-sea flux of CO_2, vertical diffusion and entrainment, horizontal advection, and biological production. The annual cycle of mixed-layer DIC is shown in Fig. 4.7a. The normalization of DIC (and TA) to a constant salinity removes the effect of freshwater fluxes from the measured concentrations. Variability in the salinity normalized concentrations (DIC_{norm} and TA_{norm}, Fig. 4.7b) is thus primarily controlled by water temperature (i.e., by the solubility of CO_2), biological processes, air-sea exchange of CO_2, and the mixing of water masses. The DIC drawdown by the spring phytoplankton bloom was visible in both the observed and normalized DIC (Fig. 4.7). However, the continued decrease in DIC seen after yearday 150 is significantly reduced in the time series of DIC_{norm}, indicating the dominance of advection (Jtrsp) over this period. Similarly, the late summer decrease in TA was absent from the time series of TA_{norm}, and there was a modest increase in TA over the period from roughly yearday 175 to 275, as a result of the arrival of St. Lawrence River water, which has a non-zero TA at S=0, and highlights the limitation of the salinity-normalization for river-influenced waters (*Friis et al.*, 2003). Between yearday 200 and 250, there was a significant increase in DIC (Fig. 4.7, highlighted section). This could indicate a dissolution of $CaCO_3$ which would add DIC, and TA, to the system, decreasing the pCO_2. However, over the same period, there was an increase in salinity, and a decrease in temperature (Fig. 4.5), along with an increase in pCO_2 (Fig. 4.4b, highlighted section). It is therefore more likely that this increase in DIC (and salinity, and pCO_2) was the result of the upward mixing of DIC-rich water from below, confirmed by the decrease in temperature over the same period. However, since the annual cycle of DIC was computed from measurements of pCO_2 and computed values of TA, based on a relationship between TA and salinity, we cannot exclude the possibility of a contribution from the formation/dissolution of $CaCO_3$ which would require measurements of TA with the same temporal resolution as the pCO_2 time-series.

The flux of CO_2 between the ocean and the atmosphere either adds (by invasion), or removes (by out-gassing), DIC from from the surface waters. The annual cycle of air-sea CO_2 flux is shown in Fig. 4.13. The surface waters on the Scotian Shelf acted as a net source of CO_2 to the atmosphere for most of the year, with a reversal of this process occurring only for a short period during, and following, the spring phytoplankton bloom.

There was therefore a reduction in the surface water DIC pool as a result of out-gassing; the annual air-sea flux was $F = -1.4$ mol C m^{-2} yr^{-1}. Profiles of DIC from April

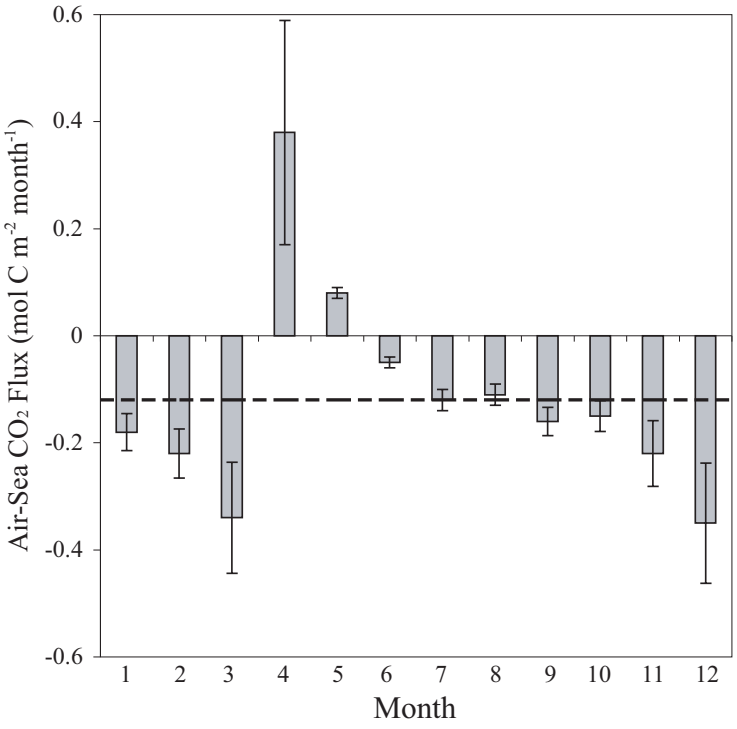

Figure 4.13: Annual cycle of air-sea CO_2 fluxes computed using pCO_2 data from the CARIOCA buoy. The uncertainty is estimated from the standard deviation between monthly fluxes computed using the wind speed parameterization of *Wanninkhof* (1992) and *Nightingale et al.* (2000). Annual integration of these monthly fluxes yields an out-gassing of -1.4 mol C m^{-2} yr^{-1} (see also Table 2). The annual mean value ($F_{mean} = -0.12$ mol C m^{-2} month^{-1}) is indicated by the black dashed line.

(spring), August (summer), and October (autumn) occupations at station HL2 are shown in Fig. 4.11a. The corresponding profiles of apparent oxygen utilization (AOU = $[O_2]$sat - $[O_2]$obs), are shown in Fig. 4.11b. The oxygen profiles are from same (monthly) occupations of station HL2 as the temperature and salinity profiles. Dissolved oxygen ($[O_2]$obs) was measured using a Sea-Bird electrochemical oxygen sensor. The saturation oxygen concentration was computed for the observed temperature, salinity and pressure. It can be seen that with the onset of the spring bloom, which occurs at the temperature minimum, the surface waters quickly became undersaturated with respect to CO_2. DIC in the surface waters was reduced due to photosynthesis, while negative surface values of AOU corresponded to a production of oxygen by the phytoplankton. Organic matter was exported to the subsurface layer, and remineralization of this organic matter increased the

concentration of DIC in waters below a depth of roughly 40 meters. The positive subsurface AOU concentrations reflect this remineralization, or respiration, process. Primary production was reduced, though ongoing, in summer and autumn, when surface DIC concentrations were additionally influenced by the input of freshwater from the outflow of the Gulf of St. Lawrence. The ongoing biological production in summer and autumn was confirmed by the negative values of surface AOU in both August and October. Respiration further increased DIC, and AOU, in the subsurface layer in summer and autumn, while the deepening of the mixed-layer in winter introduced DIC-rich waters from below the thermocline into the surface layer.

4.5.3 Model Results

The monthly changes in DIC due to vertical entrainment, lateral transport (Jtrsp), air-sea flux, biological production (Jncp), and the total observed monthly changes are shown in Fig. 4.14 and 4.15a. The air-sea flux (Fig. 4.14b) made a contribution of similar magnitude as the Jtrsp term to the water column DIC budget, and as described above, the region acted as a source of CO_2 to the atmosphere over the annual scale. Vertical entrainment delivered DIC-rich waters to the mixed-layer from June to November (Fig. 4.14c). The impact of transport was greatest in the second half of the year, both increasing and decreasing mixed-layer DIC concentration (Fig. 4.14d). The change in DIC due to biology dominated the total change in spring, with a diminishing influence over the rest of the year. There was a persistent biological signal throughout the year on the Scotian Shelf (Fig. 4.14e), despite the apparent depletion of nutrients following the spring phytoplankton bloom. Respiration increased DIC from November to March and in May due to the decay of the spring bloom. Production of organic matter occurred in April and from June to October. The most important processes for variability of DIC in the surface mixed-layer were biological production, and to a lesser extent, entrainment, and transport (Fig. 4.15a).

Table 4.2: Monthly estimates of each of the terms in Eq. 4.6 along with the (net) annual contributions to changes in DIC from air-sea CO_2 flux (F_{CO_2}), vertical entrainment (V.Ent.), Jtrsp and Jncp. All monthly values are given in mol C m^{-2} $month^{-1}$ and the annual values are given in mol C m^{-2} yr^{-1}. The uncertainties associated with the annual values were computed by propagating monthly uncertainties.

Month	dDIC/dt	F_{CO_2}	H	dh/dt	$DIC_{tc} - DIC$	V.Ent.	Jtrsp	-Jncp
1	0.25±0.64	-0.18±0.03	52	11	0.20	0.20±0.27	0.00±0.97	0.23±1.19
2	0.32±0.66	-0.22±0.05	53	1	0.02	0.02±0.27	0.120±0.31	0.40±0.79
3	0.05±0.41	-0.34±0.10	33	-20	0.00	0±0.17	0.33±0.20	0.06±0.49
4	-1.96±0.42	0.40±0.21	34	1	0.04	0.04±0.17	0.13±0.56	-2.53±0.75
5	0.60±0.21	0.08±0.01	7	-17	0.00	0±0.09	0.00±0.37	0.52±0.44
6	-1.19±0.11	-0.05±0.01	9	-9	0.00	0±0.04	-0.02±0.60	-1.16±0.57
7	-1.02±0.11	-0.12±0.02	9	0	0.00	0±0.05	-0.17±0.80	-0.73±0.81
8	-0.45±0.11	-0.11±0.02	9	0	0.01	0.01±0.05	-0.08±0.88	-0.27±0.89
9	-0.75±0.13	-0.16±0.03	10	1	0.14	0.14±0.05	-0.25±1.05	-0.48±1.06
10	0.28±0.24	-0.15±0.03	20	10	0.91	0.91±0.10	0.04±1.04	-0.52±1.08
11	1.43±0.37	-0.22±0.06	31	11	0.79	0.79±0.16	0.56±0.66	0.30±0.78
12	1.32±0.51	-0.35±0.11	41	11	0.45	0.45±0.21	0.73±1.1	0.49±1.30
Annual	-1.12±1.32	1.42±0.30				2.56±0.55	1.39±0.55	-3.65±2.91

The changes in pCO_2 due to temperature, vertical entrainment, Jtrsp and Jncp are illustrated in Fig. 4.15b. The temperature control was computed with the initial value of pCO_2 (in January) and subsequent monthly values computed by assuming that the only change was that of temperature. For example, the water cooled by 1.5°C between Januray and Februray, which corresponds to a 6% decrease in pCO_2 (from roughly 420 μatm in January to roughly 395 in February, and applying the empirical relationship between temperature and pCO_2 of *Takahashi et al.* (2002)) assuming no process other than temperature was acting on the pCO_2. Between February and April, the water temperature remained constant; the increase in temperature from April (0.8°C) through August (17°C) corresponded to an increase in pCO_2 of nearly 70% (Fig. 4.15b); the estimated uncertainty associated with (monthly values of) this term was 10 μatm. The effect of vertical entrainment, Jtrsp and Jncp on pCO_2 were computed via the following method. The initial pCO_2 was computed as a function of the initial DIC and TA:

$$\mathrm{pCO_2^{t=0}} = f(\mathrm{DIC_0}, \mathrm{TA_0}), \tag{4.9}$$

where the subscripts on DIC and TA refer to these initial values. The change in pCO_2 to Jtrsp (pCO_2(Jtrsp)) was then computed from the initial value of pCO_2, the initial value of DIC, the change in DIC due to Jtrsp in the month of January, and the January TA concentration, with the following equation:

$$\mathrm{pCO_2^{t=1}(Jtrsp)} = f(\mathrm{DIC_0} + \mathrm{DIC_{Jtrsp1}}, \mathrm{TA_1}), \tag{4.10}$$

where $\mathrm{DIC_{Jtrsp1}}$ is the change in DIC due to Jtrsp in Januray (see Table 4.2). The same procedure was followed for each month, and for vertical entrainment, and Jncp (Fig. 4.15b). The uncertainty associated with monthly values of pCO_2(Jtrsp), pCO_2(Vent), and pCO_2(Jncp) was estimated to be 40 μatm.

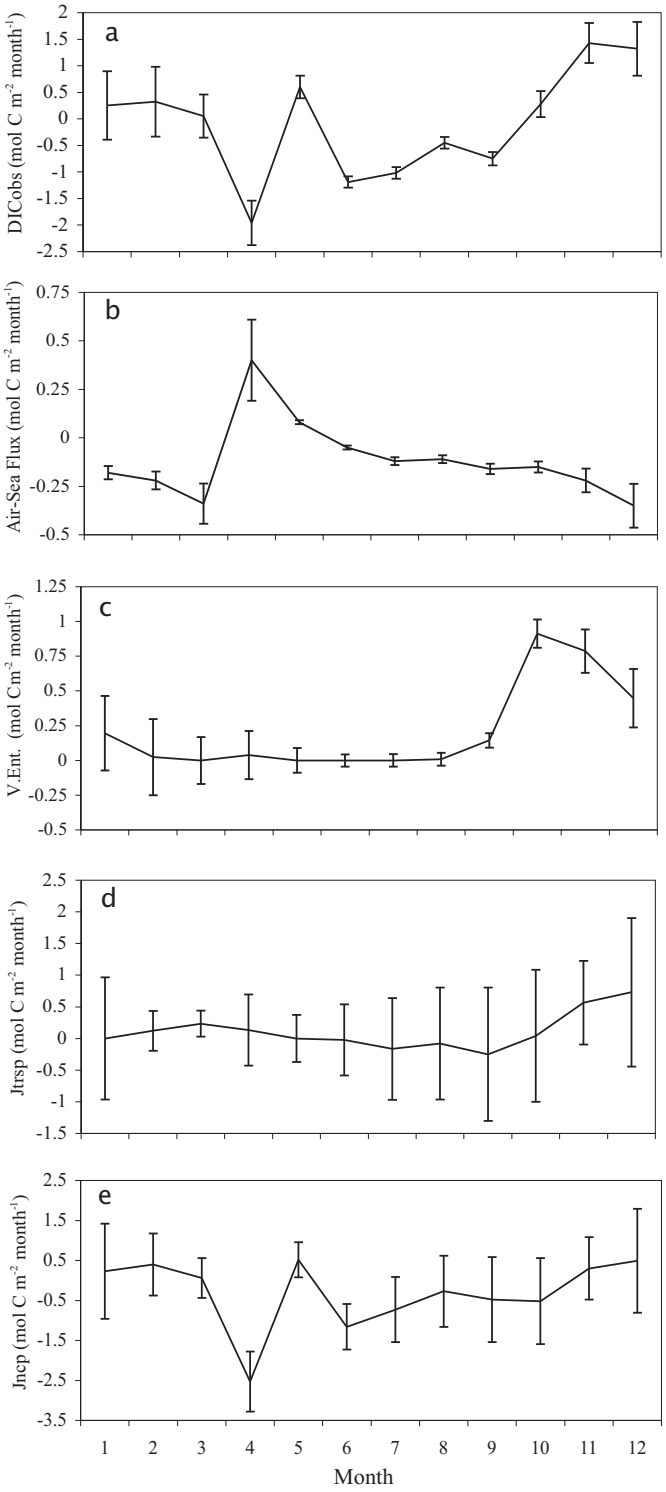

Figure 4.14: The annual cycles of each of the terms in Eq. 6: (a) the observed monthly change (dDIC/dt), (b) the air-sea CO_2 flux, (c) vertical entrainment, (d) Jtrsp, and (e) Jncp.

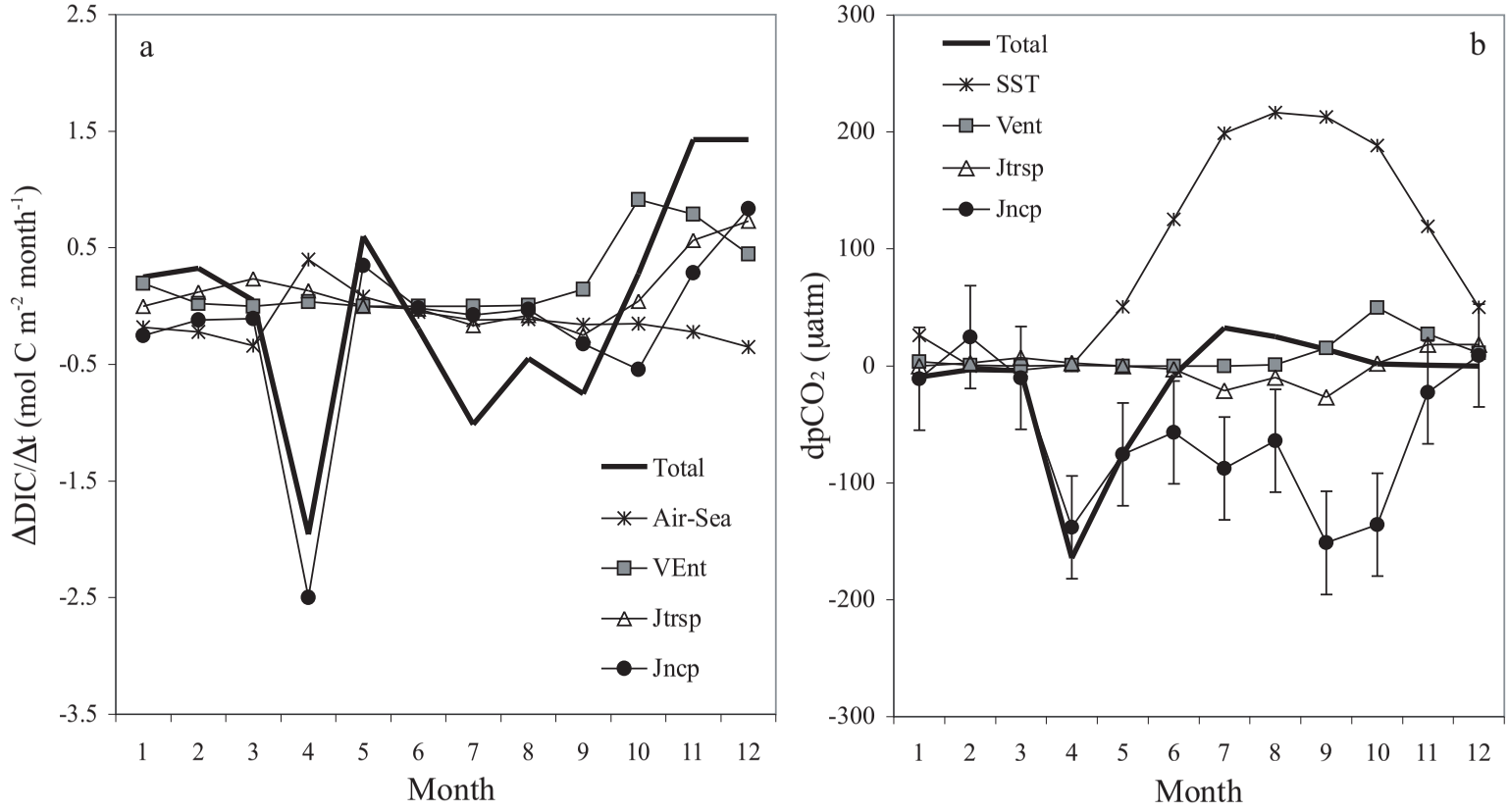

Figure 4.15: (a) Computed monthly variations of DIC in units of mol C m^{-2} $month^{-1}$. The total change (dDIC/dt), the change due to air-sea exchange of CO_2, vertical entrainment, transport (Jtrsp), and net community production (Jncp) are shown. (b) The controls on pCO_2 are shown as cumulative values relative to January.

The large seasonal amplitude of surface water temperature is particularly important to the carbon system on the Scotian Shelf. The region experiences near, or sub-zero temperatures during the winter season, due to its position downstream of the Labrador Sea and the Gulf of St. Lawrence. Temperatures peak at nearly 20°Cin the late summer due to the region's latitude and the relatively stable, stratified water column throughout the summer season. As discussed in more detail in Section 4.6.1, this large amount of surface warming was only partially off-set by biological production, and surface waters however remained supersaturated throughout the year, outside of the brief spring bloom period. Biological production was reduced in autumn, while over the same period the waters cooled, and the winds strengthened introducing DIC-rich waters from below and resulting in the continued supersaturation with respect to the atmosphere. The absence of biology from June through September would result in a near doubling of surface $\mathrm{pCO_2}$ compared to the observed in-situ values (Fig. 4.15b). The region acted a source of $\mathrm{CO_2}$to the atmosphere despite the productivity of the shelf, due to the magnitude of the temperature control. The waters at station HL2 originate in the cold, biologically productive Gulf of St. Lawrence, as these waters move south via the Nova Scotia current they warm, increasing the surface $\mathrm{pCO_2}$. *Schiettecatte et al.* (2006)) found that the Scheldt plume in Belgian coastal waters of similar latitude, is similarly supersaturated outside of the spring bloom period, but concluded that the biological control in this system dominated the temperature control. These results highlight the importance of case-by-case studies of the carbon system in coastal ocean environments.

4.5.4 Net Community Production

Net community production (NCP) is the difference between net primary production (NPP) and heterotrophic respiration (R):

$$\mathrm{NCP} = \mathrm{NPP} - \mathrm{R}. \tag{4.11}$$

Quantifying changes in DIC due to photosynthesis and respiration, i.e. (Jncp), allowed the annual NCP (3.7$\pm$2.9 mol C $\mathrm{m^{-2}\ yr^{-1}}$) to be estimated (see Table 4.2). A satellite-based estimate of annual primary production (PP) based on particulate organic carbon (POC) was made using the Giovanni online data system (*Acker and Leptoukh*, 2007). The annual PP on the Scotian Shelf resulting from the POC estimate was $\mathrm{PP_{SAT}}$ = 95 g C $\mathrm{m^{-2}}$

yr^{-1}, which is in general agreement with the literature values which range from 60 to 130 g C m^{-2} yr^{-1} (*Mills and Fournier*, 1979; *Mousseau et al.*, 1996). Our estimate of annual NCP (3.7 mol C m^{-2} yr^{-1} or 44 g C m^{-2} yr^{-1}) thus corresponded to approximately 46% of PP (using an average value of PP = 95 g C m^{-2} yr^{-1}).

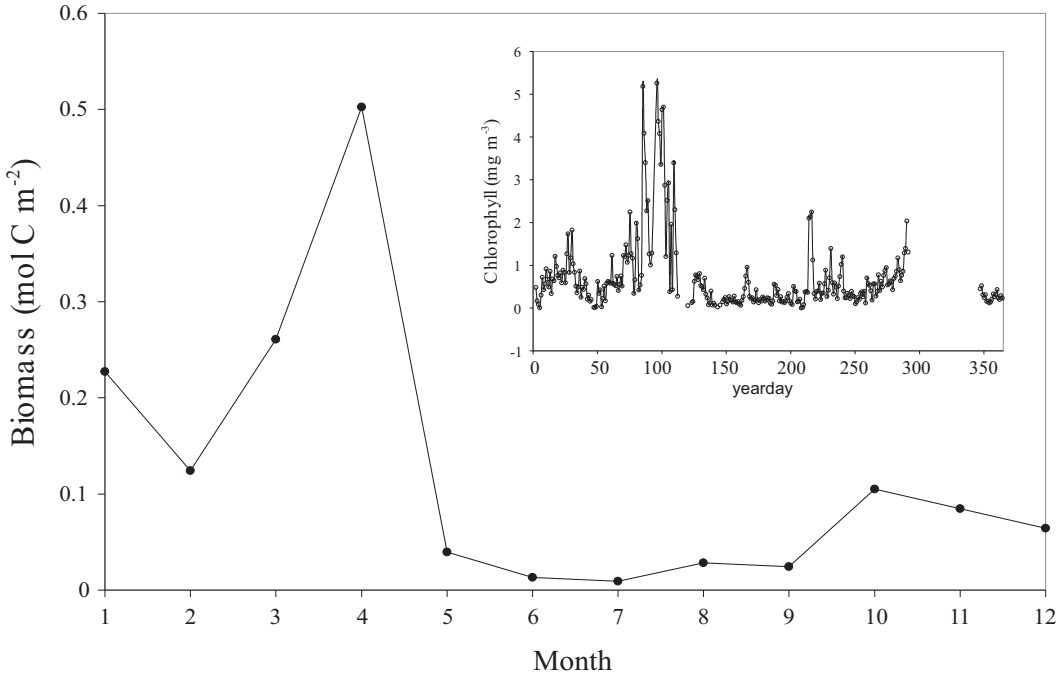

Figure 4.16: Monthly values of biomass, computed from the time-series of chlorophyll-a, a carbon-to-chlorophyll ratio of 70 mg C (mg Chl)$^{-1}$, and monthly mixed-layer depth. Inset: the calibrated time-series of chlorophyll-a fluorescence.

An additional, independent, estimate of NCP, can be made by exploiting the time-series of chl-a measured by the CARIOCA buoy. Biomass (B) was estimated from the time-series of chl-a and carbon-to-chlorophyll ratio 70 mg C $(\mathrm{mg\ Chl})^{-1}$ (Fig. 4.16). While not accounting for a possible seasonal variability in the carbon-to-chlorophyll ratio, this value is consistent with literature values for the Scotian Shelf region (*Platt et al.*, 1991). The biomass based estimate of NCP ($\mathrm{NCP_B}$) was computed from the annual integral of monthly biomass estimates. The uncertainty (70%) reflects the uncertainty in the chlorophyll-to-carbon ratio estimate. Compared to the above DIC-based assessment, the biomass based estimate appeared to underestimate NCP. This underestimate may be due to the substantial losses of chl-a from the surface layer due to sinking and grazing (up to 45% of the surface waters being cleared of particles in a given day, e.g. *Banse* 1994, 1995). These losses diminish the chl-a concentration, thus leading to lower observed

values, although DIC has been consumed. In other words, while the above DIC based NCP estimate includes this carbon uptake, the chl-a based estimate ($\mathrm{NCP_B}$) does not and would produce lower chl-a values which would result in an underestimate of carbon uptake. Furthermore, the chl-a signal (Fig. 4.16) was driven primarily by the spring bloom, while in late spring and summer, only modest chl-a concentrations were observed. However, we provide evidence here (see also Section 5.1) of substantial carbon uptake in the late spring and summer, after the exhaustion of nutrients (see for example *Fogg* 1983, *Thomas et al.* 1999, *Schartau et al.* 2007), which cannot be accounted for by the chl-a based $\mathrm{NCP_B}$ estimated. As discussed in detail in Chapter 5, this discrepancy has serious implications for satellite based assessments of NCP, or related CO_2 fluxes (e.g. *Lefèvre et al.* 2002, *Chierici et al.* 2009), since even modest carbon uptake in summer may strongly influence surface water pCO_2 due to the shallow summer mixed-layer. Inorganic carbon based approaches, such as the investigation presented here, may therefore play an essential role in constraining optical, space-borne, or in-situ approaches.

4.6 Discussion

4.6.1 Post-Bloom Summer Production

Production in the Scotian Shelf region was ongoing after the decay of the spring phytoplankton bloom and the exhaustion of surface nutrients as evidenced by in-situ observations of DIC and AOU in summer and autumn (Fig. 4.11), and by the model estimate of Jncp (Table 2). The uptake of more DIC than expected from the canonical Redfield ratios is often referred to as carbon overconsumption (*Redfield et al.*, 1963; *Toggweiller*, 1993). This non-Redfield production, or carbon overconsumption has been widely observed and discussed (*Droop*, 1973; *Sambrotto et al.*, 1993; *Thomas et al.*, 1999; *Osterroht and Thomas*, 2000; *Arrigo*, 2005; *Schartau et al.*, 2007). New production, as defined by *Dugdale and Goering* (1967) is the production by phytoplankton based on the conversion from nitrate uptake to carbon uptake using the elemental (Redfield) ratio found in organic matter. During the month of April we assume that the NCP was equal to net primary production in the region, which is compared to new production. We estimated new production on the Scotian Shelf from the difference in surface nitrate concentrations

between the end of March (6.23 μmolkg^{-1}) and the end of April (0.28 μmol kg^{-1}), after the spring bloom. The total change in nitrate was ΔNO_3=5.95 μmol kg^{-1}, which corresponds to an inorganic carbon uptake of ΔDIC_N = 39.42 μmol kg^{-1} = 1.3 mol C m^{-2}, using the Redfield ratio of C:N=106:16, and a mixed-layer depth of 34 m (see Table 4.2). If this is compared to the computed biological DIC draw-down in April, (ΔDIC_{bio} = 2.5 mol C m^{-2} and Table 4.2), new production accounted for roughly 54% of the DIC drawdown observed during the spring bloom. Please note that this simplified approach of comparing NO_3 concentration from one month to the next does not account for the several possible sources and sinks, both physical and biological (i.e., advection, vertical diffusion, atmospheric deposition, nitrification) that will certainly influence the water column NO_3 concentration. If atmospheric nitrogen deposition is taken into account, the ratio of DIC:NO_3 in the post-bloom summer season would likely be much closer to the Redfield ratio observed in spring (*Thomas et al.*, 1999; *Doney et al.*, 2007).

Integrating the monthly estimates of ΔDIC_{bio}, (Jncp), from June through October yielded a post-bloom summer production of 3.2 mol C m^{-2} over the five month period, which corresponds to roughly 125% of the production generated by the spring bloom in April. This production occurred during a period of surface nitrate depletion, and must therefore be fueled by allochthonous nutrients. The POC-based estimate of PP from June through October however yielded a value of PP_{SAT} = 0.77 mol C m^{-2} over the five month period, which would imply that in the late summer $PP_{SAT} <$ NCP. This is due to the fact that this post-bloom production is not accounted for in the (chl-a based) satellite POC estimate of PP, emphasizing the advantage of the DIC based approach (see also Section 4.5.4).

This summer production, which occurred when the mixed-layer was very shallow, had a large impact on surface water pCO_2. This impact can best be seen in the relationship between the temperature corrected surface pCO_2 and the in-situ water temperature (Fig. 4.12). After the decay of the spring bloom from June to early September, the surface water warmed from 8°C to 20°C. Over the same period, the temperature corrected pCO_2 decreased from roughly 420 μatm (at 8°C) to less than 300 μatm at the temperature maximum. The summer production resulted in a decrease in pCO_2 of more than 100 μatm. Despite this draw-down, the waters remained supersaturated with respect to atmospheric CO_2 throughout the summer and early autumn due to the effect of temperature on surface

pCO_2. The remineralization of the organic matter produced in summer and early autumn increased pCO_2 as the water cooled and the mixed-layer deepened, entraining DIC-rich water from below.

4.6.2 Trophic Status

In autotrophic systems, such as the mixed-layer on the Scotian Shelf, there is a net production of organic matter at the expense of inorganic carbon and nutrients (i.e. $\mathrm{NCP} > 0$). In contrast, heterotrophic systems are defined by a net consumption of organic organic matter and release of inorganic carbon and nutrients (i.e. $\mathrm{NCP} < 0$). Autotrophic systems may therefore potentially act as sinks of atmospheric $\mathrm{CO_2}$. However, as described above the Scotian Shelf region was found to be a moderate net source of $\mathrm{CO_2}$ to the atmosphere, with an out-gassing of $F = -1.4\ \mathrm{mol\ C\ m^{-2}\ yr^{-1}}$, and a reversal of this process occurring only during the spring bloom. Other regions at similar latitude, with large annual deliveries of fresh water, like the North Sea, and the Baltic Sea, are heterotrophic systems that act as sinks for atmospheric $\mathrm{CO_2}$ (*Thomas and Schneider*, 1999; *Thomas et al.*, 2005b). The Scotian Shelf behaved similarly to an upwelling system, which are often biologically productive systems which release $\mathrm{CO_2}$ to the atmosphere due to the delivery of DIC-rich waters from below (*Lendt et al.*, 2003; *Thomas et al.*, 2005b). The majority of the outgassing of CO_2 on the Scotian Shelf occurred during autumn and winter when the destratification of the water column maintained pCO_2 supersaturation despite the near-zero water temperature. This is in contrast to the interpretation of *Chen and Borges* (2009) for temperate continental shelves, which on the global scale, tend to act as sinks for CO_2 in the autumn and winter seasons, as in the case of the South and Middle Atlantic Bights (*DeGrandpre et al.*, 2002; *Jiang et al.*, 2008). A recent modelling study (*Fennel and Wilkin*, 2009) suggests that the continental shelf pump mechanism (*Tsunogai et al.*, 1999) which has the potential to transport DIC-rich water off the shelf and into the adjacent deep ocean does not operate on the Scotian Shelf. Vertical sinking of organic material is insufficient for carbon export since this material is re-exposed to the surface under conditions of deep winter mixing (*Fennel and Wilkin*, 2009), and the horizontal transport of carbon across the shelf break is not well constrained.

4.7 Conclusion

Based on highly temporally resolved observations from an autonomous moored instrument, and complementary ship-based sampling over the wider spatial scale, the processes governing the variability of surface pCO_2 and DIC on the Scotian Shelf were evaluated. Biological processes, lateral transport, and entrainment were the dominant factors controlling the variability of mixed-layer DIC. Annual mixed-layer net community production was $\mathrm{NCP} = 3.7\ \mathrm{mol\ C\ m^{-2}\ yr^{-1}}$, with a significant portion of this production occurring in summer after the decay of the spring bloom and under nutrient depleted conditions. While the 1-D approach has limitations, particularly with respect to the effect of advection and mixing, this method does allow the temporal changes in mixed-layer carbonate system in this coastal system to be understood.

4.8 Acknowledgements

We are grateful to the captains, officers and crew of the *CCGS Hudson* for their cooperation in the collection of field data. The authors would like to extend their sincere thanks to K. R. Thompson for his thoughtful comments on the analysis and the manuscript. Many thanks to R. Davis for his assistance with the initial processing of the CARIOCA data, to A. Comeau for the fluorometer calibration, and to D. Worthy at Environment Canada for providing the atmospheric CO_2 data. We are grateful to J. Barthelotte and M. Scotney for the deployment and recovery of the buoy, and to J. Spry and the Bedford Institute of Oceanography for making the archived data from station HL2 accessible. We thank two anonymous reviewers and Nick Bates for their thoughtful and constructive comments. This project was funded by the Canadian Natural Sciences and Engineering Research Council (NSERC) and MetOcean Data Systems, and contributes to IGBP/LOICZ.

CHAPTER 5

AIR-SEA CO_2 FLUXES ON THE SCOTIAN SHELF

5.1 Abstract

We develop an algorithm to compute pCO_2 in the Scotian Shelf region (NW Atlantic) from satellite-based estimates of chlorophyll-a concentration, sea-surface temperature, and observed wind speed. This algorithm is based on a high-resolution time-series of pCO_2 observations from an autonomous mooring. At the mooring location (44.3°N and 63.3°W), the surface waters act as a source of CO_2 to the atmosphere over the annual scale, with an outgassing of -1.10 mol C m^{-2} yr^{-1} in 2007/2008. A hindcast of air-sea CO_2 fluxes from 1999 to 2008 reveals significant variability both spatially and from year to year. Over the decade, the shelf-wide annual air-sea fluxes range from an outgassing of -1.70 mol C m^{-2} yr^{-1} in 2002, to -0.02 mol C m^{-2} yr^{-1} in 2006. There is a gradient in the air-sea CO_2 flux between the northeastern Cabot Strait region which acts as a net sink of CO_2 with an annual uptake of 0.50 to 1.00 mol C m^{-2} yr^{-1}, and the southwestern Gulf of Maine region which acts as a source ranging from -0.80 to -2.50 mol C m^{-2} yr^{-1}. There is a decline, or a negative trend, in the air-sea pCO_2 gradient of 23 μatm over the decade, which can be explained by a cooling of 1.3°C over the same period. Regional conditions govern spatial, seasonal, and interannual variability on the Scotian Shelf, while multi-annual trends appear linked to the North Atlantic Oscillation.[1]

[1]This chapter comprises a manuscript by E. H. Shadwick, H. Thomas, A. Comeau, S. E. Craig, C. W. Hunt, and J. E. Salisbury entitled *Satellite observations reveal high variability and a decreasing trend in CO_2 fluxes on the Scotian Shelf* submitted to Biogeosciences.

5.2 Introduction

The rise in atmospheric carbon dioxide (CO_2) from anthropogenic emissions is partially offset by the oceans' CO_2 uptake (*Sabine et al.*, 2004); direct estimates of this uptake require accurate measurements of the partial pressure of CO_2 (pCO_2) in the surface-ocean, and knowledge of its seasonal and interannual variability. Measurements of pCO_2 in the open ocean have become increasingly available (*Boutin and Merlivat*, 2009; *Takahashi et al.*, 2009; *Watson et al.*, 2009). The increased availability of pCO_2 data has facilitated a deeper understanding of the variability of CO_2 fluxes, particularly for the North Atlantic Ocean (*Schuster and Watson*, 2007; *Thomas et al.*, 2008; *Schuster et al.*, 2009). These investigations have been complemented by the application of satellite data (*Lefèvre et al.*, 2002; *Olsen et al.*, 2008; *Chierici et al.*, 2009) and modelling studies to respectively increase both spatial and temporal coverage, and to gain a mechanistic understanding of the systems (*Etcheto et al.*, 1999; *Wanninkhof et al.*, 2007; *Lefèvre et al.*, 2008; *Padin et al.*, 2008; *Thomas et al.*, 2008; *Ullman et al.*, 2009). However, while fundamental understanding of air-sea CO_2 exchange in coastal oceans has yet to be achieved, the few available studies provide evidence for highly variable CO_2 fluxes in these regions (*Cai et al.*, 2006; *Thomas et al.*, 2007; *Borges et al.*, 2008). Despite relatively large CO_2 fluxes in coastal oceans (*Tsunogai et al.*, 1999; *Thomas et al.*, 2004), the temporal and spatial variability of pCO_2 remains particularly poorly understood (*Borges*, 2005; *Borges et al.*, 2005; *Cai et al.*, 2006), and the reliability of assessments employing space-borne sensors in these regions has not been established (*Lohrenz and Cai*, 2006; *Salisbury et al.*, 2008).

In the present study we combine highly temporally resolved autonomous observations, in-situ data from monthly shipboard sampling, and space-borne observations to investigate the variability of CO_2 fluxes in the Scotian Shelf region of the Canadian northwestern Atlantic. The use of these three independent observational techniques allows an assessment of the governing processes at seasonal, interannual, and multi-annual time scales to be made.

5.3 Oceanographic Setting

The Scotian Shelf comprises a 700 km long section of the continental shelf off the Canadian province of Nova Scotia. The Scotian Shelf is bounded by the Gulf of St. Lawrence

to the northeast, and by the Gulf of Maine to the southwest, varying in width from 120 to 240 km (Fig. 5.1). The Scotian Shelf is uniquely located at the junction of the North Atlantic sub-polar and sub-tropical gyres, downstream of the St. Lawrence River system (*Loder et al.*, 1997). The seasonal shelf-scale circulation is dominated by the Nova Scotia Current flowing to the southwest roughly parallel to the coast, and an extension of the Labrador Current, flowing in the same direction, along the shelf edge (*Loder et al.*, 1997). The water masses on the northeastern North American coast are well-studied (*Bigelow*, 1927; *Hachey*, 1942; *Chapman and Beardsley*, 1989; *Loder et al.*, 1998). As many as eight distinct water masses have been identified in the Scotian Shelf region (*Khatiwala et al.*, 1999; *Houghton and Fairbanks*, 2001). However, for simplicity, the water column on the Scotian Shelf can be characterized by a two-layer system in winter when relatively fresh shelf water overlies more saline slope water. In summer, it is characterized by a three-layer system with the development of a warm, shallow, surface layer overlying the two-layer system (*Loder et al.*, 1997). The seasonal cycle of sea-surface temperature on

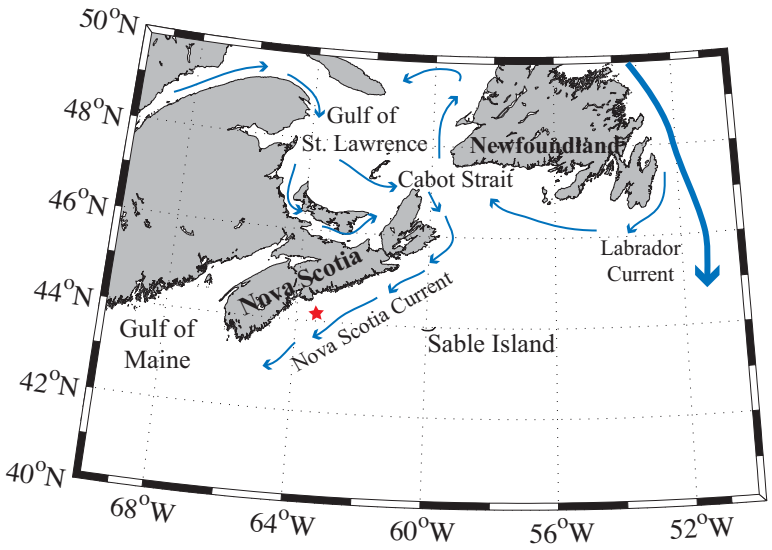

Figure 5.1: The hydrographic setting on the Scotian Shelf. The position of the CARIOCA buoy (red star) and the Sable Island Meteorological Station are indicated.

the Scotian Shelf has an annual range of roughly 16°C to 20°C, which is among the largest in the world (*Umoh and Thompson*, 1994). The southwestern outflow from Cabot Strait is the major source of freshwater to the region. Salinity on the Scotian Shelf increases

with distance offshore due to the northward transport of Gulf Stream waters In autumn the warmest surface temperature is observed in the central Scotian Shelf, increasing with the distance from shore. The peak in river discharge from the St. Lawrence is delivered to the Scotian Shelf between June and October; surface salinity is typically decreased by 1 part, from roughly 30.5 to 29.5, as a result of this input (*Loder et al.*, 1997).

Coastal upwelling events on the Scotian Shelf have long been recognized (*Hachey*, 1935; *Petrie*, 1983). Upwelling events have frequently been observed in the coastal regions of the Scotian Shelf, and modeling studies have reproduced these observed events (*Petrie*, 1983; *Donohue*, 2000). Furthermore, these events may play a role in initiating and sustaining the spring phytoplankton bloom by displacing nutrient-depleted surface water and bring nutrient-rich waters up to the surface (*Greenan et al.*, 2004). Convection occurs in winter season on the Scotian Shelf. In this region wind speed exerts some control over the depth of convective mixing; an increase in wind strength removes more heat from the surface waters and deepens the extent of the convection.

5.4 Methods

Hourly, autonomous observations of surface water pCO_2 (μatm), chlorophyll-a fluorescence (F_{Chl}), and sea-surface temperature (SST), were made using a CARIOCA buoy moored roughly 30km offshore from Halifax, at 44.3°N and 63.3°W, between April 2007 and June 2008. Hourly CARIOCA data were uploaded and transmitted daily via the ARGOS satellite system. The pCO_2 measurements were made by an automated spectrophotometric technique (*Bates et al.*, 2000; *Bakker et al.*, 2001; *Copin-Montégut et al.*, 2004). A Sea-Bird (SBE 41) conductivity and temperature sensor was used to measure temperature (°C) and to determine salinity; chlorophyll-a fluorescence (μg l^{-1}) was determined by a WET Labs miniature fluorometer (WETstar).

Non-photochemical effects that are related to the intensity of the incoming solar radiation may decrease F_{Chl} up to 80% during the day (*Kiefer*, 1973). This effect can be avoided by using night-time data which, to a large extent, are free of the effects of non-photochemical quenching, for fluorometer calibration. Night-time data were taken as a mean F_{Chl} between 0300 and 0600 (UTC); data points were temporally interpolated to match discrete chlorophyll-a measurements (Chl-a [mg m^{-3}]) from monthly or twice-monthly occupations at the mooring site. A linear regression (r^2=0.76, N=29, $p<0.001$)

was used to determine the relationship between the $\mathrm{F_{Chl}}$ and Chl-a, and applied to the CARIOCA fluorescence-derived chlorophyll-a time-series ($\mathrm{Chl_F}$ [mg $\mathrm{m^{-3}}$], see Table 5.1 for a summary of notation used to distinguish between the time-series of chlorophyll-a).

Table 5.1: Notation for different time-series of chlorophyll-a

Symbol	Description
$\mathrm{F_{Chl}}$	chlorophyll-a fluorescence determined by fluorometer
Chl-a	discrete chlorophyll-a determined by extraction
$\mathrm{Chl_F}$	fluorescence-derived chlorophyll-a used in Eq. 5.2
$\mathrm{Chl_{SAT}}$	satellite derived chlorophyll-a concentration

Wind speed (m $\mathrm{s^{-1}}$) and atmospheric CO_2 (μatm) were measured hourly by Environment Canada at the Sable Island Meteorological Station (43.9°N and 60.3°W) at a height of 10 m using a sonic anemometer and an open-path infra-red CO_2 analyser (Fig. 5.1). Monthly mean values of $\mathrm{pCO_2}$, $\mathrm{Chl_F}$, and SST, were computed from the CARIOCA time series, comprising more than 2000 observations over a 14 month period. Monthly integrals of the gas transfer velocity (*k* [cm $\mathrm{hr^{-1}}$]) were computed from hourly winds and the formulation of *Wanninkhof* (1992). It has been suggested that the parameterization of *Wanninkhof* (1992) may overestimate the gas transfer velocity (*Sweeney et al.*, 2007). The uncertainty associated with the monthly air-sea flux (20%) was estimated from the standard deviation of the flux computed with the parameterization of *Wanninkhof* (1992) and the flux computed with the parameterization of *Nightingale et al.* (2000). The air-sea CO_2 fluxes (F [mol C $\mathrm{m^{-2}}$ $\mathrm{month^{-1}}$]) were computed via:

$$\mathrm{F} = k\alpha\Delta\mathrm{pCO_2}, \tag{5.1}$$

where α is the coefficient of solubility (*Weiss*, 1974) and $\Delta\mathrm{pCO_2}$ is the gradient in $\mathrm{pCO_2}$ between the ocean and the atmosphere. It has been shown that the winds at Sable Island are representative of the winds over the Scotian Shelf (*Petrie and Smith*, 1977); values of *k* computed from Sable Island winds were therefore used in the flux computations in each grid box. A negative flux indicates a transfer from the ocean into the atmosphere. Annual flux estimates between different years are compared with the same high precision as the values of $\Delta\mathrm{pCO_2}$ (13 μatm, see Section 4.1), which is essential for a reliable assessment of interannual variability. The accuracy of the flux computations is however lower (20%)

due to the large error associated with the gas transfer parameterization (*Naegler et al.*, 2006; *Sweeney et al.*, 2007; *Watson et al.*, 2009).

5.5 Results and Discussion

5.5.1 Multiple Linear Regression

A multiple linear regression (MLR) (Eq. 1) was applied using monthly mean values of pCO_2, $\mathrm{Chl_F}$, SST, and the gas transfer velocity, *k,* as predictor variables (i.e. N=14). The regression was also applied to the hourly (night-time) observations (n=2000), and the resulting regression coefficients were similar to those presented in Eq. 5.2. The choice of monthly means to generate Eq. 5.2 was made for temporal consistency with the remotely-sensed data obtained on a monthly timescale which was used, along with Eq. 1 to compute pCO_2, and is described in Section 5.5.3. The April value of $\mathrm{Chl_F}$ acted as a leverage point, dominating the regression, and allowing the pCO_2 minimum to be reproduced by the model. During the remainder of the year, pCO_2 is influenced to a lesser degree by $\mathrm{Chl_F}$, and more strongly by the annual cycle of SST.

$$\mathrm{pCO_2} = 354.4 - 24.6\mathrm{Chl_F} + 4.6\mathrm{SST} + 3.7k \tag{5.2}$$

$$\mathrm{X_t} = \frac{1.7}{12}\Delta\mathrm{t} \tag{5.3}$$

Surface water pCO_2 on the Scotian Shelf was reconstructed from January 1999 to December 2008 using Eq. (5.2). A correction term, $\mathrm{X_t}$ (μatm) (Eq. 5.3), was applied to account for the rise of surface ocean pCO_2 of approximately 1.7 μatm $\mathrm{yr^{-1}}$, relative to January 1999, due to the uptake of anthropogenic atmospheric CO_2 (*Thomas et al.*, 2008). This term is added to the right hand side of Eq. (5.2) for each month 't', with Δt (months) equal to the number of months since January 1999. For example, in February 1999 $\mathrm{X_t}$ would be computed with: $\mathrm{X_t}$=(1.7/12) μatm. The multiple linear regression (Eq. 5.2) is applied to absolute values of $\mathrm{Chl_F}$, SST, and *k,* to compute monthly, values of pCO_2. This approach allows the use of predictor variables that can be observed remotely, and captures the underlying physical and biological mechanisms in the system.

Further information regarding the predictive capacity of $\mathrm{Chl_F}$, SST, and *k* to estimate pCO_2 was gained by computing the normalized, or β coefficeints. These coefficients are

dimensionless and directly comparable. The magnitude of the β coefficients then allows an assessment of the relative contribution, or weight, of each of the predictor variables (i. e. $\mathrm{Chl_F}$, SST, and *k*) in the estimate of pCO_2 (Table 5.2). $\mathrm{Chl_F}$ makes the strongest contribution, and that both the $\mathrm{Chl_F}$ and SST coefficients are roughly double the magnitude of the *k* coefficient (Table 5.2). The standard error associated with the computation of pCO_2 using the MLR is 13 μatm, and the associated $r^2 = 0.81$. The inclusion of the gas transfer velocity (*k*) in the MLR reduced the standard error (from 19 μatm) and increased the r^2 (from 0.73). The gas transfer velocity was used to reflect wind stress, as opposed to wind speed, the former being the quantity of interest when computing air-sea CO_2 fluxes.

Table 5.2: Non-standardized, or 'B' regression coefficients (see Eq. 1) and the normalized, β coefficients

	$\mathrm{Chl_F}$	SST	*k*
B	-24.6	4.6	3.7
β	-0.65	0.50	0.25

5.5.2 Interpretation of Regression Coefficients

The value of the $\mathrm{Chl_F}$ regression coefficient obtained in Eq. (5.2) (24.6 μatm $(\mathrm{mg\ m^{-3}})^{-1}$), is dominated by the spring bloom, and is consistent with a value obtained in a recent regression study in the North Atlantic south of Greenland (*Chierici et al.*, 2009). The $\mathrm{Chl_F}$ coefficient corresponds to a ratio of inferred net inorganic carbon assimilation to accumulated chlorophyll on the order of 115 mg C $(\mathrm{mg\ chl\text{-}a})^{-1}$, that is higher than literature values of $\sim$ 50 mg C $(\mathrm{mg\ chl\text{-}a})^{-1}$) (*Platt et al.*, 1991). This difference may be explained by the fact that the literature C:Chl-a ratios do not account for losses of chlorophyll both due to sinking - whereby chlorophyll leaves the system but the inorganic carbon deficit remains- and grazing leading to the accumulation of detritus and heterotrophic biomass (*Weeks et al.*, 1993; *Banse*, 1995; *Taylor et al.*, 1997).

The SST regression coefficient obtained in Eq. (5.2) (4.6 μatm $(^\circ\mathrm{C})^{-1}$) is lower than the thermodynamically expected value, which would be roughly 16 μatm $(^\circ\mathrm{C})^{-1}$ at 400 μatm (*Takahashi et al.*, 2002). The SST regression coefficient obtained is composed of the competing influences of the thermodynamic temperature dependence of pCO_2, and

the pCO_2 dependence on biological processes at the monthly time scale. The spring and summer pCO_2 drawn-down occurs in the period of nutrient depletion, but is not necessarily resolved by the chlorophyll record. Furthermore, the SST coefficient likely comprises additional effects of changes in salinity, which are also anti-correlated with temperature. However, these salinity changes play only a minor role in changing pCO_2 due to the opposing effects of alkalinity and dissolved inorganic carbon on pCO_2 (see Appendix A for a more detailed discussion of the SST coefficient).

The gas transfer velocity (*k*) here serves as a directly assessable representation of the mixed-layer depth. Mixed-layer depth, estimated from monthly profiles of temperature (i.e. changes in temperature between depth levels greater than 0.5°C) at the mooring station (see also Chaper 4), is plotted versus monthly values of gas transfer velocity for the year 2008 in Fig. 5.2. A linear regression revealed a significant correlation between the two variables (r^2=0.79, N=12, $p<0.001$). By using *k,* stronger winds, and a deeper mixed-layer, make a large contribution to the monthly value of pCO_2, while weaker winds, and a shallow mixed-layer, make a smaller, though still positive contribution to pCO_2. Mechanistically, with increasing winds, *k* represents the deepening of the mixed-layer in autumn and winter, which implies an intrusion of CO_2 rich subsurface water into the surface-layer. On the other hand, in spring and particularly in summer, weak winds, and thus lower values of *k,* yield lower values of pCO_2. In summer, if the moderate biological activity is confined to a shallower mixed-layer, it has a stronger impact on the pCO_2 (or the CO_2 concentration), than if it occurred within a deeper mixed-layer. In the regression model presented here, the *k* coefficient thus helps assign a third dimension to the two-dimensional satellite view. This is required to parameterize the CO_2 concentration changes as driver of the air-sea CO_2 flux rather than changes in the CO_2 inventory. The effect of gas exchange itself plays a subordinate role in altering water column CO_2 concentrations on the short, monthly, time scales applicable here.

The change in pCO_2 due to each of the predictor variables was computed using equations 5.4-5.6, using the 12 monthly mean values of $\mathrm{Chl_F}$, SST and k (Fig. 5.3). For example, the change in pCO_2 due to chlorophyll, $pCO_2(\mathrm{Chl_F})$, was computed (Eq. 5.4) by keeping SST and *k* constant, at their initial, January 2008, values (subscript 'J'), and

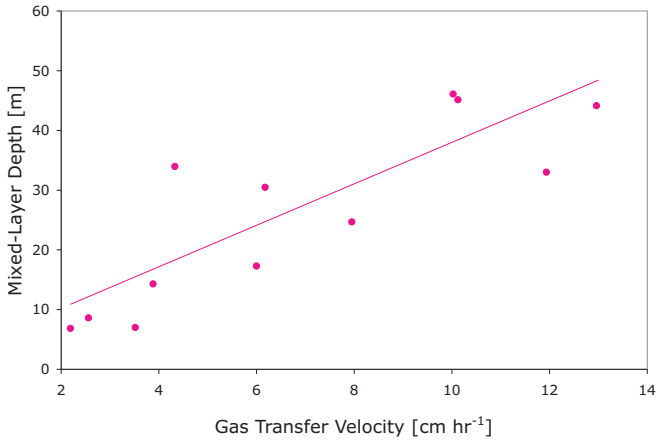

Figure 5.2: The relationship between mixed-layer depth and gas transfer velocity. Mixed-layer depth is estimated from monthly profiles of temperature and salinity measured at the same location as the CARIOCA mooring.

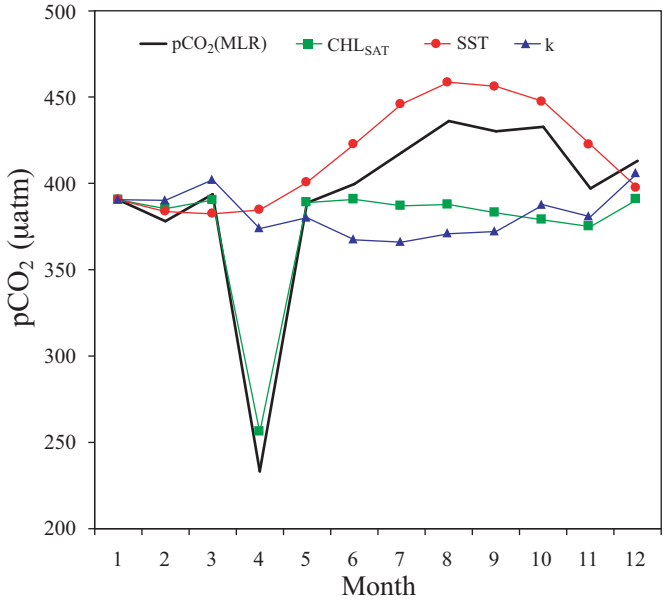

Figure 5.3: The individual contributions of the three predictor variables: $\mathrm{Chl_F}$ (green), SST (red), and k (blue) to the annual cycle of $\mathrm{pCO_2}$ (in black).

allowing $\mathrm{Chl_F}$ to vary. The change in pCO_2 due to SST and *k* were similarly computed.

$$\mathrm{pCO_2(Chl_F)} = 354.4 + 24.6\mathrm{Chl_F} + 4.6\mathrm{SST_J} + 3.7k_J \quad (5.4)$$

$$\mathrm{pCO_2(SST)} = 354.4 + 24.6\mathrm{Chl_{FJ}} + 4.6\mathrm{SST} + 3.7k_J \quad (5.5)$$

$$\mathrm{pCO_2(k)} = 354.4 + 24.6\mathrm{Chl_{FJ}} + 4.6\mathrm{SST_J} + 3.7k \quad (5.6)$$

The influence of $\mathrm{Chl_F}$ (Fig. 5.3 in green) dominates the total change (in black) in April, and plays a lesser, though non-zero, role during the rest of the year, reflecting the contribution of the late summer production (Chapter 4). The SST control (Fig. 5.3 in red) increases pCO_2 from April to September, decreases pCO_2 from September to December, and is near neutral from December to April. The gas transfer velocity (Fig. 5.3 in blue) acts to increases pCO_2 most strongly in the autumn and winter when wind driven mixing enhances the entrainment of high-carbon water into the surface layer.

5.5.3 Spatial Extapolation and Validation

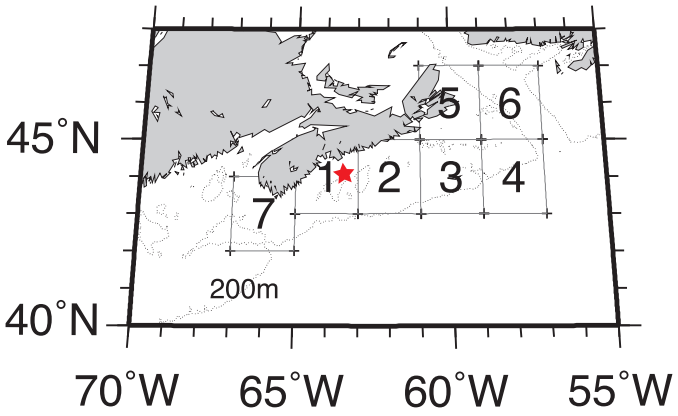

Figure 5.4: The investigation is extrapolated spatially to include seven 2°×2° grid boxes covering the entire Scotian Shelf region (222,700 km^2). The CARIOCA buoy (red star) was moored at 44.3°N, 63.3°W, within grid box 1. Wind speed measurements were made at the Sable Island Meteorological Station at 43.9°N and 60.3°W, within grid box 3.

Seven 2°×2° grid boxes, covering the Scotian Shelf were defined (Fig. 5.4). The MLR (Eq. 5.2) was used to generate a hindcast of pCO_2 that was extrapolated spatially using monthly means of satellite-derived chlorophyll-a concentration ($\mathrm{Chl_{SAT}}$ [mg m^{-3}]) and SST, along with the gas transfer velocity (*k)* computed with hourly winds measured at Sable Island (Fig. 5.5). The estimates of $\mathrm{Chl_{SAT}}$ were acquired from the Level 3

equal-area 9-km data from the Sea-viewing Wide Field-of-view Sensor (SeaWiFS) on the SeaStar platform, while SST was acquired from the Pathfinder AVHRR equal-area 9-km best-SST data product. The monthly $\mathrm{Chl_{SAT}}$ data were regressed against the (night-time calibrated), monthly mean, CARIOCA $\mathrm{Chl_F}$ timeseries, (r^2 = 0.68, N=14, $p<0.002$) and scaled accordingly. Thisscaling was done primarily to account for low monthly mean values of $\mathrm{Chl_{SAT}}$ within the grid box 1 (comprising the mooring location) relative to the calibrated $\mathrm{Chl_F}$ time series, and it was assumed that the scaling was valid for all seven grid boxes. The relationship between $\mathrm{Chl_F}$ and $\mathrm{Chl_{SAT}}$ was roughly 1:1; the satellite derived mean chlorphyll estimate (over the $2^\circ \times 2^\circ$ grid box) was in good agreement with the data from the CARIOCA fluorometer. However, the CARIOCA buoy was moored near the coast, and the discrete Chl-a measurements were made at this location. There are shortcomings associated with SeaWiFS data in coastal regions due to the potentially high concentrations of color dissolved organic matter (CDOM) and suspended particulate matter in coastal waters (*Lohrenz and Cai*, 2006; *Salisbury et al.*, 2008) which may bias the $\mathrm{Chl_{SAT}}$ concentrations. The standard deviation for the average monthly $\mathrm{Chl_{SAT}}$ concentration within a grid box (containing 576 pixels) ranged from 0.1 to 0.49 mg m^{-3}, with higher variation in the nearshore boxes.

The pCO_2(MLR) was validated against measurements of pCO_2 (pCO_2(underway)) made by a continuous flow equilibration system (see for example *Körtzinger et al.* (1996) for a description of the method) in: October 2006, April, August, and October 2007, and April and October, 2008 on board the *CCGS Hudson*. The underway measurements were obtained on monitoring cruises on the Scotian Shelf (see Chapter 4 for details of the field program). Measurements of pCO_2(underway) were made by a non-dispersive, infrared spectrometer (LiCor, LI-7000). The system was located in the aft-laboratory of the ship and the intake depth was approximately 3 meters below the water surface. Measurements were made every minute and used to compute hourly averages. The system was calibrated daily with both a CO_2-free reference gas (N_2) and a CO_2 calibration gas (328.99 ppm) provided by the U.S. National Oceanic and Atmospheric Administration (NOAA). The data were corrected to in-situ water temperature and to 100% humidity and has an associated uncertainty of less than 3μatm. On the same cruises, discrete seawater samples were collected at the surface (depths of 3 or 5 m) and concentrations of dissolved inorganic carbon (DIC) and total alkalinity (TA) were measured (see Chapter 4

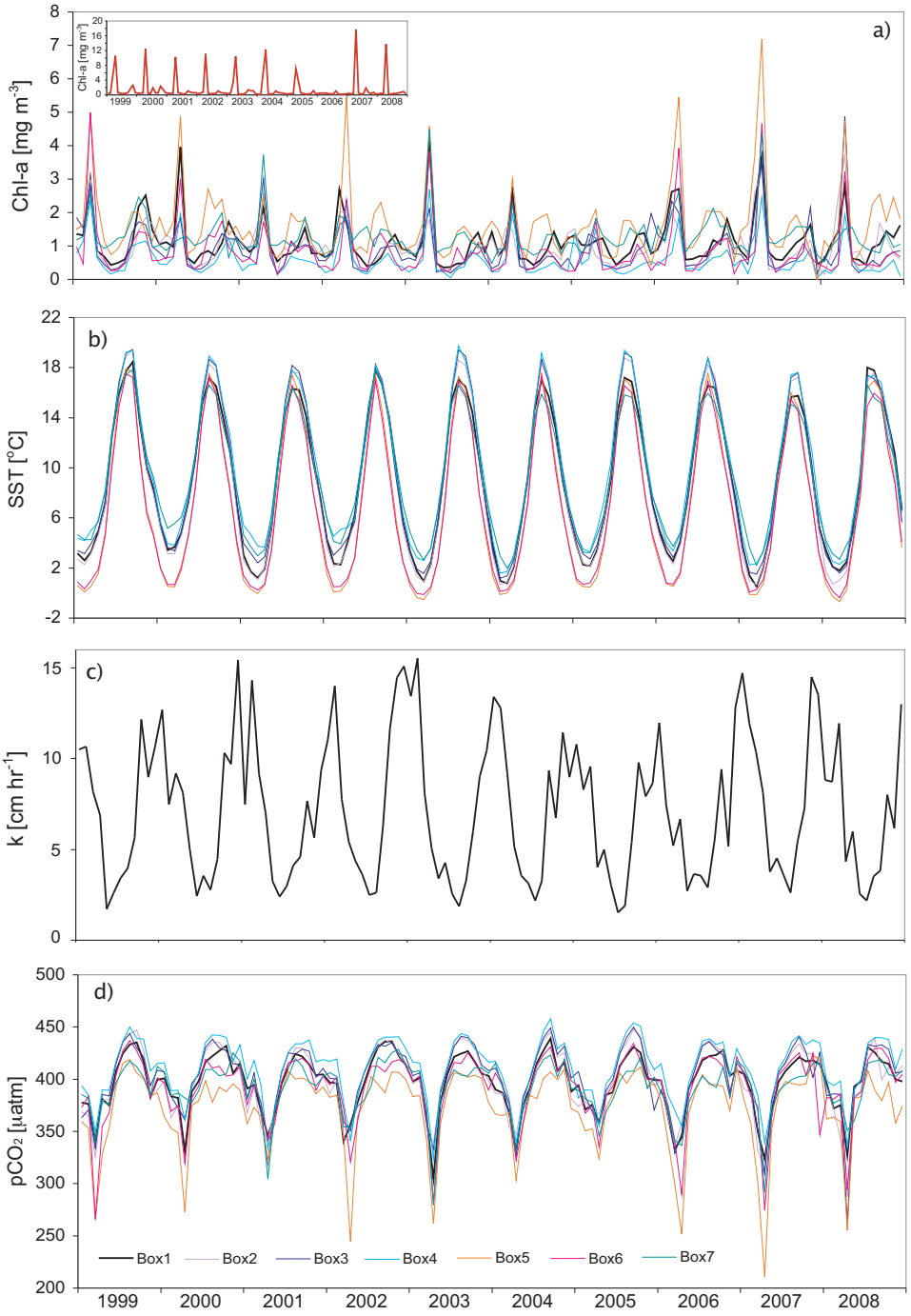

Figure 5.5: (a) Monthly values of $\mathrm{Chl}_{\mathrm{SAT}}$, inset: discrete Chl-a data from monthly shipboard occupations of the CARIOCA mooring location. These data are not monthly means, but once-per month occupations expressly biased to catch the spring chlorophyll maximum at the mooring site. (b) SST, (c) gas transfer velocity (k) and (d) computed pCO_2. For the locations of the grid boxes see Fig. 5.4.

for details). The DIC and TA measurements had an uncertainty of less than 2 and 3 μmol kg^{-1}, respectively. Following the determination of DIC and TA, discrete values of pCO_2 (pCO_2(DIC,TA)), were computed, using the standard set of carbonate system equations, excluding nutrients, with the CO_2Sys program of *Lewis and Wallace* (1998). We used the equilibrium constants of *Mehrbach et al.* (1973) refit by *Dickson and Millero* (1987). The calcium (Ca^{2+}) concentration was assumed to be conservative and calculated from salinity. The uncertainty associated with the pCO_2(DIC,TA) is 4μatm.

The pCO_2(MLR) is further compared to surface available pCO_2 in the Scotian Shelf region from the CARINA data base (pCO_2(CARINA)) from May 2004 to April 2008 (Figs. 5.6, 5.7 and Table 5.3) (*CARINA*, 2009). The pCO_2(underway) and pCO_2(CARINA) data represent mean values within a given $2^\circ \times 2^\circ$ grid box over 12 to 36 hours, depending on the length of time the ship spent in a given box during the cruise. The different timescales of the computed pCO_2(MLR) (monthly) and measured pCO_2(underway), pCO_2(DIC,TA), and pCO_2(CARINA) (12 to 36 hours)hinder a direct comparison. However, the agreement between the observed and computed pCO_2 supports the spatial extrapolation of the regression (Eq. 5.2). The pCO_2(MLR) overestimates the April pCO_2(CARIOCA) in both 2007 and 2008 (Fig. 5.8). The spatial variance of the of the satellite-derived Chl-a ($\mathrm{Chl_{SAT}}$) was particularly high near the location of the CARIOCA mooring in April 2007 (Fig. 5.4). The pCO_2(CARIOCA) is an average of hourly values over one month in an area that experienced particularly high concentrations of Chl-a in April 2007. The computed pCO_2(MLR) relies on $\mathrm{Chl_{SAT}}$ that has been both spatially and temporally averaged, which may explain the discrepancy between the peak values, seen for example, in April. A ten-year time series of discrete Chl-a measurements from the mooring location (Fig. 5.5a inset) indicates much higher concentrations than the $\mathrm{Chl_{SAT}}$ time-series used to predict pCO_2(MLR) (Fig. 5.5a and d). However, these data are not monthly mean values, but once-per-month measurements that are expressly biased to produce snapshots of the dominant features of the system, most notably the spring Chl-a maximum, corresponding to the annual pCO_2 minimum. The April cruise on the Scotian Shelf is similarly biased; sampling takes place at the height of the bloom. The computed pCO_2(MLR) represensts a monthly average, and the peak values are thus smoothed compared to the short-term ship-board observations. The computed pCO_2 reproduces very well the regional summer and autumn concentrations. There is good agreement between the pCO_2(MLR),

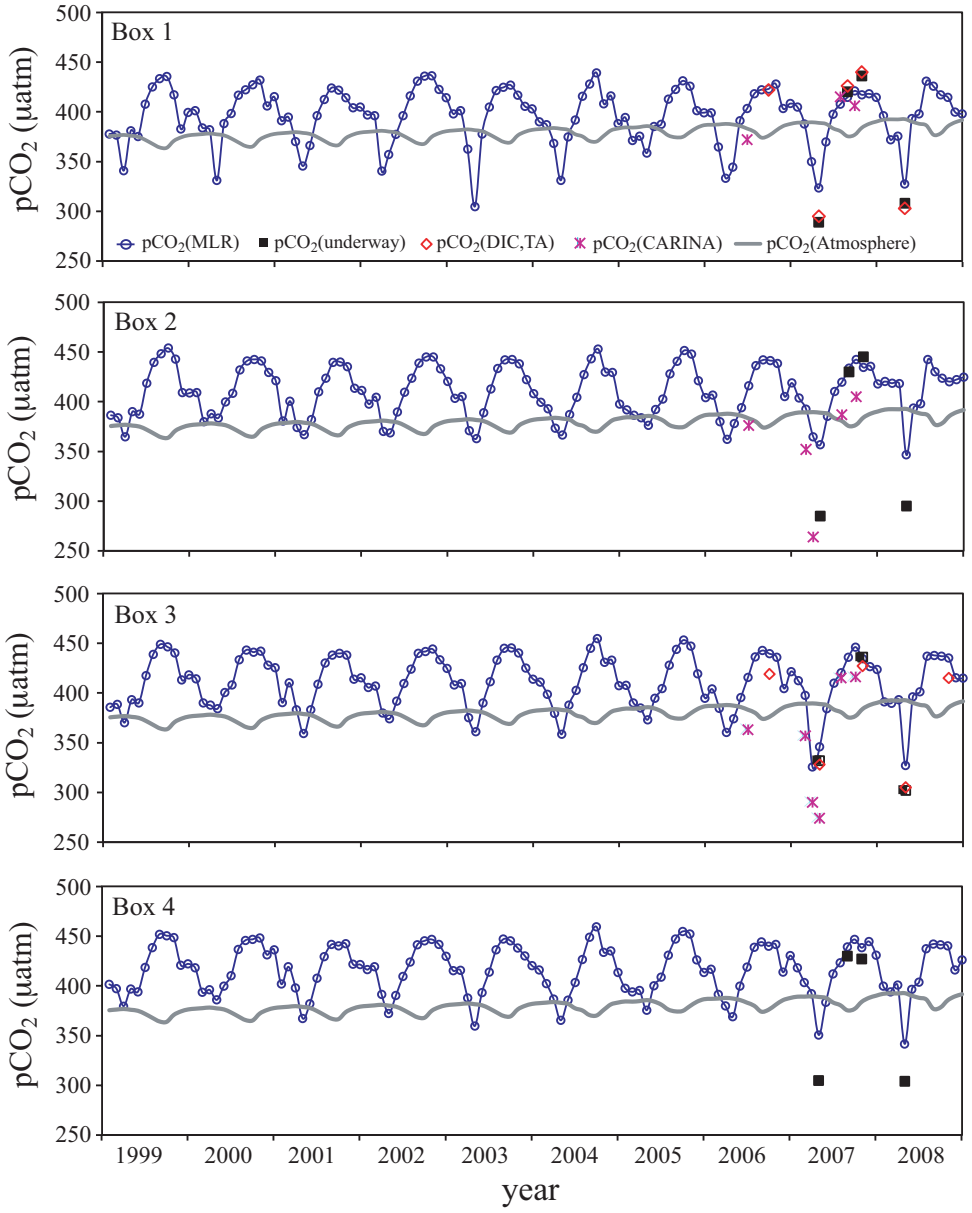

Figure 5.6: The computed pCO_2(MLR) (blue line with symbols) is validated against three independent time-series of observations: pCO_2(underway), pCO_2(DIC,TA) and pCO_2(CARINA) in grid boxes 1 through 4. For the locations of the grid boxes see Fig. 5.4.

pCO_2(underway), pCO_2(DIC,TA), and pCO_2(CARINA) outside of the spring bloom period in all grid boxes (Figs. 5.6, 5.7, Table 5.3).

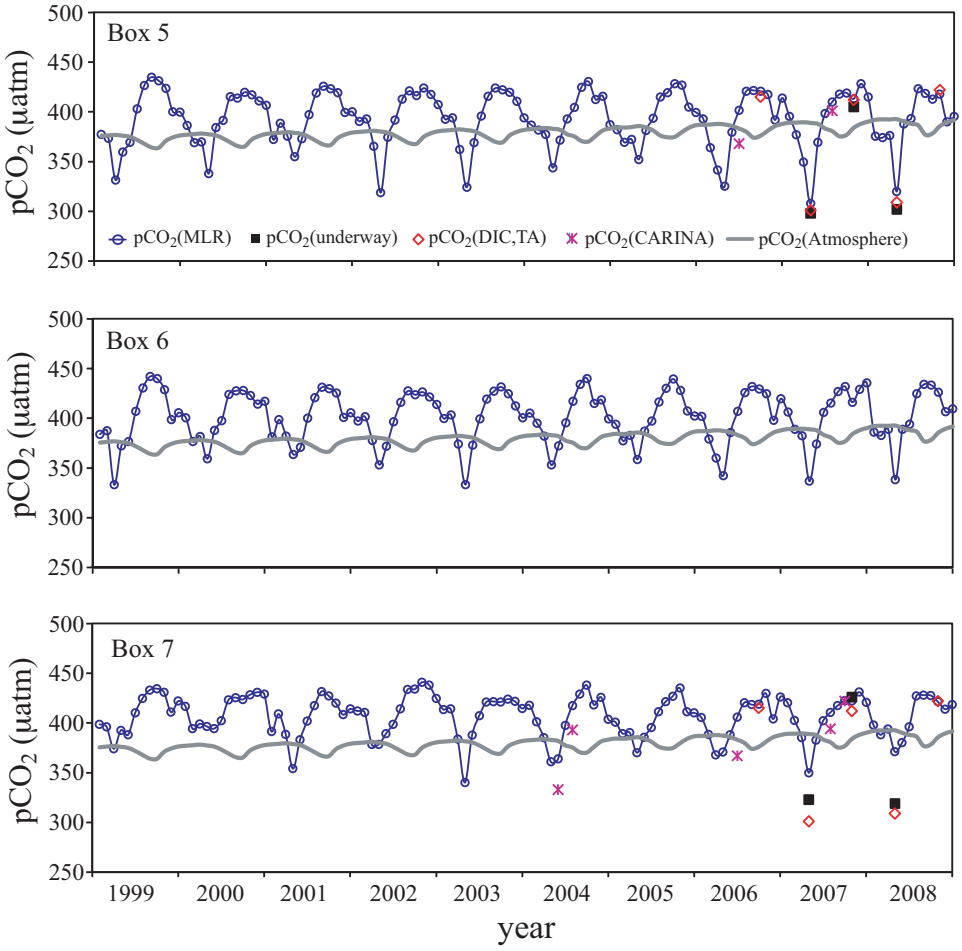

Figure 5.7: The computed pCO_2(MLR) (blue line with symbols) is validated against three independent time-series of observations: pCO_2(underway), pCO_2(DIC,TA) and pCO_2(CARINA) in grid boxes 5, 6 and 7. For the locations of the grid boxes see Fig. 5.4.

5.5.4 Seasonal and Interannual Variability of pCO_2

On the Scotian Shelf the spring bloom occurs at the SST minimum allowing the effects of temperature and biology to be clearly distinguished (see Chapter 4). The annual cycle of pCO_2 on the Scotian Shelf is dominated by the large seasonal amplitude of SST (Fig. 5.8a), with near 0°C winter minimum, and summer maximum approaching 20°C. The rapid and pronounced pCO_2 draw-down by the spring phytoplankton bloom in March or April is short-lived. The post-bloom recovery of pCO_2 is coincident with the warming of

Table 5.3: Comparison of pCO_2(MLR) with 3 sets of independent observations: the underway system pCO_2(UW); from discrete DIC and TA pCO_2(D); , and from the CARINA data base pCO_2(C). All values are in μatm. See also Figs. 5.6 and 5.7, and Fig. 5.4 for the locations of the grid boxes.

(mm/yyyy)	Box	pCO_2(MLR)	pCO_2(UW)	pCO_2(D)	$pCO2_2$(C)
05/2004	7	363			333
07/2004	7	417			393
06/2006	1	403			372
06/2006	3	415			363
06/2006	5	401			368
06/2006	7	406			367
09/2006	1	423		422	
09/2006	3	439		419	
09/2006	5	420		415	
10/2006	7	429		417	
02/2007	2	392		417	352
03/2007	2	354			264
04/2007	1	323	289	295	
04/2007	2	356	285		
04/2007	3	345	328	332	274
04/2007	4	349	305		
04/2007	5	307	298		301
04/2007	7	349	314	323	
07/2007	1	407			415
07/2007	2	392			387
07/2007	3	420			415
07/2007	5	409		332	401
07/2007	5	410		332	394
08/2007	1	414	420	426	
08/2007	2	433	430		
08/2007	4	439	430		
09/2007	1	421			406
10/2007	1	417	436	440	
10/2007	2	434	445		
10/2007	3	434	427	436	
10/2007	4	438	427		
10/2007	5	413	405	412	
10/2007	7	422	420	426	
04/2008	1	327	308	313	
04/2008	2	346	295		
04/2008	3	327	305	303	
04/2008	4	341	304	3	
04/2008	5	319	302	309	
04/2008	7	371	320	324	

the surface waters, which acts to increase pCO_2. In autumn and winter, the deepening of the mixed layer facilitates intrusion of CO_2-rich waters into the surface layer and damps the decrease of pCO_2 due to the cooling of surface waters. Overall, the surface waters of the Scotian Shelf act as a source of CO_2 to the atmosphere throughout most of the year (Fig. 5.8b). A reversal of this trend generally occurs only during, and immediately following, the spring phytoplankton bloom when the waters become undersaturated with respect to the atmosphere (Fig. 5.8b, c).

The overall direction and inter-annual variability of the annual CO_2 fluxes are preconditioned by temperature and wind speed in the winter and, less significantly, in the late summer and autumn. This occurs primarily through the control of the depth of the winter mixed-layer, and thus the availability of nutrients to fuel the spring bloom (*Greenan et al.*, 2008). A more detailed investigation of the years 2002, 2003 and 2005 serves to illustrate the governing mechanisms (see also Fig. 5.8). The winter of 2001/2002 had warmer minimum temperatures, and weaker winds than the 10-year average. This permitted an early onset of stratification with the initiation of the spring bloom beginning in March. Since mixing the previous winter was shallow, the bloom was inferred to be weak due to the reduced availability of nutrients from deeper waters. Following the weak bloom, strong late summer and autumn winds enhanced out-gassing in the second half of the year and yielded a large annual CO_2 flux to the atmosphere during 2002 (Fig. 5.8c). The winter of 2002/2003 had, in contrast, particularly cold minimum temperatures and strong winds resulting in a high degree of mixing; the 2003 spring bloom was therefore pre-conditioned with high nutrient concentrations which is reflected in the magnitude of the CO_2 uptake in March and April, and the reduction in annual CO_2 release to the atmosphere relative to the previous year. It is not only the winter conditions that control the expression of the spring bloom. For example, a comparably weak wind regime during spring 2005 permitted the bloom and the CO_2 undersaturation of the surface waters to persist from February through May. In addition, cold summer maximum temperature and weak autumn winds inhibited outgassing in the second half of the year, and resulted in weak CO_2 release during 2005 (Fig. 5.8).

5.5.5 Multi-Annual Variability of pCO_2

The 10-year hindcast of pCO_2 and air-sea CO_2 fluxes reveals multi-annual to decadal trends in addition to the interannual variability (Fig. 5.8c). The mean seasonal cycles of

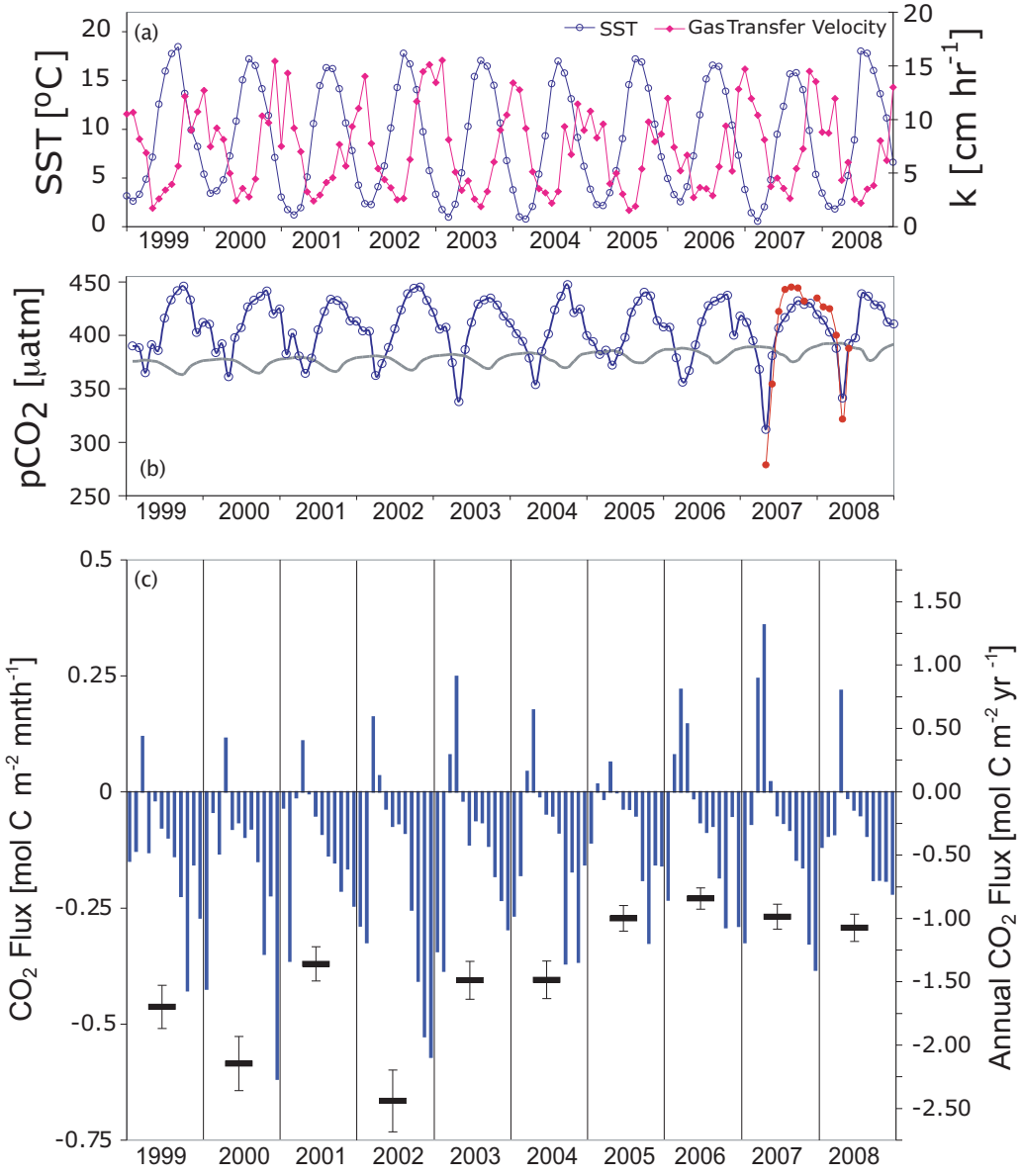

Figure 5.8: (a) SST (blue line open symbols) and gas transfer velocity (pink line, closed symbols) for the 10-year period. (b) Computed pCO_2(MLR) for grid box 1 (see Fig. 5.4) comprising the mooring station (thick blue line with symbols). The computed pCO_2(MLR) has a standard error of 13 μatm. The CARIOCA pCO_2 used in derivation of the MLR are plotted in red. The solid grey line gives the monthly atmospheric CO_2 concentration. (c) The monthly CO_2 fluxes (vertical lines, left hand side y-axis) and integrated annual CO_2 fluxes (horizontal lines, right hand side y-axis) with an estimated 20% error.

SST and pCO_2 were computed using the mean value for each month over the ten-year period (i.e. mean of all January values, mean of all February values, etc.). The SST and ΔpCO_2 anomalies were defined as the deviation from the mean seasonal cycle. The SST anomaly reveals a decrease of 0.13°C per year, or 1.3°C over the 10-year period of computation (Fig. 5.9). Simultaneously, the ΔpCO_2 ($\Delta pCO_2 = pCO_2^{Ocean} - pCO_2^{Atm}$), in which the anthropogenic atmospheric CO_2 increase has been explicitly included (Eq. 5.2), decreased by 2.3 μatm per year, or 23 μatm over the decade (Fig. 5.9). This decrease in the ΔpCO_2 anomaly can satisfactorily be explained by the observed temperature decrease. The thermodynamic temperature correction for pCO_2 results in a 4% change in pCO_2 for a 1°C change in temperature (*Takahashi et al.*, 2002). Applying this correction to the decadal mean pCO_2 (roughly 420 μatm), the observed decrease in temperature anomaly (0.13°C per year) would account for a decrease in ΔpCO_2 of 2.2 μatm per year, as revealed by the ΔpCO_2 anomaly. The negative, or near neutral, North Atlantic Oscillation (NAO) index over the past decade is associated with an increased transport of cold Labrador Current Water onto the Scotian Shelf, and thus with anomalously cold waters in the region (*Thompson and Wallace*, 2001; *Petrie*, 2007; *Thomas et al.*, 2008). The cooling of the water effectively shifts the position of the equilibrium ΔpCO_2 state, driving the system toward uptake. Conversely, warming of the water drives the system toward outgassing. Thus, while the interannual variability is controlled by local atmospheric forcing, the multi-annual to decadal changes appear to be controlled by larger scale hemispheric processes, in this case represented by the local expression of the NAO.

5.5.6 Shelf-Wide CO_2 Fluxes

The satellite-based extrapolation of the pCO_2 algorithm to include the wider Scotian Shelf region allows the spatial variability in the region to be assessed (Figs. 5.10 to 5.13). From 1999-2008 the shelf integrated fluxes vary substantially between -1.70 mol C m^{-2} yr^{-1} or (-380 Gmol C yr^{-1}, over the shelf area) and -0.01 mol C m^{-2} yr^{-1} or (-3.9 Gmol C yr^{-1}, over the shelf area, see also Fig. 5.13 and Table 5.4). A gradient exists between the northern Cabot Strait, and the southwestern region in the Gulf of Maine. The Cabot Strait region has consistently weaker annual CO_2 release, and even acts in some years as a sink for CO_2. The Cabot Strait region (grid boxes 5 and 6) exhibited the coldest (below freezing) winter temperatures due to the outflow of water from the seasonally ice-coved Gulf St. Lawrence (Fig. 5.11). The highest values of Chl_{SAT} were also observed in

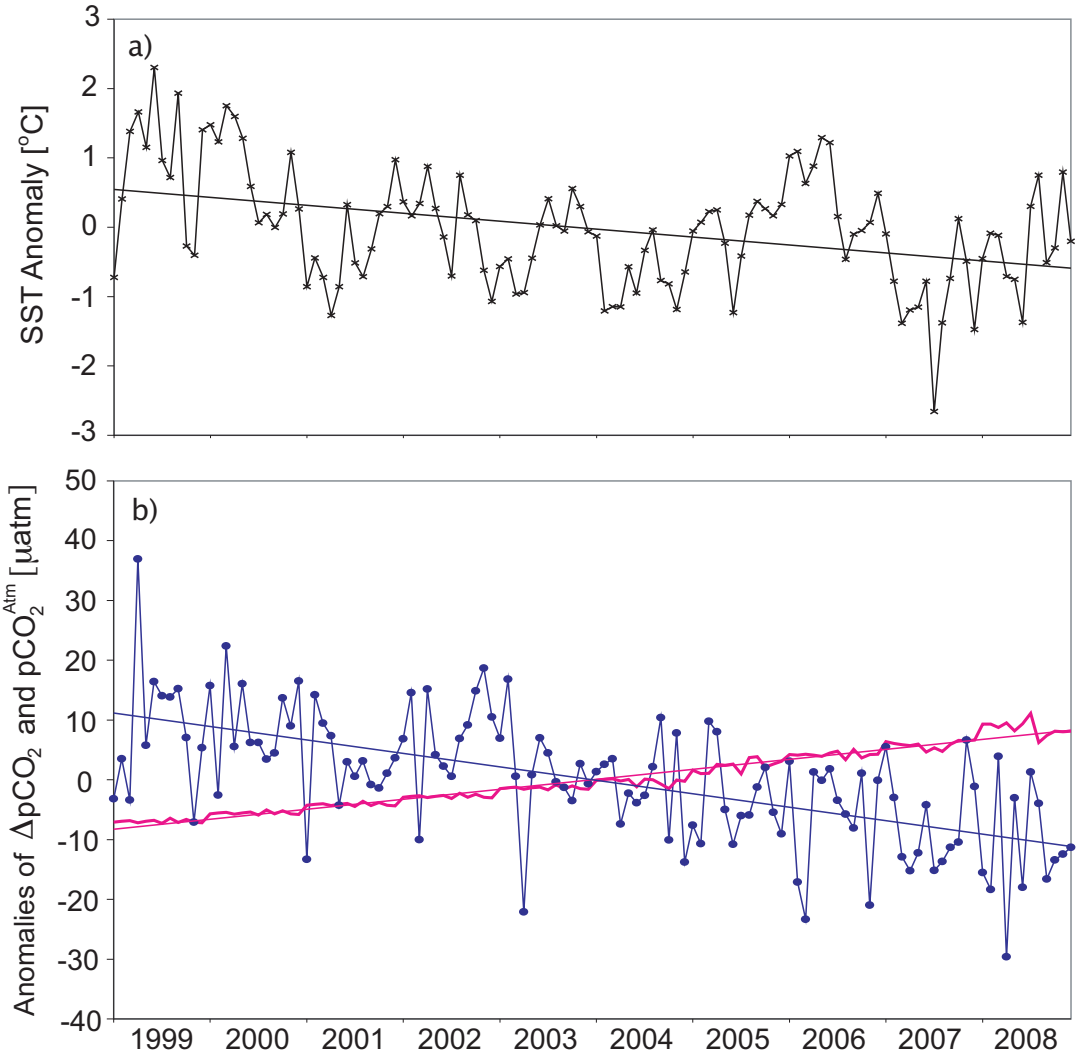

Figure 5.9: Anomalies of (a) SST, and (b) ΔpCO_2 (blue circles) and atmospheric pCO_2 (pink solid line). The slope of SST linear regression line (solid black line) corresponds to a cooling of roughly 0.13°C year^{-1}. The slope of the atmospheric CO_2 anomaly (bold pink line) is roughly 1.7 μatm year^{-1}, in line with the annual increase due to anthropogenic emissions. The slope of the ΔpCO_2 anomaly (solid blue line) is 2.3 μatm year^{-1}, or 23 μatm over the decade.

grid boxes 5 and 6, resulting in the and strongest spring blooms and corresponding to the largest seasonal CO_2 uptake during the year (Figs. 5.5, 5.10 and 5.13). In contrast, the Gulf of Maine (grid box 7), under greater influence of the Gulf Stream, and less influence of the Labrador Current, is warmer (Fig. 5.11). In the Gulf of Maine region the spring bloom, and corresponding CO_2 uptake, is weaker (Fig. 5.13). Both the Cabot Strait and Gulf of Maine regions exhibit large post-bloom $\mathrm{Chl_{SAT}}$ (Fig. 5.5) relative to the central Scotian Shelf (grid boxes 1 to 4). The central Scotian Shelf region also exhibits the warmest summer temperatures, and the largest CO_2 outgassing in summer and autumn (Fig. 5.5). There is a north-south gradient in theannual mean pCO_2 (Fig. 5.12) with the lowest mean values observed in the Cabot Strait region increasing southward, with relatively higher annual mean pCO_2 in the Gulf of Maine. There is also a gradient between the offshore and coastal boxes, with lower pCO_2, colder temperatures, and higher $\mathrm{Chl_{SAT}}$ concentration in the near-shore boxes relative to the grid boxes further offshore (Figs. 5.10, 5.11, and 5.12). While particularly large CO_2 release is computed for 2000 and 2002 over the whole region (see also Fig. 5.8c), the general trend for the 10-year period is a weakening CO_2 release consistent with the decreasing trend in the ΔpCO_2 anomaly over the shelf (Fig. 5.9). The gradual change toward stronger CO_2 uptake on the Scotian shelf is in line with interpretations of the role of the NAO in controlling hydrographic patterns (*Schuster and Watson*, 2007; *Thomas et al.*, 2008; *Ullman et al.*, 2009). However, consistent with suggestions of a longer-term decline in the CO_2 sink in the North Atlantic Ocean as a whole (*Watson et al.*, 2009), we cannot presently exclude the possibility that long-term changes in North Atlantic circulation patterns would potentially cause similar trends due to a weakened northward, and strengthened southward, water transport (*Bryden et al.*, 2005).

This approach to understand the dynamics of the CO_2 system on the Scotian Shelf and a recent observation-based approach (Chapter 4) yield conflicting results to modelling studies of the same region (*Fennel et al.*, 2008; *Previdi et al.*, 2009). However, our observations produce results in agreement with a similar process study in the neighboring Gulf of Maine (*Vandemark et al.*, 2010). *Previdi et al.* (2009) have suggested that interannual variability in air-sea CO_2 flux on the eastern North American continental shelf is due in part to NAO forcing. They suggest that warming between (low NAO) 1985 and (high

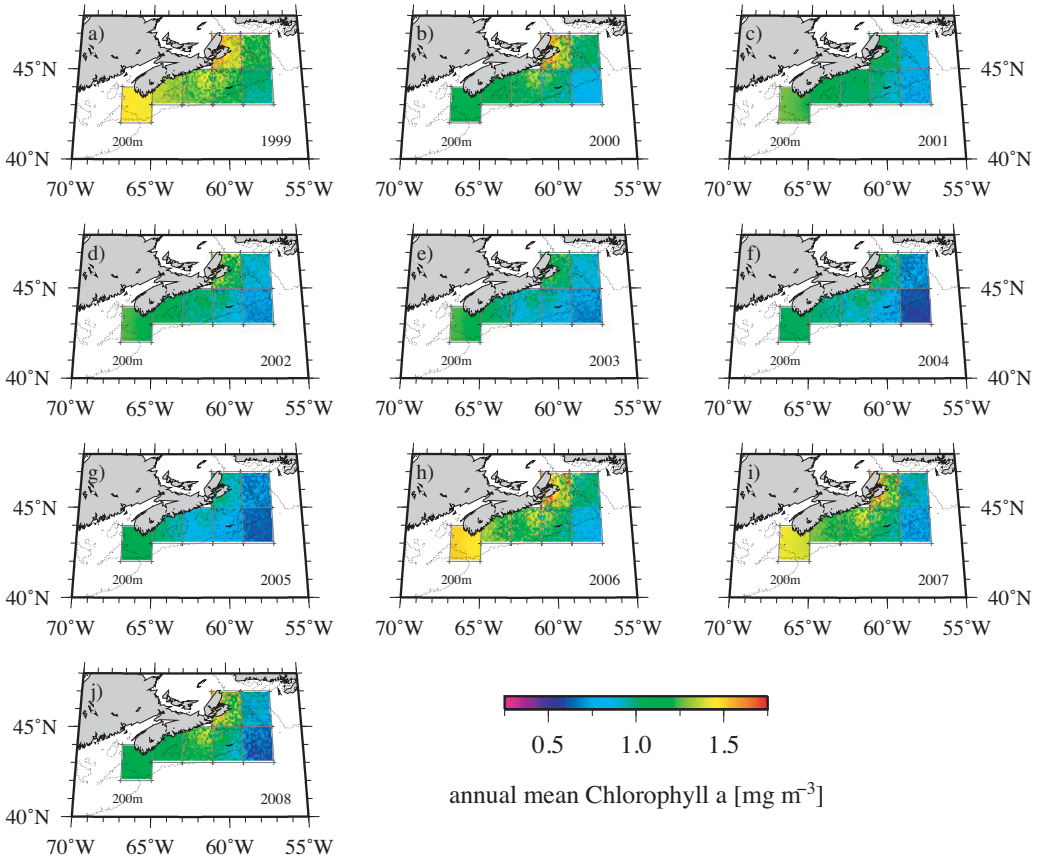

Figure 5.10: The annual mean $\mathrm{Chl}_{\mathrm{SAT}}$ from 1999 (top left) to 2008 (bottom left).

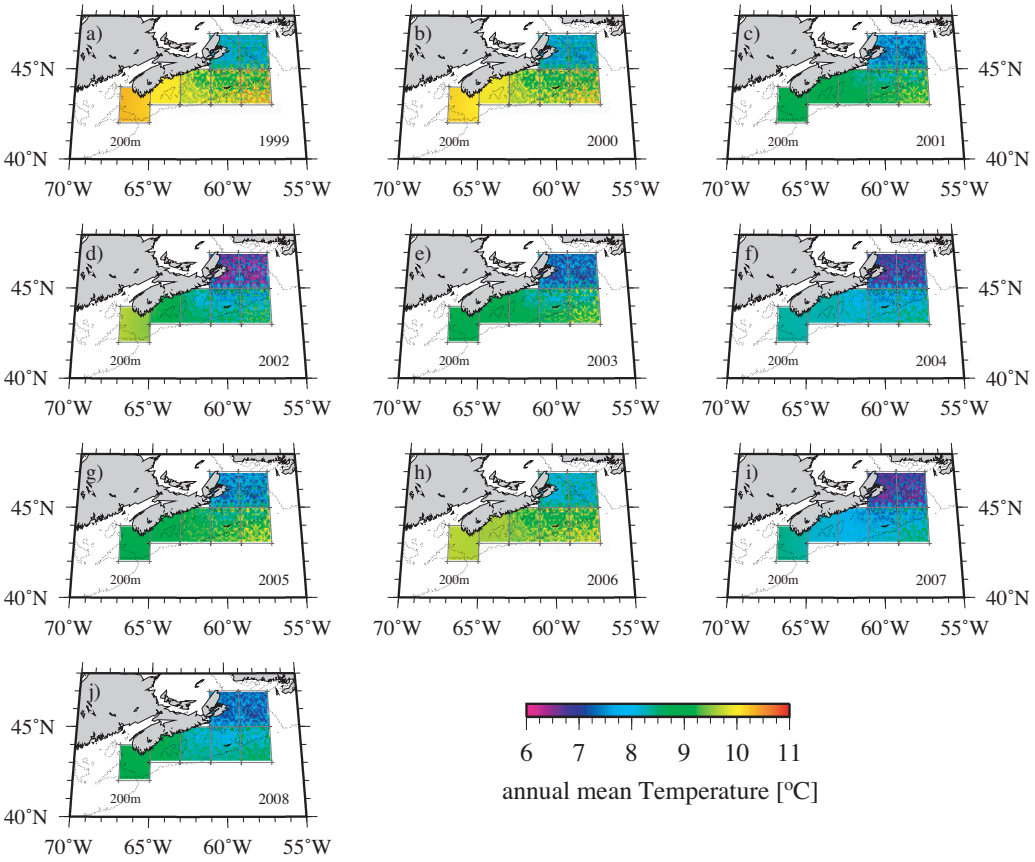

Figure 5.11: The annual mean SST from 1999 (top left) to 2008 (bottom left).

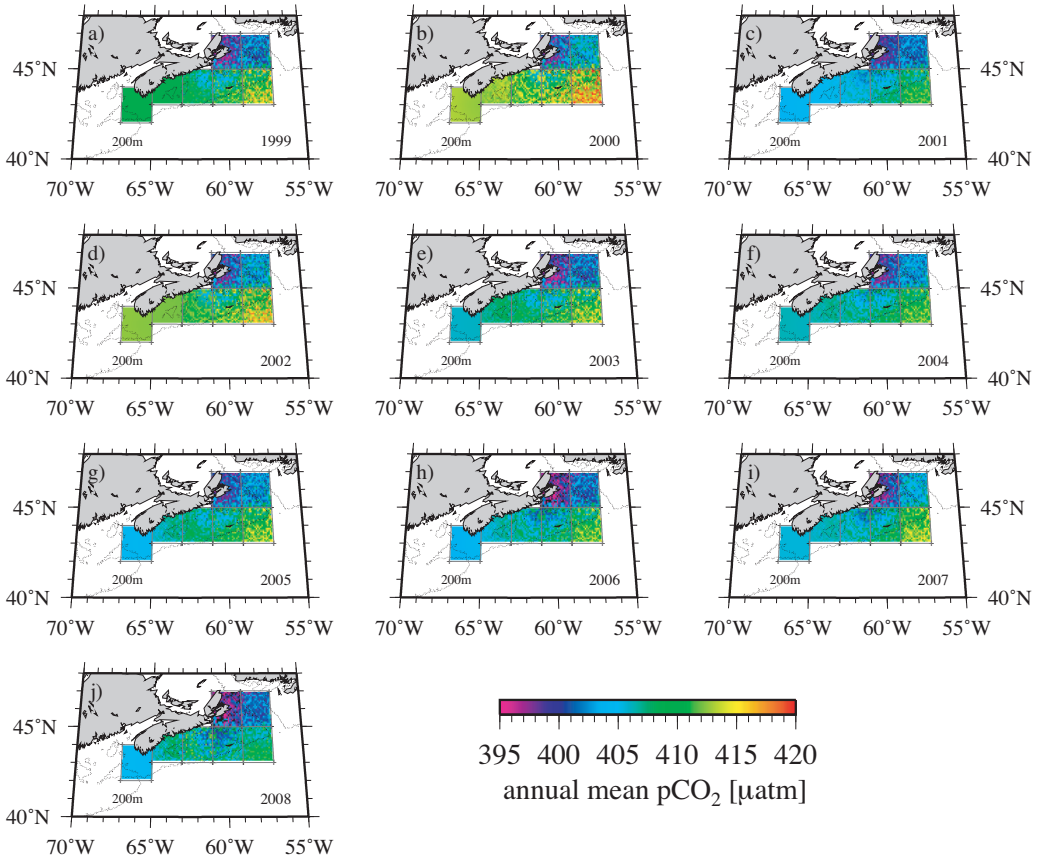

Figure 5.12: The annual mean pCO_2(MLR) from 1999 (top left) to 2008 (bottom left).

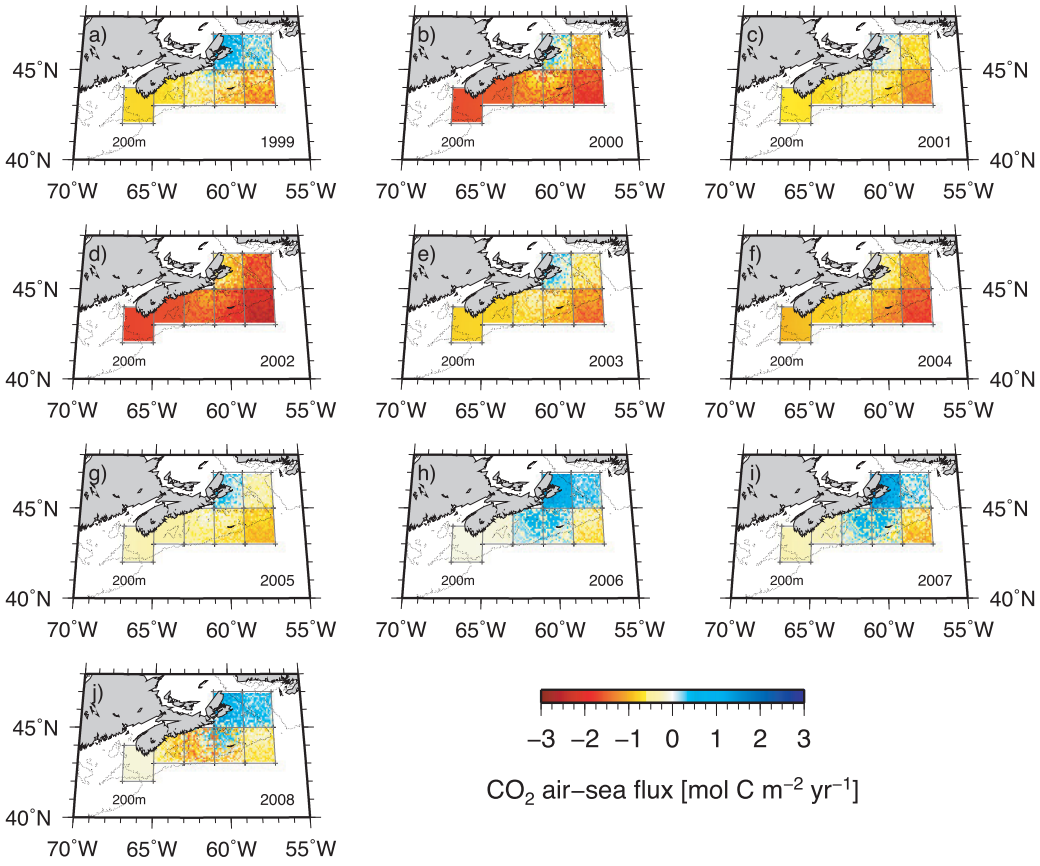

Figure 5.13: The investigation is extrapolated spatially to include the entire Scotian Shelf region (222,700 km^2). The integrated annual air-sea CO_2 fluxes from 1999 (top left) to 2008 (bottom left) are shown (see also Table 5.4). Negative values indicate CO_2 release to the atmosphere.

NAO) 1990 drove the system in the Gulf of Maine towards weaker uptake; this interpretation is agreement with our finding that the decadal cooling on the Scotian Shelf has driven the system towards stronger uptake. The reasons for the discrepancy betwen the observation- and model-based approaches is currently unknown and is beyond the scope of this study.

Table 5.4: The annual air-sea CO_2 fluxes from 1999 to 2008, both shelf-wide, and in Box 1 containing the CARIOCA mooring, in units of mol C m^{-2} yr^{-1}. Negative values indicate an outgassing of CO_2 to the atmosphere. The 7 gird boxes covering the Scotian Shelf region have an area of 222,700 km^2; Box 1 has an area of 31,800 km^2 (see also Fig. 5.13).

	1999	2000	2001	2002	2003	2004	2005	2006	2007	2008
Shelf-wide	-0.6	-1.3	-0.7	-1.7	-0.8	-1.1	-0.5	-0.02	-0.1	-0.1
Box 1	-1.75	-2.25	-1.4	-2.45	-1.5	-1.5	-1.0	-0.8	-0.95	-1.1

5.5.7 The Scotian Shelf in the Larger Global Context

Our findings indicate that the Scotian Shelf acts a source of CO_2, contrary to findings in many high-latitude continental shelf seas that act as net sinks for atmospheric CO_2 (*Thomas et al.*, 2004; *Chen and Borges*, 2009). The East China Sea, an example of a continental shelf sea in the western Pacific, is similar to the Scotian Shelf with respect to its location on the western side of the ocean basin under the influence of a warm northward flowing boundary current. Hydrography on the Scotian Shelf is additionally influenced by the southward flow of the cold Labrador Current; these waters warm significantly as they transit, increasing the pCO_2. The East China Sea has been well studied with respect to the inorganic carbon system (e.g. *Tsunogai et al.*, 1997; *Chen and Wang*, 1999; *Tsunogai et al.*, 1999; *Wang et al.*, 2000). The East China Sea absorbes roughly twice as much CO_2 as is emitted annually from the Scotian Shelf region. The outgassing of CO_2 on the Scotian Shelf is primarily due to the competing effects of temperature and biology in the system, along with the late-autumn and winter destratification of the water column. The spring bloom on the Scotian Shelf results in a significant but brief CO_2 drawdown, and occurs at the temperature minimum. The decay of this bloom, and resulting production of CO_2 through the remineralization of organic matter is coincident with surface warming,

which increases the pCO_2 to supersaturation with respect to the atmosphere. Continued biological production in the summer and early autumn is not sufficient to overcome this supersaturation. The water cools in late autumn, reducing pCO_2. Over the same period the water column becomes destratified maintaining the surface supersaturation until the following spring. The Scotian Shelf behaves similarly to an upwelling system, which are often biologically productive systems which release CO_2 to the atmosphere due to the delivery of DIC-rich waters from below (*Lendt et al.*, 2003; *Thomas et al.*, 2005b). By contrast, the North Sea, which acts a sink for atmospheric CO_2 of roughly the same magnitude as the Scotian Shelf source (*Thomas et al.*, 2005b), could be classified as a downwelling system (*Huthnance et al.*, 2009). It has been suggested that the downwelling circulation in the North Sea promotes the transport of dissolved inorganic carbon off the shelf to the deep ocean facilitating the uptake of atmospheric CO_2 in the subsequent productive season (*Huthnance et al.*, 2009).

The physical system on the Scotian Shelf may alternatively be thought of as estuarine; there is an inflow of deep, nutrient- and carbon-rich water and an outflow of nutrient-deplete surface waters. By contrast, Amundsen Gulf, in the southwestern region of the Canadian Arctic Archiplelago, which exports subsurface water to the Beaufort Sea (*Lanos*, 2009) may be thought of as an anti-estuarine system; there is an outflow (to the Beaufort Sea) of carbon- and nutrient-rich subsurface waters, and an inflow (from the Beaufort Sea) of nutrient-poor surface waters (see Chapter 7). The Amundsen Gulf system may also be considered downwelling system, like the North Sea, in which the transport of carbon-rich subsurface waters from the Gulf facilitates the uptake of atmospheric CO_2 in the subsequent productive season (Chapter 7). The two systems are shown schematically in Fig. 5.14. In both cases the DIC losses due to NCP are balanced over the annual cycle by inputs of DIC from below (see Chapters 4 and 7). As described above, in the case of the Scotian Shelf this carbon-rich water is brought to the surface in the autumn and winter by a combination of wind, upwelling and convective mixing. In Amundsen Gulf the water column is strongly stratified throughout the year, and nutrients and inorganic carbon are brought to the surface either in the brief ice-free period in autumn when storms increase and the region is subject to wind mixing, or by diffusive mixing throughout the year. In general, vertical input DIC and nutrient rich waters are inhibited by the downwelling, or anti-estuaring circulation. Furthermore, sea-ice cover in winter prevents

the convective mixing seen on the Scotian Shelf as a result of heat lost from the surface ocean to the atmosphere. During the majority of the open water season in Amundsen Gulf the surface waters, and air-temperatures, are relatively warm. The remainder of the DIC lost to biological production NCP in Amundsen Gulf is resupplied by the uptake of atmospheric CO_2 during the open water season (Fig. 5.14, see also Chapter 7). Under this upwelling (estuarine) or downwelling (anti-estuarine) characterization, the source or sink status with respect to atmospheric CO_2 of both the Scotian Shelf and Amundsen Gulf systems are in line with the synthesis of *Chen and Borges* (2009) and the most recent climatology of *Takahashi et al.* (2009).

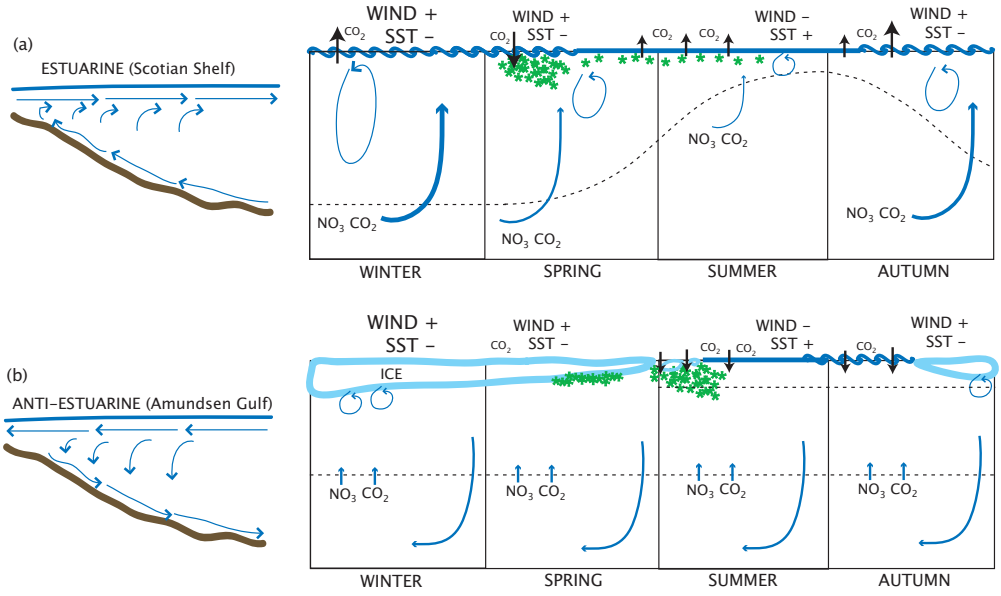

Figure 5.14: A schematic representation of the systems in (a) the Scotian Shelf and (b) Amundsen Gulf. The Scotian Shelf may be thought of as an estuarine system; there is an outflow of surface water, and an inflow subsurface waters delivered to the surface by a combination of wind mixing, upwelling and convection (blue arrows). The mixed-layer depth is represented by the dashed line. In contrast, Amundsen Gulf may be thought of as an anti-estuarine, or downwelling, system, with an inflow of surface waters and a outflow of subsurface water. Wind and convective mixing are inhibited by ice-cover in winter and nutrient-rich waters are delivered to the surface layer only by diffusive processes. Density driven mixing by the release of brine during sea-ice formation makes a contribution in the autumn and winter (blue arrows). The mixed-layer depth is roughly 50 meters (dashed line) throughout the year; strong surface stratification in the upper 10-20 meters is observed following sea-ice melt.

5.6 Conclusion

High frequency in-situ time-series observations deepen our understanding of individual regional characteristics of the CO_2 system particularly in coastal regions, where temporal and spatial variability is high. This allows reliable relationships between pCO_2 and remotely sensed variables to be established and understood. Coupled to such in-situ observations, the application of satellite data has the potential to improve the understanding and assessment of air-sea CO_2 fluxes in the coastal ocean, which, as shown here, can vary by two orders of magnitude at interannual to decadal times scales.

5.7 Acknowledgements

We thank R. Davis for his assistance with the CARIOCA data processing, K. Thompson and J. Cullen for assistance with the statistical analysis and in-depth comments on the manuscript, and D. Worthy at Environment Canada for providing the atmospheric CO_2 data. We are grateful to J. Barthelotte, M. Scotney, and B. Greenan for the deployment and recovery of the CARIOCA buoy, and to J. Spry and the Bedford Institute of Oceanography for making the archived data from station HL2 accessible. We wish to thank Nick Bates and three anonymous reviewers for their constructive comments that have improved the manuscript. This work was supported by the National Science and Engineering Research Council of Canada, the Canadian Foundation for Climate and Atmospheric Sciences, the National Science Foundation, NASA, and by MetOcean Data Systems. This work contributes to IGPB/IHDP-LOICZ.

5.8 Appendix A: Interpretation of the SST Regression Coefficient

A detailed analysis of the time series, paying particular attention to the relationship between pCO_2 and SST, in the frequency domain facilitates an understanding of the deviation of the temperature coefficient (4.6 μatm $(°C)^{-1}$) in the regression (Eq. 1) from the expected thermodynamic value. Using a frequency analysis, we decomposed the temperature coefficient into genuine thermodynamic temperature effects, and effects with timing correlated to temperature, which are also encompassed by the SST coefficient.

We computed the cross-spectrum of pCO_2 and SST in order to examine the strength of the relationship between these two parameters over a range of frequencies; the gain in pCO_2 due to SST is plotted in Fig. 5.15a (in blue). The dominant energies in the pCO_2-temperature relationship are found at frequencies, f, $\leq$0.04 hr^{-1}, and corresponding to periods of P$\geq$24-hours. At the daily frequency, f=0.04 hr^{-1}, (highlighted by pale blue vertical bar in Fig. 5.15a), the gain has a value of approximately 16 μatm $(°C)^{-1}$, which is what the thermodynamic relationship between pCO_2 and temperature predicts (a 4% change in pCO_2 for a 1°C change in temperature (*Takahashi et al.*, 2002), with a mean annual pCO_2 of roughly 400 μatm). Mechanistically, this is caused by the fact that the seasonal variability of temperature on the Scotian Shelf is primarily driven by surface heat fluxes (*Umoh and Thompson*, 1994), reflected here by the dominance of SST controlling the daily variability in pCO_2. At frequencies less than f=0.04 hr^{-1}, or for periods longer than 24-hours, the temperature related gain in pCO_2 tends away from the thermodynamic value, towards the lower value (4.6 μatm $(°C)^{-1}$) obtained in the regression presented here (Eq. 1).

To evaluate the effects correlated with temperature outside of the diurnal cycle, the daily, or 24-hour, cycle was removed from the SST time series. This was done by computing the mean temperature over a given, discrete 24-hour period, starting at midnight, and subtracting this value from each hourly value of SST over the same period:

$$\mathrm{SST}_{(\mathrm{in-situ})} - \mathrm{SST}_{(\mathrm{dailymean})} = \Delta\mathrm{SST}^{*} \tag{5.7}$$

This daily cycle in SST was subsequently removed from the pCO_2 time series via the following equation:

$$\mathrm{pCO}_2^{*} = \mathrm{pCO}_2 - (\mathrm{pCO}_2[\exp(0.0423\Delta\mathrm{SST}^{*})]) \tag{5.8}$$

where the second term on right-hand side of the equation is the temperature correction of *Takahashi et al.* (2002), and the superscript '*' indicates the time series with the 24-hour cycle removed.

The gain in pCO_2* due to SST* is shown in Fig. 5.15a (red dashed line). The energy of the daily frequency has vanished to a large degree (f=0.04 hr^{-1}, highlighted by the pale blue vertical bars in Fig. 5.15), and the temperature correlated pCO_2* gain at f=0.02 hr^{-1}, which correspond to periods shorter than 50 hours, (highlighted by the pink vertical bars in Fig. 5.15), lies between 4 and 6 μatm $(°C)^{-1}$ which is consistent with the SST coefficient obtained in the regression (Eq. 5.2). The dominant gain in the temperature corrected pCO_2 data however is now observed at a frequency of f=0.007 hr^{-1}, (highlighted by the green vertical bars in Fig. 5.15), corresponding to periods from several days to a month. The gain at this frequency is 13 μatm $(°C)^{-1}$, with a phase lag of roughly 180 degrees (highlighted by the green vertical bars in Fig. 5.15b), or -13 μatm $(°C)^{-1}$, and can be attributed to biological CO_2 uptake, with seasonal cycle strongly anti-correlated to that of temperature. This anti-correlation has been confirmed (Chapter 4), by employing an alternate 1-D modelling approach. Furthermore, a linear regression of the temperature corrected pCO_2 data with in-situ temperature, (as shown in Fig. 4.12), yields a coefficient of -13 μatm $(°C)^{-1}$, as described above. For frequencies shorter than f=0.007 hr^{-1}, (periods longer than 6 days), the gain in pCO_2 due to SST in the in-situ data (Fig. 5.15, blue line) approaches the value of 4.6 μatm $(°C)^{-1}$ obtained with the regression.

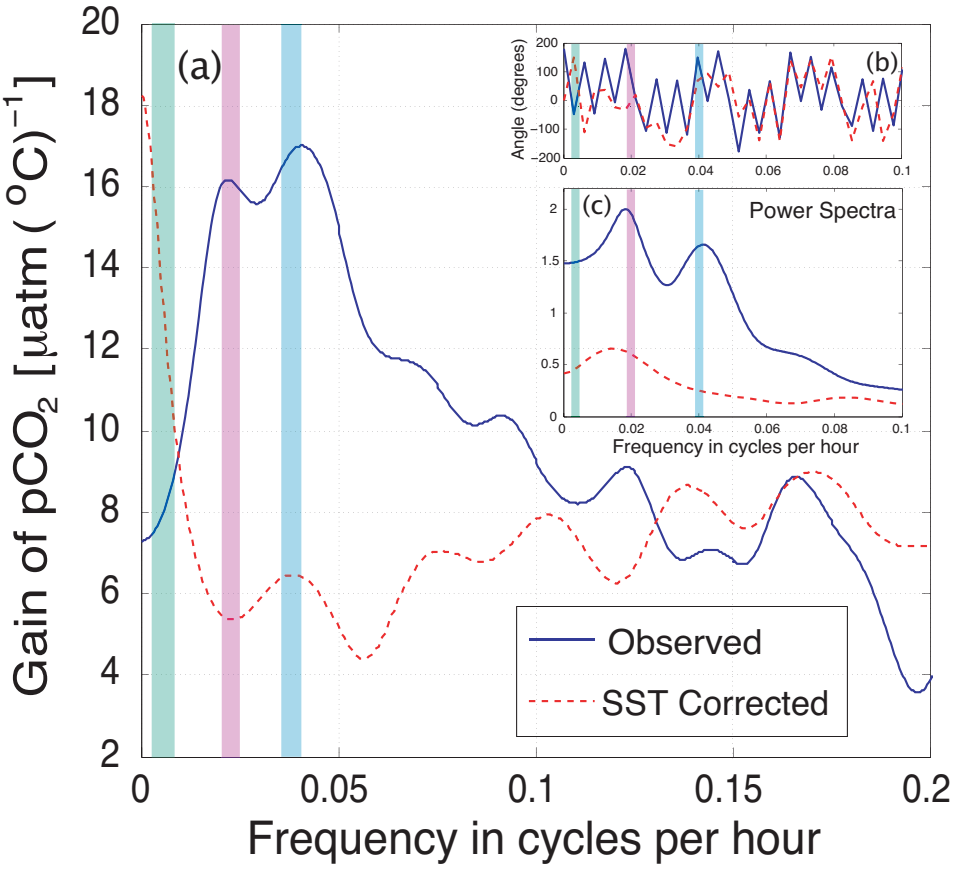

Figure 5.15: (a) The gain of pCO_2 due to SST using the in-situ hourly data (blue), and the gain of pCO_2* due to SST* (red dashed). Frequencies of f=0.04 hr^{-1}, or 24-hours (blue bar), f = 0.02 hr^{-1} or roughly 40 hours (pink bar), and f=0.007 hr^{-1} or 6 days (green bar) are indicated. (b) The phase spectra for the in-situ pCO_2 (blue line) and pCO_2* (red dashed line) series. (c) The power spectra for the in-situ pCO_2 (blue) and pCO_2* series (red dashed). The in-situ data is dominated by the 24-hour cycle of SST, while the pCO_2* series is dominated over longer time scales

5.9 Appendix B: Sable Island Winds Versus Model Winds

To test the assumption that winds measured at one location, on Sable Island (within grid box 3, see Fig. 5.1), are valid over the larger shelf scale, a comparison with modelled winds (NCEP/NCAR reanalysis product, see *Large and Yeager* (2004) for details) was made (Fig. 5.16). It has previously been suggested that wind measured at Sable Island is representative of the winds over the Scotian Shelf (*Petrie and Smith*, 1977). The modelled winds for grid boxes 1 through 4 indicate that while the magnitude of the wind speed changes from one location to another, primarily increasing with distance offshore, but that the trends (increase/decrease) and timing are consistent between locations. On the other hand, a comparison between modelled and observed winds (Fig. 5.16, bold lines) at the same location (box 1) indicates that the model consistently, and significantly, underestimates the wind as measured at Sable Island, particularly in the winter and early spring. The air-sea CO_2 fluxes for grid box 1 were recomputed using the modelled winds and are compared to the fluxes computed using Sable Island winds (Fig. 5.17). It can be seen that there is a large discrepancy between the two flux extimates, both with respect to the winter outgassing, and the spring uptake. The spring bloom occurs at the temperature minimum on the Scotian Shelf under essentially winter conditions. The flux of atmospheric CO_2 into the ocean is driven partly by the air-sea gradient of CO_2 (ΔpCO_2, see Eq. 5.1) but also by the magnitude of the gas transfer velocity, parameterized as a function of wind speed (*Wanninkhof*, 1992). Thus, if the modelled winds underestimate (or overestimate) the winter and early spring winds, the annual CO_2 uptake/release will not correctly be computed. A comparison between the annual fluxes computed with the measured and modelled winds (Fig. 5.17, horizontal bars) a considerably weaker net release of CO_2 to the atmosphere using the modelled winds, primarily due to the weaker winter winds (Fig. 5.16).

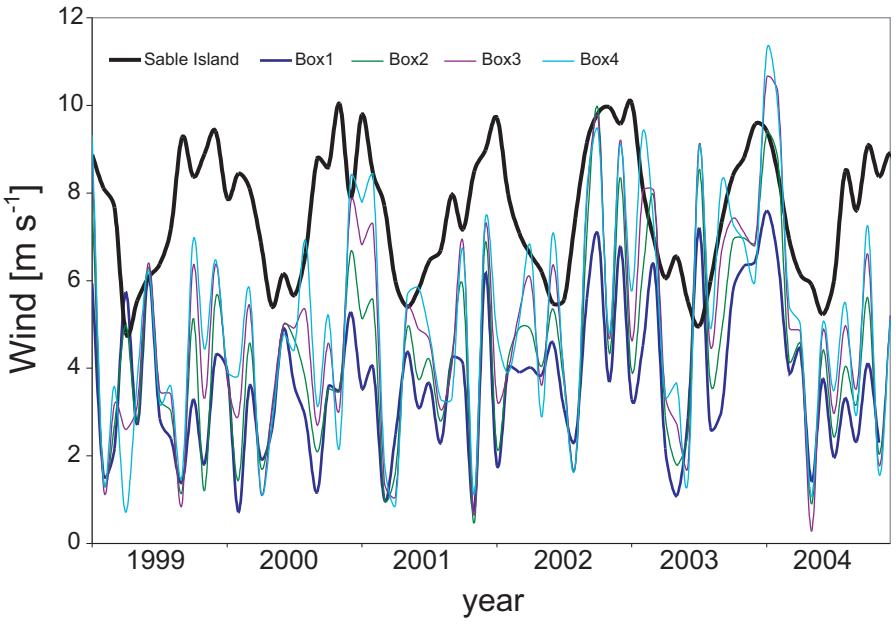

Figure 5.16: A comparison of observed winds at Sable Island (bold black), and modelled winds in grid boxes 1 to 4. Sable Island is located in grid box 1 (heavy blue line).

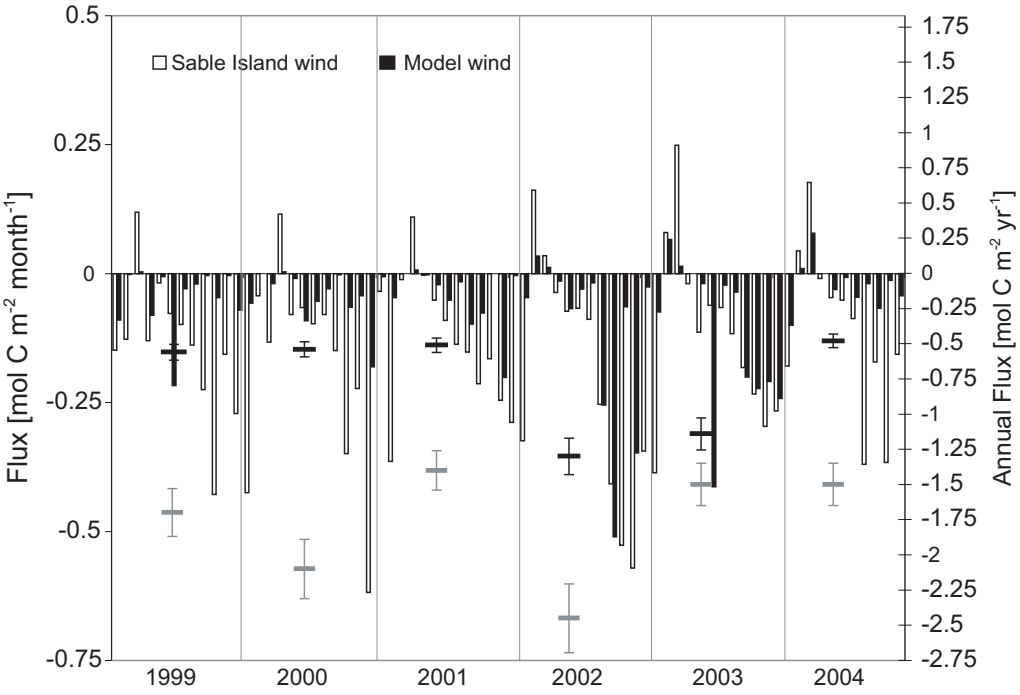

Figure 5.17: A comparison of monthly air-sea CO_2 flux (left hand y-axis) computed with winds measured at Sable Island (white vertical bars) and with modelled winds (black vertical bars). The annual fluxes (right hand y-axis) using Sable Island winds (horizontal gray bars) and modelled winds (horizontal black bars) are also shown.

CHAPTER 6

INORGANIC CARBON IN THE ARCTIC ARCHIPELAGO

6.1 Abstract

During an east-to-west transect through the Canadian Arctic Archipelago, dissolved inorganic carbon (DIC) and total alkalinity (TA) were measured. The composition of the waters throughout the Archipelago were computed using TA and $\delta^{18}O$ data, and the carbon characteristics of these waters is examined. The influence of the Mackenzie River was primarily limited to the upper water column in the western Archipelago while the fraction of sea-ice melt water in the surface waters increased eastward with maximum values at the outflows of Jones and Lancaster Sounds. The depth of penetration of Pacific-origin upper halocline waters increases eastward through the Archipelago. In the western Archipelago, non-conservative variations in deep water DIC were used to compute a subsurface carbon surplus, which appears to be fueled by organic matter produced in the surface layer and by benthic respiration. The eastward transport of carbon from the Pacific, via the Arctic Archipelago, to the North Atlantic was estimated. The impact of increased export of sea-ice melt water to the North Atlantic is also discussed[1].

[1]This chapter comprises a manuscript by E. H. Shadwick, H. Thomas, D. Leong, S. A. Moore, T. Papakyriakou and A. E. F. Prowe entitled *Export of Pacific Carbon through the Arctic Archipelago to the North Atlantic* under revision in Continental Shelf Research

6.2 Introduction

In recent years much research has been devoted to understanding the ocean carbon cycle because of its prominent role in controlling global climate. Roughly half of the carbon dioxide (CO_2) released to the atmosphere from the burning of fossil fuels and other anthropogenic activities has been absorbed by the oceans (*Sabine et al.*, 2004). More than 98% of the carbon in the atmosphere-ocean system is in the ocean; small changes in the ocean carbon cycle can therefore greatly influence atmospheric CO_2 concentrations (*Zeebe and Wolf-Gladrow*, 2001). Much attention has been given to the oceans' ability to take up anthropogenic carbon dioxide, and regions of deep water formation are of particular importance for this process. Seasonally ice-covered waters are sites of exceptionally high heat exchange, and may potentially transfer carbon dioxide into the deep ocean with greater efficiency than their lower latitude counterparts (*Smith and Gordon*, 1997; *Miller et al.*, 2002). The Arctic Ocean, and its carbon cycle in particular have been the subject of much recent study (e.g. *Yager et al.*, 1995; *Anderson et al.*, 1998a,b; *Fransson et al.*, 2001; *Miller et al.*, 2002; *Bates et al.*, 2005; *Kaltin and Anderson*, 2005; *Mathis et al.*, 2005, 2007; *Semiletov et al.*, 2007; *Bates and Mathis*, 2009; *Chierici and Fransson*, 2009; *Mathis et al.*, 2009; *Yamamoto-Kawai et al.*, 2009; *Mucci et al.*, 2010). The high-latitude oceans are ecologically sensitive areas where the impacts of climatic changes may first be detected. Polar oceans are also chemically sensitive due to the relatively high Revelle factor and correspondingly weaker buffer capacity of these waters (*Orr et al.*, 2005; *Thomas et al.*, 2007; *Chierici and Fransson*, 2009; *Fabry et al.*, 2009). The buffer capacity of seawater, described by the Revelle factor, determines its capacity to absorb CO_2 (*Takahashi et al.*, 1993; *Sabine et al.*, 2004). The Revelle factor quantifies the change in the seawater CO_2 partial pressure (pCO_2) for a given change in dissolved inorganic carbon (DIC), and is proportional to the ratio of DIC to total alkalinity (TA) (*Revelle and Suess*, 1957). Waters with low Revelle factor (e.g. 8-10) have a large potential capacity to absorb anthropogenic CO_2 and vice-versa (*Sabine et al.*, 2004). Warm tropical and subtropical waters have relatively low Revelle factor and therefore a large potential for the uptake of anthropogenic CO_2, despite the lowered CO_2 solubility at high temperature. High latitude and polar oceans by contrast have relatively higher Revelle factors and a smaller potential capacity for the uptake of anthropogenic CO_2 (*Sabine et al.*, 2004; *Orr et al.*, 2005).

A greater understanding of the linkage between the export of freshwater from the Arctic Ocean to the North Atlantic and the dominant regional climate modes has emerged in recent years (*Anderson et al.*, 2004; *Peterson et al.*, 2006; *Greene and Pershing*, 2007). A positive North Atlantic Oscillation (NAO) enhances and diverts the prevailing westerly winds, causing an eastward shift of the Eurasian river discharge and greater precipitation over Northern Europe (*Thompson and Wallace*, 2001). This eastward diversion of Eurasian runoff has been linked to a freshening of the Canada Basin (*Macdonald et al.*, 2002). The Arctic Oscillation (AO) has also been linked to changes in circulation and associated distribution of freshwater in the Arctic Ocean (*McLaughlin et al.*, 1996; *Morison et al.*, 1998). Changes in freshwater export from the Arctic Ocean are thought to have consequences for North Atlantic Deep Water formation (*Rahmstorf*, 2002). It has been suggested that the decline in CO_2 uptake in the subpolar and temperate North Atlantic Ocean in the last decade is linked to the low or neutral NAO over the same period (*Thomas et al.*, 2008). The export of DIC-rich Pacific-origin water from the Arctic Ocean may have implications for the uptake of atmospheric CO_2 in the North Atlantic, particularly in the northwestern region (*Thomas et al.*, 2008). An understanding of the distribution and cycling of DIC in the waters of the Canadian Arctic Archipelago, which funnels roughly one third of the volume outflow from the Arctic Ocean (*Coachman and Aagaard*, 1974), is therefore of great importance to understanding carbon cycling in the Arctic Ocean as a whole.

We present DIC and TA measurements from west of Banks Island in the southeastern Beaufort Sea, eastward through the Archipelago to Jones and Lancaster Sounds (Fig. 6.1). These data were collected on an ArcticNet cruise on board the Canadian Coast Guard Ship Amundsen. Inorganic carbon data were complemented by measurements of the seawater oxygen isotope ratio (δ^{18}O) and hydrographic variables. The relative contributions of (1) meteoric water, (2) sea-ice melt (3) Pacific-origin upper halocline water, and (4,5) two sources of Atlantic water: from the Arctic interior, and from Baffin Bay via Nares Strait and the West Greenland current, were computed. The corresponding eastward transport of carbon through the Archipelago to Baffin Bay is estimated. The impact of increasing the fraction of sea-ice melt water exported from the Archipelago, with respect to aragonite saturation state and pH is discussed. Non-conservative variations in deep-water DIC at stations located in the southwestern Archipelgo are used compute a carbon surplus, or

respiration inventory, in this region.

6.3 Oceanographic Setting

The Arctic Ocean is the most land-dominated of the ocean basins, almost entirely enclosed by the wide Siberian Shelf and the numerous islands of the Canadian Arctic Archipelago. Atlantic waters enter the Arctic Ocean through Fram Strait and the Barents Sea. These waters flow cyclonically around the Arctic Basin, exiting via Fram Strait, Nares Strait, and the many channels of the Canadian Arctic Archipelago (*Rudels et al.*, 1994, 1996). Pacific water enters the Arctic Ocean through the relatively narrow and shallow Bering Strait (*Coachman and Aagaard*, 1988). In the Beaufort Sea, circulation is dominated by the Beaufort Gyre, a wind-driven circulation caused by a mean anticyclonic high pressure dome in the atmosphere (*Carmack and MacDonald*, 2002). This feature maintains the high concentrations of sea-ice in the central Arctic Ocean (*Macdonald et al.*, 1999). The surface circulation in the Beaufort Sea is dominated by the anticyclonic Beaufort Gyre. The flow of subsurface waters is reversed, dominated by the cyclonic Beaufort Undercurrent (*Carmack and MacDonald*, 2002). This undercurrent forces waters of both Pacific and Atlantic origin to the east along the continental margin, providing (offshore) nutrients to the Arctic shelves (*Macdonald et al.*, 1987; *McLaughlin et al.*, 2004).

The Arctic Ocean plays an important role in the global freshwater cycle, receiving disproportionately large inputs of riverine dissolved inorganic and organic material (*Dittmar and Kattner*, 2003). Both Siberian and North American rivers contribute freshwater inputs to the Arctic Ocean. In winter, the Arctic Ocean is sea-ice covered, except in polynyas and flaw leads, whith multi-year ice in the central Arctic Ocean and thinner seasonal ice-cover on the shelves. The seasonal production and melting of sea-ice makes a significant contribution to the mixing of water masses in the Arctic Ocean (*Carmack and Chapman*, 2003). Sea-ice melt and brine rejection during sea-ice formation modify the physical and chemical properties of the surface and halocline layers (*Steele and Boyd*, 1998; *Carmack and Chapman*, 2003).

The Arctic Ocean and adjacent polar continental seas play an important role in the biogeochemical cycling of carbon and nutrients. There are large reservoirs of terrestrial and oceanic carbon in the Arctic region (*Dittmar and Kattner*, 2003; *Hansell et al.*, 2004;

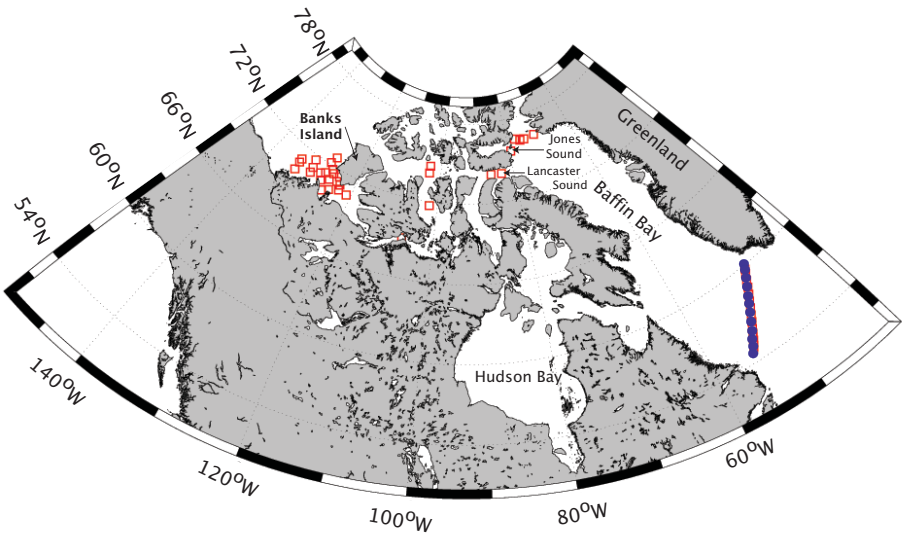

Figure 6.1: Locations of stations sampled for dissolved inorganic carbon (DIC) and hydrographic data. Open squares indicate stations occupied in 2007, closed circles indicate stations from which an older data set from the Labrador Sea was used (*Jones*, 1998).

Mathis et al., 2007), and many uncertainties in the response of these stocks to projected climate shifts. The freshwater fluxes, on a volume basis, of dissolved organic and dissolved inorganic carbon to the Arctic Ocean are disproportionately large compared to other basins, and more susceptible to climate change (*Dittmar and Kattner*, 2003). The Arctic shelf seas host high rates of primary production during the brief photosynthetic season (*Carmack et al.*, 2004; *Arrigo et al.*, 2008; *Mathis et al.*, 2009). Sea-ice cover controls the availability of light, and limits the development of water column stratification. Despite available nutrients in spring, the light environment may inhibit the growth of phytoplankton until surface stratification, due to solar heating, or sea-ice melt, is achieved in summer (*Arrigo et al.*, 2008; *Tremblay et al.*, 2008). The Arctic Ocean continental shelves have been classified as 'inflow', 'interior' and 'outflow' (*Carmack and Wassmann*, 2006). The Barents and Chukchi Seas can be characterized as inflow shelves, importing nutrient-rich (and carbon-rich) water from the Pacific and Atlantic Oceans to sustain the relatively high seasonal production in these regions (*Cota et al.*, 1996; *Carmack and Wassmann*, 2006; *Bates et al.*, 2009). The East Siberian and Beaufort Sea shelves are characterized as interior shelves which are under the influence of other adjacent shelf environments. The Canadian Arctic Archipelago constitutes an outflow shelf through which water from the Arctic Ocean is exported to the North Atlantic via Baffin Bay.

There have been relatively few studies of the Canadian Arctic Archipelago with respect to the carbonate system (*Bates and Mathis*, 2009; *Macdonald et al.*, 2009). In this region, as in other Arctic shelf regions, the inorganic carbon cycle is influenced by both physical and biological processes (*Anderson et al.*, 1998a; *Bates et al.*, 2005; *Bates and Mathis*, 2009). Exchange of CO_2 with the atmosphere takes place during seasonal sea-ice retreat. Vertical and horizontal mixing of water masses and the addition of freshwater from runoff and sea-ice melt play an important role (*Carmack et al.*, 2004; *Chierici and Fransson*, 2009). In the open water season, inorganic carbon is taken up by phytoplankton and organic matter subsequently exported from the surface to the subsurface (*Bates et al.*, 2005; *Mathis et al.*, 2007). These processes will be explored in more detail in the following sections.

6.4 Data and Methods

6.4.1 Sample Collection and Analysis

Samples were collected at 31 stations throughout the Canadian Archipelago from Baffin Bay westward to Banks Island (Fig. 6.1) during September and October, 2007. Approximately 500 samples were collected from the surface to depths of roughly 600 m, with higher vertical resolution within the euphotic zone (0 to 50 m), at all stations (Fig. 1). Dissolved inorganic carbon (DIC) and total alkalinity (TA) samples were collected from 20-L Niskin bottles mounted on a General Oceanic 24-bottle rosette fitted with a SeaBird CTD such that all chemical data are associated with high precision in-situ temperature, salinity and oxygen data. Following water collection, DIC and TA samples were poisoned with a solution of $HgCl_2$ to halt biological activity and stored in the dark at $4°C$ to await analysis. All DIC and TA samples were analyzed on board by coulometric, and potentiometric titration, respectively, using a VINDTA 3C (Versatile Instrument for the Determination of Titration Alkalinity, by Marianda). Analytical methods for determination of DIC and TA have been fully described elsewhere (*Johnson et al.*, 1993; *Fransson et al.*, 2001; *Bates et al.*, 2005). Routine analyses of Certified Reference Materials (provided by A. G. Dickson, Scripps Institution of Oceanography) ensured that the uncertainty of the DIC and TA measurements was less than 2 and 3 μmol kg^{-1}, respectively. Following the determination of DIC and TA, we computed pH (on the total scale) and aragonite

saturation (Ω_{Ar}) using the standard set of carbonate system equations, excluding nutrients, with the CO_2Sys program of *Lewis and Wallace* (1998). We used the equilibrium constants of *Mehrbach et al.* (1973) refit by *Dickson and Millero* (1987). The calcium (Ca^{2+}) concentration was assumed to be conservative and calculated from salinity. For a complete description of the carbonate system in seawater see, for example, *Zeebe and Wolf-Gladrow* (2001), and for the Arctic in particular, *Bates and Mathis* (2009) or *Chierici and Fransson* (2009).

6.4.2 Water Mass Definitions

Previous studies have reported various classifications and names for the portions of the Arctic Ocean water column (*Anderson et al.*, 1994; *Jones et al.*, 1998; *Ekwurzel et al.*, 2001). The water masses of the Arctic ocean can be simplistically classified based on their salinities (*Aagaard et al.*, 1981; *Aagaard and Carmack*, 1994; *Mathis et al.*, 2005). The polar mixed layer (PML) is defined by salinity $29.5 < \mathrm{S} < 31$ (following the range of salinity values for the Canada Basin reported by *Yamamoto-Kawai and Tanaka*, 2005). The PML is a mixture of meteoric water (MW), sea-ice melt (SIM) and Pacific-origin upper halocline water. A fourth water mass of Atlantic origin (ATL, S>34.8) is also present.

In general, knowing the seawater oxygen isotope (δ^{18}O) and TA of all water masses in a three end-member system and assuming conservative behaviour, one can compute their relative fractions in a seawater sample with known δ^{18}O and TA (e.g. *Fransson et al.*, 2001; *Anderson et al.*, 2004; *Yamamoto-Kawai and Tanaka*, 2005). The upper 150 meters of the water column was assumed to be comprised of MW, SIM and UHL and the following system of equations was used:

$$\mathrm{f_{MW}} + \mathrm{f_{SIM}} + \mathrm{f_{UHL}} = 1 \tag{6.1}$$

$$\delta^{18}\mathrm{O_{MW}f_{MW}} + \delta^{18}\mathrm{O_{SIM}f_{SIM}} + \delta^{18}\mathrm{O_{UHL}f_{UHL}} = \delta^{18}O \tag{6.2}$$

$$\mathrm{TA_{MW}f_{MW}} + \mathrm{TA_{SIM}f_{SIM}} + \mathrm{TA_{UHL}f_{UHL}} = \mathrm{TA}. \tag{6.3}$$

For depths greater than 150 m, the water column was assumed comprised of UHL, ATL

and net SIM, and the following system of equations was used:

$$f_{SIM} + f_{UHL} + f_{ATL} = 1 \quad (6.4)$$

$$\delta^{18}O_{SIM} f_{SIM} + \delta^{18}O_{UHL} f_{UHL} + \delta^{18}O_{ATL} f_{ATL} = \delta^{18}O \quad (6.5)$$

$$TA_{SIM} f_{SIM} + TA_{UHL} f_{UHL} + TA_{ATL} f_{ATL} = TA. \quad (6.6)$$

The end-member values used in the analysis are given in Table 6.1. The TA associated with the MW fraction is the flow-weighted average of the Mackenzie River (*Cooper et al.*, 2008). Additional North American rivers flow into the Beaufort Sea and Canadian Arctic Archipelago and these freshwater sources likely have somewhat different TA (and DIC) than the Mackenzie River, which adds to the uncertainty of the estimate of the MW fraction computed here. The δ^{18}O value associated with the MW fraction of *Khatiwala et al.* (1999) for Arctic rivers was used. Direct precipitation minus evaporation over land is accounted for in the MW end-member,and will have the same properties as the runoff. Precipitation minus evaporation occurring over the ocean adds freshwater (S=0) with TA=0. This contribution comprises only a small input of the total freshwater fluxto the Arctic region (*Serreze et al.*, 2006) and this contribution has been neglected by assigning the Mackenzie River value to the TA end-member for MW. We have assumed that the salinity and TA of SIM are null, i.e., sea-ice does not constitute a net source of salinity or TA to the underlying seawater. The salinity and TA trapped in the sea-ice during formation are subsequently released during ice melt. The end-member TA and δ^{18}O associated with the UHL fraction were determined from the mean values corresponding to a salinity of 33.1 at all stations. The end-member TA and δ^{18}O associated with the ATL were the mean values corresponding to the temperature maximum at each station following *Yamamoto-Kawai and Tanaka* (2005).

Table 6.1: End-member properties used in the three component mass balance equations.

Water Mass	Salinity	δ^{18}O ($^o/_{oo}$)	TA μmol kg^{-1}	DIC μmol kg^{-1}
MW	0	-20	1540	1390
SIM	0	-2.0	0	0
UHL	33.1	-1.5	2283	2236
ATL	34.8	0.19	2301	2154

6.5 Results

6.5.1 Water mass Composition

The fractions of MW and SIM in three regions are shown in Fig. 6.2. These profiles are computed from average values of (a) 5 stations located West of Banks Island, in the southeastern Beaufort Sea; (b) 3 stations centrally located in the Canadian Archipelago; and (c) 3 stations within the outflow of Lancaster Sound to Baffin Bay (see also Fig. 6.1). In the western region (Fig. 6.2a), MW amounted to roughly 3% in the upper 40 meters of the water column. Over the same depth range SIM was roughly roughly 5%. Below 60 meters, MW was between 0 and 1% while SIM in this depth range amounted to between 0 and 2%. In the central region (Fig. 6.2b), the fraction of MW in the upper 20 meters was roughly 1%, with a peak value of roughly 3% at 30 meters and values of MW$<$1% below 40 m. In the same region, the SIM fraction was roughly 6% in the upper 20 meters and ranged from 1% to 2% below a depth of 40 m. At the eastern station in Lancaster Sound (Fig. 6.2c), the MW fraction ranged from 0 to less than 1%. In the same region, the SIM fraction reached the maximum value of nearly 8% in the upper 20 meters of the water column. Below a depth of 40 m in Lancaster Sound, the SIM fraction ranged from roughly 2% to 3%.

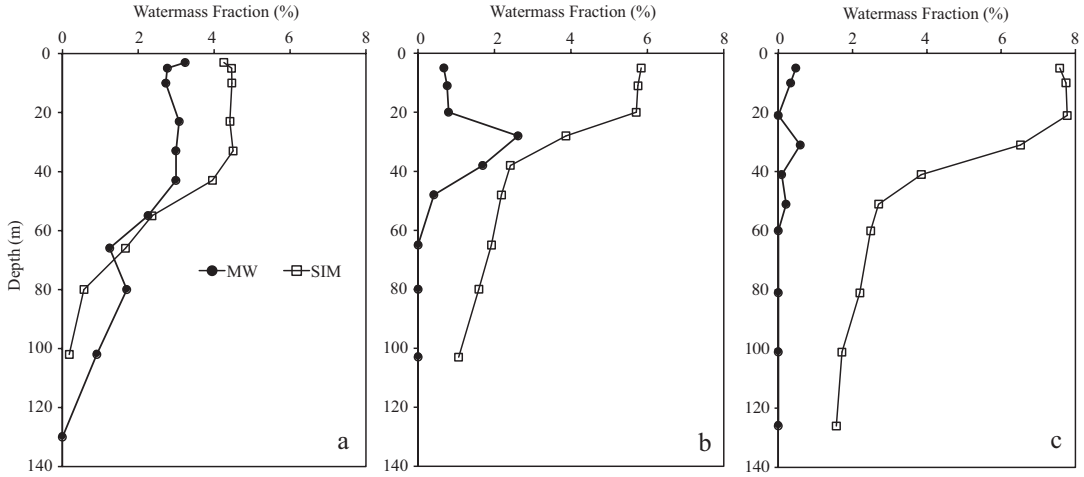

Figure 6.2: Fractions of MW and SIM for an average of stations located (a) west of Banks Island, (b) centrally located in the Canadian Archipelago, and (c) located near the outflow of Lancaster Sound to Baffin Bay.

In the western region the fraction of UHL ranged from 93% at the surface to 100% at a depth of 130 m; below 200 m the fraction of ATL was 100%. In the central region,

the fraction of UHL ranged from 94% at the surface to 100% at a depth of 120 m; at a depth of 140 m the fraction of UHL was 95% and ATL was 5%. In the eastern region in Lancaster Sound at a depth of 130 m the fraction of SIM was 1% and UHL was 98%. At a depth of 400 m the SIM fraction was 1%, UHL was 51% and ATL was 48%. At a depth of 500 m in Lancaster Sound the SIM fraction was 0%, UHL was 51% and ATL was 49%, indicating that the depth of penetration of UHL increases through the Archipelago in the eastward direction, towards Baffin Bay. The ATL water present in the deep samples from the Lancaster Sound region is Atlantic water coming both from the south via the West Greenland Current (WGC), and from the north via Nares Strait, and not Atlantic water from the Arctic interior. Previous studies have reported a mixing of UHL and Atlantic-derived WGC waters in the North Water region of Baffin Bay (*Melling et al.*, 2000; *Miller et al.*, 2002; *Lobb et al.*, 2003).

6.5.2 The Carbonate System

The distribution of DIC, TA, pH, and Ω_{Ar} with depth for the three regions described in the preceding section are shown in Figs. 6.3 and 6.4. DIC profiles reflect the influence of freshwater and biology at the surface, both of which decrease DIC concentrations. The lowest surface DIC concentrations ($\sim$1925 μmol kg^{-1}) are observed in the western region, where the combined input of MW and SIM amounts to roughly 7% of the water in the upper 40 meters. In the eastern region, where the dilution of the surface waters is primarily due to SIM (roughly 8%) which does not contribute DIC (see Table 6.1), the minimum surface DIC concentration ($\sim$1970 μmol kg^{-1}) is enhanced relative to the western station. This may indicate a larger contribution from surface primary production in the western region, which would decrease surface DIC concentration. The surface waters in the western region are most influenced by MW, primarily from the nearby Mackenzie River. The Mackenzie River is supersaturated with the respect to the atmosphere with pCO_2 on the order of 700 μatm (*Vallières et al.*, 2008) and correspondingly low pH. The influence of runoff from the Mackenzie River is seen in the low surface pH values in the western region relative to the central and eastern regions where the effect of MW is diminished (Figs. 6.2 and 6.4). The aragonite saturation state (Ω_{Ar}) decreases with increasing SIM due to the dilution of chemical constituents with the addition of freshwater (*Bates and Mathis*, 2009; *Chierici and Fransson*, 2009). This reduction is seen in the upper 30 meters of the water column in the central and eastern regions corresponding to

the largest values of SIM fraction (Figs. 6.4 and 6.2). However, the lowest surface values of Ω_{Ar} were observed at the western station where the smallest contribution from SIM was computed (Figs. 6.2a and 6.4a). The DIC minimum observed in the western region is likely the result of biological production during the preceding growing season which increases the surface Ω_{Ar}. However, the western region is under the additional influence of Mackenzie River runoff. The input of MW and SIM to the surface waters in this region outcompete the biologically-mediated increase in Ω_{Ar} and result in the low observed surface values (see also Chapter 7).

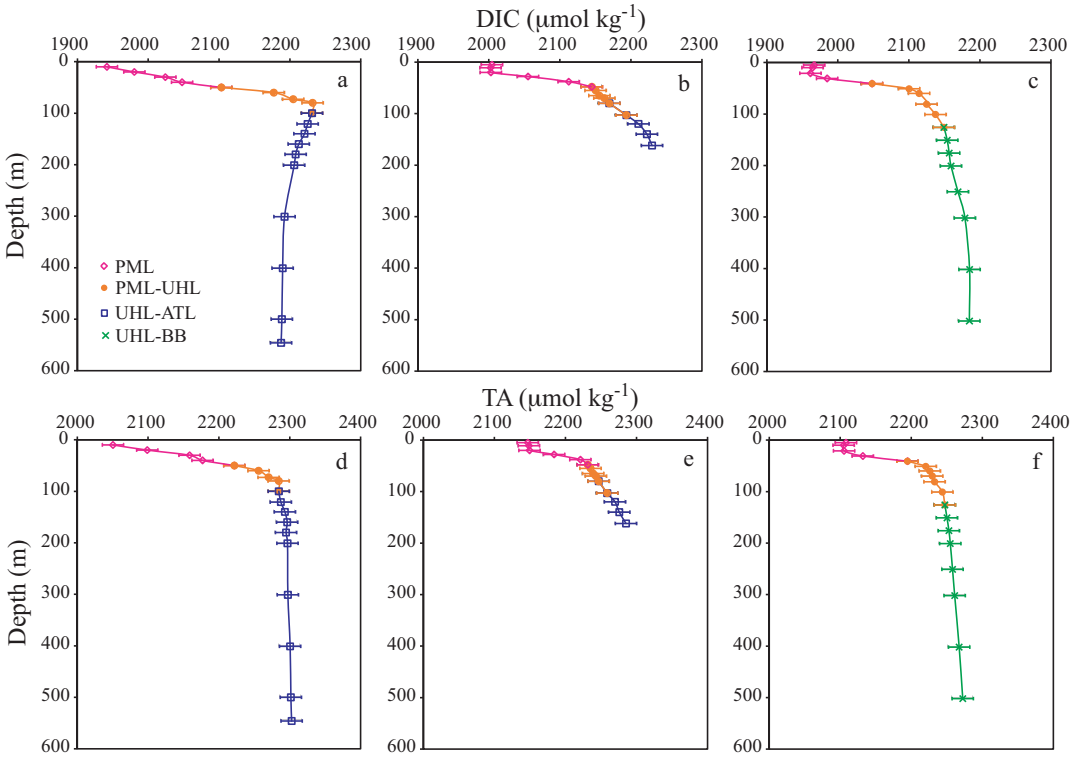

Figure 6.3: Profiles of DIC and TA for an average of stations located (a, d) west of Banks Island, (b, e) centrally located in the Canadian Archipelago, and (c, f) located near the outflow of Lancaster Sound to Baffin Bay, with the dominant water masses identified. The PML is comprised of MW, SIM, and UHL water. The error bars reflect spatial variability between stations used to compute the regional means shown.

There is a subsurface DIC maximum at a depth of roughly 100 meters in both the western ($\sim$ 2230 μmol kg^1) and eastern ($\sim$ 2150 μmol kg^{-1}) regions, though this feature is less pronounced in the eastern region. This subsurface increase in DIC is due to the large fraction of (carbon-rich) UHL water at this depth, and also indicates the remineralization of organic matter. Below a depth of roughly 120 m in the western region there is a modest

decrease in DIC with depth indicating the influence of relatively lower-DIC ATL waters in this region of the water column. The DIC concentrations are notably higher at the depth range of 100 to 200 meters in the central region than is seen at the same depth in the western region, while TA in the central region is reduced relative to the western region. The pH over this same depth range decreases at the central region, while there is an increase in pH in the western region. We propose that organic matter remineralization over the shallow sill at the central location, which increases DIC relative to TA, is the reason for the observed elevated DIC, and reduced pH in this region. The bottom waters (below 200 m) in the western region have higher concentration of TA than the waters atthe same depth in the eastern region. This is due to the composition of the deep water, which in the western region has a larger fraction of ATL, with lower DIC and higher TA (and salinity), while in the eastern region the contribution of ATL at this depth is reduced, lowering the TA (and salinity) relative to the western region.

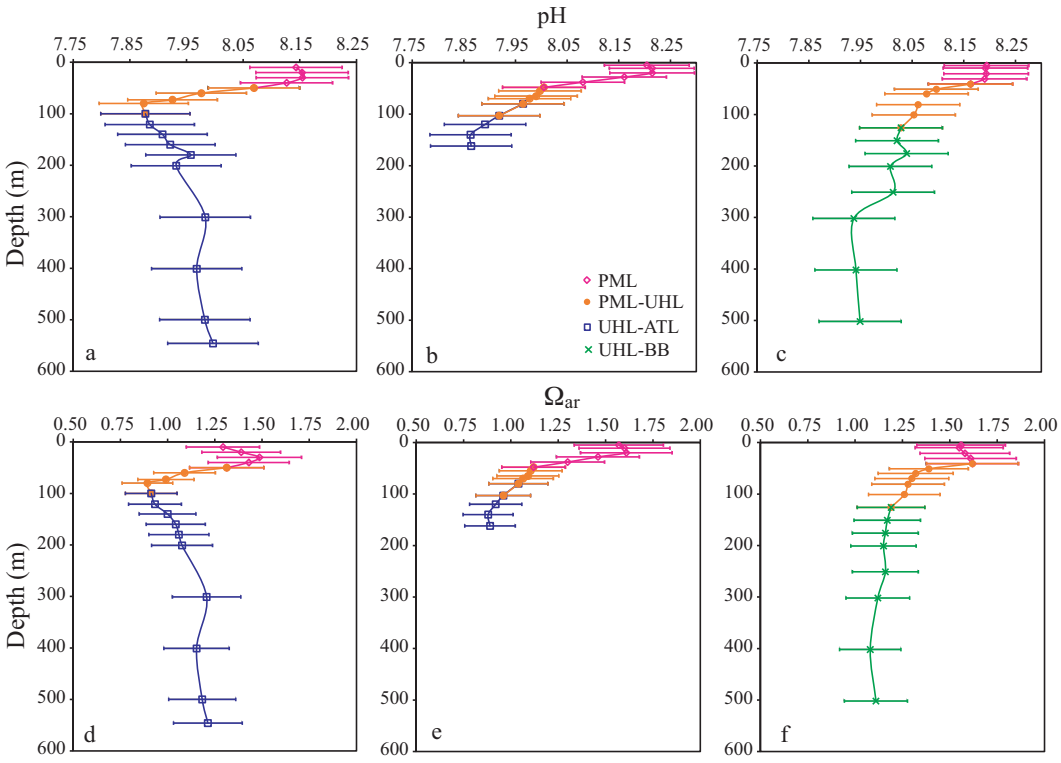

Figure 6.4: Profiles of pH and Ω_{Ar} for an average of stations located (a, d) west of Banks Island, (b, e) centrally located in the Canadian Archipelago, and (c, f) located near the outflow of Lancaster Sound to Baffin Bay with the dominant water masses identified. The PML is comprised of MW, SIM, and UHL water.The error bars reflect spatial variability between stations used to compute the regional means shown.

The range of DIC and TA concentration over all measured samples throughout the Archipelago is quite broad (Fig. 6.5). The relationships between DIC and salinity and TA and salinity are shown in Fig. 6.5a and b. The lowest concentrations of DIC (<1800 μmol kg^{-1}) and TA ($\sim$1850 μmol kg^{-1}) are associated with the salinity minimum (S$\sim$26) resulting from contributions from both MW and SIM to the PML. The extrapolation to S=0 of a linear regression of DIC, (and TA) for all samples with MW>0 and/or SIM>0 in the upper 50 meters of the water column yields values for the MW end-member of: DIC = 1390 μmol kg^{-1} and TA = 1425 μmol kg^{-1}, roughly consistent with the flow-weighted Mackenzie River value of TA used in the MW fraction computation of *Cooper et al.* (2008) (see Section 6.5.1 and Table 6.1).

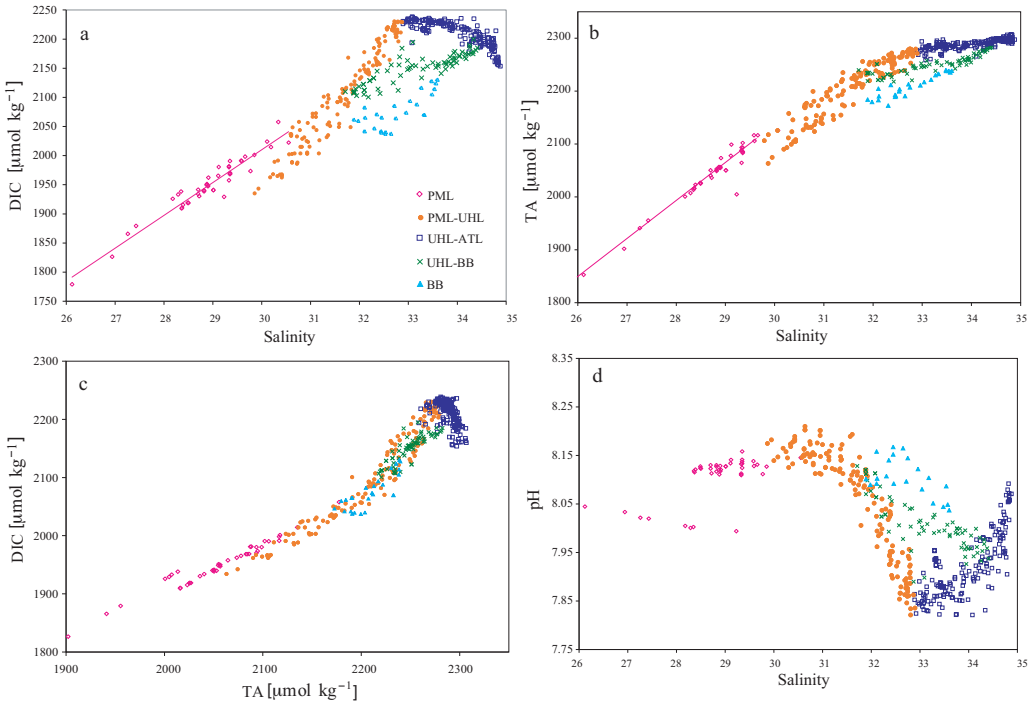

Figure 6.5: (a) Dissolved inorganic carbon (DIC) versus salinity, (b) TA versus salinity, (c) DIC versus TA and (d) pH versus salinity for samples collected at the stations indicated by the open squares in Fig. 1. Five water masses are identified: PML (pink diamonds), PML-UHL (orange dots), UHL-ATL (blue squares), and UHL-BB (green x's). Surface water samples from stations located in the North Water region of Baffin Bay are plotted in pale blue. These waters result from a contribution from sea-ice melt which adds water with $S = 0$, with very low DIC concentration. The color coding is according to the water mass identification described in Fig. 6.6.

From the surface to a depth of roughly 150 m, covering the salinity range from 26 to roughly 31, DIC concentration ranged from less than 1800 μmol kg^{-1} to greater than 2200

μmol kg^{-1}. The TA concentration increased from roughly 1850 μmol kg^{-1} to 2250 μmol kg^{-1} over the same range of depth (0 to 150 m) and salinity (S=26 to S$\sim$33). The DIC maximum (on the order of 2240 μmol kg^{-1}) is coincident with the maximum fraction of UHL (at S=33.1). The TA maximum (on the order of 2300 μmol kg^{-1}) is coincident with the maximum fraction of ATL and the salinity maximum (S=34.88). The ratio between DIC and TA is roughly 1:1 in the PML (Fig. 6.5c). This ratio increases slightly to 1.2:1 in the UHL as a result of the remineralization of organic matter which increases DIC relative to TA. In the deeper water column, and for salinities S>33, ATL water dominates and the concentration of TA continues to increase (relative to the PML and UHL) primarily as a function of increasing salinity. The concentration of DIC in the ATL water is reduced, relative to the UHL due to the reduction of respiration, or remineralization of organic matter, as a function of depth. The pH of the surface waters ranges from roughly 8.05 to 8.15 (Fig. 6.5d). The pH maximum, roughly 8.20, occurs in the PML and is associated with salinities of roughly S=31. The pH minimum,on the order of 7.80, is associated with the maximum fraction of UHL and reflects the high concentrations of DIC in the Pacific-origin waters.

While there has been some debate as to the utility of the salinity normalization in the analysis of water mass properties, particularly in the coastal zone (Friis et al. 2003; Robbins 2001), we find that salinity-normalized DIC, ($\mathrm{DIC_{norm}}$), is a powerful parameter in the identification of water masses and mixing relationships. In brief, the normalization of DIC to a constant salinity removes the effect of freshwater fluxes from the measured DIC concentrations. $\mathrm{DIC_{norm}}$ is thus primarily controlled by the water temperature (i.e., by the solubility of $\mathrm{CO_2}$), biological processes, air-sea exchange of $\mathrm{CO_2}$, and by the mixing of water masses. Furthermore, the use of $\mathrm{DIC_{norm}}$ allows us to determine whether non-conservative processes, such as biological production or air-sea $\mathrm{CO_2}$ flux, are dominant at the timescales over which mixing occurs. DIC was normalized to a regional mean salinity of $\mathrm{S^{mean}} = 32.5$, computed using all samples collected at all stations indicated in Fig. (6.1), (i.e. $\mathrm{DIC_{norm}} = 32.5\mathrm{DIC/S}$). Because the application of a salinity normalization as described above is not appropriate for waters subject to riverine influence, due to the non-zero concentration of DIC in the river water, samples with a MW component were normalized following *Friis et al.* (2003).

The relationship between $\mathrm{DIC_{norm}}$ and salinity is shown in Fig. 6.6, and four mixing regimes are identified. In the low-salinity surface waters the mixing of MW, SIM and UHL waters form the PML. As previously discussed the contribution from MW decreases with distance from the Mackenzie river, with MW fractions at the easternmost stations of less than 1%. The salinity-normalized DIC allows MW with high $\mathrm{DIC_{norm}}$ to be distinguished from sea-ice melt, represented by the y-intercept of the orange line in Fig 6.6, with a much lower DIC concentration (see Table 6.1). Mixing can be clearly identified as the dominant process between the PML and UHL water, observed at most stations throughout the archipelago in the depth range of roughly 30 to 100 meters. Over the given time scale, mixing dominates while the effects of non-conservative processes can hardly be determined, if at all, from the correspoding data. Mixing of ATL and UHL was found in the deepest waters. Samples from the western region (Fig. 6.6, in blue) (i.e. west of $100°$W), display the least amount of scatter about the proposed idealized 'mixing line'. The non-conservative behavior seen in the UHL and ATL samples collected in the western region is, as discussed in Section 5.1, due to the remineralization of organic matter. The fourth mixing regime is between UHL and Baffin Bay ATL source water of slightly lower salinity and higher DIC relative to samples from the western region (Fig. 6.6 in green). The contribution of ATL water seen at stations in Jones and Lancaster Sounds does not originate from the Archipelago, but from Baffin Bay or Nares Strait. This is consistent with Jones et al. (2003), who, using nutrient ratios as water mass tracers, found no Atlantic water, from the Arctic interior, in the outflow from either Lancaster or Jones Sound.

6.5.3 Deep Water Carbon Storage

The mixing of Pacific and Atlantic waters in the lower water column of the westernmost stations, clustered in the southeastern Beaufort Sea region, southwest of Banks Island (Fig. 1) is now investigated in more detail. If DIC concentrations observed in the range of mixing of UHL and ATL waters resulted only from conservative mixing, all samples should fall along the proposed 'mixing line' (shown in blue in Fig. 6.6). The bowed structure of the relationships between DIC and salinity (Fig. 6.5a, in blue) and $\mathrm{DIC_{norm}}$ and salinity (Fig. 6.6) and the deviation from the general linear trend in the plot of DIC versus TA (Fig. 6.5c, in blue), imply that another, non-conservative process is at play. This process is assumed to be the result of biological activity, and not air-sea exchange,

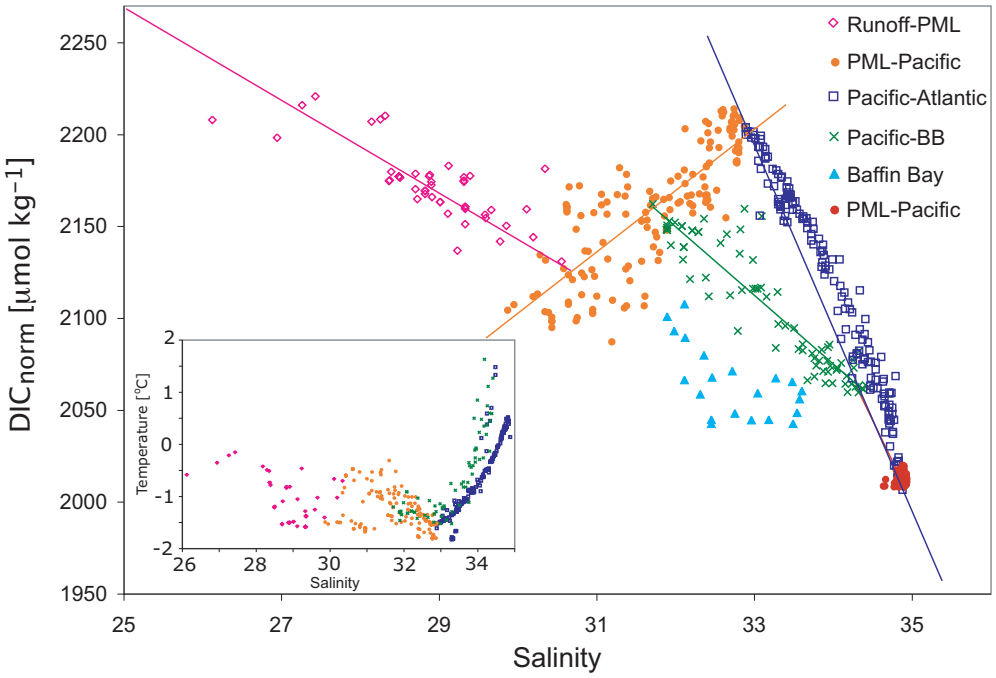

Figure 6.6: Salinity normalized DIC versus salinity. Five idealized mixing lines are indicated: runoff-PML (pink), PML-Pacific (orange), Pacific-Atlantic (blue), PML-Pacific-BB (green), and WGC-Labrador Sea (red). Surface water samples from stations located in the North Water region of Baffin Bay are plotted in pale blue. These waters result from a contribution from sea-ice melt, which adds fresh water, while making a negligible addition of DIC, in contrast to the fresh water addition from rivers which has a much higher DIC concentration. Inset: a T-S plot with the same color coding as in the $\mathrm{DIC}_{\mathrm{norm}}$ versus salinity plot. The two Atlantic-origin water masses (in blue and green) are clearly distinguishable, while the PML and runoff have a wider range of both temperature and salinity.

due to the depth range of the waters (from roughly 80 - 600 meters). Further confirmation that this is indeed a biological process, is the absence of a water mass with high salinity ($S \geq 34$), and high DIC ($\mathrm{DIC} > 2250\ \mu\mathrm{mol\ kg^{-1}}$), that would act as a third end member, attributing this bowed structure to a physical process. Non-conservative variations in DIC are thus attributed to biology ($\Delta\mathrm{DIC_{bio}}$), and can be expressed as the differences between the expected ($\mathrm{DIC_{ex}}$) (i.e. the idealized mixing) and the observed ($\mathrm{DIC_{obs}}$) values:

$$\Delta\mathrm{DIC_{bio}} = \mathrm{DIC_{obs}} - \mathrm{DIC_{ex}}. \tag{6.7}$$

Negative values of $\Delta\mathrm{DIC_{bio}}$ correspond to inorganic carbon deficits implying that production exceeds respiration in the system. Conversely, positive values of $\Delta\mathrm{DIC_{bio}}$ imply that respiration exceeds production and correspond to a surplus of inorganic carbon. Profiles of $\mathrm{DIC_{ex}}$ are computed from salinity and the following relationship: $\mathrm{DIC_{ex}} = -48.24\mathrm{S} + 3832$ derived from the DIC and salinity of the UHL and ATL end-members (see Table 6.1) and shown graphically by the idealized mixing line in Fig. 6.7a. Using Eq. (7), $\Delta\mathrm{DIC_{bio}}$ was computed for for each sample. These values were integrated over the depth range of UHL and ATL waters, as prescribed by their salinities, and a mean value of $\mathrm{DIC_{bio}}$=5.8$\pm$0.2 mol C $\mathrm{m^{-2}}$, subsequently referred to as 'carbon surplus', was computed. Further confirmation that biology is driving the increased DIC concentrations is evident from a plot of apparent oxygen utilization (AOU) for the same discrete samples (Fig. 6.7). A bowed structure analogous to that of DIC is also found in the AOU distribution. As in the case of DIC, AOU is integrated over the same range of salinity, and we find a total oxygen utilization of 7.7 ± 0.5 mol $\mathrm{O_2}$ $\mathrm{m^{-2}}$, yielding a ratio of AOU:DIC = 1.22, roughly consistent with the Redfield ratio of $\mathrm{O_2}$:$\mathrm{CO_2}$ = 138:106$\simeq$1.30 (*Millero*, 2006). The remineralization of organic carbon in the subsurface waters, derived from primary production in the euphotic zone, results in the excess carbon seen in the deep water. Assuming that the residence time for subsurface water in the southeastern Beaufort Sea is on the order of 1 to 2 years (*Lanos*, 2009), we arrive at a carbon drawdown ranges from 2.9 to 5.8 mol C m-2 $\mathrm{yr^{-1}}$ (with a mean value of 4.4 mol C $\mathrm{m^{-2}}$ $\mathrm{yr^{-1}}$). This estimate is in general agreement with the rather sparse primary production data for this region, which ranges from 7 to 15 mol C $\mathrm{m^{-2}}$ $\mathrm{yr^{-1}}$ (*Arrigo and van Dijken*, 2004). This calculated respiratory carbon surplus corresponds to an export production of roughly 30% to 60% of the primary production. A recent estimate of vertical export in the region

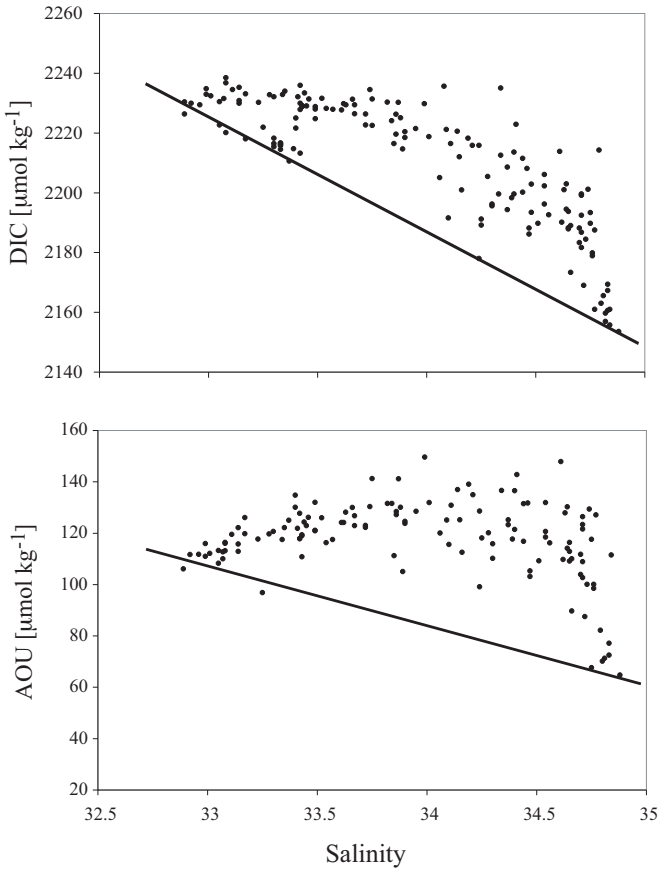

Figure 6.7: Water masses of Pacific and Atlantic origin, from the southwestern Archipelago are plotted in the top panel, while the corresponding AOU is plotted over the same salinity range in the bottom panel. Integrating $\Delta\mathrm{DIC}_{\mathrm{bio}}$, and AOU over the salinity range of Pacific ($S = 33.1$) and Atlantic ($S = 34.8$) waters yields a total carbon surplus, or respiration inventory, of 5.8 ± 0.2 mol C m^{-2}, and a corresponding oxygen utilization of 7.7 ± 0.5 mol oxygen m^{-2}.

suggests that roughly 2 mol C m^{-2} yr^{-1}, or less than 20% of primary production, leaves the surface layer (*Jull-Pedersen et al.*, 2010). Sediment trap data from the southeastern Beaufort Sea indicates that roughly 0.45 mol C m^{-2} yr^{-1} of marine particulate organic carbon (POC) reaches a depth below 200 m, with an additional contribution from terrestrial sources (*Forest et al.*, 2008) which implies a subsurface respiration of only 1.55 mol C m^{-2} yr^{-1}. An additional source of inorganic carbon to the subsurface layer is benthic respiration which may be significant in this region (*Renaud et al.*, 2007). Alternatively a portion of the subsurface respiration estimated here may be fueled by organic material delivered laterally to the region from the adjacent Mackenzie Shelf waters which contain a significant pool of POC (*Macdonald et al.*, 1987).

6.5.4 Carbon Export to the North Atlantic

The Beaufort Sea communicates with the Atlantic Ocean through Fram Strait, and those passages in the Arctic Archipelago that enter Baffin Bay. Lancaster Sound, Nares Strait and Jones Sound all exit the Archipelago to Baffin Bay. Several estimates of volume transport from the Archipelago, from Jones and Lancaster Sound have been made (*Rudels*, 1986; *Cuny et al.*, 2005; *Prinsenberg and Hamilton*, 2005). We applied the estimate of Ingram et al. (2002), which assumes that the net Eastward outflow from Jones Sound and Lancaster Sounds are 0.3×10^6 m^{-3} s^{-1}, and 1.1×10^6 m^{-3} s^{-1}, respectively. Multiplying this volume transport by the water column DIC inventories in Jones and Lancaster Sounds yields an estimate of carbon exported from the Archipelago to Baffin Bay at each location. The export of carbon from Jones Sound to Baffin Bay is roughly 1.23×10^{14} g C yr^{-1}, while that from Lancaster Sound is roughly 3.25×10^{14} g C yr^{-1}. The total carbon transport is then estimated at 4.48×10^{14} g C yr^{-1}. Using the volume transport estimate of *Ingram et al.* (2002) for the Baffin Current (1.7×10^6 m^{-3} s^{-1}), the outflows from Jones and Lancaster Sounds then supply roughly 18% and 65% of this water respectively, making the Arctic Archipelago an important source of both water and carbon to Baffin Bay and subsequently to the North Atlantic.

An alternate approach is to compare the DIC concentration of water entering Baffin Bay via the WGC with the DIC concentration in the outflow from the Archipelago. In this way the carbon enrichment resulting from the outflow of SIM, UHL and ATL waters via the Archipelago was estimated. Salinity, DIC, and total alkalinity (TA) data from the Labrador Sea in 1998 (*Jones*, 1998) were corrected for the increased atmospheric, and subsequently oceanic, CO_2 concentration over the 10-year period since the data were collected. DIC and TA from the 1998 Labrador Sea data set were used to compute pCO_2 (*Millero*, 2006), which was then scaled up according to an increase of 1.7 ppm per year (*Thomas et al.*, 2008). Assuming that TA remained constant over this 10 year period, TA and the augmented pCO_2 values were then used to compute the present day DIC concentrations. We assume that the most northeastern station of the Labrador Sea transect (Fig. 6.1) represents WGC water with a mean DIC concentration of 2125 μmol kg^{-1}. The outflow from the Archipelago via Jones and Lancaster Sounds, which includes the addition of Atlantic water from Nares Strait, has a DIC concentration of 2140 μmol kg^{-1}. The difference between these values allows us to estimate the carbon enrichment at roughly

15 μmol kg^{-1}, or 0.18 g C m^{-3}.

6.5.5 *Impact of Increased Sea-ice Melt*

Over the last several hundred years, the surface ocean pH has decreased by roughly 0.1 units (*Caldeira and Wickett*, 2003). A further pH decrease of 0.3 units has been predicted (*Feely et al.*, 2004; *Orr et al.*, 2005), and model results have indicated that high-latitude oceans will become undersatured with respect to aragonite (i.e. $\Omega_{\mathrm{Ar}} < 1$), and calcite before other regions (*Orr et al.*, 2005; *Fabry et al.*, 2009). The observed loss of sea-ice from the Arctic over the past decade has been faster than even the most pessimistic global model prediction (*Moritz et al.*, 2002; *Maslanik et al.*, 2007; *Stroeve et al.*, 2007) and a sustained and wide-spread freshening of the Arctic has been reported (*McPhee et al.*, 1998; *Dickson*, 1999; *Lammers et al.*, 2001; *Peterson et al.*, 2002, 2006). Furthermore, with a warming climate the Arctic hydrologic cycle is expected to undergo additional change, and significant increases in precipitation have been projected (*Peterson et al.*, 2006).

The addition of freshwater, particularly from sea-ice melt and precipitation which have very low concentrations of DIC and TA, to the surface of the Arctic Ocean dilutes the water with respect to its chemical constituents. It has recently been reported that increases in SIM in the Canada Basin have resulted in lower surface Ω_{Ar} (*Chierici and Fransson*, 2009; *Yamamoto-Kawai et al.*, 2009). To assess the impact of changing the composition of water masses exiting the Archipelago, we varied the relative fraction of SIM in the upper 30 meters of the Lancaster Sound outflow. By altering the amount of SIM, we consequently dilute the relative concentrations of surface DIC and TA flowing into Baffin Bay. To see the impact that such a change would have on acidification of the North Atlantic, the new pH and Ω_{Ar} are computed. The observed pH and Ω_{Ar} in upper 30 meters of the water column in Lancaster Sound were 8.19 and 1.52, respectively. Undersaturation ($\Omega_{\mathrm{Ar}} < 1$) of the surface waters was reached when the sea-ice melt fraction exceeded 30%; the corresponding pH was increased to a value of 8.27 with this dilution of the surface waters. Dilution of the surface waters also decreases the pCO_2, and may potentially allow enhanced uptake of atmospheric CO_2 by the surface waters decreasing Ω_{Ar} and pH. On the other hand, ice-free surface waters in the Arctic will be considerably warming than ice-covered waters, and the resulting thermodynamic increase in pCO_2 may outcompete the decrease due to dilution.

Pacific-origin UHL water has a higher DIC than both PML and ATL water, (and a lower TA than Atlantic water), and consequently lower pH, and Ω_{Ar}. An increase in the UHL fraction in the outflow from Lancaster Sound would deliver waters with low pH and Ω_{Ar} to Baffin Bay, while a decrease in the fraction of UHL in this outflow would have the opposite effect. It can be seen from the distribution of pH in Fig. (6.5d) that PLM water has higher pH (and lower DIC and TA) than both the Pacific and Atlantic water. Photosynthesis in the surface waters decreases DIC and increases both pH and Ω_{Ar}, while respiration, or remineralization of organic matter, which takes place in the subsurface, at the level of the Pacific-origin core, increases DIC and decreases both pH and Ω_{Ar}. Increases in export production as a possible consequence of an extended growing season in the increasingly ice-free Arctic would increase the DIC and reduce the pH and Ω_{Ar} in the subsurface waters exiting the archipelago, and potentially deliver more carbon-rich water to the North Atlantic. Export of high carbon Pacific water to the North Atlantic has implications for the uptake of anthropogenic carbon, and hence ocean acidification in this area. However, natural variablity may also be important, and NAO and/or AO driven changes in composition of waters leaving the Arctic may also influence carbon uptake and saturation states in the subpolar and temperate North Atlantic.

6.6 Conclusions

Inorganic carbon system data collected throughout the Canadian Arctic Archipelago allowed an assessment of the distribution and carbon characteristics of the water masses in this region. Meteoric water (MW) comprises roughly 3% of the surface waters in the western region of the Archipelago while sea-ice melt (SIM) water contributes roughly 4%. The fraction of MW decreases eastward contributing less than 1% to the surface waters in Jones and Lancaster Sounds. There is a corresponding increase in SIM from the western Archipelago to the eastern outflows to Baffin Bay. Low surface dissolved inorganic carbon (DIC) concentrations were observed in the upper water column throughout the Archipelago resulting from biological production and freshwater input, with minimum DIC in the western region. The depth of penetration of Pacific-origin upper halocline water (UHL) increases eastward through the Archipelago. The export of carbon through the Archipelago to Baffin Bay at the outflows of Jones and Lancaster Sounds was estimated.

In the subsurface waters of the western Archipelago there was a respiratory carbon surplus, which was likely fueled by inputs of organic material from the surface layer and by benthic respiration.

6.7 Acknowledgments

This research is part of the Canadian IPY initiatives and the Circumpolar Flaw Lead System (CFL) Study, and was supported by the Natural Sciences and Engineering Research Council of Canada (NSERC), ArcticNet, and MetOcean Data Systems. The authors are grateful for the enthusiastic co-operation of the crew of the CCGS Amundsen and colleagues on board. We wish to thank Al Mucci for his insight and contribution to the field program, Nick Bates, and two anonymous reviewers, for their helpful suggestions. This work contributes to IGBP/IHDP-LOICZ.

CHAPTER 7

SEASONAL VARIABILITY OF THE CO_2 SYSTEM IN AMUNDSEN GULF

7.1 Abstract

During a year round occupation of Amundsen Gulf in the Canadian Arctic Archipelago dissolved inorganic and organic carbon (DIC, DOC), total alkalinity (TA), partial pressure of CO_2 (pCO_2) and related parameters were measured over a full annual cycle. A two-box model was used to identify and assess physical, biological, and chemical processes responsible for the seasonal variability of DIC, DOC, TA, and pCO_2. Surface waters were undersaturated with respect to atmospheric CO_2 throughout the year and constituted a net sink of 1.2 mol C m^{-2} yr^{-1}, with ice coverage and ice formation limiting the CO_2 uptake during winter. CO_2 uptake was largely driven by under ice and open water biological activity, with high subsequent export of organic matter to the deeper water column. Annual net community production (NCP) was 2.1 mol C m^{-2} yr^{-1}. Approximately one-half of the overall NCP during the productive season (4.1 mol C m^{-2} from April through August) was generated by under ice algae and amounted to 1.9 mol C m^{-2}. The surface layer was autotrophic, while the overall heterotrophy of the system was fueled by either sedimentary or lateral inputs of organic matter[1].

[1]This chapter comprises a manuscript by E. H. Shadwick, H. Thomas, M. Chierici, B. Else, A. Fransson, C. Michel, L. A. Miller, A. Mucci, A. Niemi, T. N. Papakyriakou and J.-É. Tremblay entitled *Seasonal Variability of the Inorganic Carbon System in the Amundsen Gulf Region of the Southeastern Beaufort Sea* under revision in Limnology and Oceanography.

7.2 Introduction

The record low sea-ice coverage in the Arctic in 2007 contributes to a growing body of evidence supporting global climate change (*Moritz et al.*, 2002; *Maslanik et al.*, 2007; *Stroeve et al.*, 2007; *Arrigo et al.*, 2008). The Arctic Ocean is an ecologically sensitive area where the early detection of climatic changes may be possible (*Serreze et al.*, 2000). Many arctic marine ecosystems are ice-dependent and are vulnerable to small shifts in ambient water temperature (*Vallières et al.*, 2008). Furthermore, this region is also chemically sensitive due to the relatively high ratio between dissolved inorganic carbon and alkalinity, and the correspondingly weak buffer capacity (*Orr et al.*, 2005; *Thomas et al.*, 2007), making the Arctic Ocean particularly responsive to increases in atmospheric CO_2, and especially susceptible to the effects of ocean acidification.

Coastal and shelf seas play an important role in the global carbon cycle by linking atmospheric, terrestrial, and open ocean systems (*Borges et al.*, 2005; *Bozec et al.*, 2006). The role of the global coastal ocean in the uptake of atmospheric CO_2 has been under debate for some time (*Walsh*, 1991; *Frankignoulle and Borges*, 2001; *Borges et al.*, 2005; *Borges*, 2005). A recent synthesis by *Chen and Borges* (2009) suggests that high-latitude and temperate continental shelves tend to act as sinks for atmospheric CO_2, while tropical and sub-tropical coastal regions tend to act as CO_2 sources. The continental shelves make up roughly 50% of the surface area of the Arctic Ocean (*Walsh*, 1991). At present, the Arctic continental shelves as a whole are undersaturated with respect to atmospheric CO_2, and may therefore potentially act as CO_2 sinks (*Bates and Mathis*, 2009).

Compared to other open ocean and coastal ocean systems, the Arctic Ocean remains relatively poorly studied. Most observational studies have been limited to the summer and autumn seasons, when reduced ice-cover allows access (*Macdonald et al.*, 2002; *Mathis et al.*, 2007; *Mucci et al.*, 2010). Observational data of the inorganic carbon system in the Arctic, particularly outside of the summer and autumn seasons, are therefore sparse. Long-term time-series observations (*Bates et al.*, 1996; *Bates*, 2007), and repeat surveys (*Sabine et al.*, 2004), which have much improved our understanding of the marine carbon cycle in open ocean environments, have not yet been carried out in the Arctic Ocean.

We present dissolved inorganic carbon (DIC), total alkalinity (TA), and partial pressure of CO_2 (pCO_2) measurements covering a complete annual cycle in the Amundsen Gulf

region of the southeastern Beaufort Sea. These data were collected during the Circumpolar Flaw Lead System Study (CFL) field program as part of the Canadian International Polar Year (IPY) initiatives. These measurements were complemented by dissolved organic carbon (DOC) and nutrient data. The annual cycles of the inorganic carbon system parameters (DIC, TA, $\mathrm{pCO_2}$, pH, and aragonite saturation state (Ω_{Ar})) are presented and their seasonal variations examined. The physical and biological processes responsible for the seasonal variations in water column DIC are identified. A two-box model was constructed for the surface and subsurface layers in order to compute the monthly changes in DIC and TA due to: horizontal advection, vertical exchange between the boxes, air-sea exchange of $\mathrm{CO_2}$, freshwater input from river runoff and sea-ice melt, and biological processes. Quantitative considerations of these processes yield an estimate of net community production for Amundsen Gulf on the basis of the inorganic carbon data collected in the region.

7.3 Oceanographic Setting

Amundsen Gulf is bounded by Banks Island and the Beaufort Sea to the North, the Mackenzie Shelf to the West, the northern Canadian coast to the South, and the Arctic Archipelago to the East (Fig. 7.1). The surface circulation in the Beaufort Sea is dominated by the anticyclonic Beaufort Gyre, while the flow of subsurface waters is reversed, dominated by the cyclonic Beaufort Undercurrent (*Aagaard*, 1984). This undercurrent forces waters of both Pacific and Atlantic origin to the east along the continental margin, providing (offshore) nutrients to the Arctic shelves (*Macdonald et al.*, 1987; *McLaughlin et al.*, 2004).

The Mackenzie Shelf, defined by the 200 m isobath, covers an area of 6.4×10^4 $\mathrm{km^2}$ and is the largest shelf in the North American sector of the Arctic Ocean (*Macdonald et al.*, 1987). The physical system dynamics on the shelf and surrounding waters can be described according to season. In winter, when the sea is ice-covered, the effect of wind forcing is diminished, and density driven flows, due to the release of brine during ice formation, can occur (*Melling*, 1993). Ice breakup begins in the headwaters of the Mackenzie River in late April, moving progressively offshore and occurring on the shelf in mid-May (*Carmack and MacDonald*, 2002). Between mid-May and June, there is a peak in river discharge; the Mackenzie River discharges roughly 2.9×10^{11} $\mathrm{m^3\ yr^{-1}}$

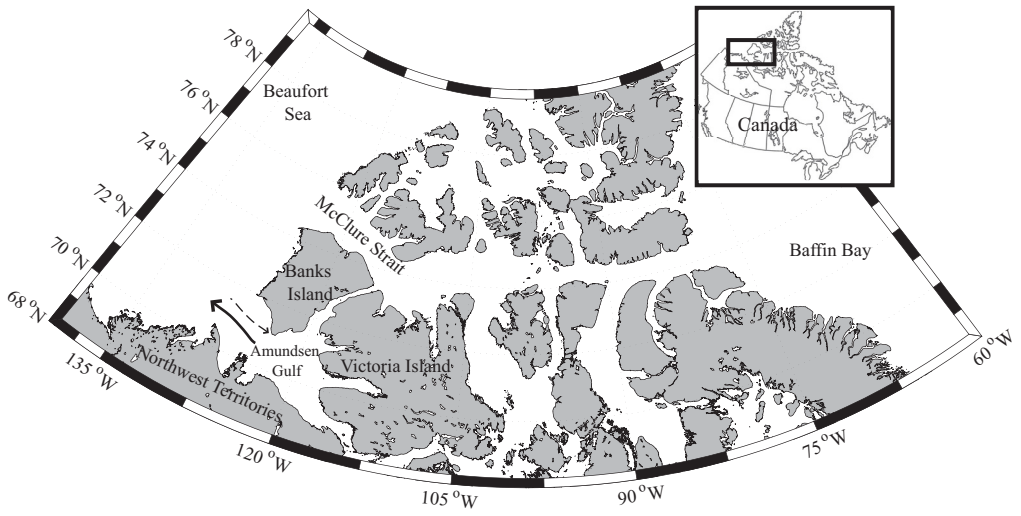

Figure 7.1: Amundsen Gulf is located south of Banks Island in the southeastern Beaufort Sea. The arrows indicate schematically the flow of water in Amundsen Gulf; the dashed arrow represents the (weak) surface inflow from the west, while the solid arrow indicates the (stronger) subsurface flow towards the Beaufort Sea. The water transport follows Lanos (2009).

(*Stewart et al.*, 1998). As the breakup progresses, the land-fast ice disappears. During the summer months, the upper 20 to 30 meters of the water column on the shelf and in the neighboring Amundsen Gulf are strongly stratified due to the combined effects of ice melt and inflow from the river (*Carmack and MacDonald*, 2002). Throughout the summer and early autumn, storms mix the ice melt and runoff into the upper water column and weaken the stratification (*Carmack and MacDonald*, 2002). Freeze-up begins in early to mid-October and is influenced by the summer ice conditions as well as the strength and direction of autumn winds (*Stewart et al.*, 1998).

A recurrent feature of the central Arctic Ocean is the flaw lead system. Polynyas are formed when the first-year pack is pushed away from the coast, leaving an area of open water behind. New ice is then free to form in this open water area, and it will subsequently be pushed downwind toward the first-year pack ice. This creates the opening of a flaw lead in the winter season. The flaw lead is circumpolar, with interconnected polynyas forming in both the North American and Eurasian sectors of the Arctic (*Barber and Massom*, 2006). The flaw lead system is a site of high ice production and, consequently, there is potential for significant fluxes of brine from the continental shelf regions to the deeper basins (*Barber and Massom*, 2006). In the Beaufort Sea, flaw leads form both along

the northern Canadian and Alaskan coasts. Amundsen Gulf encompasses part of the Cape Bathurst polynya, which plays an important role in both the physical and biological processes in the system. In winter, this area of open water is a site of enhanced air-sea exchange and wind forcing.

Water masses in the Arctic Ocean can be classified on the basis of their salinities (*Aagaard et al.*, 1981; *Aagaard and Carmack*, 1994; *Mathis et al.*, 2005) and be simplistically represented by a three-layer system. The uppermost water column is dominated by the polar mixed layer (PML), a seasonally ice-covered, relatively low-salinity water mass ($\mathrm{S} < 29$) (*Yamamoto-Kawai and Tanaka*, 2005; *Hansell et al.*, 2004). Immediately beneath the PML are the upper halocline waters (UHL) of Pacific origin ($\mathrm{S} = 33.1$) (*Macdonald et al.*, 2002; *McLaughlin et al.*, 2004), and the lower halocline waters (LHL) of Atlantic origin ($\mathrm{S} > 34$).

7.4 Methods

7.4.1 Sampling and Analytical Measurements

Samples were collected on board the Canadian Coast Guard Ship *Amundsen* at roughly 50 stations in the Amundsen Gulf and Cape Bathurst polynya region of the Southeastern Beaufort Sea from October 2007 to August 2008. Approximately 2000 samples were collected from the entire water column, with higher vertical resolution within the euphotic zone, at all stations shown in Fig. 7.2. Dissolved inorganic carbon (DIC) and total alkalinity (TA) samples were tapped from 20-L Niskin bottles mounted on a General Oceanics 24-bottle rosette fitted with a SeaBird conductivity temperature and depth sensor such that all chemical data were associated with high precision in-situ temperature and salinity data. Following water collection, DIC and TA samples were poisoned with a saturated $\mathrm{HgCl_2}$ solution to halt biological activity and stored in the dark, at $4°\mathrm{C}$, to await analysis. All DIC and TA samples were analyzed on board by coulometric and potentiometric titration respectively, using a Versatile Instrument for the Determination of Titration Alkalinity (VINDTA 3C, Marianda). Analytical methods for determination of DIC and TA have been fully described elsewhere (*Johnson et al.*, 1993; *Dickson et al.*, 2007). Routine analysis of Certified Reference Materials (provided by A. G. Dickson, Scripps Institution of Oceanography) ensured the accuracy of the DIC and TA measurements whereas

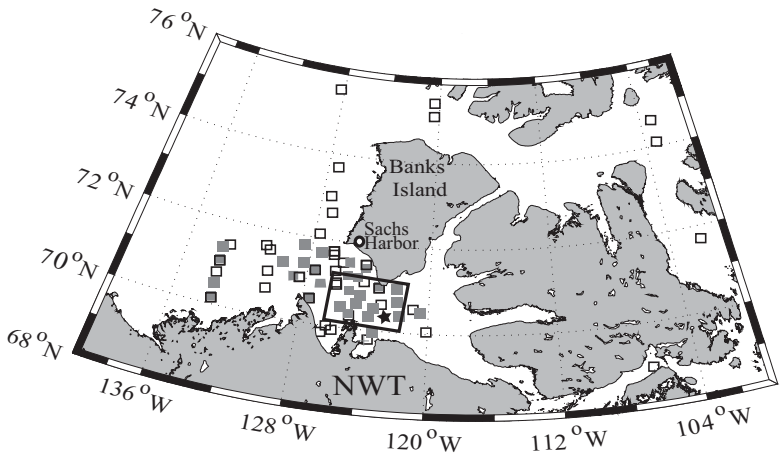

Figure 7.2: Locations of sampling stations occupied from October 2007 to August 2008, and the limits of the budgeting area containing the surface and subsurface layers in Amundsen Gulf (box). The open black squares indicate stations occupied only once, and the closed gray squares indicate stations occupied more than once. The station indicated by the star (70.6°N, 122.4°W) was occupied many times and seasonal profiles from this location are presented in Fig. 7.7.

reproducibility was better than 1 μmol kg^{-1} and 2 μmol kg^{-1}, respectively. Following the determination of DIC and TA, the in-situ partial pressure of CO_2 (pCO_2), pH (on the total scale), and aragonite saturation state (Ω_{Ar}) were computed, using the standard set of carbonate system equations, excluding nutrients, with the CO_2Sys program of *Lewis and Wallace* (1998). We used the equilibrium constants of *Mehrbach et al.* (1973) refit by *Dickson and Millero* (1987). The calcium (Ca^{2+}) concentration was assumed to be conservative and calculated from salinity.

In addition to rosette samples, sea-ice samples were collected for DIC and TA analysis from December to June. The ice was cored using a 9-cm diameter corer (Mark II, Kovacks Enterprises, Inc.), and the cores were immediately laid out on an area of ice that had been cleared of snow. The top, middle, and bottom 10 cm of the ice core were cut with a steel saw and placed in plastic bags (Tedlar ©) with a few micro-liters of saturated $HgCl_2$ solution to halt biological activity. The bag was sealed and air was withdrawn with a vacuum pump. These bags are gas impermeable, with a clamp-type closure seal and small spigot for withdrawing air or water. The core sections were allowed to thaw, and the sample was then delivered directly from the bag, via the spigot, to the VINDTA for DIC and TA analysis as described above.

Dissolved organic carbon (DOC) samples were collected directly from the rosette. An

acid-washed plastic syringe was mounted directly on the rosette port to collect the sample. The sample was then passed through an acid-washed Swinnex filter holder containing a 25 mm GF/F filter combusted at 450°C for 24 h. The first 5-10 mL of sample were discarded and the rest was poured into an acid-washed, pre-combusted borosilicate glass sample bottle. Each sample was immediately acidified 200 μL of 50% H_3PO_4 per 40 mL of sample. Samples are stored in amber EPA glass vials sealed with an acid-washed teflon-lined septa and cap at 4°C. Measurements of DOC were carried out at the Freshwater Institute (Winnipeg, Manitoba) by high-temperature catalytic combustion, on a Shimadzu total organic carbon analyzer, according to procedures described by Dickson et al. (2007). DOC measurements were systematically checked against reference material low-carbon water (ca. 2 μmol L^{-1} DOC) and deep Sargasso Sea reference water (ca. 44-47 μmol L^{-1} DOC) (provided by D. A. Hansell, University of Miami).

Nutrient samples were collected in acid-washed 15-mL polypropylene tubes. A 5.0 μm polycarbonate filter, mounted on a 47-mm filter holder, was attached directly to the sampling bottle to remove large particles. Colorimetric determinations of nitrate (NO_3^-), and silicate (Si) were performed on an Autoanalyzer 3 using routine methods (*Grasshoff*, 1999). Analytical detection limits were 0.03 μmol L^{-1} for NO_3^-, and 0.1 μmol L^{-1} for Si.

The pCO_2 of the surface waters, for the computation of air-sea CO_2 fluxes, was measured using a continuous flow equilibration system (*Körtzinger et al.*, 1996). The detection of pCO_2 was made by a non-dispersive, infrared spectrometer (LiCor, LI-7000). The system was located in the engine room of the ship and the intake depth was approximately 3 meters below the water surface. Measurements were made every minute and used to compute hourly averages. The system was calibrated daily with both a CO_2-free reference gas (N_2) and a CO_2 calibration gas provided by the U.S. National Oceanic and Atmospheric Administration (NOAA). The temperatures at the intake and at the equilibrator were monitored and the pCO_2 corrected to account for warming of the water in transit to the equilibrator. The data were corrected to in-situ water temperature and to 100% humidity. The relationship between the underway pCO_2 measurements and the computed pCO_2 from discrete DIC and TA had a slope of roughly 1:1, which was significant at a confidence interval of $> 99\%$. There was a slight positive offset (+24 μatm), with the measured pCO_2 consistently higher than the computed values. The offset was not

statistically significant at a confidence interval of 90%. The most frequent problem encountered with the pCO_2 measurement was low flow through the system, typically caused by ice blockage in the intake line. A second (less common) problem was pressure spikes in the LI-7000 caused by blockages of air lines. In both cases, these pCO_2 data were removed from the dataset. Atmospheric $\mathrm{pCO_2}$ was measured by a non-dispersive, open path infra-red $\mathrm{CO_2}$ analyzer (LiCor, LI-7500) mounted on a meteorological tower on the ship's foredeck; air temperature was measured simultaneously. The atmospheric pCO_2 were processed to remove any measurements when the ship's exhaust might have been blowing over the tower. Hourly wind data measured by Environment Canada at the Sachs Harbor meteorological station (71.99°N, 125.25°W, see Fig. 7.2) at a height of 10 meters were used to compute the gas transfer velocity using the formulation of *Wanninkhof* (1992).

7.4.2 Model Description

A region in central Amundsen Gulf was defined (from 122°W to 126°W, and from 70°N to 71.5°N), and divided into a surface and subsurface box (Figs. 7.1 and 7.3). The surface box extends from 0 to 50 meters, whereas the subsurface box extends from 50 to 300 meters. The region covers an area of roughly $1.7\times10^{10}\ \mathrm{m}^2$, and the surface and subsurface layers have a volume of approximately $8.4 \times 10^{11}\ \mathrm{m}^3$ and $5.0 \times 10^{12}\ \mathrm{m}^3$ respectively.

The annual cycles of DIC, TA, and other hydrographic variables, was reconstructed using data collected from October 2007 through December 2007, and January through August 2008. The temporal resolution chosen for the inorganic carbon budget presented here is monthly, and the September values were computed as the mean of the months of August and October. The concentration of DIC and TA were calculated for each station for both the upper (50 m) and lower (50-300 m) layers of the water column, and the average of all stations occupied in a month was computed. Sampling took place weekly during the winter season, and increased to twice weekly, then daily in the spring, summer and autumn. Accordingly, the monthly DIC and TA concentrations computed for the surface and deep boxes relied on 15 to 80 measurements, depending on the number of stations sampled per month and the vertical sampling resolution. We assume that the (computed) monthly mean observed DIC and TA concentrations are spatially homogeneous within the box and valid over the entire month. The changes in DIC and TA from one month to the next were computed by difference and are denoted $\Delta\mathrm{DIC_{obs}}$ and $\Delta\mathrm{TA_{obs}}$.

Changes in DIC and TA result from both physical and biological processes, with biological changes having a lesser influence on TA than on DIC. Photosynthesis, and respiration, and the formation of calcium carbonate ($CaCO_3$) are biologically mediated processes affecting both DIC and TA. Lateral and vertical advection, diffusion, and air-sea exchange of CO_2 are physical processes, the latter only influencing DIC concentration. A schematic representation of the 2-box model used here and the processes affecting DIC concentration are shown in Fig. 7.3. The methods used to quantify the changes in DIC and TA due to the various processes are detailed in the following sections.

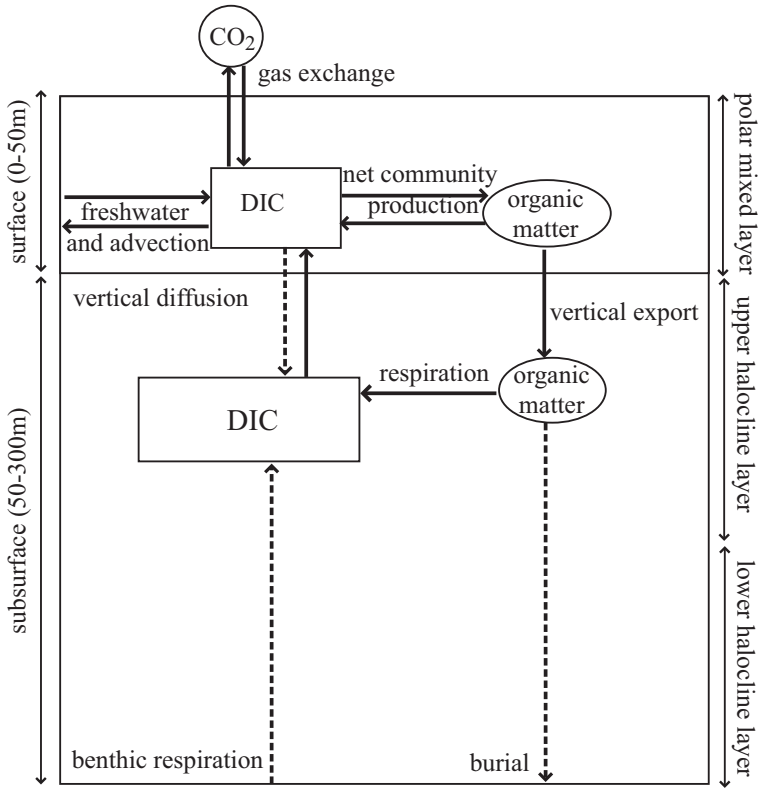

Figure 7.3: Schematic representation of the two-box model used to compute the monthly changes in DIC (and TA) due to: lateral advection, freshwater input, air-sea exchange, vertical diffusion and biology. The solid arrows indicate the dominant processes, while the dashed arrows represent secondary processes. The surface and subsurface layers are indicated (left hand side) along with the locations of the dominant water masses (right hand side).

7.4.3 Advection

Contrary to the general west-to-east flow through the Arctic Archipelago (*McLaughlin et al.*, 2005), recent in-situ current measurements reveal that Amundsen Gulf exports

more water to the Beaufort Sea than it receives (*Lanos*, 2009). There is a weak surface flow (0.002 Sv) into Amundsen Gulf from the west, but the circulation in the Gulf is dominated by a subsurface (below 50 m) flow with an annual mean value of 0.19 Sv towards the Beaufort Sea (*Lanos*, 2009). *Lanos* (2009) suggests that the source of this water is McClure Strait and that it enters Amundsen Gulf from the north via the Prince of Whales Strait separating Banks and Victoria Island. The annual mean (net) water mass transports of *Lanos* (2009) were used to compute the contribution from lateral advection. The subsurface box receives 6.0×10^{12} m^3 of water per year (5.0×10^{11} m^3 month^{-1}) flowing towards the Beaufort Sea. The surface box receives 6.3×10^{10} m^3 per year (5.3×10^9 m^3 month^{-1}) from the Southern Beaufort Sea and the Mackenzie Shelf. The flushing time for the surface and subsurface boxes are roughly 14 and 19 months respectively. These values are in general agreement with literature values for the region (*Bates and Mathis*, 2009).

Multiplying the monthly volume transport by the DIC concentrations at stations located east of the subsurface box and west of the surface box gives the monthly contribution to the total change in DIC due to lateral advection. For the subsurface box, DIC concentrations for stations located just outside the area of interest were available for the months of February, April, and July 2008, and October 2007. It was assumed that the resulting differential between two locations, on the order of 35 $\mu\mathrm{mol}$ kg^{-1}, were valid over the season, (i.e., the same DIC concentration gradient was used for three months), and a fraction of the volume in the subsurface box was exchanged to reflect the 19-month flushing time. The advective change in TA was computed using the same method. A comparison of the surface DIC concentration inside the budgeting area with the surface concentration at stations immediately to the west revealed only a small concentration differential (ca. 1 $\mu\mathrm{mol}$ kg^{-1}) throughout the year; the change in DIC and TA due to lateral advection in the surface layer was therefore neglected. Furthermore, the dominant effect in the surface box resulted from to the addition or removal of freshwater, which was quantified independently.

Horizontal advection is not perfectly constrained in the model by empirically estimating horizontal transport with observed volume transport and horizontal concentration gradients. This method does not allow for a complete description of lateral processes in the region, however, the inclusion of the horizontal advection term in the 1-D approach used

here allows changes due to transport and biology, often grouped together (*Olsen et al.*, 2008; *Omar et al.*, 2010), to be separated.

7.4.4 Freshwater

The surface waters of the Amundsen Gulf region, and the Arctic shelves in general, are heavily influenced by the addition (and removal) of freshwater, both from river runoff and from the melting (and formation) of sea-ice. Whereas runoff from the Mackenzie River contributes significantly to the input of terrestrial freshwater in the North American sector of the Arctic, much of this runoff is directed to the west, making its way into the surface waters of the Beaufort Gyre (*Macdonald et al.*, 2002; *Yamamoto-Kawai and Tanaka*, 2005). In contrast, the freshwater input to Amundsen Gulf is dominated by the formation and melting of sea-ice, with runoff playing a more minor role (*Tremblay et al.*, 2008; *Lanos*, 2009). This is also reflected in the lack of terrigenous material accumulation in the Amundsen Gulf sediments (*Magen et al.*, 2010).

Salinity-dependent changes in DIC can be quantified by analyzing the relationship between the seasonal (or monthly) changes in DIC and salinity (*Thomas and Schneider*, 1999; *Bozec et al.*, 2006). Nevertheless, because changes in surface DIC concentration are also influenced by salinity-independent processes (i.e., air-sea exchange of CO_2, and biological activity), we quantified the influence of freshwater sources from the relationship between monthly changes in surface salinity and surface TA concentration. TA is also influenced by biological processes (nutrient consumption and regeneration through photosynthesis and respiration), but the effect is less significant than for DIC.

We computed the differences in surface salinity (dS) and surface TA (dTA), for all re-occupations of stations in the region. For instance, each point (dS, dTA), plotted in Fig. 7.4, was generated from the difference between the surface salinity and surface TA at one particular station in October and November. Changes are positive, indicating increase in salinity (dS>0) and TA (dTA>), or negative, indicating a decrease in salinity (dS<0) and TA (TA<0). Null values of dS indicate that the surface salinity remained constant between the two occupations of one particular station. The plot of all values of (dS, dTA) reveals a linear relationship between the two variables (n= 27, r^2= 0.86, p <0.01) (Fig. 7.4), and the slope represents the change in TA due to the change in salinity with a standard error of 4.7 μmol kg^{-1}. We computed the ratio between DIC and TA for the monthly mean surface concentrations and multiplied this ratio by the expected change

in TA due to the change in salinity, to obtain the change in DIC due to the addition (or removal) of freshwater.

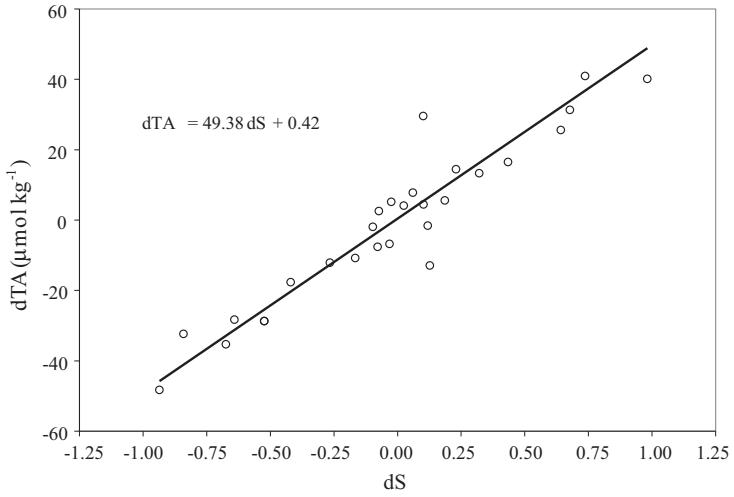

Figure 7.4: Changes in surface TA (dTA) versus changes in surface salinity (dS), for repeated, monthly or seasonal, occupations of the same stations. The slope of the best-fit line (n=27, r^2= 0.86, $p<0.01$) represents the change in TA due to the change in salinity. The changes in TA not due to changes in salinity (i.e. biological processes) are represented by the y-intercept, which in this case is not different from zero.

The contribution from river runoff was incorporated in the freshwater addition or removal term; the computation of the change in DIC (and TA) due to freshwater is based on changes in surface salinity and, therefore, implicitly includes contributions from both sea-ice and runoff. A linear regression of DIC (and TA) versus salinity (see Fig. 7.5) yields y-intercepts, or zero-salinity end-members of DIC(S=0) = 649 μmol kg^{-1} and TA(S=0) = 797 μmol kg^{-1}, much smaller than the concentrations of samples collected in the Mackenzie River in July: DIC(Mackenzie) = 1786 μmol kg^{-1} and TA(Mackenzie) = 1880 μmol kg^{-1}. The DIC and TA concentration in sea-ice however ranges from 300 to 600 μmol kg^{-1}, indicating a stronger contribution from sea-ice melt than from runoff.

7.4.5 Air-Sea CO_2 Flux

The air-sea CO_2 flux, F_{CO_2} (mol C m^{-2} month^{-1}), was computed using the following equation:

$$F_{CO_2} = k\alpha\Delta pCO_2, \tag{7.1}$$

where k (cm hr^{-1}) is the gas transfer velocity, parameterized as a function of the Schmidt number of the gas and the wind speed, α is the in-situ CO_2 solubility (*Weiss et al.*, 1982),

and ΔpCO_2 (μatm) is the gradient in pCO_2 between the ocean and the atmosphere, as measured by the underway system. The gas transfer velocity, k, was computed using, hourly winds measured on board and the formulation of Wanninkhof (1992). A positive flux implies a transfer from the atmosphere into the ocean. The hourly fluxes were averaged spatially over the area of the surface box and integrated over one month, representing the monthly change in DIC due to the air-sea exchange of CO_2.

The CO_2 fluxes were computed assuming ice-free conditions and then scaled using a multiplier equal to 100% minus the percentage ice cover following *Bates* (2006) and *Mucci et al.* (2010) (see Table 7.1). This method assumes that sea-ice is an effective barrier to air-sea gas exchange, and that the resulting air-sea fluxes of CO_2 are a linear function of sea-ice cover. Several recent studies have suggested that sea-ice does not fully inhibit air-sea exchange of biogenic gases (*Semiletov et al.*, 2004; *Loose et al.*, 2009). However, the mechanisms controlling the CO_2 transfer through sea-ice likely differ from those controlling air-sea gas exchange and have not yet been adequately parameterized. Sea-ice cover was estimated using monthly ice cover images from the Canadian Ice Service[2].

Table 7.1: Monthly estimates of percente ice-cover in the budgeting area in Amundsen Gulf.

month	1	2	3	4	5	6	7	8	9	10	11	12
% ice-cover	100	100	100	100	80	10	0	0	10	20	90	100

7.4.6 Diffusion

The (vertical) diffusive fluxes of DIC and TA from the deep box into the surface box, were computed using the following equation,

$$F_d = K_v \times \frac{dDIC}{dz}\rho, \tag{7.2}$$

where F_d (μmol kg^{-1} month^{-1}) is the diffusive flux, K_v (m^2 s^{-1}) is the coefficient of vertical diffusion, and $dDIC/dz$ (μmol kg^{-1} m^{-1}) is the vertical gradient of DIC at the boundary between the surface and subsurface layer, and ρ (kg m^{-3}) is the seawater density. Several estimates of vertical diffusion in the Arctic region have been made (*Munk*,

[2]Canadian Ice Service (http://www.ec.gc.ca/glaces-ice/)

1966; *Rudels et al.*, 1996; *Meincke et al.*, 1997). We used a constant value, (K_v = 1.1 × 10^{-6} m^2 s^{-1}), from *Rudels et al.* (1996).

7.4.7 Biological Processes

The net effect of biological processes on the monthly variation in DIC in the surface layer was estimated by the difference between the total observed change and the sum of the changes due to: freshwater (ΔDIC_{fw}), air-sea CO_2 flux (ΔDIC_{as}), and vertical diffusion (ΔDIC_{vd}):

$$\Delta DIC^{s}_{bio} = \Delta DIC_{obs} - (\Delta DIC_{fw} + \Delta DIC_{as} + \Delta DIC_{vd}) + \psi_s. \tag{7.3}$$

The last term on the right-hand side, ψ_s, represents the error, with the subscript 's' indicating the surface layer. The ψ term includes the uncertainty associated with each of the terms in Equation 7.3. The net effect of biological processes was similarly estimated for the subsurface (ΔDIC^{d}_{bio}), excluding the effects of freshwater and air-sea exchange, but including advection (ΔDIC_{adv}):

$$\Delta DIC^{d}_{bio} = \Delta DIC_{obs} - (\Delta DIC_{adv} + \Delta DIC_{vd}) + \psi_d, \tag{7.4}$$

with ψ_d representing the uncertainty, and the subscript 'd' referring to the subsurface layer. The resulting ΔDIC_{bio} terms include the effect of photosynthesis and respiration, the formation and dissolution of biogenic calcium carbonate ($CaCO_3$) and, in the case of the subsurface box, exchanges of carbon with the sediments. The particulate organic carbon (POC) flux in a near-shore region of the neighboring Franklin Bay is 6.8 g C m^{-2} yr^{-1} at a depth of 200 m (*Forest et al.*, 2008). Estimates of primary production in the Amundsen Gulf region range from 90 to 175 g C m^{-2} yr^{-1} (*Arrigo and van Dijken*, 2004); the POC flux at 200 m thus accounts for between 4% and 8% of primary production. Carbon losses due to burial in the sediments, at a depth of 350 to 380 meters thus accounts for a small percentage of primary production, and was assumed negligible over the annual time scale of interest (*Mucci et al.*, 2008). Furthermore, it has been shown that in Amundsen Gulf sediment hardly accumulates (*Richerol et al.*, 2008; *Macdonald et al.*, 1998). Respiration of organic matter in the surface sediments may be considered a source of DIC and TA to the water column immediately above the sediments (*Fennel et al.*, 2008; *Thomas et al.*, 2009a); the possible contribution to the subsurface DIC (and TA) budget

has been neglected. The biological contribution to the monthly changes in TA, in both the surface and subsurface layers, were computed with the following equations:

$$\Delta \mathrm{TA}^{\mathrm{s}}_{\mathrm{bio}} = \Delta \mathrm{TA}_{\mathrm{obs}} - (\Delta \mathrm{TA}_{\mathrm{fw}} + \Delta \mathrm{TA}_{\mathrm{vd}}) + \chi_{\mathrm{s}} \tag{7.5}$$

$$\Delta \mathrm{TA}^{\mathrm{d}}_{\mathrm{bio}} = \Delta \mathrm{TA}_{\mathrm{obs}} - (\Delta \mathrm{TA}_{\mathrm{adv}} + \Delta \mathrm{TA}_{\mathrm{vd}}) + \chi_{\mathrm{d}}, \tag{7.6}$$

where χ_{s} and χ_{d} represent the uncertainty for the surface and subsurface layer respectively, as described above.

7.4.8 Error Estimation

The uncertainty associated with the observed monthly changes in DIC and TA (i.e. $\Delta \mathrm{DIC}_{\mathrm{obs}}$ and $\Delta \mathrm{TA}_{\mathrm{obs}}$ ranges from 2 to 3 μmol kg^{-1} in line with the uncertainty associated with the measurement of DIC and TA; however, averaging within the budgeting area may increase the uncertainty associated with the observed monthly changes. The uncertainty associated with the freshwater term is estimated from the standard error in the computation of dTA from dS (see Fig. 7.4 and Section 7.4.4) and is roughly 5 μmol kg^{-1}.However, since changes in TA may be independent of salinity (i.e. nutrient uptake or regeneration during biological production or respiration), the standard error in the relationship between dTA and dS should be considered a lower limit on the uncertainty associated with changes in DIC due to freshwater inputs ($\Delta \mathrm{DIC}_{\mathrm{fw}}$). The uncertainty associated with the air-sea flux term is relatively high (20%, or roughly 1.5 μmol kg^{-1}) and is largely due to uncertainty in the parameterization of the gas transfer velocity (*see*Eq. 1) (*Naegler et al.*, 2006; *Sweeney et al.*, 2007; *Watson et al.*, 2009). The uncertainty associated with the vertical diffusion term is quite high ($\pm$ 100%), reflecting the range in estimates of $\mathrm{K_v}$, but the contribution from vertical diffusion is small, resulting in an error of less than 2μmol kg^{-1}. The uncertainty associated with the horizontal advection term is also large ($\pm$50%, or roughly 1μmol kg^{-1}) due to the large error reported by *Lanos* (2009) on the annual mean water transports in Amundsen Gulf. Propagation of the above uncertainties results in an uncertainty for the (computed) surface $\Delta \mathrm{DIC}^{\mathrm{s}}_{\mathrm{bio}}$ term of roughly 6 μmol kg^{-1}, and for the subsurface $\Delta \mathrm{DIC}^{\mathrm{d}}_{\mathrm{bio}}$ of roughly 3 μmol kg^{-1}. The resulting uncertainty in the $\Delta \mathrm{TA}^{\mathrm{s}}_{\mathrm{bio}}$ term is roughly 6 μmol kg^{-1}.

We estimated ψ and χ by means of Monte Carlo simulations of $\Delta \mathrm{DIC}_{\mathrm{bio}}$ and $\Delta \mathrm{TA}_{\mathrm{bio}}$,

and assume that the standard deviation of the simulated series yield reasonable estimates of ψ and χ. The inputs for the simulation were randomly generated from distributions which most closely match the data; 10,000 points were chosen randomly for each of the model variables (i.e. each of the terms on the right-hand sides of Eqs. 7.3 to 7.6), using a random number generator. Following a test for normality and uniformity, the observed monthly changes, and the changes due to freshwater were represented by normal distributions. A uniform distribution was used to represent the air-sea flux, vertical diffusion, and advection terms. The uniform distribution requires the maximum value, while the normal distribution requires the mean and standard deviation; these values were taken from the monthly values of each of the terms on the right hand sides of Equations 7.3 to 7.6. For example, the following equation was used to compute the uncertainty associated with $\Delta\mathrm{DIC}^{\mathrm{s}}_{\mathrm{bio}}$:

$$\psi_{\mathrm{s}} = \mathrm{M}_{\mathrm{obs}} - \mathrm{M}_{\mathrm{fw}} - \mathrm{M}_{\mathrm{as}} - \mathrm{M}_{\mathrm{vd}}, \tag{7.7}$$

where 'M' indicates the randomly generated series. The equation was solved 10,000 times, and the standard deviation used as the magnitude of ψ_{s}. The resulting uncertainties associated with the surface and subsurface estimates of $\Delta\mathrm{DIC}_{\mathrm{bio}}$ and $\Delta\mathrm{TA}_{\mathrm{bio}}$ are summarized in Table 7.2.

Table 7.2: Estimates of the uncertainty associated with the monthly computation of surface and subsurface values of $\Delta\mathrm{DIC}_{\mathrm{bio}}$ and $\Delta\mathrm{TA}_{\mathrm{bio}}$ using a depth of 50 m for the surface layer and 250 m for the subsurface layer (see also Eqs. 7.3 to 7.7).

Term	Error [μmol kg^{-1} month^{-1} (mol m^{-2} month^{-1})]
ψ_{s}	9.0 (0.5)
ψ_{d}	1.0 (0.3)
χ_s	11.0 (0.6)
χ_{d}	1.0 (0.3)
ϵ_s	1.0 (0.5)

7.4.9 Dissolved Organic Carbon

The observed, monthly, changes in DOC were computed analogously to changes in DIC and TA using the method described in Section 7.4.2. Mixed-layer DOC concentrations are influenced by the addition and removal of freshwater. As discussed in Section 7.4.4,

the freshwater input to Amundsen Gulf is dominated by the formation and melting of sea-ice. The salinity-dependent changes in DOC were computed by multiplying the monthly value of $\Delta\mathrm{DIC_{fw}}$ by the ratio of DOC to DIC in sea-ice (melting), or by the monthly ratio of DOC to DIC in the surface waters (formation). A constant value of DIC in sea-ice (350 μmol kg^{-1}) was computed from the mean of all bottom 10 cm ice samples (see Section 7.4.1). A constant value of DOC in sea-ice (64 $\mu\mathrm{mol\ kg^{-1}}$), which is the average value of samples measured in February and March in the same region by *Riedel et al.* (2008), was used. These measurements reflect bottom ice-DOC concentration, and may therefore potentially over estimate DOC in ice melt. The diffusive flux, from the surface to the subsurface box, were computed as described in Section 7.4.6 (Eq. 7.2).

DOC is produced by a host of biological processes, including excretion by zooplankton, direct release by phytoplankton and the lysis of algal or bacterial cells. This DOC may be mixed downward, or remineralized to inorganic carbon making a positive contribution to biologically mediated changes in surface DIC (i.e. $\Delta\mathrm{DIC_{bio}} > 0$). In the subsurface waters, labile DOC is remineralized, while biologically refractory material may accumulate (*Hansell and Carlson*, 2001).

A similar approach to that described in Section 7.4.7 was used to compute the change in mixed-layer DOC due to biological processes using the following equation:

$$\Delta\mathrm{DOC^{s}_{bio}} = \Delta\mathrm{DOC_{obs}} - (\Delta\mathrm{DOC_{fw}} + \Delta\mathrm{DOC_{vd}}) + \epsilon_{\mathrm{s}}, \tag{7.8}$$

where ϵ_{s} is the uncertainty. We estimated ϵ_{s} via the Monte Carlo simulation described in Section 7.4.8, and the value is given in Table 7.2.

7.5 Results

The relationships between DIC and salinity, and TA and salinity for the study area are shown in Fig. 7.5. In the upper 50 meters of the water column, the salinity in the PML ranged from roughly 28 to greater than 31. Over the same depth range, the minimum DIC and TA concentrations were roughly 1900 and 2000 μmol kg^{-1} respectively, and the maximum DIC and TA concentrations (in the PML) were roughly 2150 and 2250 μmol kg^{-1} respectively. Beneath the PML, the salinity range in the UHL extended from roughly 32 to 33.5. In this Pacific-origin layer, the maximum water column DIC concentrations of

2240 μmol kg^{-1} were observed. In the UHL, TA ranged from 2240 to 2290 μmol kg^{-1}. The deepest waters were comprised of Atlantic-origin LHL waters and the salinity ranged from 33.5 to 35. The maximum TA concentration (2305 μmol kg^{-1}) was coincident with the salinity maximum. DIC concentrations ranged from 2230 μmol kg^{-1} (at S=33.5) to 2165 μmol kg^{-1} at S=35. TA displayed nearly conservative behavior with the slope of the linear relationship between TA and salinity changing with respect to the water mass. The relationship between DIC and salinity on the other hand was nearly conservative within the PML, and non-conservative in the deeper water column, implying the dominance of a process other than mixing between the UHL and LHL waters. The non-linear, or bow-shaped, relationship between DIC and salinity in the UHL and LHL waters will be explored in more detail (see Section 7.6.1).

The relationship between salinity-normalized DIC ($\mathrm{DIC_{norm}} = 35\mathrm{DIC/S}$) is shown in Fig. 7.5c and the relationship between salinity-normalized TA ($\mathrm{TA_{norm}} = 35\mathrm{TA/S}$) is shown in Fig. 7.5d. The normalization of DIC (and TA) to a constant salinity removes the effect of freshwater inputs from the measured concentrations. Variability in the salinity normalized concentrations are thus primarily controlled by water temperature (i.e., by the solubility of CO_2), biological processes, air-sea exchange of CO_2, and mixing of water masses. The relationship between $\mathrm{DIC_{norm}}$ and salinity (Fig. 7.5c) indicates that biology dominates at low salinity (S$<$32, the upper 50 meters of the water column, or the PML). Additional influences of mixing and air-sea exchange, with a relatively small range of $\mathrm{DIC_{norm}}$ from roughly 2300 μmol kg^{-1} to 2350 μmol kg^{-1} also occur over this salinity (and depth) range. In the subsurface layer, mixing and biological processes dominate over the salinity range of 32$<$S$<$35 with $\mathrm{DIC_{norm}}$ ranging from a maximum of roughly 2300 μmol kg^{-1} (near S=32) and a minimum of 2175 μmol kg^{-1} at salinities of roughly S=35 (see Section 7.6.1).

The relationship between DIC and TA is shown in Fig. 7.5e. The ratio between DIC and TA is roughly 1:1 in the PML. This ratio increases to 1.2:1 in the UHL; respiration, or the remineralization of organic matter produced in the surface layer, or PML, occurs primarily in the UHL increasing DIC and also the ratio of DIC:TA. In the LHL, the TA continues to increase (relative to the PML and UHL) primarily as a function of increasing salinity. DIC in the LHL is reduced, relative to the UHL due to the reduction of respiration, or remineralization of organic matter, as a function of depth. The Pacific-origin UHL waters

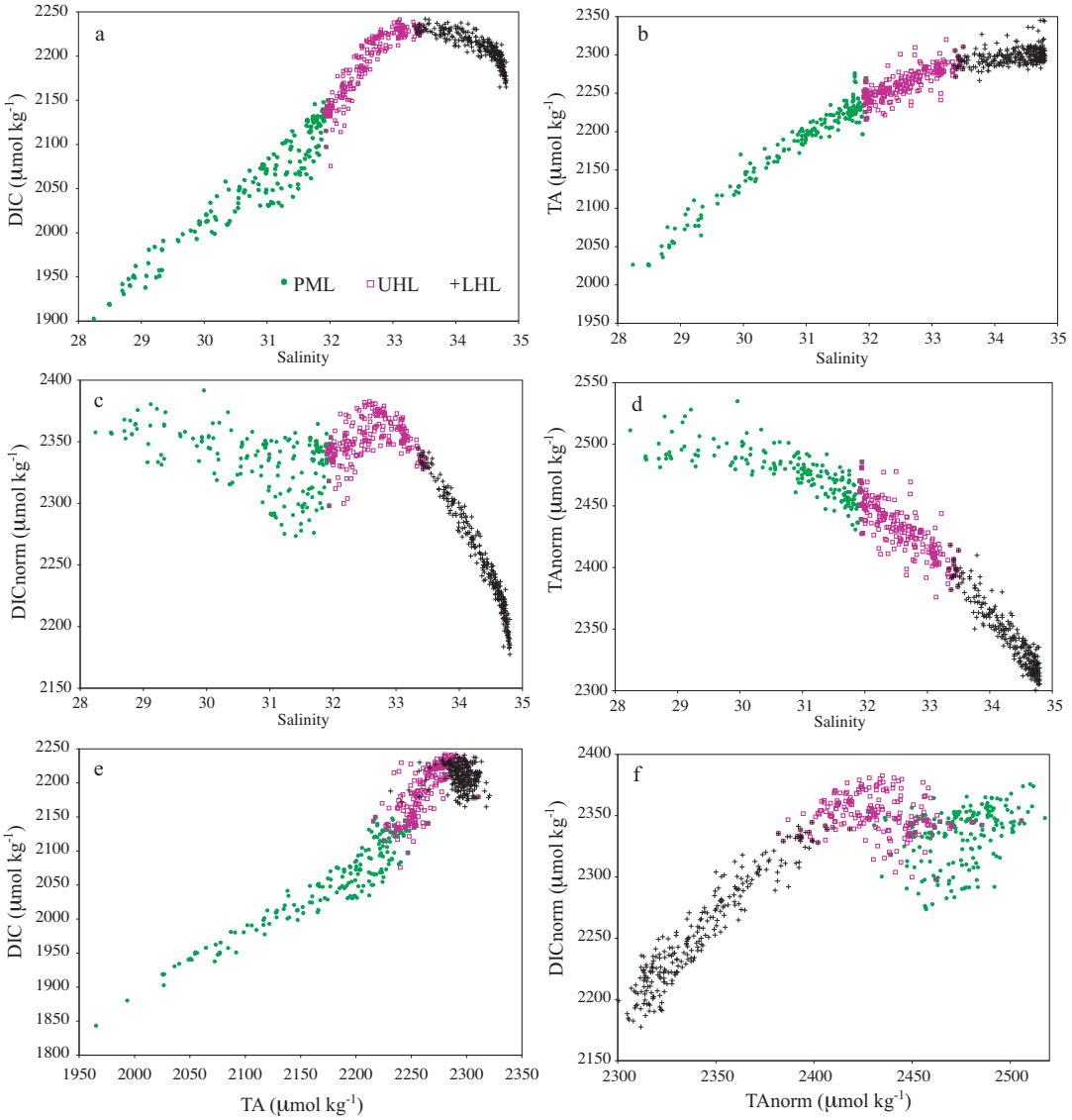

Figure 7.5: The relationship between (a) DIC and salinity (b) TA and salinity (c) DIC_{norm} and salinity (d) TA_{norm} and salinity (e) DIC and TA and (f) DIC_{norm} and TA_{norm} with the three water masses indicated. A salinity of S=35 was used in the normalization. Linear regression of DIC and TA with salinity reveals the y-intercepts, or zero-salinity end members with DIC(S=0) = 649 μmol kg^{-1} (n=300, r^2=0.7), and TA(S=0)=797 μmol kg^{-1} (n=300, r^2=0.7).

have the highest concentrations of DIC, while the most saline Atlantic-origin LHL waters have the highest concentration of TA with lower DIC relative to the UHL. The relationship between $\mathrm{DIC_{norm}}$ and $\mathrm{TA_{norm}}$ is shown in Fig. 7.5f. With the effect of freshwater addition and removal discarded from the observed concentrations biological processes dominate in the PML while the lower water column is dominated by mixing, indicated by the nearly 1:1 relationship between $\mathrm{DIC_{norm}}$ and $\mathrm{TA_{norm}}$ in the LHL and UHL

7.5.1 Annual Cycles

The annual cycles of water column salinity, temperature, DIC, TA, $\mathrm{pCO_2}$, pH, Ω_{Ar}, and the Revelle Factor are plotted in Fig. 7.6. The water temperature (Fig. 7.6b) was relatively homogeneous both with depth and throughout the year, with values ranging from roughly -1.5°C to 1.5°C. During the brief summer season ice retreat allowed a warming of the near-surface waters to 7°C or 8°C. In the salinity profile (Fig. 7.6a), the effect of sea-ice formation and melt was clearly seen in the upper (PML) water column. Below the PML is the Pacific-origin upper halocline layer (UHL) which overlies the saline Atlantic water mass. This structure is also reflected in the DIC profile (Fig. 7.6c), where lower concentrations, with large seasonal variations, were seen at the surface, due both to the input and removal of freshwater, and to the carbon draw-down by photosynthesis. High DIC concentrations in the UHL result from the export and remineralization of organic matter from the surface layer (Fig. 7.6e), and also reflects the presence of older Pacific source-water in this layer. Maximum values of $\mathrm{pCO_2}$, and minimum values of pH and Ω_{Ar}, are also found within this depth range (Fig. 7.6d - f). The seasonal changes in TA (Fig. 7.6d), generally followed the same surface patterns as DIC and salinity. The formation and melting of sea-ice exerts a significant control on surface concentrations of both DIC and TA. Unlike river water which adds freshwater as well as relatively high concentrations of DIC and TA (on the order of 1800 μmol kg^{-1}) to the system, sea-ice melt-water contains much lower concentrations of DIC and TA (on the order of 300 μmol kg^{-1}) and dilutes the surface waters, reducing the concentration of DIC and TA. Conversely, the formation of sea-ice removes fresh water leaving salinity, a process referred to as brine rejection, and DIC and TA behind, concentrating the surface waters with respect to salinity, DIC and TA. The rejected brine is more dense than the surrounding waters and sinks; this process provides a potential export pathway for carbon from the surface waters. If the high salinity, and DIC-rich brine, sinks below the PML the carbon contained in the brine

is potentially sequestered from the surface layer and from exchange with the atmosphere (*Bates*, 2006; *Bates and Mathis*, 2009). Changes in DIC and TA due to the melting and formation of sea-ice will be discussed in more detail in Section 7.5.2.

Surface $\mathrm{pCO_2}$ was undersaturated with respect to the atmosphere throughout the year within the study area. There was a decrease in $\mathrm{pCO_2}$ and DIC (and an increase in pH) corresponding to the growth of under-ice algae (*Riedel et al.*, 2006), between day of year (DOY) 100 and DOY 150, before the onset of sea-ice melt following DOY 150. The growth of phytoplankton in sea-ice decreases the $\mathrm{pCO_2}$ by consuming DIC. The DIC concentration in the bottom 10 cm of ice decreased from 384 $\mu\mathrm{mol\ kg^{-1}}$ on DOY 115, to to 319 $\mu\mathrm{mol\ kg^{-1}}$ on DOY 130 at the same station (see Table 7.3). After DOY 200, the ice began to melt and much lower concentrations of DIC in the ice (roughly 180 μmol kg^{-1}) were observed. There was an increase in $\mathrm{pCO_2}$ and decrease in pH in the surface waters following DOY 200, after the ice had begun to melt, and the summer phytoplankton bloom had depleted the surface water DIC. The open water bloom coincided with the peak Mackenzie River discharge to the region. The Mackenzie River has relatively high DIC (1786 μmol kg^{-1}) and TA (1880 μmol kg^{-1}) concentrations, as well as a large pool of particulate organic carbon (POC) (*Macdonald et al.*, 1987). With a $\mathrm{pCO_2}$ of roughly 700 μatm, runoff from the Mackenzie River is supersaturated with respect to the atmosphere (*Vallières et al.*, 2008). However, we detected only a very small contribution of runoff from the Mackenzie River in Amundsen Gulf. This short lived increase in $\mathrm{pCO_2}$, and corresponding decrease in pH is the result of the brief summer warming of the surface waters (Fig. 7.6b). The thermodynamic effect of temperature on seawater $\mathrm{pCO_2}$ results in a $\mathrm{pCO_2}$ increase of roughly 4% for each 1°C increase in temperature (*Takahashi et al.*, 2002). The warming of the surface waters from 1°C to 8°C would increase $\mathrm{pCO_2}$ by roughly 90 μatm (with an initial value of 325 μatm). Over the same period one would expect a corresponding decrease in surface water Ω_{ar}, however, the decrease is buffered by the phytoplankton bloom which increases the saturation state in the surface layer by the uptake of inorganic carbon.

Seasonal profiles from repeated (October, February, May and July), occupations of the same station (indicated by the x in Fig. 7.2) are presented in Fig. 7.7. Each of these profiles are mean values generated from between 2 and 4 occupations of the station within a given season. Subsurface salinity and DIC and TA concentrations were fairly constant

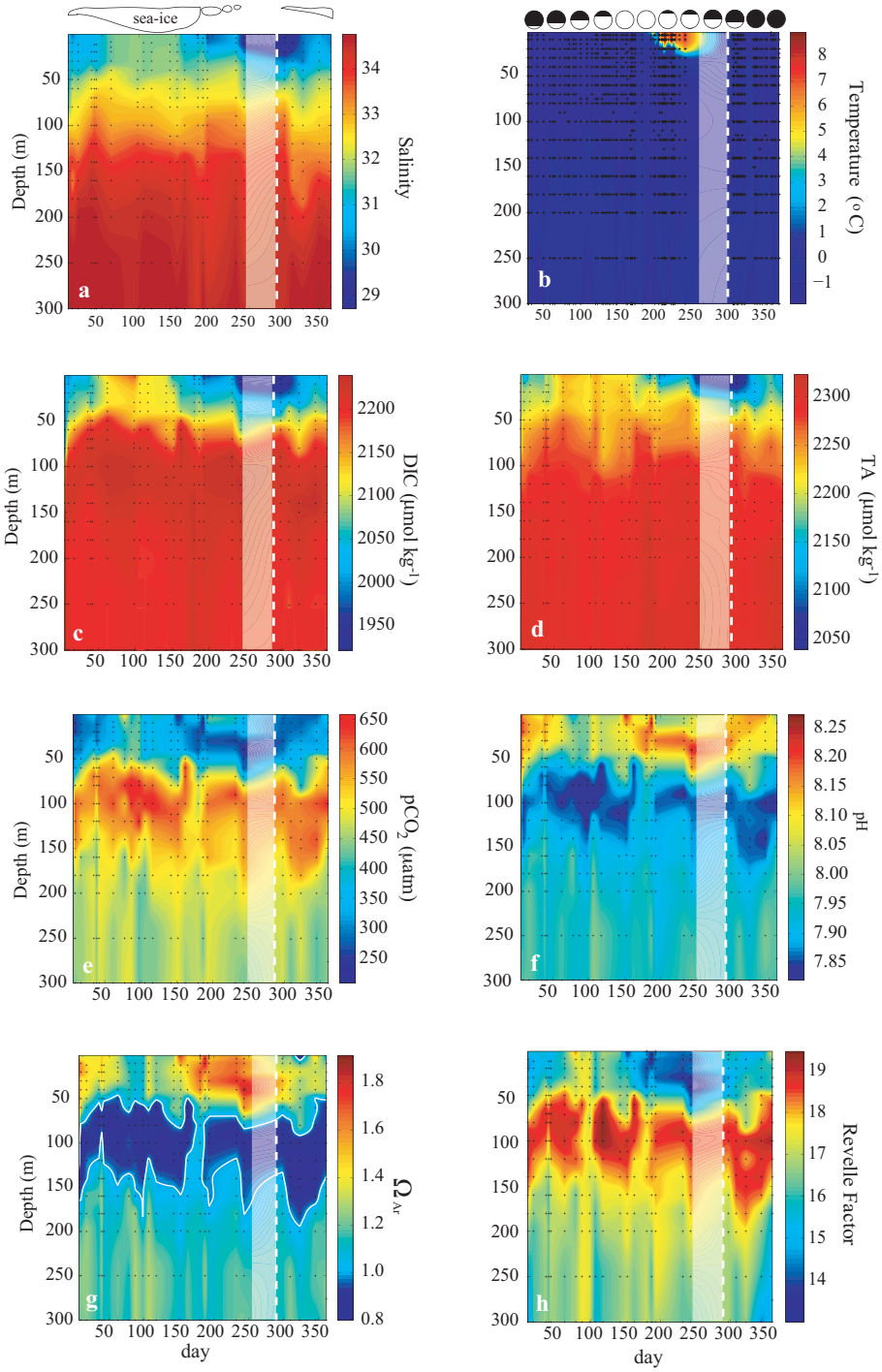

Figure 7.6: Temporal evolution of (a) temperature, (b) salinity, (c) DIC, (d) TA, (e) pCO_2, (f) pH, (g) Ω_{ar} (with the contour line indicating $\Omega_{ar} = 1.0$), and (h) the Revelle factor in Amundsen Gulf. The data to the right of the vertical white dashed line is from October through December 2007, while the data to the left of this line is from January to August 2008. The data within the white shaded area is an interpolation between August 2008 and October 2007. The annual cycle of sea-ice cover and sunlight are shown schematically above panels a and b respectively.

Table 7.3: Concentrations of DIC (μmol kg^{-1}) measured in the bottom 10 cm of ice. The growth of under-ice algae after yearday 115 decreases the concentration of DIC.

yearday	station position	DIC
17	71.5N, 125.7W	393
23	71.4N, 125.4W	404
115	70.5N, 122.4W	384
126	70.5N, 1224.W	356
130	70.5N, 122.4W	319

throughout the year, whereas the surface DIC concentrations ranged from $2125\ \mu\mathrm{mol\ kg^{-1}}$ in winter to $1934\ \mu\mathrm{mol\ kg^{-1}}$ in autumn. Sea-ice covered the water in both winter and spring, and the salinity profiles showed stable surface stratification and a well developed polar mixed-layer (PML) in the upper 50 meters. The winter profiles of salinity and TA indicated near uniform concentrations from the surface to a depth of roughly 40 meters. In the transition from winter to spring there was a salinity increase from approximately 31.5 to 32 (Fig. 7.7a). Over the same period the surface DIC concentration decreased (Fig. 7.7b). An increase in salinity, if it were the only process acting on DIC, would result in an addition of DIC to the surface waters, and the DIC profile would resemble the upper portion of the TA profile in spring (Fig. 7.7). The observed change in DIC between winter and spring was thus the result of biological uptake by under-ice algae, which was confirmed by a coincident increase in dissolved oxygen (not shown), and the accumulation of DOC in the bottom ice (*Riedel et al.*, 2008).

If we suppose that the winter-to-spring transition comprises only salinity-dependent changes in DIC, we can compute a profile of expected spring DIC concentration ($\mathrm{DIC_{ex}}$) based on the change in salinity between winter and spring (Fig. 7.7b inset). The $\mathrm{DIC_{ex}}$ profile would represent the spring DIC concentrations resulting from changes in salinity alone. If we compare this computed profile with the in situ DIC profile from spring in the surface mixed-layer, we see that the in situ spring concentrations were much lower than predicted by the change in salinity. As discussed above this decrease in DIC is attributed to the growth of under-ice algae. Integrating the difference between these two profiles over the 50 meter depth range (shaded area), yields an estimate of the biologically-mediated change in DIC (1.2 mol C m^{-2} per month) at this station. We compare this value to the monthly estimates of production over the same period, (1.7 mol C m^{-2} from

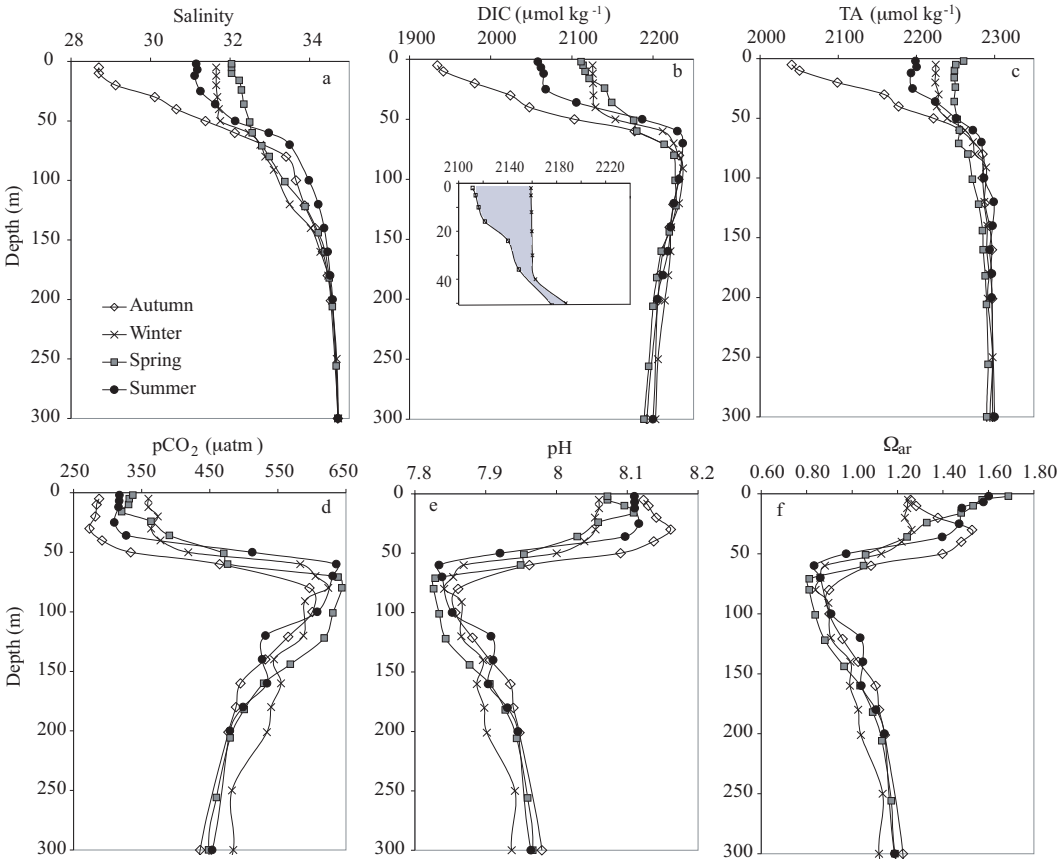

Figure 7.7: Seasonal profiles of (a) salinity, (b) DIC, (c) TA, (d) $\mathrm{pCO_2}$ (e) pH, and (f) Ω_{ar} generated from repeated sampling at the same station (see Fig. 2 for station location); the autumn profile is given by the open diamonds, winter by the x's, spring by the open squares, and summer by the closed circles. Inset: the in-situ winter DIC profile in the upper 80 meters is given by the x's, and the expected spring DIC profile computed from the winter-to-spring salinity change is given by the open squares.

February to May), in Section 7.6.1. The uptake of inorganic carbon by under-ice algae precedes the open-water phytoplankton bloom (*Gradinger*, 1996; *Renaud et al.*, 2007), the effect of which was seen in the further reduction of surface DIC between spring and summer. Both summer and autumn DIC data reflect open-water conditions and the reduction in salinity resulting from sea-ice melt. With the return of sunlight, the onset of (open-water) photosynthesis decreased surface DIC concentrations.

Seasonal profiles of $\mathrm{pCO_2}$, pH, and Ω_{ar} are given in Fig. 7.7d-f. Photosynthetic uptake of carbon by phytoplankton in the surface layer decreased DIC and $\mathrm{pCO_2}$, while increasing pH and Ω_{ar}. The effect of biological activity between winter and summer can also be seen in the $\mathrm{pCO_2}$ profiles, which showed a reduction from winter through spring and into summer; pH and Ω_{ar} both increased over the same period. In the subsurface waters, respiration, or remineralization of organic matter, increased DIC and $\mathrm{pCO_2}$, while pH and Ω_{ar} were depressed. Accordingly, between spring and summer, below a depth of roughly 50 meters, DIC increased (Fig. 7.7b), and both pH and Ω_{ar} increased (Fig. 7.7e, f). Between summer and autumn the largest decrease in surface DIC was observed, coincident with the largest decrease in surface salinity (from roughly 31.2 to 28.7). Surface $\mathrm{pCO_2}$ also decreased, while there was an increase in Ω_{ar} over the same period. In the Amundsen Gulf region, changes in salinity are attributed to both runoff and sea-ice melt and formation (see Section 7.4.7); Ω_{ar} has been shown to decrease with increasing sea-ice melt water (*Bates et al.*, 2009; *Chierici and Fransson*, 2009), as observed in the summer to autumn transition (Fig. 7.7f). The autumn DIC, TA, and $\mathrm{pCO_2}$ minima result from the dilution of the mixed-layer by sea-ice melt-water, resulting in a decreased Ω_{ar}, unbuffered by photosynthetic $\mathrm{CO_2}$ uptake seen during the winter-spring and spring-summer transitions.

It should be noted that the above discussion regarding summer to autumn transitions, which will be revisited in the following section, is based on data collected in two different years. Hence, we assumed that interannual variability does not compromise the reconstruction of the annual cycle using data from October 2007 through August 2008.

7.5.2 Processes Controlling Variability of DIC and TA

The results of the DIC mass balance computations (Eqs. 7.3 to 7.6) are shown in Figure 7.8. The observed, monthly mean changes in surface DIC and TA (Fig. 7.8 a, b) range

from $-60\ \mu\mathrm{mol\ kg^{-1}}$ to $60\ \mu\mathrm{mol\ kg^{-1}}$, and are mainly dominated by changes due to freshwater inputs and biological processes. From March to October, contributions from sea-ice melt decreased surface DIC and TA concentrations; from November to February the formation of sea-ice and corresponding brine rejection increased surface concentrations of DIC and TA. The largest positive changes in DIC due to freshwater fluxes occurred in March and December and were associated with sea-ice formation; the largest negative changes in DIC due to freshwater fluxes were observed in June and October and resulted from sea-ice melt, with additional contributions from river runoff in late June and early July.

Lateral advection and vertical diffusion played a minor role with respect to surface changes in both DIC and TA. The surface waters of Amundsen Gulf were weakly undersaturated with respect to atmospheric $\mathrm{CO_2}$ throughout the year. Hence, during the open-water months, the region acted as a moderate sink for atmospheric $\mathrm{CO_2}$, as reported by *Mucci et al.* (2010), but these inputs made only a minor contribution to the monthly changes in surface DIC. Biological processes thus made up the balance of the observed monthly changes in surface DIC and TA. Photosynthesis decreased surface DIC concentrations by roughly $20\ \mu\mathrm{mol\ kg^{-1}}$ per month from April through July, and biological processes made a modest contribution to changes in DIC during the remainder of the year, with increases in DIC due to respiration in the surface waters occurring in December and January.

The effect of biological activity on surface TA was small (Fig. 7.8b), with small increases in July and August corresponding to nutrient assimilation (and decreases in $\mathrm{NO_3}$ during photosynthesis, while the negative values in September through December corresponded to the regeneration of nutrients (and increases in $\mathrm{NO_3}$) through respiration. There is no evidence that the negative values of $\Delta\mathrm{TA_{bio}}$ in April and May, and the positive value of $\Delta\mathrm{TA_{bio}}$ in January were the result of the respective formation (in spring) and dissolution (in winter) of $\mathrm{CaCO_3}$, despite the correspondence with changes in DIC. As shown in Fig. 7.8b, the primary control on TA is freshwater input, and any other effects are minor. The reliable quantification of these minor processes, however, goes beyond the limits of our method.

The observed monthly changes in subsurface DIC (Fig. 7.8c) were more modest than those in the surface waters. Lateral advection reduced DIC, with lower inorganic carbon

waters from the east flowing into Amundsen Gulf throughout the year. The contribution from vertical diffusion, represented by a loss of higher inorganic carbon water to the surface layer was near-zero, when integrated over the large volume of the subsurface layer. Respiration, fueled by the delivery of organic matter produced in the surface, was ongoing throughout the year, as supported by the positive values of $\Delta\mathrm{DIC}_{\mathrm{bio}}$ (Fig. 7.8c). The maximum change in subsurface DIC due to biological activity takes place in July, roughly one month out of phase with the maximum surface production.

Results of the surface DOC mass balance computation (Eq. 12) are shown in Fig. 7.8d. Changes due to freshwater inputs those in surface DIC and TA, as described above (also Sections 7.4.7 and 7.4.9). Advection and diffusion played only a minor role. The variations of DOC from April to October, were dominated by positive changes due to contributions from biological processes. Modest increases in mixed-layer DOC in March and April, coinciding with DIC draw-down over the same period, were followed by a more significant production of DOC in June, and from July to October. The large, significant increase in DOC attributed to biological processes in the surface layer in June was nearly the same magnitude as the subsequent late-summer production that occurred over a shorter period. This increase in DOC is attributed to the release of DOC from melting ice. There was a large (biological) accumulation of DOC in the bottom ice in spring (*Riedel et al.*, 2008) (see Section 7.5.1) which was released to the surface water upon ice-melt. Sea-ice DOC concentrations as high as 2000 μmol kg^{-1} have been measured in April and May in the Amundsen Gulf region (*Riedel et al.*, 2008). We used a much lower, constant value ($\mathrm{DOC}_{\mathrm{ice}} = 65\ \mu\mathrm{mol\ kg}^{-1}$) to compute the $\Delta\mathrm{DOC}_{\mathrm{fw}}$ consistent with the method used to estimate $\Delta\mathrm{DIC}_{\mathrm{fw}}$ (see Sections 7.4.4 and 7.4.9). Hence the addition of sea-ice melt water resulted in a dilution of DOC, and was attributed in spring and summer to biology. The post-bloom increase in DOC, from July to October, was likely associated with both ice-melt, and nutrient limited conditions. In the latter case, DOC was produced from the consumption of DIC in the absence of nitrate, and by the degradation of (recently produced) organic matter.

7.5.3 Atmospheric CO_2 Uptake

The monthly integrated air-sea CO_2 fluxes are plotted in Fig. 7.9. The surface waters in Amundsen Gulf were undersaturated with respect to atmospheric CO_2 throughout the year. As described in Section 7.4.5, the air-sea fluxes were scaled to account for ice-cover

in the region as it is assumed to inhibit gas transfer between the ocean and the atmosphere. Both the uncorrected and the ice-cover corrected fluxes are shown in Fig. 7.9. A large gradient in $\mathrm{pCO_2}$ drove the strong (uncorrected) fluxes seen from January to May. The ice began to melt in June and decreased surface water $\mathrm{pCO_2}$, increasing the $\Delta\mathrm{pCO_2}$. The water warms through the summer and the lowered CO_2 solubility counteracts the uptake of DIC by phytoplankton. With ice formation in November and December, the ice-cover corrected fluxes are diminished despite the persistence of a strong air-sea gradient in $\mathrm{pCO_2}$. We estimate that the annual uptake of $\mathrm{CO_2}$ in Amundsen Gulf is $\mathrm{F_{CO_2}}$ = 1.2 mol C m^{-2} yr^{-1}. If ice-atmosphere CO_2 fluxes prove significant, then the method used to scale the fluxes under conditions of ice-cover may result in an underestimate of the Amundsen Gulf sink for $\mathrm{CO_2}$ on the annual scale. Nevertheless, at this time reliable parameterization for gas fluxes between the ocean and the ice are lacking. Furthermore, the role of sea-ice as an inter-facial medium between the ocean and the atmosphere is not well constrained. The method used here reflects the state of available knowledge, and estimates can be considered a lower limit on the annual air-sea $\mathrm{CO_2}$ flux.

7.6 Discussion

7.6.1 Nutrient Uptake and Net Community Production

Net community production (NCP) is the difference between net primary production (NPP) and heterotrophic respiration (R), and can therefore be related to biologically mediated changes in DIC:

$$\mathrm{NCP} = \mathrm{NPP} - \mathrm{R} = -\Delta\mathrm{DIC_{bio}}. \tag{7.9}$$

NCP is commonly computed from nitrate or phosphate uptake and converted to carbon units using the conventional Redfield ratio of $\mathrm{C : N : P} = 106 : 16 : 1$. This method is reliable when nitrate and phosphate are not depleted, and DIC, nitrate and phosphate are taken up in Redfield proportions (*Arrigo*, 2005; *Bozec et al.*, 2006). However, DIC may still be consumed when nutrients are depleted, and carbon based estimates of NCP often exceed nitrogen based estimates (*Thomas et al.*, 1999; *Bozec et al.*, 2006; *Tremblay et al.*, 2008).

Monthly values of $\Delta\mathrm{DIC_{bio}}$, $\Delta\mathrm{NO_3}$, ΔSi, and the ratios of $\Delta\mathrm{DIC} : \Delta\mathrm{NO_3}$, and $\Delta\mathrm{Si} : \Delta\mathrm{NO_3}$ are given in Table 7.4. Increased consumption of silicate relative to nitrate has

been linked to iron or nutrient limitation in phytoplankton (*Hutchins and Bruland*, 1998; *Takeda*, 1998). The southern Beaufort Sea is nitrate limited after sea-ice break up and the onset of the spring/summer phytoplankton bloom (*Tremblay et al.*, 2008). However, NCP can be sustained upon nitrate depletion by regenerated nitrogen, nitrogen fixation, or by an allocthonous nitrogen source. From April to June, DIC and NO_3 were taken up in roughly Redfield proportions, with the mean value of $DIC : NO_3 = 6.2$ over this period. In April the $Si : NO_3$ was near unity, but increased significantly in May and June, indicating nutrient limitation most likely attributable to a nitrate depletion in the surface layer. The under-ice algae are dominated by diatom species (*Horner and Schrader*, 1982) which may explain the ratio of $Si : NO_3$ at the beginning of the productive season. After the ice break-up, nutrients quickly become depleted by the open-water phytoplankton bloom which is dominated in June and July by flagellates which may explain the some of the change in the $Si : NO_3$ over this period (*Jull-Pedersen et al.*, 2010).

Table 7.4: Monthly values of ΔDIC_{bio}, ΔNO_3, ΔSi, in units of μmol kg^{-1}, the ratios of $\Delta DIC : \Delta NO_3$, and $\Delta Si : \Delta NO_3$, NCP and air-sea CO_2 flux (F_{CO_2}) in units of mol C m^{-2} $month^{-1}$, during the productive season, and the annual value of ΔDIC_{bio} (in μmol kg^{-1} yr^{-1}), and annual NCP and F_{CO_2} in units of mol C m^{-2} yr^{-1}. In July and August, nutrients were exhausted and the carbon and nutrient ratios were therefore not computed. See also Figs. 7.8a, 4.13, and 7.10.

Month	ΔDIC_{bio}	ΔNO_3	ΔSi	$\Delta DIC : \Delta NO_3$	$\Delta Si : \Delta NO_3$	NCP	F_{CO_2}
April	-21.6	-3.4	-3.7	6.2	1.1	1.11	0.003
May	-16.1	-2.6	-6.6	6.2	2.5	0.81	0.012
June	-17.2	-1.8	-5.5	9.4	3.0	0.86	0.38
July	-20.4					1.02	0.19
August	-5.6					0.28	0.24
Annual	-42.2					2.1	1.2

An estimate of NCP from biologically-driven changes in DIC (Eq. 7.9) is plotted in Fig. 7.10. In winter, NCP was negative in the surface waters corresponding to a positive change in DIC (respiration). From April to August, during the productive summer period, NCP was positive. The subsurface indicated a maximum respiration in July, as a result of an increased delivery of organic matter from the surface layer. Integrating the monthly values of NCP over the year yields a value of $NCP_s = 2.1 \pm 1.7$ mol C m^{-2} yr^{-1} in the surface and a respiration inventory of $R = 3.8 \pm 1.0$ mol C m^{-2} yr^{-1} in the subsurface.

Integrating the monthly values of NCP from winter (February) to spring (May) yields a value of 1.7 mol C m^{-2} over the winter-spring transition, in good agreement with the estimate made by graphical integration (1.2 mol C m^{-2}, see Section 7.5.1). Integrating the biologically mediated changes in mixed-layer DOC, over the annual cycle yields a production of 0.61 ± 0.24 mol C m^{-2} yr^{-1}, which corresponds to 28% of NCP; this value is somewhat higher than an estimate of DOC production in the nearby Chukchi Shelf (10%) (*Mathis et al.*, 2007), but in line with the estimate of *Gosselin et al.* (1997) for the Arctic Ocean.

We made an alternate estimate of subsurface respiration (following Section 6.5.3). In brief, the deviation of in-situ DIC from a linear relationship between DIC and salinity indicates a non-conservative, biological process (respiration). The linear relationship between DIC and salinity is based on the two-end member mixing of Pacific- and Atlantic-origin water of salinity 33.1 and 34.8 respectively. Non-conservative variations in DIC ($\Delta\mathrm{DIC_{resp}}$) are expressed as the difference between the expected DIC ($\mathrm{DIC_{ex}}$, resulting from idealized mixing), and the observed DIC ($\mathrm{DIC_{obs}}$):

$$\Delta\mathrm{DIC_{resp}} = \mathrm{DIC_{obs}} - \mathrm{DIC_{ex}} \tag{7.10}$$

Positive values of $\Delta\mathrm{DIC_{resp}}$ indicate that respiration exceeds production and correspond to a surplus of inorganic carbon. Profiles of $\mathrm{DIC_{ex}}$ are computed from salinity data and the following relationship: $\mathrm{DIC_{ex}} = -48.24\mathrm{S} + 3832$. Using Eq. 7.10, $\Delta\mathrm{DIC_{resp}}$ is computed for each sample. These values were then integrated over the depth range of the subsurface layer (50 to 300 meters), and a mean value of $\Delta\mathrm{DIC_{resp}} = 4.1$ mol C m^{-2} was computed. Applying the residence time (18 months) of the water in the subsurface box obtained from the transport estimates of *Lanos* (2009), we arrive at a subsurface respiration of 2.7 mol C m^{-2} yr^{-1}, which is in agreement with the above estimate (see also Fig. 7.10).

Estimates of primary production in Amundsen Gulf range from 7 to 15 mol C m^{-2} yr^{-1} (*Arrigo and van Dijken*, 2004). We assume that between 15% and 30% of primary production is exported from the surface layer in Amundsen Gulf, following a recent estimate of vertical export by *Jull-Pedersen et al.* (2010). Thus, roughly 2 mol C m^{-2} yr^{-1} POC leaves the surface layer. According to the carbon flux estimates of *Forest et al.* (2008) roughly 0.45 mol C m^{-2} yr^{-1} of marine POC reaches a depth below 200 meters, with

an additional contribution of 0.15 mol C m^{-2} yr^{-1} from terrestrial sources (Fig. 7.11). The amount of carbon available for respiration in the subsurface layer is then 1.55 mol C m^{-2} yr^{-1}. This implies that there is a subsurface carbon excess of 1.2 to 2.3 mol C m^{-2} yr^{-1}. A possible source of this excess inorganic carbon is benthic respiration, which was neglected in the subsurface DIC budget (see Section 7.4.7). Using the benthic oxygen demand of *Renaud et al.* (2007), based on data from January to July, and assuming the mean value is valid over the whole year, and the Redfield ratio of O_2:CO_2=138:106, this contribution ranges from 0.7 to 1.4 mol C m^{-2} yr^{-1} (see Fig. 7.11). It has been suggested that little, if any, sediment accumulation occurs in the Amundsen Gulf region (*Richerol et al.*, 2008), and high turbidity above the sediment surface has been reported (*Mucci et al.*, 2008; *Magen et al.*, 2010). If all, or the majority of the POC flux observed was consumed by the benthic community, respiration of this organic matter could account for the excess DIC computed here, within the uncertainty of the budget computations. An alternate explanation is that the excess subsurface respiration is fueled by organic material delivered laterally to the region. This influx of particulate and, or, dissolved organic matter is difficult to constrain using the present approach, which assumes that lateral or horizontal advection in the subsurface occurs only along the direction of the mean water flow (north-northwest) from Amundsen Gulf towards the Southern Beaufort Sea (*Lanos*, 2009).

In autotrophic systems, such as the surface layer in Amundsen Gulf, there is a net production of organic matter at the expense of inorganic carbon and nutrients. In contrast, heterotrophic systems, are defined by a net consumption of organic organic matter and release of inorganic carbon and nutrients. Amundsen Gulf is therefore overall net heterotrophic (*Alonso-Sáez et al.*, 2008; *Garneau et al.*, 2008), despite the autotrophy of the surface layer, which acts as a sink for atmospheric CO_2. Previous studies have indicated that stratified systems are often partitioned this way (*Bozec et al.*, 2005; *Thomas et al.*, 2005a). The annual cycle of biologically-meditated changes in surface and subsurface DIC are shown schematically in Fig. 7.12. In the surface layer, respiration dominated between January and March when the waters are ice-covered and the region receives very little sunlight. In April, the growth of under-ice algae reduced surface DIC (and nutrient) concentrations; production continued under the ice until June, when ice break-up gave way to the open water phytoplankton bloom which rapidly depleted the surface nutrients

and continues to decrease surface DIC through August. A portion of the DIC lost to the production of organic matter was replaced by the uptake of atmospheric CO_2 from June through September. In October, sea-ice began to reform and the surface layer became dominated by respiration. In the subsurface layer carbon accumulated due to organic matter respiration. The delivery of heavy (diatom) under-ice algae was seen in the first of two subsurface respiration peaks in May, roughly one month after the onset of the under-ice bloom. The delivery of organic matter from the open-water bloom was seen in July, also about a month out of phase with the onset of the phytoplankton bloom. The subsurface peak in July was in consistent with the sediment trap data of *Forest et al.* (2008) which also shows an annual maximum in July. The material was exported from of the surface layer in spring and summer upon aggregation with terrigenous material which promotes sinking; this land-derived material may come from the rivers, or from the melting of land-fast sea-ice.

7.6.2 Surface CO_2 Undersaturation

The upper 50 meters of the water column in Amundsen Gulf were undersaturated with respect to atmospheric CO_2 throughout the year (Figs. 7.6e, and Section 7.5.1). The capacity of seawater to absorb CO_2 depends on its buffer capacity (*Takahashi et al.*, 1993; *Sabine et al.*, 2004), which is described by the Revelle factor. This factor quantifies the change in pCO_2 for a given change in DIC, and is proportional to the ratio of DIC to TA (*Revelle and Suess*, 1957). Waters with low Revelle factor (e.g. 8-10) have a larger potential capacity to absorb anthropogenic CO_2 and vice-versa (*Sabine et al.*, 2004). Warm tropical, and subtropical, waters have relatively a low Revelle factor and therefore a large potential anthropogenic CO_2 uptake, despite the lower CO_2 solubility at high temperature, since the Revelle factor quantifies a response to a change and not the steady state of the system. High latitude and polar oceans have relatively higher Revelle factors, and a smaller potential capacity to absorb anthropogenic CO_2 (*Sabine et al.*, 2004; *Orr et al.*, 2005). In January the waters of the study area were cold ($<0°C$) with relatively low pCO_2 (<300 μatm) and characterized by a Revelle factor near 15. In March (near DOY 75) there was a significant increase in surface salinity (see Fig. 7.6b) attributed to brine rejection. It resulted in an increase in pCO_2 on the order of 30 μatm and a parallel increase in the Revelle factor. The effect of brine rejection is also seen in the (uncorrected) air-sea CO_2 flux estimate for the month of March which is less than half of the value of the February

flux due to the decrease in ΔpCO_2 brought about by the injection of DIC-rich, brine to the surface waters (Fig. 7.9). Over the same period, there was a further increase in pCO_2 of roughly 20 μatm attributed to respiration which increased DIC by roughly 7 μmol kg^{-1} between February and March. In April (after DOY 100) the growth of under-ice algae reduced DIC concentrations by roughly 20 μmol kg^{-1} (or roughly 1.1 mol C m^{-2} over the month *see* Fig. 7.10), reducing surface pCO_2 (and ΔpCO_2) by 30 to 50 μatm, and increasing the (uncorrected) April air-sea flux (Fig. 7.9). In June (after DOY 200), and through July and August, ice-melt gave way to the open water phytoplankton bloom. The open water bloom was coincident with the warming of the surface waters (Fig. 7.6b) and in June, the biologically mediated reduction in pCO_2 ($\sim$40 μatm) was dominated by the increase in pCO_2 ($\sim$90 μatm) caused by warming (Fig. 7.6e). Over the summer period, the lowest Revelle factors ($<$14) were observed (Fig. 7.6h). This is due primarily to the decrease in the ratio of DIC to TA in the surface waters resulting from the removal of DIC (42 μmol kg^{-1}, or 2.1 mol C m^{-2} from June through August see also Figs. 7.8a and 7.10) by primary production. The capacity of the surface waters in Amundsen Gulf to absorb atmospheric CO_2 was therefore greatest during the open water bloom, despite the fact that the water temperature was at a maximum during this period, suppressing some of this potential absorption (Fig. 7.9). In September (following DOY 250), and through the remainder of the year, the surface waters cooled, and the pCO_2 decreased.

Yager et al. (1995) proposed a 'seasonal rectification hypothesis' to describe the CO_2 dynamics in the Northeast water polynya with a possible extrapolation to other Arctic polynya and shelf regions (*Bates*, 2006). This hypothesis requires that the summer season be dominated by CO_2 uptake by phytoplankton in the surface water, followed by a replenishment of CO_2 from the atmosphere by strong winds in autumn before sea-ice formation (*Yager et al.*, 1995). The organic matter generated by the summer production is retained in the mixed-layer and remineralized in winter such that the mixed-layer becomes supersaturated with respect to atmospheric CO_2, and at which time sea-ice provides a barrier to out-gassing. The growth of ice-algae in the following early spring is then supported by this respiratory carbon (*Yager et al.*, 1995) and followed by the open water bloom which occurs under strong surface stratification due to the delivery of ice-melt. The inorganic carbon system in Amundsen Gulf displays some similarities to the annual process described by *Yager et al.* (1995): saturation with respect to atmospheric CO_2 was observed

in winter only briefly as a result of brine rejection during ice formation, and organic matter respiration, both increasing DIC and pCO_2 in the surface waters. While there is evidence of respiration, or remineralization of organic carbon, in winter (Figs. 7.8a, 7.10), this accounted for only half of the organic matter produced, while the rest was vertically exported, and was not sufficient to increase pCO_2 above the atmospheric concentration. Most of the annual influx of atmospheric CO_2 ($F_{CO_2} = 1.2$ mol C m^{-2} yr^{-1}) occurred between May and October; over the same 6-month period NCP was roughly 2.4 mol C m^{-2}. The annual uptake of atmospheric CO_2 was equal to roughly 60% of the annual (net) production (NCP = 2.1 mol C m^{-2} yr^{-1}). In Amundsen Gulf, pCO_2 was depressed by primary production both by under-ice algae in spring, and by the open water phytoplankton bloom in summer. The warming of the surface waters hindered the open water sink for atmospheric pCO_2. During the ice-covered periods, the cold surface waters remained undersaturated despite the partial rectification of pCO_2 by respiration of organic matter.

7.7 Conclusion

A high resolution time series covering, for the first time, a full annual cycle, in an Arctic continental shelf region has allowed us to assess processes controlling the seasonal variability of mixed-layer and subsurface carbonate system parameters, revealing an autotrophic surface layer, but a net heterotrophic system in Amundsen Gulf. The cold, relatively low-salinity surface waters were undersaturated with respect to atmospheric CO_2 throughout the year. The melting and formation of sea-ice strongly controlled the properties of the surface mixed-layer. The dissolved inorganic carbon (DIC) draw-down by under-ice algae began in early April, and was followed by the spring phytoplankton bloom which occurred after the ice break up and the return of sunlight to the region. During the spring bloom, DIC and nitrate were consumed in roughly Redfield proportions; post-bloom DIC draw-down, and corresponding production of dissolved organic carbon (DOC), continued in non-Redfield proportions under nutrient limited conditions. We estimated that roughly 30% of NCP (computed from inorganic carbon) was converted to DOC in the surface mixed-layer. Respiration in the subsurface layer exceeded the estimated surface production and is therefore likely supported by inorganic carbon generated by benthic respiration.

7.8 Acknowledgments

We are grateful to the captains, officers, and crew of the Canadian Coast Guard Ship *Amundsen* for their co-operation in the collection of field data, and also to the chief scientists. We thank Yves Gratton and his team of rosette operators for the collection and distribution of hydrographic data. Many thanks to Friederike Prowe, Stelly Lefort, Constance Guignard, Nes Sutherland, Stephanie Moore, and Doris Leong for their assistance with sample collection and analysis. We are grateful to two anonymous reviewers and to Nick Bates for their insightful comments. This work was supported by the Swedish Research Council, the Royal Society of Arts and Sciences in Göteborg, the Canadian Natural Science and Engineering Research Council (NSERC), ArcticNet, and MetOcean Data Systems. This research contributes to the Canadian International Polar Year (IPY) initiatives, as part of the Circumpolar Flaw Lead System Study (CFL) project, and to International Geosphere Biosphere Programme, International Human Dimensions Programme, Land Ocean Interactions in the Coastal Zone.

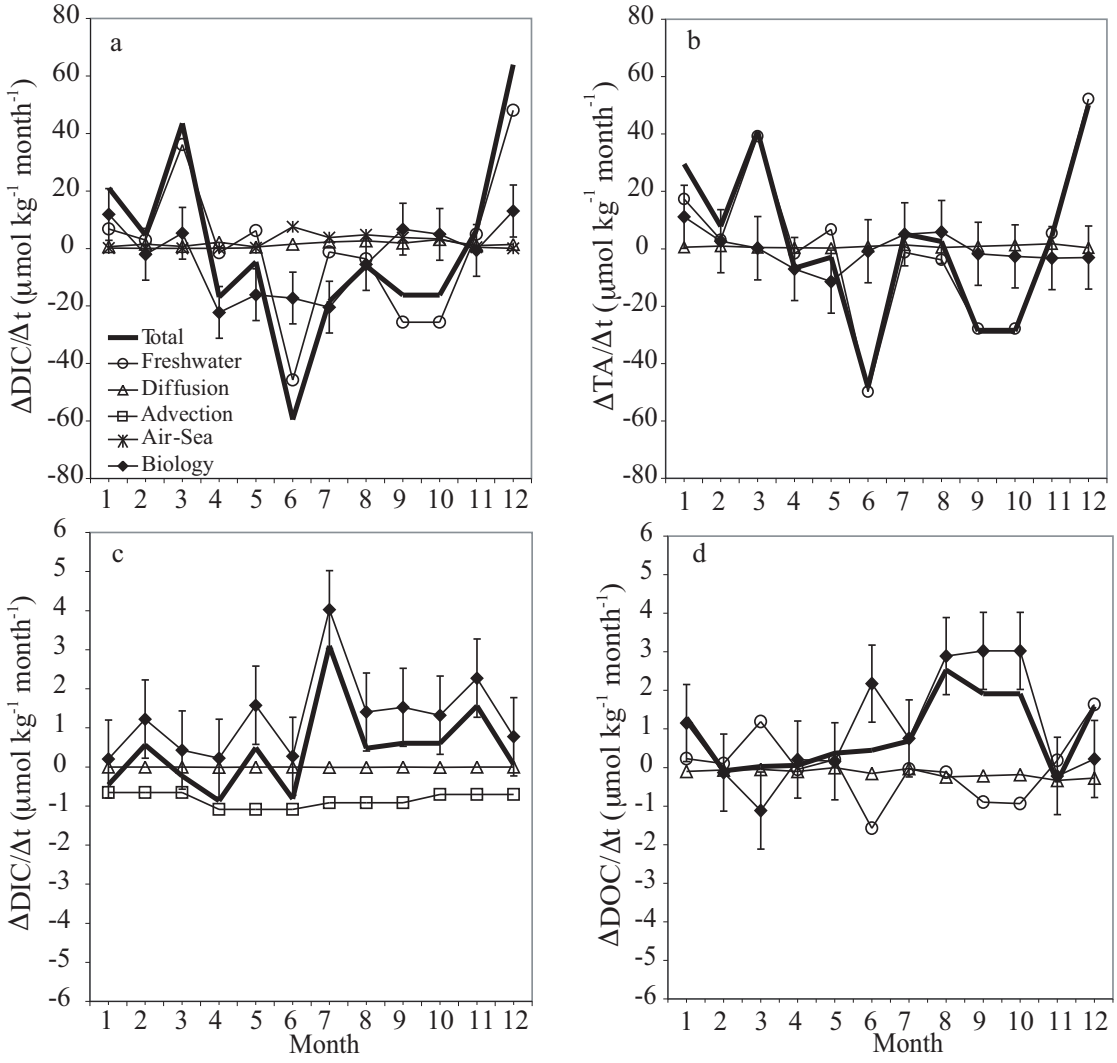

Figure 7.8: Controls on (a) surface DIC, (b) surface TA, (c) subsurface DIC, and (d) surface DOC. The surface extends from 0 to 50 m, and the subsurface from 50 to 300 m. Please note that the October through December values are based on samples collected in 2007, while the January through August values are based on samples collected in 2008. The September values are the mean of the computed monthly concentrations from August and October.

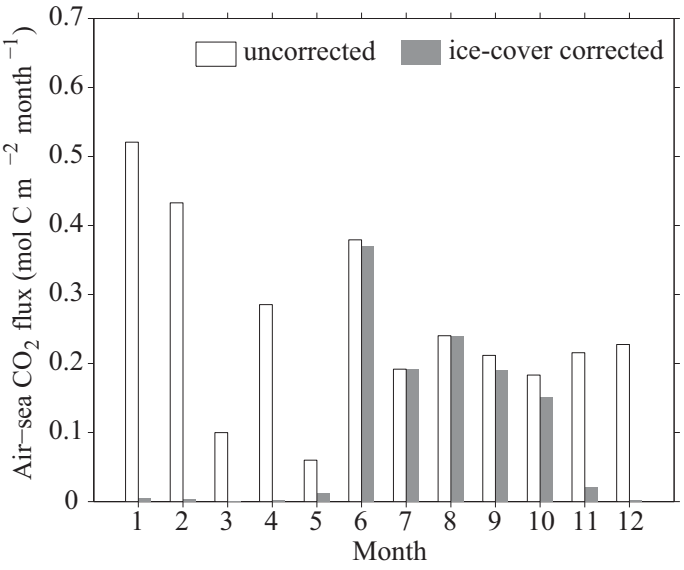

Figure 7.9: The monthly air-sea CO_2 fluxes in Amundsen Gulf, with positive values indicating a transfer from the atmosphere to the ocean. The white bars are the uncorrected fluxes, computed without taking ice-cover into account. The gray bars are the ice-cover corrected fluxes (Table 2). The region acts as a sink for atmospheric CO_2 throughout the year. The annual (ice-corrected) flux is F_{CO_2}=1.2 mol C m^{-2} yr^{-1}, the annual uncorrected flux would be F=3.0 mol C m^{-2} yr^{-1}.

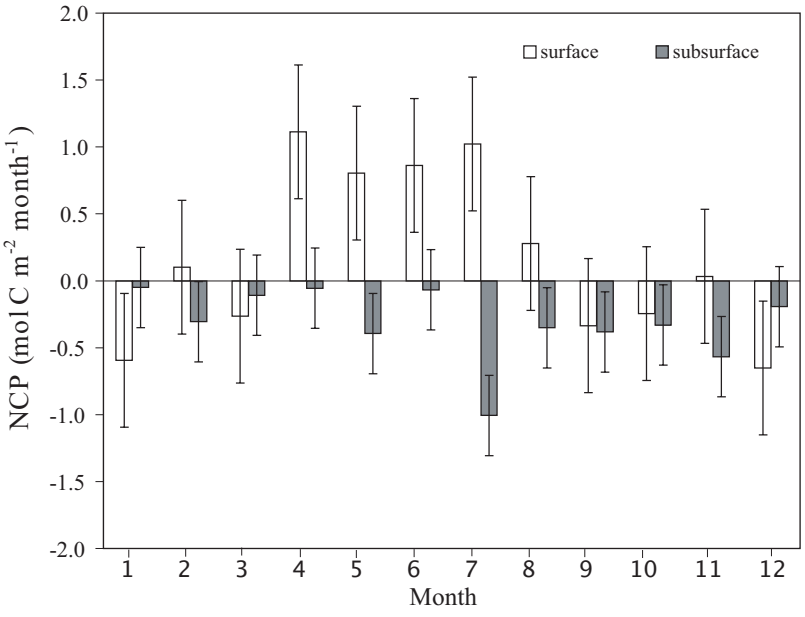

Figure 7.10: Monthly values of net community production (NCP), with surface values shown in white, and subsurface values shown in gray. Error bars indicate the estimated 0.5 mol C m^{-2} month^{-1} uncertainty in the surface layer, and and 0.3 mol C m^{-2} month^{-1} in the subsurface layer estimated from the Monte Carlo simulation (see Section 7.4.8 and Table 7.2).

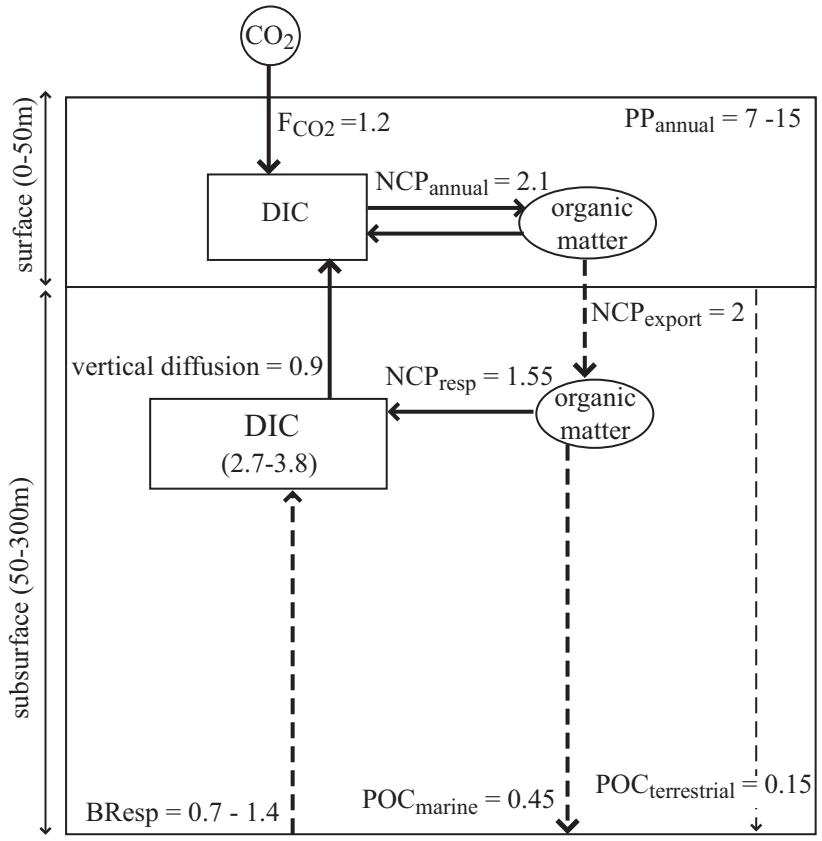

Figure 7.11: A schematic representation of the inorganic carbon budget for Amundsen Gulf. All values are given in units of [mol C m^{-2} yr^{-1}]. The solid arrows indicate computations made in the current study; dashed arrows indicate values take from the literature. The surface DIC losses to NCP are balanced by atmospheric CO_2 uptake and the delivery of carbon-rich water from below. NCP is exported from the surface layer and respired in the subsurface. POC fluxes below 200 meters amount to 3 to 6% of surface primary production (Forest et al. 2008). Benthic respiration (Renaud et al. 2007) balances the excess carbon computed with the simple two-box model within the uncertainty of the computation (Eq. 3-6, and Fig. 7.3), with possible contribution from lateral advection which cannot be accounted for with the method presented here.

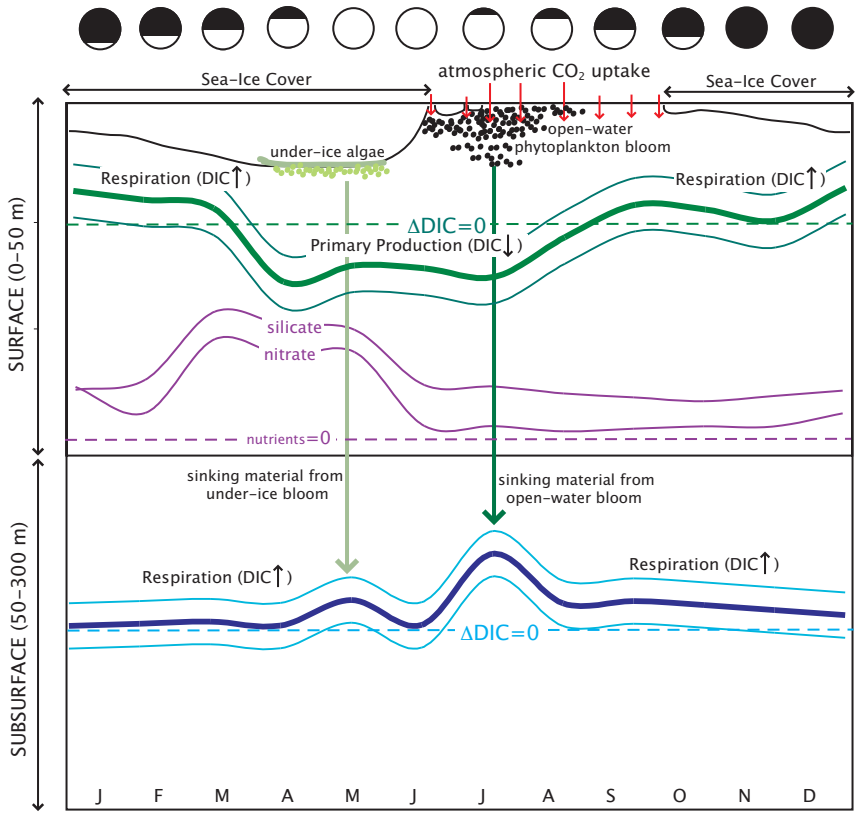

Figure 7.12: The annual cycle of biologically-mediated changes in DIC in the surface and subsurface layers are shown schematically. The bold and thin lines indicate the computed monthly values and the associated uncertainty respectively (see Fig. 7.10), the dashed lines indicated $\Delta\mathrm{DIC}_{\mathrm{bio}} = 0$ such that positive values are associated with respiration and negative values with production. The annual cycles of surface nitrate and silicate are also shown; please note that the nutrient lines indicate concentrations and not changes, so that the dashed line indicates nutrient depletion. The sinking of organic material due to the under ice and open water blooms, the annual cycle of sea-ice and sunlight, and the uptake of atmospheric CO_2 during the open water season are also shown schematically.

CHAPTER 8

CONCLUSION

The research presented here focuses on the processes controlling the variability of inorganic carbon in two very different Canadian regions. While the regional case studies presented are not immediately linked geographically, the Scotian Shelf may be thought of as located downstream from the Arctic Archipelago. The insights gained from the two field locations contribute to the overarching goal of advancing our understanding of CO_2 in the coastal ocean, with a particular focus on Canadian waters. A recent global synthesis of observational data from continental shelf regions suggests that temperate and high-latitude shelves largely act as sinks for atmospheric CO_2 (*Chen and Borges*, 2009). With respect to their role in the absorption of atmospheric CO_2, Amundsen Gulf acts according to expectations drawn from the synthesis of *Chen and Borges* (2009), while the Scotian Shelf acts contrary to these expectations. The primary controls on CO_2 in these regions are quite different and due to the unique aspects of the particular coastal system.

8.1 The Scotian Shelf

The Scotian Shelf is an open, temperate, continental shelf region. The Scotian Shelf is adjacent to the Gulf of Maine, and upstream from the South and Middle Atlantic Bights, three additional examples of open continental shelves in both temperate and subtropical regions. Both the South (*Jiang et al.*, 2008) and the Middle Atlantic Bight (*Boehme et al.*, 1998; *DeGrandpre et al.*, 2002) have been found to act as net sinks of atmospheric CO_2 in line with the synthesis of *Chen and Borges* (2009) and the most recent surface ocean pCO_2 climatology of *Takahashi et al.* (2009). The majority of the outgassing of CO_2 on the Scotian Shelf occurs during autumn and winter (see Figs. 4.13 and 5.8c)

when the destratification of the water column maintains pCO_2 supersaturation despite the near-zero water temperature. This is in contrast to the interpretation of *Chen and Borges* (2009) for temperate continental shelves, which on the global scale, tend to act as sinks for CO_2 in the autumn and winter seasons, as in the case of the South and Middle Atlantic Bights (*DeGrandpre et al.*, 2002; *Jiang et al.*, 2008). A further difference between the Scotian Shelf and the more southern regions of the North American east coast is the role of temperature in controlling the seasonal changes in pCO_2. In both the South and Middle Atlantic Bights, temperature is found to be the dominant control on the variability of pCO_2 (*DeGrandpre et al.*, 2002; *Jiang et al.*, 2008). While temperature exerts an important control on seasonal changes in pCO_2 on the Scotian Shelf it is opposed by a biological control of nearly the same magnitude (see Chapter 4, Fig. 4.13) which persists from April through October in the region.

The results presented in Chapter 4 indicate that the chlorophyll-based satellite estimate of primary production is in general agreement with literature values for the Scotian Shelf on the annual scale. However, the summer production in the region, estimated from the CARIOCA buoy, which amounts to 40% the production generated by the spring bloom, is significantly underestimated by the satellite-based estimate for the same period. Production, or biomass, estimates based on remotely-sensed chlorophyll-a concentration capture only the chlorophyll-a, or POC, remaining in a very shallow surface layer. The remote sensing estimates cannot include the carbon losses due to sinking or grazing since these particles are no longer present in the surface layer, despite their contribution to changes in the surface DIC pool. Estimates of primary production relying on chlorophyll-a concentration are therefore likely to underestimate the amount of carbon uptake. Furthermore, carbon uptake may occur in the absence of an increase in surface chlorophyll-a concentration. Evidence of substantial carbon uptake in the late spring and summer on the Scotian Shelf which is not associated with increases in surface chlorophyll-a concentration has been presented here.

The Scotian Shelf is characterized by an autotrophic mixed-layer acting as a net source of CO_2 to the atmosphere. The timing and extent of the spring phytoplankton bloom, and subsequent CO_2 draw down vary from year to year. Furthermore, a trend of decreasing ΔpCO_2, or weakened outgassing, has occurred over the last decade. This negative trend

in ΔpCO_2 can be explained by a 1.3°C cooling of the surface waters over the same period. Modelling studies on the eastern North American continental shelf have suggested that the interannual variability in the air-sea CO_2 flux is due in part to NAO forcing (*Previdi et al.*, 2009). This interpretation is in agreement with the research presented here; a decadal cooling over a period of negative or near neutral NAO has driven the Scotian Shelf system toward stronger atmospheric CO_2 uptake. The research presented here documents the seasonal and annual cycles of inorganic carbon in the Scotian Shelf region and quantifies the primary controls on variability. This analysis indicates that the CO_2 system on Scotian Shelf differs significantly from the South and Middle Atlantic Bight systems and contributes to the larger community effort to accurately assess the North American coastal ocean carbon budget (*Najjar et al.*, 2010).

8.2 Amundsen Gulf

While there have been many recent investigations of the CO_2 system in other temperate and high-latitude coastal regions, the Arctic Ocean remains poorly studied in general, and very few coastal studies have been undertaken. This is largely due to the difficulty of accessing these remote areas which are ice-covered for much of the year. The full annual cycle of inorganic carbon system observations from Amundsen Gulf documented here is thus a particularly relevant contribution. Amundsen Gulf is located at the southwestern corner of the Canadian Arctic Archipelago. This region is a typical coastal archipelago surrounded by islands on the wide continental shelf. Amundsen Gulf is bounded to the east by the numerous islands of the Canadian Archipelago and to the west by the Mackenzie Shelf. Further west lies the Chukchi Sea shelf, an area of the Arctic which has been relatively well studied with respect to the CO_2 system, in the summer and autumn seasons (e.g. *Bates et al.*, 2005; *Mathis et al.*, 2005; *Bates*, 2006; *Mathis et al.*, 2007; *Bates et al.*, 2009). Both Amundsen Gulf and the neighboring Chukchi Sea shelf act as sinks of atmospheric CO_2, in agreement with the assessment of *Chen and Borges* (2009) for high-latitude shelf systems. On the Chukchi Sea shelf, CO_2 undersaturation is maintained in part by a cooling of Pacific-origin waters as they move northward from the Bering Sea. An additional control on surface CO_2 in on the Chukchi shelf is the brief, but intense, primary production that occurs in the ice-free summer period. Much of the summer production is exported vertically out of the surface layer, and laterally off the shelf into the

deeper basins of the Arctic Ocean (*Bates*, 2006). The CO_2 system in Amundsen Gulf reveals some similarity to the nearby Chukchi Sea despite its location in a significantly deeper basin. The surface waters in Amundsen Gulf are undersaturated with respect to atmospheric CO_2 throughout the year. The surface layer is found to be net autotrophic, as in the case of the Scotian Shelf, despite the brief period of light and nutrient availability, and unlike the Scotian Shelf, the region acts a a net sink for atmospheric CO_2.

The major physical difference between Amundsen Gulf and the Scotian Shelf is the presence of sea-ice in the former region. The freshwater fluxes resulting from the melting and formation of sea-ice exert a strong control on the properties of the mixed-layer in Amundsen Gulf. In winter, the surface waters are undersaturated with respect to atmospheric CO_2 despite the increases in DIC due to both increased salinity from brine rejection, and to the respiration of organic matter in the upper water column, in part due to the very low surface temperature. Biological production begins in April by under-ice algae requiring very little light, and, as in the case of the Scotian Shelf, when the water temperature is still near the annual minimum. In summer, ice-melt gives way to the open water phytoplankton bloom which is coincident with the surface warming. During the ice-free period, the biological CO_2 draw down is counteracted by the temperature-driven pCO_2 increase. In autumn, the cooling of the water reduces surface pCO_2, and stratification inhibits upward mixing of DIC-rich water, thus the surface waters remain undersaturated. Over longer time scales, the large input of riverine alkalinity to the largely enclosed, land-dominated, Arctic Ocean may contribute to the CO_2 undersaturation on the continental shelves (*Bates*, 2006).

8.3 Similarities and Differences

Both the Scotian Shelf and Amundsen Gulf are considered coastal ocean regions; the Scotian Shelf is an open continental shelf sea, while Amundsen Gulf is part of a coastal archipelago. The Scotian Shelf is a temperate system and Amundsen Gulf is a high latitude system. Both regions are influenced by freshwater input. The Scotian Shelf is located downstream of the St. Lawrence estuary system, and surface salinity on the inner Scotian Shelf is decreased by roughly 1 part over the annual cycle as a result of the delivery of runoff from the St. Lawrence estuary. Amundsen Gulf is located east of the Mackenzie Shelf, and is influenced by runoff from the Mackenzie along with runoff from smaller

rivers. However, the freshwater influence in Amundsen Gulf is dominated by the melting and formation of sea-ice. Temperature plays an important role in controlling surface pCO_2 in both regions. On the Scotian Shelf the sea-surface temperature warms from near-zero in winter to 16 to 20°C in summer, resulting in a increase in pCO_2 by more than 150 μatm over the summer season. In the absence of biological production occuring during the period of warming, surface pCO_2 on the Scotian Shelf would reach values on the order of 650 μatm. Surface warming occurs during the brief open-water period in Amundsen Gulf increasing the sea-surface temperature from -1°C to roughly 8°C and increasing pCO_2 by roughly 90 μatm. In both systems the summer increase in pCO_2 due to surface warming is coincident with decreases in pCO_2 due to biologically-mediated DIC uptake.

The productive season on the Scotian Shelf begins in April and continues through early or mid-October; nutrients are depleted in May, immediately after the spring phytoplankton bloom. By contrast, in Amundsen Gulf the productive season begins a few weeks earlier in mid-March with the growth of under-ice algae. The open water bloom follows the ice break-up in mid- or late June, and similar to the situation on the Scotian Shelf, nutrients are quickly depleted by the open water phytoplankton bloom, reaching minimum values in July. Net community production (NCP) by the spring bloom on the Scotian Shelf in April amounts to 2.4 mol C m^{-2} with new production accounting for 1.3 mol C m^{-2} over this month. In Amundsen Gulf, NCP during the open water bloom in June and July amounts to 1.9 mol C m^{-2} (over two months) with new production accounting for an estimated 0.6 mol C m^{-2}. The growth of under-ice algae in Amundsen Gulf contribute a further 1.9 mol C m^{-2} (over two months) to the annual NCP in March and April. Annually, NCP on the Scotian Shelf exceeds that in Amundsen Gulf, though production in the two systems is of similar magnitude (Table 8.1). The air-sea CO_2 flux acts in opposing directions in the two systems; there is outgassing of 1.5 mol C m^{-2} yr^{-1} on the Scotian Shelf, and an uptake of 1.2 mol C m^{-2} yr^{-1} in Amundsen Gulf. On the Scotian Shelf, mixed-layer DIC losses due to biological production and outgassing of CO_2 are balanced by the delivery of DIC-rich water from below via wind-mixing, upwelling, and convective mixing, and by the lateral advection of water with higher concentration of DIC. By contrast, in Amundsen Gulf losses of DIC from the mixed-layer due to the production of organic matter are balanced by the uptake of atmospheric CO_2 and by the vertical diffusion of DIC-rich water from below the thermocline. The annual contributions of the

processes acting in each region are summarized in Table 8.1.

Table 8.1: A comparison between the controls on mixed-layer DIC on the Scotian Shelf (SS) and in Amundsen Gulf (AG). On the Scotian Shelf the processes contributing to changes in DIC are net community production (NCP), air-sea CO_2 flux (F_{CO_2}), horizontal advection and horizontal and vertical diffusion (Jtrsp), and vertical entrainment (VEnt). In Amundsen Gulf, mixed-layer DIC is affected by NCP, F_{CO_2}, freshwater (Fresh), and vertical diffusion (VDiff). All values are annual, given in units of mol C m^{-2} yr^{-1}.

	SS		AG
NCP	-2.5	NCP	-2.1
F_{CO_2}	-1.5	F_{CO_2}	1.2
Jtrsp	1.4	Fresh	0.0
VEnt	2.6	VDiff	0.9

On the Scotian Shelf, wind forcing, episodic upwelling and convective mixing all bring DIC-rich water to the surface, predominantly in the autumn and winter seasons. The Scotian Shelf behaves similarly to an upwelling system in which biologically productive surface waters are supersaturated with respect to atmospheric CO_2 due to the delivery of carbon-rich waters from below. The physical system on the Scotian Shelf may also be described as an estuarine system; there is an inflow of deep, nutrient- and carbon-rich water and an outflow of nutrient-deplete surface waters. By contrast, and as discussed briefly in Chapter 5, Amundsen Gulf, behaves like a downwelling system, exporting carbon-rich subsurface water to the adjacent Beaufort Sea. The combination of biological production and the sinking of organic matter, exports carbon from the surface to the subsurface layer. In Amundsen Gulf, this carbon-rich subsurface water is subsequently transported from the region, removing CO_2 from the surface waters, maintaining the undersaturation with respect to atmospheric CO_2, and facilitating atmsopheric CO_2 uptake the next productive season. The Amundsen Gulf system may alternatively be described as an anti-estuarine system; there is an outflow (to the Beaufort Sea) of carbon- and nutrient-rich subsurface waters, and an inflow (from the Beaufort Sea) of nutrient-poor surface waters (*Lanos*, 2009).

The Scotian Shelf and Amundsen Gulf systems are shown schematically in Figure 8.1. In both cases, the surface DIC losses due to biological production, or NCP, are balanced over the annual cycle by inputs of DIC from below. In the case of the Scotian Shelf this DIC-rich water is introduced to the surface in the autumn and winter by a combination of

wind, upwelling and convective mixing. In Amundsen Gulf, the water column is strongly stratified throughout the year and nutrients and DIC are brought to the surface, to a significantly lesser extent compared to the Scotian Shelf, either in the brief ice-free period in autumn when storms increase and the region is subject to wind mixing, or by vertical diffusion throughout the year. Winter sea-ice cover prevents the convective mixing seen on the Scotian Shelf as a result of heat lost from the surface ocean to the atmosphere. During the majority of the open water season in Amundsen Gulf the surface waters, and air-temperatures, are relatively warm. The remainder of the DIC lost to NCP in Amundsen Gulf is resupplied by the uptake of atmospheric CO_2 during the open water season (Fig. 8.1 and Table 8.1).

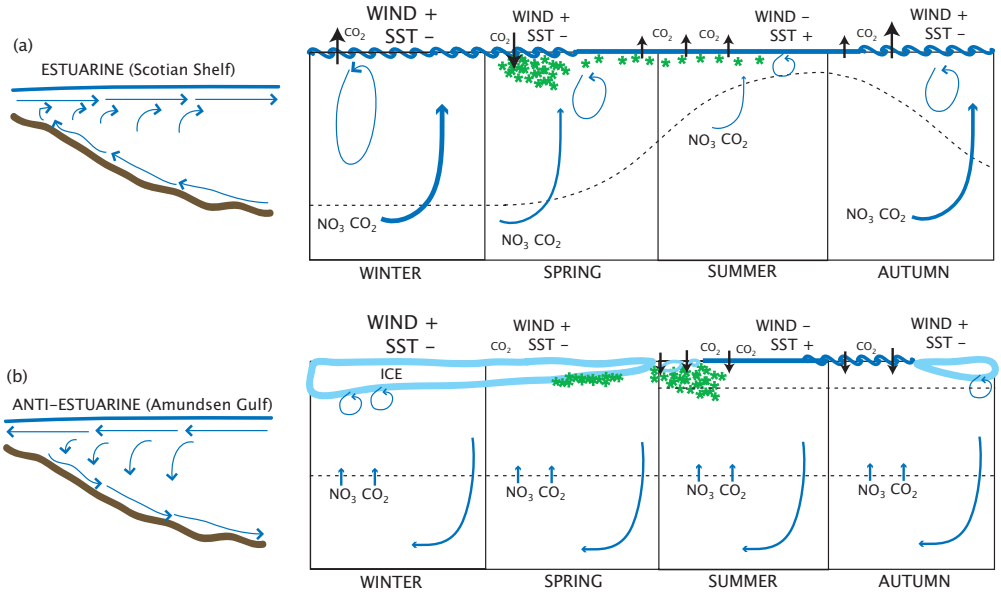

Figure 8.1: A schematic representation of the systems in (a) the Scotian Shelf and (b) Amundsen Gulf. The Scotian Shelf may be thought of as an estuarine system; there is an outflow of surface water, and an inflow subsurface waters delivered to the surface by a combination of wind mixing, upwelling and convection (blue arrows). The mixed-layer depth is represented by the dashed line. In contrast, Amundsen Gulf may be thought of as an anti-estuarine, or downwelling, system, with an inflow of surface waters and a outflow of subsurface water. Wind and convective mixing are inhibited by ice-cover in winter and nutrient-rich waters are delivered to the surface layer only by diffusive processes. Density driven mixing by the release of brine during sea-ice formation makes a contribution in the autumn and winter (blue arrows). The mixed-layer depth is roughly 50 meters (dashed line) throughout the year; strong surface stratification in the upper 10-20 meters is observed following sea-ice melt.

8.4 Perspectives

8.4.1 Natural versus Anthropogenic Variability

The surface ocean is currently experiencing changes due to both natural and anthropogenic factors including warming and acidification (*Serreze et al.*, 2000; *Orr et al.*, 2005; *Doney*, 2006). Shallow, high-latitude regions are expected to be particularly vulnerable to acidification. Both the Scotian Shelf and the Arctic Archipelago are thus regions which would benefit from monitoring of the carbon system in order to detect longer term trends.

The Scotian Shelf and adjacent continental shelf regions play and important role in the cycling of carbon in the North Atlantic Ocean. The research presented here has shown a decadal scale trend in surface pCO_2 and air-sea CO_2 fluxes in the Scotian Shelf region. A cooling of the waters in the region over the last decade, potentially linked to a greater transport of water from the Labrador Sea to the Scotian Shelf, have caused a weakening of the CO_2 release, driving the system towards uptake. The uptake of anthropogenic carbon by the ocean continues to increase, and the North Atlantic Ocean has particularly high concentrations of fossil-fuel derived CO_2 (*Sabine et al.*, 2004). The natural variability on the Scotian Shelf over the past decade has caused an increase in CO_2 uptake, and corresponding decrease in surface pH. The Scotian Shelf is also subject to episodic upwelling events which bring high-carbon, low-pH waters to the surface. Natural variability adds complexity to the system and may potentially mask longer term trends of anthropogenic change, such as decreasing pH. Baseline assessments and high-resolution observational data sets are required to unravel the natural and anthropogenic changes. Inorganic carbon data has been collected as part of the AZMP since 2006 in the Scotian Shelf region; these observations contribute to an extensive hydrographic and biological database for the region. Continued efforts to understand and characterize baseline conditions in this coastal system should lead to improvements in the prediction of potential future changes.

The Arctic Ocean is, by contrast to the North American east coast, very poorly studied. The Arctic Ocean is expected to be disproportionately responsive to environmental change including warming (*Serreze et al.*, 2000), sea-ice loss (*Maslanik et al.*, 2007), changes to production and ecosystems (*Arrigo et al.*, 2008; *Pabi et al.*, 2008), and changes to the freshwater cycle (*Peterson et al.*, 2002, 2006). At present, few baseline assessments of the carbon system in the Arctic Ocean exist, and the few observational studies rely on field data from the summer and autumn seasons only. The Arctic, and Antarctic, received

a great deal of attention during the recent International Polar Year (IPY)[1]. The results of many of the field programs that took place under the auspices of the IPY will soon make their way into the literature, improving the general outlook for detecting changes in the Arctic Ocean and Arctic coastal regions.

8.4.2 Arctic Sea-Ice Retreat

One striking change to the Arctic environment is clearly detectable; the observed rapid loss of sea-ice from the Arctic over the past decades has been faster than even the most pessimistic global model prediction (*Moritz et al.*, 2002; *Maslanik et al.*, 2007; *Stroeve et al.*, 2007). The Arctic sea-ice extent declined by as much as 25% in 2007 (*Maslanik et al.*, 2007). While the Arctic Ocean response to the decrease in sea-ice cover is uncertain, one can speculate about the possible impact on the inorganic carbon system. Surface waters in many regions of the Arctic Ocean are highly under-saturated with respect to atmospheric CO_2, including the Amundsen Gulf region as presented here. This undersaturation is maintained by the draw down of dissolved inorganic carbon over the shelves of the western Arctic, the input of excess alkalinity from the Mackenzie River, and the presence of sea-ice over the central Arctic, which retards air-sea exchange of CO_2 (*Bates and Mathis*, 2009). However, as sea-ice retreat continues, a large area of water will be exposed to the atmosphere, allowing air-sea exchange to occur. With an abrupt change in sea-ice extent, the CO_2 sink in the Arctic Ocean may become globally significant, amounting to an estimated 10% of the global ocean CO_2 sink based on the *Takahashi et al.* (2002) climatology for global air-sea CO_2 fluxes (*Bates and Mathis*, 2009).

Any increased atmospheric CO_2 flux into the Arctic Ocean as a result of decreased sea-ice cover is based on the assumption that sea-ice inhibits the exchange of CO_2 between the atmosphere and the surface ocean. This assumption has been under debate for some time (*Gosink et al.*, 1976; *Semiletov et al.*, 2004; *Zemmelink et al.*, 2006; *Semiletov et al.*, 2007; *Loose et al.*, 2009), and it has been suggested that CO_2 does indeed pass through sea-ice under certain conditions. Current estimates of the magnitude of the Arctic Ocean sink for CO_2, based on exchanges occurring only during the open water season may therefore underestimate the annual contribution of the Arctic Ocean in absorbing CO_2. An increase

[1]The IPY is a collaborative, international research effort to study the polar regions. The first IPY took place in 1882 with the second occurring 50 years later in 1932. The most recent IPY began in 2007 and finished in 2009 (http://www.ipy.org)

in the duration of the open water season may thus potentially alter the annual air-sea CO_2 fluxes less than projected. In any case, the contribution of the Arctic Ocean to the global ocean uptake of CO_2 is subject to greater uncertainty than other regions.

It has been further suggested that an increase in the duration of the open water season in the Arctic will lead to increased primary production due to the greater availability of light, potentially increasing the strength of the biological carbon pump in the region (*Arrigo et al.*, 2008). If a longer growing season lead to an increase in the export of primary production beneath the mixed-layer additional carbon would potentially be sequestered from the atmosphere. However, any increase in production leading to an enhanced uptake of CO_2 from the atmosphere would be counteracted by an increase in the surface pCO_2 due to warming, potentially out-competing the biologically mediated CO_2 uptake. From a solar radiation point of view, an ice-free Arctic Ocean is essentially a black body with the potential to absorb much more heat than the white, ice-covered, surface that reflects the majority of incoming solar radiation. Furthermore, an increase in the availability of light is a necessary but not sufficient condition in increasing production; the Arctic Ocean and continental shelves are predominantly nutrient limited (*Tremblay et al.*, 2008). Thus an increase in the amount of nutrients supplied to the euphotic zone would be required to sustain any additional production in an ice-free scenario. Furthermore, a significant carbon draw-down is presently observed preceding the seasonal ice melt (*Riedel et al.*, 2006); under-ice algae play a non-negligible, but poorly constrained, role in the primary production of the Arctic Ocean. The loss of ice in the region will certainly impact these ice-dependent organisms. A decrease in primary production in the absence of ice-algae should be expected, though the magnitude of the contribution of under ice algae to Arctic primary production has not been accurately quantified (*Gosselin et al.*, 1997; *Riedel et al.*, 2008; *Mundy et al.*, 2009). Due to the logistical difficulty of conducting field work in the Arctic outside the brief ice-free season, primary production is often assessed using remote sensing (*Arrigo et al.*, 2008; *Pabi et al.*, 2008), under ice algae are therefore often excluded in the estimates of Arctic primary production.

8.4.3 Carbon-based Approaches to Constrain Remote-Sensing

Satellite assessments of surface ocean chlorophyll-a concentration used to estimate primary production are dependent on the availability of clear sky. In other words, surface

chlorophyll-a concentration cannot be estimated under cloudy conditions, or under conditions of snow or ice cover. This poses a problem in many coastal regions, including the Scotian Shelf, where cloud cover may be observed the majority of the time. The Arctic Ocean is ice-covered throughout most of the year. The research presented here (Chapter 7) indicates that under ice primary production makes a non-negligible contribution to the annual production in the Amundsen Gulf region; roughly 50% of the spring/summer production occurs under complete or partial ice cover. This cannot be accounted for using satellite-based estimates of primary production requiring open water. Furthermore, a substantial proportion of the primary production occurring on the Scotian Shelf occurs in the absence of significant increases in surface chlorophyll-a concentration (Chapters 4 and 5). As the oceanographic community moves towards autonomous instrumentation, like the CARIOCA buoy, and remote-sensing applications, inorganic carbon-based approaches, in addition to chlorophyll-a concentration, may play an important role in constraining optical approaches.

BIBLIOGRAPHY

Aagaard, K., *The Beaufort undercurrent, in: The Alaskan Beaufort Sea: ecosystems and environments*, Academic Press, Orlando, FL, USA, 1984.

Aagaard, K., and E. C. Carmack, *The Arctic Ocean and climate: a perspective, in The Polar Oceans and Their Role in Shaping the Global Environment*, AGU, Washington, D.C., 1994.

Aagaard, K., L. K. Coachman, and E. C. Carmack, On the halocline of the arctic ocean, *Deep-Sea Res.*, *28*, 529–545, 1981.

Acker, J. G., and G. Leptoukh, Online analysis enhances use of NASA earth science data, *EOS Trans. AGU*, *88*, 14–17, 2007.

Alonso-Sáez, L., O. Sánchez, J. M. Gasol, V. Balagué, and C. Perdós-Alio, Winter-to-summer changes in the composition and single-cell activity of near-surface arctic prokaryotes, *Environ. Microbiol.*, *10*, 2444–2454, 2008.

Anderson, L. G., K. Olsson, and M. Chierici, A carbon budget for the Arctic Ocean, *Global Biogeochem. Cycles*, *12*, 455–465, 1998a.

Anderson, L. G., K. Olsson, E. P. Jones, M. Chierici, and A. Fransson, Anthropogenic carbon dioxide in the Arctic Ocean: Inventory and sinks, *J. Geophys. Res.*, *103*, 27,707–27,716, 1998b.

Anderson, L. G., S. Jutterström, S. Kaltin, E. P. Jones, and G. Björk, Variablility in river runoff distribution in the Eurasian Basin of the Arctic Ocean, *J. Geophys. Res.*, *109*, C01,016, 2004.

Anderson, L. G., et al., Water masses and circulation in the Eurasian Basin: Results from the Oden 91 expedition, *J. Geophys. Res.*, *99*, 3273–3283, 1994.

Andersson, A. J., and F. T. Mackenzie, Shallow-water oceans: a source or a sink of atmospheric CO_2, *Frontiers in Ecology and the Environment*, *2*, 348–353, 2004.

Arrigo, K. R., Marine microorganisms and global nutrient cycles, *Nature*, *437*, 349–355, 2005.

Arrigo, K. R., and G. L. van Dijken, Annual cycles of sea ice and phytoplankton in Cape Bathurst polynya, southeastern Beaufort Sea, Canadian Arctic, *Geophys. Res. Lett.*, *31*, L08,304, 2004.

Arrigo, K. R., G. van Dijken, and S. Pabi, Impact of a shrinking arctic ice cover on marine primary production, *Geophys. Res. Lett.*, *35*, L19,603, 2008.

Bakker, D. C. E., J. Etcheto, J. Boutin, and L. Merlivat, Variability of surface water fCO_2 during seasonal upwelling in the equatorial Atlantic Ocean as observed by a drifting buoy, *J. Geophys. Res.*, *106*, 9241–9253, 2001.

Banse, K., Grazing and zooplankton production as key controls of phytoplankton production in the open ocean, *Oceanogr.*, *7*, 13–20, 1994.

Banse, K., Zooplankton: Pivotal role in the control of ocean production, *J. Mar. Sci.*, *52*, 265–277, 1995.

Barber, D. G., and R. Massom, *The role off sea ice in bipolar polynya processes*, Elsevier Oceanography Series, Elsevier, 2006.

Bates, N. R., Air-sea CO_2 fluxes and the continental shelf pump of carbon in the Chukchi Sea adjacent to the Arctic Ocean, *J. Geophys. Res.*, *111*, C10,013, 2006.

Bates, N. R., Interannual variability of the oceanic CO_2 sink in the subtropical gyre of the North Atlantic over the last 2 decades, *J. Geophys. Res.*, *112*, C09,013, 2007.

Bates, N. R., and J. T. Mathis, The arctic ocean marine carbon cycle: evaluation of air-sea CO_2 exchanges, ocean acidification impacts and potential feedbacks, *Biogeosciences*, *6*, 2433–2459, 2009.

Bates, N. R., A. F. Michaels, and A. H. Knap, Seasonal and interannual variability of oceanic carbon dioxide species at the U.S. JGOFS Bermuda Atlantic time-series study (BATS) site, *Deep-Sea Research II*, *43*, 347–383, 1996.

Bates, N. R., L. Merlivat, L. Beaumont, and A. C. Pequignet, Intercomparison of shipboard and moored carioca buoy seawater fCO_2 measurements in the Sargasso Sea, *Marine Chemistry*, *72*, 239–255, 2000.

Bates, N. R., L. Samuels, and L. Merlivat, Biogeochemical and physical factors influencing seawater fCO_2 and air-sea CO_2 exchange on the Bermuda coral reef, *Limnol. Oceanogr.*, *46*, 833–846, 2001.

Bates, N. R., M. H. P. Best, and D. A. Hansell, Spatio-temporal distribution of dissolved inorganic carbon and net community production in the Chukchi and Beaufort Seas, *Deep-Sea Research II*, *52*, 3303–3323, 2005.

Bates, N. R., J. T. Mathis, and L. Cooper, The effect ocean acidification on biologically induced seasonality of carbonate mineral saturation states in the western Arctic, *J. Geophys. Res.*, *114*, C11,007, 2009.

Bigelow, H. B., Physical oceanography of the Gulf of Maine, *Bull. U.S. Bur. Fish.*, *640*, 511–1027, 1927.

Boehme, S. E., C. L. Sabine, and C. E. Reimers, CO_2 fluxes from a coastal transect: a time-series approach, *Mar. Chem.*, *63*, 49–67, 1998.

Borges, A. V., Do we have enough pieces of the jigsaw to integrate CO_2 fluxes in the coastal ocean?, *Estuaries*, *28*, 3–27, 2005.

Borges, A. V., and N. Gypens, Carbonate chemistry in the coastal zone responds more strongly to eutrophication than to ocean acidification, *Limnol. Oceanogr.*, *55*, 346–353, 2010.

Borges, A. V., B. Delille, and M. Frankignoulle, Budgeting sinks and sources of CO_2 in the coastal ocean: Diversity of ecosystems counts, *Geophys. Res. Lett.*, *32*, L14,601, 2005.

Borges, A. V., B. Tilbrook, N. Metzl, A. Lenton, and B. Delille, Inter-annual variability of the carbon dioxide oceanic sink south of Tasmania, *Biogeosciences*, *5*, 141–155, 2008.

Boutin, J., and L. Merlivat, New in-situ estimates of carbon biological production rates in the Southern Ocean from CARIOCA drifter measurements, *Geophys. Res. Lett.*, *36*, L13,608, 2009.

Bowen, W. D., J. McMillan, and R. Mohn, Sustained exponential population growth of grey seals at sable island, Nova Scotia, *ICES J. Marine Science*, *60*, 1265–1274, 2003.

Bozec, Y., H. Thomas, K. Elkalay, and H. J. W. de Baar, The continental shelf pump for CO_2 in the North Sea - evidence from summer observation, *Marine Chemistry*, *93*, 131–147, 2005.

Bozec, Y., H. T. L.-S. Schiettecatte, A. V. Borges, K. Elkalay, and H. J. W. de Baar, Assessment of the processes controlling seasonal variations of dissolved inorganic carbon in the North Sea, *Limnol. Oceanogr.*, *51*, 2746–2762, 2006.

Brewer, P. G., and J. C. Goldman, Alkalinity changes generated by phytoplankton growth, *Limnol. Oceanogr.*, *21*, 108–117, 1976.

Broecker, W. S., The role of $CaCO_3$ compensation in the glacial to interglacial atmospheric CO_2 change, *Global Biogeochem. Cycles.*, *1*, 15–29, 1987.

Brown, C. W., and J. A. Yoder, Blooms of *Emiliania hyxleyi*(pymnesiophyceae) in surface waters of the nova scotia shelf and grand bank, *J. Plankton Res.*, *15*, 1429–1438, 1993.

Brown, R. G. B., Oceanographic factors as determinants of the winter range of the dovekie (alle alle) off Atlantic Canada, *Colonial Waterbirds*, *11*, 176–180, 1988.

Bryden, H. L., H. R. Longworth, and S. A. Cunningham, Slowing of the Atlantic meridional overturning circulation at 25°N, *Nature*, *438*, 655–657, 2005.

Cai, W.-J., Z. A. Wang, and Y. Wang, The role of marsh-donimated heterotrophic continental margins in transport of CO_2 between the atmosphere, the land-sea interface and the ocean, *Geophys. Res. Lett.*, *30*, 1849, 2003.

Cai, W.-J., M. H. Dai, and H. C. Wang, Air-sea exchange of carbon dioxide in ocean margins: A province-based synthesis, *Geophys. Res. Lett.*, *56*, 578–590, 2006.

Caldeira, K., and M. E. Wickett, Anthropogenic carbon and ocean pH, *Nature*, *425*, 365, 2003.

CARINA, Carbon in the atlantic ocean region - the CARINA project: Results and data, version 1.0, *Tech. rep.*, Carbon Dioxide Information Analysis Center, Oak Ridge National Laboratory, U.S. Department of Energy, Oak Ridge, TN, USA, 2009.

Carmack, E., and D. C. Chapman, Wind-driven shelf/basin exchange on an arctic shelf: The joint roles of ice cover extent and shelf-break bathymetry, *Geophys. Res. Lett.*, *30*, 1778, 2003.

Carmack, E., and P. Wassmann, Food webs and physical-biological coupling on pan-arctic shelves: Unifying concepts and comprehensive perspectives, *Prog. Oceangr.*, *71*, 466–477, 2006.

Carmack, E. C., and R. W. MacDonald, Oceanography of the Canadian Shelf of the Beaufort Sea: A setting for marine life, *Arctic*, *55*, 29–45, 2002.

Carmack, E. C., R. W. Macdonald, and S. Jasper, Phytoplankton productivity on the Canadian Shelf of the Beaufort Sea, *Mar. Ecol. Prog. Ser.*, *277*, 37–50, 2004.

Chapman, D. C., and R. C. Beardsley, On the origin of shelf water in the Middle Atlantic Bight, *J. Phys. Oceanogr.*, *19*, 384–391, 1989.

Chavez, F. P., T. Takahashi, W.-J. Cai, G. Friederich, B. Hales, R. Wanninkhof, and R. Feely, *Coastal Oceans, in: The First State of the Carbon Cycle Report (SOCCR): The North American Carbon Budget and Implications for the Global Carbon Cycle*, U.S. Climate Change Science Program, Washington DC, USA, 2007.

Chen, C.-T. A., and A. V. Borges, Reconciling opposing views on carbon cycling in the coastal ocean: Continental shelves as sinks and near-shore ecosystems as sources of atmospheric CO_2, *Deep-Sea Res. II*, *33*, L12,603, 2009.

Chen, C. T.-A., and S. L. Wang, Carbon, alkalinity and nutrient budget on the East China Sea continental shelf, *J. Geopys. Res.*, *104*, 20,675–20,686, 1999.

Chen, C.-T. A., K.-K. Liu, and R. Macdonald, *Continental Margin Exchanges, in: Ocean Biogeochemistry - The Role of the Ocean Carbon Cycle in Global Change*, Global Change - Springer, Berlin, 2003.

Chierici, M., and A. Fransson, Calcium carbonate saturation in the surface water of the Arctic Ocean: undersaturation in freshwater influenced shelves, *Biogeosciences*, *6*, 2421–2432, 2009.

Chierici, M., A. Olsen, T. Johannessen, J. Trinanes, and R. Wanninkhof, Algorithms to estimate the carbon dioxide uptake in the northern North Atlantic using shipboard observations, satellite and ocean analysis data, *Deep-Sea Res.*, *56*, 630–639, 2009.

Coachman, L. K., and K. Aagaard, *Physical Oceanography of Arctic and subarctic seas, in: Marine Geology and Oceanography of the Arctic Seas*, Springer-Verlag, New York, USA, 1974.

Coachman, L. K., and K. Aagaard, Transport through Bering Strait: annual and interannual variability, *J. Geophys. Res.*, *93*, 15,535–15,539, 1988.

Cooper, L. W., J. W. McClelland, R. M. Holmes, P. A. Raymond, J. J. Gibson, and B. J. Peterson, Flow-weighted values of runoff tracers (δ^{18}O, DOC, Ba, alkalinity) from the six largest arctic rivers, *Geophys. Res. Lett.*, *35*, L18,606, 2008.

Copin-Montégut, C., M. Bégovic, and L. Merlivat, Variability of the partial pressure of CO_2 on diel to annual time scales in the northwestern Mediterranean Sea, *Mar. Chem.*, *85*, 169–189, 2004.

Cota, G. F., L. R. Pomeroy, W. G. Harrison, E. P. Jones, F. Peters, W. M. S. Jr., and T. R. Weingartner, Nutrients, primary production and microbial heterotrophy in the southeastern Chukchi Sea: Arctic summer nutrient depletion and heterotrophy, *Mar. Ecol. Prog. Ser.*, *135*, 247–258, 1996.

Cuny, J., P. B. Rhines, and R. Kwok, Davis Strait volume, freshwater and heat fluxes, *Deep-Sea Research I*, *52*, 519–542, 2005.

DeGrandpre, M. D., G. J. Olbu, C. M. Beatty, and T. R. Hamar, Air-sea CO_2 fluxes on the U.S. Middle Atlantic Bight, *Deep-Sea Res. II*, *49*, 4355–4367, 2002.

Delille, B., et al., Repsonse of primary production and calcification to changes of pCO_2 during experimental blooms of the coccolithophorid *Emiliania hyxleyi* , *Global Biogeochemical Cycles*, *19*, GB2023, 2005.

d'Entremont, C., Growing our future: Long-term planning for aquaculture in Nova Scotia, *Tech. rep.*, Nova Scotia Agriculture and Fisheries, 2009.

Dickson, A. G., An exact definition of total alkalinity and a procedure for the estimation of alkalinity and total inorganic carbon from titration data, *Deep-Sea Res.*, *328*, 609–623, 1981.

Dickson, A. G., Thermodynamics of the dissociation of boric acid in synthetic seawater from 273.15 to 318.15 K, *Deep-Sea Res.*, *37*, 755–766, 1990.

Dickson, A. G., and F. J. Millero, A comparison of the equilibrium constants for the dissociation of carbonic acid in seawater media, *Deep-Sea Res. II*, *34*, 1733–1743, 1987.

Dickson, A. G., C. L. Sabine, and J. R. Christian, Guide to best practices for ocean CO_2 measurements, *Tech. rep.*, PICES Special Publication 3, 2007.

Dickson, B., All change in the Arctic, *Nature*, *397*, 389–391, 1999.

Dickson, R., From the Labrador Sea to global change, *Nature*, *386*, 649–650, 1997.

Dittmar, T., and G. Kattner, The biogeochemistry of the river and shelf ecosystem of the Arctic Ocean: A review, *Mar. Chem.*, *83*, 103–120, 2003.

Doney, S. C., Dangers of ocean acidification, *Scientific American*, *294*, 58–65, 2006.

Doney, S. C., N. Mahowald, I. Lima, R. A. F. F. T. Mackenzie, J.-F. Lamarque, and P. J. Rasch, Impact of anthropogenic atmospheric nitrogen and sulfur deposition on ocean acidification and the inorganic carbon system, *PNAS*, *104*, 14,580–14,585, 2007.

Donohue, S., A numerical model of an upwelling event off the coast of Nova Scotia, Master's thesis, Royal Military College of Canada, 2000.

Droop, M. R., Some thoughts on nutrient limitation on algae, *J. Phycol.*, *9*, 264–272, 1973.

Dugdale, R. C., and J. J. Goering, Uptake of new and regenerated forms of nitrogen in primary production, *Limnol. Oceanogr.*, *12*, 196–206, 1967.

Ekwurzel, B., P. Scholosser, R. A. Mortlock, R. G. Fairbanks, and J. H. Swift, River runoff, sea ice meltwater, and pacific water distribution and mean residence times in the Arctic Ocean, *J. Geophys. Res.*, *106*, 9075–9092, 2001.

Eppley, R. W., *Autotrophic production of particulate matter, in: Analysis of marine ecosystems*, Academic Press, New York, USA, 1981.

Etcheto, J., J. Boutin, Y. Dandonneau, D. C. E. Bakker, R. A. Feely, R. D. Ling, P. D. Nightingale, and R. Wanninkhof, Air-sea CO_2 flux variablity in the equatorial Pacific Ocean near 100°W, *Tellus B*, *51*, 734–737, 1999.

Fabry, V. J., J. B. McClintock, J. T. Mathis, and J. M. Grebmeier, Ocean acidification at high latitudes: the bellwether, *Oceanogr.*, *22*, 160–171, 2009.

Falkowski, P., and D. A. Kiefer, Chlorophyll a fluorescence in phytoplankton: relationship to photosynthesis and biomass, *J. Plankton Res.*, *7*, 715–731, 1985.

Feely, R. A., C. L. Sabine, K. Lee, W. Berelson, J. Kleypas, V. J. Fabry, and F. J. Millero, Impact of anthropogenic CO_2 on the $CaCO_3$ system in the ocean, *Science*, *305*, 362–366, 2004.

Feely, R. A., C. L. Sabine, J. M. Hernandez-Ayon, D. Ianson, and B. Hales, Evidence for upwelling of corrosive "acidified" water onto the continental shelf, *Science*, *320*, 1490–1492, 2008.

Fennel, K., and J. Wilkin, Quantifying biological carbon export for the northwest North Atlantic continental shelves, *Geophys. Res. Lett.*, *36*, L18,605, 2009.

Fennel, K., J. Wilkin, J. Levin, J. Moisan, J. O'Reilly, and D. Haidvogel, Nitrogen cycling in the Middle Atlantic Bight: Results from a three-dimensional model and implications for the North Atlantic nitrogen budget, *Global Biogeochem. Cycles*, *20*, GB3007, 2006.

Fennel, K., J. Wilkin, M. Previdi, and R. Najjar, Denitrification effects on air-sea CO_2 flux in the coastal ocean: Simulations for the northwest North Atlantic, *Geophys. Res. Lett.*, *35*, L24,608, 2008.

Fogg, G. E., The ecological consequence of extracellular products of phytoplankton photosynthesis, *Bot. Mar.*, *26*, 3–14, 1983.

Forest, A., M. Sampei, R. Makabe, H. Sasaki, D. G. Barber, Y. Gratton, P. Wassmann, and L. Fortier, The annual cycle of particulate organic carbon export in Franklin Bay (Canadian Arctic): Environmental control and food web implications, *J. Geophys. Res.*, *113*, C03S05, 2008.

Fournier, R. O., J. Marra, R. Bohrer, and M. van Det, Plankton dynamics and nutrient enrichment of the Scotian Shelf, *J. Fish. Res. Board Can.*, *34*, 1004–1018, 1977.

Frankignoulle, M., and A. V. Borges, European continental shelf as a significant sink for atmopsheric carbon dioxide, *Global Biogeochem. Cycles*, *15*, 569–576, 2001.

Fransson, A., M. Chierici, L. G. Anderson, I. Bussmann, G. Kattner, E. P. Jones, and J. H. Swift, The importance of shelf processes for the modification of chemical constituents in the waters of the Eurasian Arctic Ocean: implication for carbon fluxes, *Continental Shelf Res.*, *21*, 225–242, 2001.

Friis, K., A. Körtzinger, and D. W. R. Wallace, The salinity normalization of marine inorganic carbon chemistry data, *Geophys. Res. Lett.*, *30*, 1085, 2003.

Galloway, J. N., et al., Nitrogen cycles: Past, present, and future, *Biochemistry*, *70*, 153–226, 2004.

Garneau, M.-E., S. Roy, C. Lovejoy, Y. Gratton, and W. F. Vincent, Seasonal dynamics of bacterial biomass and production in a coastal arctic ecosystem: Franklin Bay, western Canadian Arctic, *J. Geophys. Res.*, *113*, C07S91, 2008.

Gass, S. E., and J. H. M. WIllison, *An assessment of the distribution of deep-sea corals in Atlantic Canada by using both scientific and local forms of knowledge, in: Cold-Water Corals and Ecosystems*, Springer, Berlin, Germany, 2005.

Gattuso, J.-P., M. Frankignoulle, and R. Wollast, Carbon and carbonate metabolism in coastal aquatic ecosystems, *Annual Reviews of Ecological Systems*, *29*, 405–434, 1998.

Gazeau, F., C. Quiblier, J. M. Jansen, J.-P. Gattuso, J. J. Middleburg, and C. H. R. Heip, Impact of elevated CO_2 on shellfish calcification, *Geophys. Res. Lett.*, *34*, L07,603, 2007.

Goldman, J. C., and P. G. Brewer, Effect of nitrogen source and gowth rate on phytoplankton-mediated changes in alkalinity, *Limnol. Oceanogr.*, *25(2)*, 352–357, 1980.

Gosink, T. A., J. G. Pearson, and J. J. Kelley, Gas movement through sea ice, *Nature*, *263*, 41–42, 1976.

Gosselin, M., M. Levasseur, P. A. Wheeler, R. A. Horner, and B. C. Booth, New measurements of phytoplankton and ice algal production in the Arctic Ocean, *Deep-Sea Res. II*, *44*, 1623–1644, 1997.

Gradinger, R., Occurence of an algal bloom under arctic pack ice, *Mar. Ecol. Prog. Ser.*, *131*, 301–305, 1996.

Grasshoff, K., *Methods of Seawater Analyses*, Weinheim, New York, 1999.

Greatbatch, R. J., The North Atlantic Oscillation, *Stoch. Environ. Res. and Risk Assess.*, *14*, 213–242, 2000.

Greenan, B. J. W., B. D. Petrie, W. G. Harrison, and N. S. Oakey, Are the spring and fall blooms on the Scotian Shelf related to short-term physical events?, *Continental Shelf Res.*, *24*, 603–625, 2004.

Greenan, B. J. W., B. D. Petrie, W. G. Harrison, and P. M. Strain, The onset and evolution of a spring bloom on the Scotian Shelf, *Limnol. Oceanogr.*, *53*, 1759, 2008.

Greene, C. H., and A. J. Pershing, Climate drives sea change, *Science*, *315*, 1084–1085, 2007.

Gruber, N., and J. L. Sarmiento, *Large-scale biogeochemical-physical interactions in elemental cycles, in: The Sea*, John Wiley and Sons, New York, NY, USA, 2002.

Gruber, N., C. D. Keeling, and T. F. Stocker, Carbon-13 constraints on the seasonal inorganic carbon budget at the BATS site in the northwestern Sargasso Sea, *Deep-Sea Res. I*, *45*, 673–717, 1998.

Gruber, N., P. Freidlingstein, C. B. Feild, R. Valentini, M. Heimanna, J. E. Richey, P. R. Lankao, E.-D. Schulze, and C.-T. A. Chen, *The Vulnerability of the Carbon Cycle in the 21st Century: An Assessment of Carbon-Climate-Human Interactions, in: The global carbon cycle: integrating human, climate and the natural world*, SCOPE, ISSN, Washington, DC, USA, 2004.

Hachey, H. B., The effect of a storm on an in-shore area with markedly stratified waters, *J. Bio. Board Can.*, *1*, 227–237, 1935.

Hachey, H. B., The waters of the scotian shelf, *J. Fish. Res. Board Can.*, *5*, 377–397, 1942.

Hannah, C. G., J. A. Shore, and J. W. Loder, Seasonal circulation on the western and central Scotian Shelf, *J. Physical Oceanography*, *31*, 591–615, 2001.

Hansell, D. A., and C. A. Carlson, Marine dissolved organic matter and the carbon cycle, *Oceanography*, *14*, 41–49, 2001.

Hansell, D. A., D. Kadko, and N. R. Bates, Degradation of terrigenous dissolved organic carbon in the western Arctic Ocean, *Science*, *304*, 858–861, 2004.

Hoegh-Guldberg, O., et al., Coral reefs under rapid climate change and ocean acidification, *Science*, *318*, 1737–1742, 2007.

Hood, E. M., and L. Merlivat, Annual to interannual variations of fCO_2 in the northwestern Mediterranean Sea: Results from hourly measurements made by CARIOCA buoys, 1995-1997, *J. Marine Res.*, *59*, 113–131, 2001.

Hooker, S. K., H. Whitehead, S. Gowans, and R. W. Baird, Fluctuations in distribution and patterns of individual range use of northern bottlenose whales, *Mar. Ecol. Prog. Ser.*, *225*, 287–297, 2002.

Horner, R., and G. C. Schrader, Relative contributions of ice algae, phytoplankton, and benthic microalgae to primary production in nearshore regions of the Beaufort Sea, *Arctic*, *35*, 485–503, 1982.

Houghton, R. W., and R. G. Fairbanks, Water sources for Georges Bank, *Deep-Sea Res. II*, *48*, 95–114, 2001.

Hurrell, J. W., Decadal trends in the North Atlantic Oscillation: regional temperature and precipitation, *Science*, *269*, 676–679, 1996.

Hutchins, D. A., and K. W. Bruland, Iron-limited diatom growth and Si:N uptake ratios in a coastal upwelling regime, *Nature*, *393*, 561–564, 1998.

Huthnance, J. M., J. T. Holt, and S. L. Wakelin, Deep ocean exhange with west-European shelf seas, *Ocean Sci.*, *5*, 621–634, 2009.

Ingram, R. G., J. Bâcle, D. G. Barber, Y. Gratton, and H. Melling, An overview of physical processes in the North Water, *Deep-Sea Res. II*, *49*, 4893–4906, 2002.

Jakobsson, M., R. McNab, L. Mayer, R. Anderson, M. Edwards, J. Hatzky, H.-W. Schenke, and P. Johnson, An improved bathymetric portrayal of the Arctic Ocean: Implications for ocean modeling and geological, geophysical and oceanographic analyses, *Geophys. Res. Lett.*, *35*, L07,602, 2008.

Jiang, L.-Q., W.-J. Cai, R. Wanninkhof, Y. Wang, and H. Luger, Air-sea CO_2 fluxes on the U.S. South Atlantic Bight: Spatial and seasonal variability, *J. Geophys. Res.*, *113*, C07,019, 2008.

Johnson, K. M., K. D. Wills, D. B. Butler, W. K. Johnson, and C. S. Wong, Coulometric total carbon dioxide analysis for marine studies: maximizing the performance of an automated gas extraction system and coulometric detector, *Marine Chemistry*, *44*, 167–188, 1993.

Johnson, K. M., et al., Coulometric total carbon dioxide analysis for marine studies: assessment of the quality of total inorganic carbon measurements made during the US Indian Ocean CO_2 survey 1994-1996, *Marine Chemistry*, *63*, 21–37, 1998.

Johnson, M. A., and I. V. Polyakov, The Laptev Sea as a source for recent Arctic Ocean salinity changes, *Geophys. Res. Lett.*, *28*, 2017–2020, 2001.

Jones, E. P., L. G. Anderson, and J. H. Swift, Distribution of Atlantic and Pacific waters in the upper Arctic Ocean: Implications for circulation, *Geophys. Res. Lett.*, *25*, 765–768, 1998.

Jones, P., Total co_2 and total alkalinity data obtained during the R/V Hudson mission in the North Atlantic Ocean during WOCE Section AR01W (AR07W) (22 June - 9 July, 1998), *Tech. rep.*, Carbon Dioxide Information Analysis Center, Oak Ridge National Laboratory, Oak Ridge, Tennessee, 1998.

Jull-Pedersen, T., C. Michel, and M. Gosselin, Sinking export of particulate organic material from the euphotic zone in the eastern Beaufort Sea, *Mar. Ecol. Prog. Ser.*, *410*, 55–70, 2010.

Kaltin, S., and L. G. Anderson, Uptake of anthropogenic carbon dioxide in the Arctic Seas: Evaluation of the relative importance of processes that influence pCO_2 in water transported over the Bering-Chukchi Sea Shelf, *Mar. Chem.*, *94*, 67–79, 2005.

Karl, D. M., and R. Lukas, The hawaii ocean time-series (HOT) program: Background, rationale and field implementation, *Deep-Sea Research II*, *43*, 129–156, 1996.

Kepkay, P. E., S. E. H. Niven, and J. F. Jellett, Colloidal organic carbon and phytoplankton speciation during a coastal bloom, *J. Plankton Res.*, *19*, 369–389, 1997.

Khatiwala, S. P., R. G. Fairbanks, and R. W. Houghton, Freshwater souces to the coastal ocean off northeastern North America: Evidence from $H_2^{18}O/H_2^{16}O$, *J. Geophys. Res.*, *104*, 18,241–18,255, 1999.

Kiefer, D. A., Fluorescence properties of natural phytoplankton populations, *Marine Biology*, *22*, 263–269, 1973.

Kleypas, J. A., and C. Langdon, *Coral reefs and changing seawater chemistry, in: Coaral reefs and climate change: science and management*, vol. 61, AGU Monograph Series, Coast. Estuar. Stud., 2006.

Kling, A. W., L. Dilling, G. P. Zimmerman, D. M. Fairman, R. A. Houghton, G. Marland, A. Z. Rose, and T. J. Wilbanks, *What is the carbon cycle and why care?, in: The*

First State of the Carbon Cycle Report (SOCCR): The North American Carbon Budget and Implications for the Global Carbon Cycle, U.S. Climate Change Science Program, Washington DC, USA, 2007.

Körtzinger, A., H. Thomas, B. Schneider, N. Gronau, L. Mintrop, and J. C. Duinker, At-sea intercomparison of two newly designed underway pCO_2 systems - encouraging results, *Marine Chemistry*, *52*, 133–145, 1996.

Lammers, R. B., A. I. Shiklomanov, C. J. Vorosmarty, B. M. Fekete, and B. J. Peterson, Assessement of contemporary arctic river runoff based on observational discharge records, *J. Geophys. Res.*, *109*, C01,016, 2001.

Lanos, R., Circulation régionale, masses d'eau,cycles d'évolution et transports entre la Mer de Beaufort et le Golfe d'Amundsen, Ph.D. thesis, Univérsité du Québec, 2009.

Large, W. G., and S. G. Yeager, Diurnal to decadal global forcing for ocean and sea-ice models: The data sets and flux climatologies, *Tech. rep.*, National Center for Atmospheric Research, USA, 2004.

Lefèvre, N., J. Aiken, J. Rutllant, G. Daneri, S. Lavender, and T. Smyth, Observations of pCO_2 in the coastal upwelling off Chile: Spatial and temporal extrapolation using satellite data, *J. Geophys. Res.*, *107*, 3055, 2002.

Lefèvre, N., A. Guillot, L. Beaumont, and T. Danguy, Variability of fCO_2 in the eastern tropical Atlantic from a moored buoy, *J. Geophys. Res.*, *113*, C01,015, 2008.

Lendt, R., H. Thomas, A. Hupe, and V. Ittekkot, Response of the near-surface carbonate system of the northwestern Arabian Sea to the southwest monsoon and related biological forcing, *J. Geophys. Res.*, *108*, 3222, 2003.

Lenhart, H. J., J. Pätsch, W. Kühn, A. Moll, and T. Pohlmann, Investigation on the trophic state of the North Sea for three years (1994 -1996) simulated with the ecosystem model ERSEM - the role of a sharp NAOI decline, *Biogeosciences Discuss.*, *1*, 725–753, 2004.

Lewis, E., and D. W. R. Wallace, Program developed for CO_2 systems calculations, *ORNL/CDIAC 105*, Carbon Dioxide Information Analysis Center, Oak Ridge National Laboratory US Department of Energy, Oak Ridge, Tennessee, 1998.

Lobb, J., A. J. Weaver, E. C. Carmack, and R. G. Ingram, Structure and mixing across an Arctic/Atlantic front in nothern Baffin Bay, *Geophys. Res. Lett.*, *30*, 1833, 2003.

Loder, J. W., C. K. Ross, and P. C. Smith, A space and time-scale characterization of circulation and mixing over submarine bank with application to the northwestern atlantic continental shelf, *Can. J. Fish. Aquat. Sci.*, *45*, 1860, 1988.

Loder, J. W., G. Han, C. G. Hannah, D. A. Greenberg, and P. C. Smith, Hydrography and baroclinic circulation in the Scotian Shelf region: winter versus summer, *Can. J. Fish. Aquat. Sci.*, *54*, 1997.

Loder, J. W., B. Petrie, and G. Gawarkiewicz, *The coastal ocean off northeastern North America: A large-scale view, in: The Sea, The Global Coastal Ocean: Regional Studies and Syntheses*, John Wiley, New York, NY, USA, 1998.

Loder, J. W., C. G. Hannah, B. D. Petrie, and E. A. Gonzalez, Hydrographic transport variability on the Halifax section, *J. Geophys. Res.*, *108*, 8003, 2003.

Lohrenz, S. E., and W.-J. Cai, Satellite ocean color assessment of air-sea fluxes of CO_2 in a river-dominated coastal margin, *Geophys. Res. Lett.*, *33*, L01,601, 2006.

Loose, B., W. R. McGillis, P. Schlosser, D. Perovich, and T. Takahashi, Effects of freezing, growth, and ice cover on gas transport processes in laboratory seawater experiments, *Geophys. Res. Lett.*, *36*, doi:10.1029/2008GL036,318, 2009.

Macdonald, R. W., C. S. Wong, and P. E. Erickson, The distribution of nutrients in the southeastern Beaufort Sea: implications for water circulation and primary production, *J. Geophys. Res.*, *92*, 2939–2952, 1987.

Macdonald, R. W., S. M. Soloman, R. E. Cranston, H. E. Welch, and M. B. Yunker, A sediment and organic carbon budget for the Canadian Beaufort Shelf, *Marine Geology*, *144*, 255–273, 1998.

Macdonald, R. W., E. C. Carmack, F. A. McLaughlin, K. K. Falkner, and J. H. Swift, Connections among ice, runoff and atmospheric forcing in the Beaufort Gyre, *Geophys. Res. Lett.*, *26*, 2223–2226, 1999.

Macdonald, R. W., F. A. McLaughlin, and E. C. Carmack, Fresh water and its sources during the SHEBA drift in the Canada Basin of the Arctic Ocean, *Deep-Sea Res. I*, *49*, 1769–1785, 2002.

Macdonald, R. W., L. G. Anderson, J. P. Christensen, L. A. Miller, I. P. Semiletov, and R. Stein, *The Arctic Ocean, in: Carbon and Nutrient Fluxes in Continental Margins: A Global Synthesis*, Global Change - The IGBP Series, Springer, New York, USA, 2009.

Magen, C., G. Chaillou, S. A. Crowe, A. Mucci, B. Sundby, A. Gao, R. Makabe, and H. Sasaki, Origin and fate of particulate organic matter in the southern Beaufort Sea-Amundsen Gulf region, Canadian Arctic, *Estuar. Coast. Shelf Sci.*, *86*, 31–41, 2010.

Maslanik, J. A., C. Fowler, J. Stroeve, S. Drobot, J. Zwally, D. Yi, and W. Emery, A younger, thinner arctic ice cover: Increased potential for rapid, extensive sea-ice loss, *Geophys. Res. Lett.*, *34*, L24,501, 2007.

Mathis, J. T., D. A. Hansell, and N. R. Bates, Strong hydrographic controls on spatial and seasonal variability of dissolved organic carbon in the Chukchi Sea, *Deep-Sea Res. II*, *52*, 3245–3258, 2005.

Mathis, J. T., D. A. Hansell, D. Kadko, N. R. Bates, and L. W. Cooper, Determining net dissolved organic carbon production in the hydrographically complex western Arctic Ocean, *Limnol. Oceanogr.*, *52*, 1789–1799, 2007.

Mathis, J. T., N. R. Bates, D. A. Hansell, and T. Babila, Net community production in the northeastern Chukchi Sea, *Deep-Sea Res. II*, *56*, 1213–1222, 2009.

McLaughlin, F. A., E. C. Carmack, R. W. Macdonald, and J. K. B. Bishop, Physical and geochemical properties across the Atlantic/Pacific water mass front in the southern Canadian Basin, *J. Geophys. Res.*, *101*, 1183–1197, 1996.

McLaughlin, F. A., E. C. Carmack, R. W. Macdonald, H. Melling, J. H. Swift, P. A. Wheeler, B. F. Sherr, and E. B. Sherr, The joint roles of Pacific and Atlantic-origin waters in the Canada Basin, 1997-1998, *Deep-Sea Res. I*, *51*, 107–128, 2004.

McLaughlin, F. A., E. C. Carmack, R. G. Ingram, W. J. Williams, and C. Michel, *Oceanography of the Northwest Passage, in: The Sea (Vol. 14) - The Global Coastal Ocean*, Harvard University Press, Cambridge, MA, USA, 2005.

McPhee, M. G., T. P. Stanton, J. H. Morison, and D. G. Martinson, Freshening of the uppper ocean in the Arctic: Is perennial sea ice disappearing?, *Geophys. Res. Lett.*, *25*, 17291,732, 1998.

Mehrbach, C., C. H. Culberson, J. E. Hawley, and R. M. Pytkowicz, Measurement of the apparent dissociation constants of carbonic acid in seawater at atmospheric pressure, *Limnol. Oceangr.*, *18*, 897–907, 1973.

Meincke, J., B. Rudels, and H. J. Friedrich, The Arctic Ocean-Nordic Seas thermohaline system, *J. Marine Science*, *54*, 283–299, 1997.

Melling, H., The formation of a haline shelf front in wintertime in an ice-covered Arctic sea, *Continental Shelf Res.*, *13*, 1123–1147, 1993.

Melling, H., Y. Gratton, and G. Ingram, Ocean circulation within the North Water polynya of Baffin Bay, *Atmosphere-Ocean*, *39*, 301–325, 2000.

Meybeck, M., H. H. Dürr, S. Roussennac, and W. Ludwig, Regional seas and their interception of riverine fluxes to oceans, *Mar. Chem.*, *10*, 301–325, 2007.

Miller, L. A., et al., Carbon distributions and fluxes in the North Water, 1998 and 1999, *Deep-Sea Res. II*, *49*, 5151–5170, 2002.

Millero, F. J., *Chemical Oceanography*, Taylor & Francis, 2006.

Mills, E. L., and R. O. Fournier, Fish production and the marine ecosystems on the Scotian Shelf, eastern Canada, *Mar. Biol.*, *54*, 101–108, 1979.

Morel, F. M. M., and J. G. Hering, *Principles and Applications of Aquatic Chemistry*, John Wiley and Sons, New York, NY, USA, 1993.

Morison, J., J. Steele, and R. Andersen, Hydrography of the upper Arctic Ocean measured from the nuclear submarine U.S.S. Pargo, *Deep-Sea Res. I*, *45*, 15–38, 1998.

Moritz, R. E., C. M. Bitz, and E. J. Steig, Dynamics of recent climate change in the Arctic, *Science*, *297*, 1497–1502, 2002.

Mousseau, L., L. Legendre, and L. Fortier, Dynamics of size-fractionated phytoplankton and trophic pathways on the Scotian Shelf and at the shelf break, northwest Atlantic, *Aquat. Microb. Ecol.*, *10*, 149–163, 1996.

Mucci, A., B. Lansard, L. A. Miller, and T. N. Papakyriakou, CO_2 fluxes across the air-sea interface in the Southeastern Beaufort Sea: the ice-free period, *J. Geophys. Res.*, *297*, 1497–1502, 2010.

Mucci, A., et al., *Organic and inorganic fluxes, In: On Thin Ice: A synthesis of the Canadian Arctic Shelf Exchange Study (CASES)*, Aboriginal Issue Press, University of Manitoba, Winnipeg, Canada, 2008.

Mundy, C. J., et al., Contribution of under-ice primary production to and ice-edge upwelling phytoplankton bloom in the Canadian Beaufort Sea, *Geophys. Res. Lett.*, *36*, L17,601, 2009.

Munk, W. H., Abyssal recipes, *Deep Sea-Res.*, *13*, 709–730, 1966.

Naegler, T., P. Ciais, K. Rodgers, and I. Levin, Excess radiocarbon constraints on air-sea gas exchange and the uptake of CO_2 by the oceans, *Geophys. Res. Lett.*, *33*, L11,802, 2006.

Najjar, R., et al., Carbon budget for the continetal shelf of the eastern United States: A preliminary synthesis, *Ocean Carbon and Biogeochemistry News*, *3*, 1–4, 2010.

Nightingale, P. D., G. Malin, C. S. Law, A. J. Watson, P. S. Liss, M. I. Liddicoat, J. Boutin, and R. C. Upstill-Goddard, In situ evaluation of the air-sea gas exchange parameterizations using novel conservative and volatile tracers, *Global Biogeochemical Cycles*, *14*, 373–387, 2000.

Olsen, A., K. R. Brown, M. Chierici, T.Johannessen, and C. Neill, Sea-surface CO_2 fugacity in the subpolar North Atlantic, *Biogeosciences*, *5*, 535–547, 2008.

Omar, A. M., A. Olsen, T.Johannessen, M. Hoppema, H. Thomas, and A. V. Borges, Spatiotemporal variations of fCO_2 in the North Sea, *Ocean Sci.*, *6*, 77–89, 2010.

Orr, J. C., et al., Anthropogenic ocean acidification over the twenty-first century and its impact on calcifying organisms, *Nature*, *437*, 681–686, 2005.

Osterroht, C., and H. Thomas, New production enhanced by nutrient supply from non-Redfield remineralisation of freshly produced organic matter, *J. Mar. Syst.*, *25*, 33–46, 2000.

Pabi, S., G. L. van Dijken, and K. R. Arrigo, Primary production in the Arctic Ocean, 1998-2006, *J. Geophys. Res.*, *113*, C08,005, 2008.

Padin, X. A., C. G. Castro, A. F. Rios, and F. F. Pérez, fCO_2^{sw} variability in the Bay of Biscay during ECO cruises, *Continental Shelf Res.*, *28*, 904–914, 2008.

Pearson, P. N., and M. R. Palmer, Atmospheric carbon dioxide concentrations over the past 60 million years, *Nature*, *406*, 695–699, 2000.

Peng, T.-H., J.-J. Hung, R. Wanninkhof, and F. J. Millero, Carbon budget in the East China Sea in spring, *Tellus*, *51*, 531–540, 1999.

Penn, J. R., *Rivers of the world: a social, geographical and environmental sourcebook*, ABC-CLIO, Inc., Santa Barbara, CA, USA, 2001.

Peterson, B., R. M. Holmes, J. McClelland, C. J. Vorosmarty, R. B. Lammers, A. I. Shiklomanov, I. A. Shiklomanov, and S. Rahmstorf, Increasing river discharge to the Arctic Ocean, *Science*, *298*, 2171–2173, 2002.

Peterson, B., J. McClelland, R. Curry, R. M. Holmes, J. E. Walsh, and K. Aagaard, Trajectory shifts in the arctic and subarctic freshwater cycle, *Science*, *313*, 1061–1066, 2006.

Petit, J. R., et al., Climate and atmospheric history of the past 420,000 years from the Vostok ice core, Antarctica, *Nature*, *399*, 429–436, 1999.

Petrie, B., Current response at the shelf break to transient wind forcing, *J. Geophys. Res.*, *88*, 9567–9578, 1983.

Petrie, B., Does the North Atlantic Oscillation affect hydrographic properties on the Canadian Atlantic continental shelf?, *Atmosphere-Ocean*, *45*, 141–151, 2007.

Petrie, B., and P. C. Smith, Low-frequency motions on the Scotian Shelf and slope, *Atmosphere*, *15*, 117–140, 1977.

Petrie, B., B. J. Topliss, and D. G. Wright, Coastal upwelling and eddy development off Nova Scotia, *J. Geophys. Res.*, *29*, 12,979 – 12,991, 1987.

Petrie, B., K. Drinkwater, D. Gregory, R. Pettipas, and A. Sandström, Temperature and salinity atlas for the Scotian Shelf and the Gulf of Maine, *Can. Tech. Rep. Hydrogr. Ocean Sci.*, *171*, 1996.

Petrie, B., P. Yeats, and P. Strain, Nitrate, silicate and phosphate atlas for the Scotian Shelf and the Gulf of Maine, *Can. Tech. Rep. Hydrogr. Ocean Sci.*, *203*, 1999.

Platt, T., D. Bird, and S. Sathyendranath, Critical depth and marine primary production, *Proc. R. Soc. London, Ser. B*, *246*, 205–217, 1991.

Previdi, M., K. Fennel, J. Wilkin, and D. Haidvogel, Interannual variability in atmospheric CO_2 uptake on the northeast U.S. continental shelf, *J. Geophys. Res.*, *114*, G04,003, 2009.

Prinsenberg, S., and J. Hamilton, Monitoring the volume, freshwater and heat fluxes passing through Lancaster Sound in the Canadian Arctic Archipelago, *Atmosphere-Ocean*, *43*, 1–22, 2005.

Rahmstorf, S., Ocean circulation and climate during the past 120,000 years, *Nature*, *419*, 207–214, 2002.

Redfield, A. C., B. H. Ketchum, and F. A. Richards, *The influence of organisms on the composition of sea water, v. 2, in The Sea*, Interscience, 1963.

Renaud, P. E., A. Riedel, C. Michel, N. Morata, M. Gosselin, T. Juul-Pedersen, and A. Chiuchiolo, Seasonal variation in benthic community oxygen demand: A respsonse to an ice algal bloom in the Beaufort Sea, Canadian Arctic?, *J. Marine Systems*, *67*, 1–12, 2007.

Revelle, R., and H. E. Suess, Carbon dioxide exchange between atmosphere and ocean and the question of an increase of atmospheric CO_2 during the past decades, *Tellus*, *9*, 18, 1957.

Richerol, T., A. Rochon, S. Blasco, D. B. Scott, T. M. Schell, and R. J. Bennett, Distribution of dinoflagellate cysts in surface sediments of the Mackenzie Shelf and Amundsen Gulf, Beaufort Sea (Canada), *J. Marine Systems*, *74*, 825–839, 2008.

Riebesell, U., I. Zondervan, B. Rost, P. D. Tortell, R. E. Zeebe, and F. M. M. Morel, Reduced calcification of marine plankton in response to increased atmospheric CO_2, *Nature*, *407*, 364–367, 2000.

Riedel, A., C. Michel, and M. Gosselin, Seasonal study of sea-ice exopolymeric substances on the Mackenzie Shelf: implications for transport of sea-ice bacteria and algae, *Mar. Ecol. Prog. Ser.*, *45*, 195–206, 2006.

Riedel, A., C. Michel, M. Gosselin, and B. LeBlanc, Winter-spring dynamics in sea-ice carbon cycling in the coastal Arctic Ocean, *J. Marine Systems*, *74*, 918–932, 2008.

Rudels, B., The outflow of polar water through the Arctic Archipelago and the oceanographic conditions in Baffin Bay, *Polar Research*, *4*, 161–180, 1986.

Rudels, B., E. P. Jones, L. G. Anderson, and G. Kattner, *On the origin and circulation of the Atlantic layer and intermediate depth waters in the Arctic Ocean, in: The Polar Oceans and Their Role in Shaping the Global Environment*, AGU, Washington, D.C., USA, 1994.

Rudels, B., L. G. Anderson, and E. P. Jones, Formation and evolution of the surface mixed layer and halocline of the Arctic Ocean, *J. Geophys. Res.*, *101*, 8807–8821, 1996.

Ryther, J. H., and W. M. Dunstan, Nitrogen, phosphorus, and eutrophication in the coastal marine environment, *Science*, *171*, 1008–1013, 1971.

Sabine, C. L., et al., The oceanic sink for anthropogenic CO_2, *Science*, *305*, 367–371, 2004.

Salisbury, J. E., D. Vandemark, C. W. Hunt, J. W. Campbell, W. R. McGillis, and W. H. McDowell, Seasonal observations of surface waters in two Gulf of Maine estuary-plume systems: relationships between watershed attributes, optical measurements and surface pCO_2, *Estuarine, Coastal and Shelf Science*, *77*, 245–252, 2008.

Sambrotto, R. N., et al., Elevated consumption of carbon relative to nitrogen in the surface ocean, *Nature*, *363*, 248–250, 1993.

Schartau, M., A. Engel, J. Schröter, S. Thoms, C. Völker, and D. Wolf-Gladrow, Modelling carbon overconsumption and the formation of extracellular particulate organic carbon, *Biogeosciences*, *4*, 433–454, 2007.

Schiettecatte, L.-S., F. Gazeau, C. van der Zee, N. Brion, and A. V. Borges, Time series of the partial pressure of carbon dioxide (2001-2004) and preliminary inorganic carbon budget in the Scheldt Plume (Belgian coastal waters), *Geochem. Geophys. Geosyst.*, *7*, Q096,009, 2006.

Schiettecatte, L.-S., H. Thomas, Y. Bozec, and A. V. Borges, High temporal coverage of carbon dioxide measurements in the southern bight of the North Sea, *Marine Chemistry*, *106*, 161–173, 2007.

Schuster, U., and A. J. Watson, A variable and decreasing sink for atmospheric co_2 in the north atlantic, *J. Geophys. Res.*, *112*, C11,006, 2007.

Schuster, U., A. J. Watson, N. R. Bates, A. Corbière, M. Gonzalez-Davila, N. MEtzl, D. Pierrot, and M. Santana-Casiano, Trends in North Atlantic sea-surface fCO_2 from 1990 to 2006, *Deep-Sea Res. II*, *56*, 620–629, 2009.

Semiletov, I., A. Makshtas, S.-I. Akasofu, and E. Andreas, Atmospheric CO_2 balance: The role of Arctic sea ice, *Geophys. Res. Lett.*, *31*, L05,121, 2004.

Semiletov, I., , I. I. Pipko, I. Repina, and N. E. Shakhova, Carbonate chemistry dynamics and carbon dioxide fluxes across the atmosphere-ice-water interfaces in the Arctic Ocean: Pacific sector of the Arctic, *J. Mar. Syst.*, *66*, 204–226, 2007.

Serreze, M. C., et al., Observational evidence of recent change in the northern high-latitude environment, *Clim. Change*, *46*, 159–207, 2000.

Serreze, M. C., et al., The large-scale freshwater cycle of the Arctic, *J. Geophys. Res.*, *111*, C11,010, 2006.

Siegel, D. A., S. C. Doney, and J. A. Yoder, The North Atlantic spring phytoplankton bloom and Sverdrup's critical depth hypothesis, *Science*, *296*, 730–733, 2002.

Sigman, D. M., and E. A. Boyle, Glacial/interglacial variations in atmospheric carbon dioxide, *Nature*, *407*, 859–869, 2000.

Smith, S. V., and J. T. Hollibaugh, Coastal metabolism and the ocean organic carbon balance, *Rev. Geophys.*, *31*, 75–89, 1993.

Smith, S. V., and F. T. Mackenzie, The ocean as a net heterotrophic system: implications from the carbon biogeochemical cycle, *Global Biogeochem. Cycles*, *1*, 187–198, 1987.

Smith, W. O., and L. L. Gordon, Hyperproductivity of the Ross Sea (Antarctica) polynya during austral spring, *Geophys. Res. Lett.*, *24*, 233–236, 1997.

Steele, M., and T. Boyd, Retreat of the cold halocline layer in the Arctic Ocean, *J. Geophys. Res.*, *103*, 10,419–10,435, 1998.

Stewart, R. E., et al., The Mackenzie GEWEX study: The water and energy cycles of a major North American river basin, *Bulletin of the American Meteorol. Society*, *79*, L24,308, 1998.

Stroeve, J., M. M. Holland, W. Meier, T. Scambos, and M. Serreze, Arctic sea ice decline: Faster than forecast, *Geophys. Res. Lett.*, *34*, L09,501, 2007.

Sweeney, C., E. G. nd Andrew R. Jacobson, R. M. Key, G. McKinley, J. L. Sarmiento, and R. Wanninkhof, Constraining global air-sea gas exchange for CO_2 with recent bomb ^{14}C measurements, *Global Biogeochem. Cycles*, *21*, GB2015, 2007.

Takahashi, T., J. Olafsson, J. G. Goddard, D. W. Chipman, and S. G. Sutherland, Seasonal variation of CO_2 and nutrients in the high-latitude surface oceans: A comparative study, *Global Biocheochem. Cycles*, *7*, 843–878, 1993.

Takahashi, T., et al., Global sea-air CO_2 flux based on climatological surface ocean pCO_2, and seasonal biological and temperature effects, *Deep-Sea Res. II*, *49*, 1601–1622, 2002.

Takahashi, T., et al., Climatological mean and decadal changes in surface ocean pCO_2, and net sea-air CO_2 flux over the global oceans, *Deep-Sea Res. II*, *56*, 554–577, 2009.

Takeda, S., Influence of iron availability on nutrient consumption ratio of diatoms in oceanic waters, *Nature*, *393*, 774–777, 1998.

Taylor, A. H., R. J. Geider, and F. J. H. Gilber, Seasonal and latitudinal dependencies of phytoplankton carbon-to-chlorophyll a ratios: Results of a modelling study, *Marine Ecology Progress Series*, *152*, 51–66, 1997.

Thomas, H., and B. Schneider, The seasonal cycle of carbon dioxide in baltic sea surface waters, *J. Marine Systems*, *22*, 53–67, 1999.

Thomas, H., V. Ittekkot, C. Osterroht, and B. Schneider, Preferential recycling of nutrients - the ocean's way to increase new production and to pass nutrient limitation?, *Limnol. Oceanogr.*, *44*, 1999–2004, 1999.

Thomas, H., Y. Bozec, K. Elkalay, and H. J. W. de Baar, Enhanced open ocean storage of CO_2 from shelf sea pumping, *Science*, *304*, 1005–1008, 2004.

Thomas, H., Y. Bozec, H. J. W. de Baar, K. Elkalay, M. Frankignoulle, L.-S. Schiettecatte, G. Kattner, and A. V. Borges, The carbon budget of the North Sea, *Biogeosciences*, *2*, 87–96, 2005a.

Thomas, H., Y. Bozec, K. Elkalay, H. J. W. de Baar, A. V. Borges, and L.-S. Schiettecatte, Controls of the suface water partial pressure of CO_2 in the North Sea, *Biogeosciences*, *2*, 323–334, 2005b.

Thomas, H., F. Prowe, I. D. Lima, S. C. Doney, R. Wanninkhof, R. J. Greatbatch, U. Schuster, and A. Corbière, Changes in the North Atlantic Oscillation influence CO_2 uptake in the North Atlantic over the past 2 decades, *Global Biogeochem. Cycles*, *22*, doi: 10.1029/2007GB003,167, 2008.

Thomas, H., L.-S. Schiettecatte, K. Suykens, Y. J. M. Koné, E. H. Shadwick, A. E. F. Prowe, Y. Bozec, H. J. W. de Baar, and A. V. Borges, Enhanced ocean carbon storage from anaerobic alkalinity generation in coastal sediments, *Biogeosciences*, *6*, 267–274, 2009a.

Thomas, H., D. Unger, J. Zhang, K.-K. Liu, and E. H. Shadwick, *Watersheds, Bays, and Bounded Seas. The Science and Management of Semi-Enclosed Marine Systems*, chap. 9, Island Press, 2009b.

Thomas, H., et al., Rapid decline of the CO_2 buffering capacity in the North Sea and implications for the North Atlantic Ocean, *Global Biogeochem. Cycles*, *21*, doi: 10.1029/2006GB002,825, 2007.

Thompson, D. W., and J. M. Wallace, Regional climate impacts of the Northern hemisphere annular mode, *Science*, *293*, 85–89, 2001.

Toggweiler, J. R., Variation of atmospheric CO_2 by ventilation of the ocean's deepest water, *Paleoceanography*, *14*, 571–588, 1999.

Toggweiler, J. R., J. L. Russell, and S. R. Carson, Midlatitude westerlies, atmospheric CO_2, and climate change during the ice ages, *Paleoceanography*, *21*, PA2005, 2006.

Toggweiller, J. R., Carbon overconsumption, *Nature*, *363*, 210–211, 1993.

Towsend, D. W., M. D. Keller, P. M. Holligan, S. G. Ackleson, and W. Balch, Blooms of the coccolithophore *Emiliania hyxleyi*with respect to hydrography in the Gulf of Maine, *Continental Shelf Res.*, *14*, 979–1000, 1994.

Tremblay, J.-E., K. Simpson, J. Martin, L. M. Y. Gratton, D. Barber, and N. M. Price, Vertical stability and the annual dynamics of nutrients and chlorophyll fluorescence in the coastal, southeast Beaufort Sea, *J. Geophys. Res.*, *113*, C07S90, 2008.

Tsunogai, S., S. Watanabe, , S. Nakamura, T. Ono, and T. Sato, A preliminary study of carbon system in the East China Sea, *J. Oceangr.*, *53*, 9–17, 1997.

Tsunogai, S., S. Watanabe, and T. Sato, Is there a 'continental shelf pump' for the absorption of atmospheric CO_2?, *Tellus*, *51*, 701–712, 1999.

Ullman, D. J., G. A. McKinley, V. Bennington, and S. Dutkiewicz, Trends in the North Atlantic carbon sink: 1992-2006, *Global Biogeochem. Cycles*, *23*, GB4011, 2009.

Umoh, J. U., and K. R. Thompson, Surface heat flux, horizontal advection, and the seasonal evolution of water temperature on the Scotian Shelf, *J. Geophys. Res.*, *99*, 20,403 – 20,416, 1994.

Urban, E. R., B. Sundby, P. Malanotte-Rizzoli, and J. M. Melillo (Eds.), *Watersheds, Bays, and Bounded Seas. The Science and Management of Semi-Enclosed Marine Systems*, Island Press, 2009.

Vallières, C., L. Retamal, P. Ramlal, C. L. Osburn, and W. F. Vincent, Bacterial production and microbial food web structure in a large arctic river and the coastal Arctic Ocean, *J. Mar. Sys.*, *74*, 756–773, 2008.

Vandemark, D., J. E. Salisbury, C. W. Hunt, S. Shellito, and J. Irish, Temporal and spatial dynamics of CO_2 air-sea flux in the Gulf of Maine, *submitted to J. Geophys. Res.*, 2010.

Vanderlaan, A. S. M., and C. T. Taggart, Vessel collisions with whales: the probablility of lethal injury based on vessel speed, *Marine Mammal Science*, *23*, 144–156, 2007.

Walsh, J. J., Importance of continental margins in the marine biogeochemical cycling of carbon and nitrogen, *Nature*, *350*, 753–55, 1991.

Wang, S. L., C. T. A. Chen, G. H. Hong, and C. S. Chung, Carbon dioxide and related parameters in the East China Sea, *Continental Shelf Res.*, *20*, 525–544, 2000.

Wanninkhof, R., Relationships between wind speed and gas exhange over the ocean, *J. Geophys. Res.*, *97*, 7373–7382, 1992.

Wanninkhof, R., A. Olsen, and J. Trinanes, Air-sea CO_2 fluxes in the Caribbean Sea from 2002-2004, *J. Mar. Sys.*, *66*, 272–284, 2007.

Watson, A. J., et al., Tracking the variable North Atlantic sink for atmospheric CO_2, *Science*, *326*, 1391–1393, 2009.

Watson, R. T. (Ed.), *IPCC Synthesis Report, Climate Change 2001: A contribution of working groups I, II, and III to the 3rd Assessment Report of the Intergovernmental Panel on Climate Change*, Cambridge University Press, Cambridge, 2001.

Weeks, A., et al., The physical and chemical environment and changes in community structure associated with bloom evolution: the JGOFS North Atlantic bloom experiment, *Deep-Sea Res. II*, *40*, 347–368, 1993.

Weiss, R. F., Carbon dioxide in water and seawater: The solubility of a non-ideal gas, *Mar. Chem.*, *2*, 203–215, 1974.

Weiss, R. F., R. A. Jahnke, and C. D. Keeling, Seasonal effects of temperature and salinity on the partial pressure of CO_2 in seawater, *Nature*, *300*, 511–513, 1982.

Wollast, R., *The Sea*, Wiley, New York, NY, 1991.

Yager, P. L., D. W. R. Wallace, K. M. Johnson, W. O. S. Jr., P. J. Minnett, and J. W. Deming, The Northeast Water polynya as an atmospheric CO_2 sink: A seasonal rectification hypothesis, *J. Geophys. Res.*, *100*, 4389–4398, 1995.

Yamamoto-Kawai, M., and N. Tanaka, Freshwater and brine behaviors in the Arctic Ocean deduced from historical data of $\delta^{18}O$ and alkalinity (1992-2002 a.d.), *J. Geophys. Res.*, *110*, C10,003, 2005.

Yamamoto-Kawai, M., F. A. McLaughlin, E. C. Carmack, S. Nishino, and K. Shimada, Aragonite undersaturation in the Arctic Ocean: effects of ocean acidification and sea-ice melt, *Science*, *326*, 1098–1100, 2009.

Zeebe, R. E., and D. Wolf-Gladrow, *CO_2 in Seawater: Equilibrium, Kinetics, Isotopes*, Elsevier, Amsterdam, 2001.

Zemmelink, H. J., B. Delille, J.-L. Tison, E. J. Hintsa, L. Houghton, and J. W. H. Dacey, CO_2 depositon over the multi-year ice of the western Weddell Sea, *Geophys. Res. Lett.*, *33*, 2006.

Zwanenburg, K. C. T., D. Bowen, A. Bundy, K. Drinkwater, K. Frank, R. O'Boyle, D. Sameoto, and M. Sinclair, *Decadal changes in the Scotian Shelf Large Marine Ecosystem, in: Large Marine Ecosystems of the North Atlantic - Changing States and Sustainability*, Elsevier, 2002.